Development of Structural and Synthetic Tools to Determine the Structure of the Active Ni(I) State of Methyl-Coenzyme M Reductase: Nature's Catalyst for Methane Synthesis, Activation, and Oxidation

by

Christopher John Ohmer

A dissertation submitted in partial fulfillment
of the requirements for the degree of
Doctor of Philosophy
(Chemical Biology)
in the University of Michigan
2023

Doctoral Committee:

Professor Stephen W. Ragsdale, Chair
Assistant Professor Markos Koutmos
Professor Nicolai Lehnert
Professor E. Neil G. Marsh

Christopher Ohmer

cjohmer@umich.edu

ORCID iD: 0000-0002-7357-2611

Dedication

This dissertation is in honor of my late parents Linda R. Ohmer and Gerald N. Ohmer. You were taken both from my life too early for preparation of any kind. While I will not be able to physically see your excitement and pride, I know it will be with me and has always been throughout my life, especially through this major milestone. I would like to discuss my parents briefly as a tribute.

Gerald "Jerry" Ohmer was a goofy man. He exuded infectious humor. My dad was very adamant about me joining sports, thinking I would have been an athlete as a son. Boy was that a huge miscalculation, because I endured wrestling for 3 full years and hated every single moment of it. At the end of his life, I could tell how proud he was of me and I'm very thankful for that. My dad was a bit of a troubled man, and I believe some of that was passed down genetically for me and was exacerbated by graduate school. However, he became very soft in his last couple of years and left this world a kindhearted father who was proud of his two children.

My mom instilled my love for the sciences early. She was a biology teacher and counselor for the local school in my rural town and always showed whimsy for Nature and every being derived from it. She was the most supporting person I have ever met and not just to her children but to everyone. My mom was sick with cancer for most of my life, but you would never have known it. She would touch anyone's life that she interacted with. I still, 13 years after she had passed, hear about the lives she touched from her previous students. Words cannot describe the heartbreak I feel that she cannot be here to see where I am today, but I am overfilled with joy at the pride she would feel for me.

I'd like to thank the people that kept me going through grad school, to start I'd like to thank my old master's student mentor, Dr. Rachel Pricer. She showed me a home not just in a lab, but also literally during a very difficult point in my life. Nothing could ever make up for what Rachel and her husband Rob have done for me. They were always there and always supported me. Thank you so much you two. Next is Dr. Stephen Ragsdale for his mentorship, but better yet for believing in me when I did not believe in myself. Steve rejuvenated a love for research when I was devoid of one and about to leave the field entirely. He gave me a purpose for pursuing science, and no words can express the gratitude I have.

Thank you to the previous members of my previous lab, Johnny Mendoza, Minshik Jo, Dr. Jianxin Liu, Dr. Bin Li, David Boggs, and Dr. Jiayi Tian for an incredible amount of support and wonderful friendships. Thank you to the Ragsdale Lab, especially Dr. Anjali Patwardhan and Dr. Angela Fleischacker for the guidance on this incredibly hard project, brain storming, and reading copious amounts of edits. Thank you to Dr. Medhanjali Dasgupta, Dr. Kaiyuan Zheng, Dr. Liu Liu, Dr. Anindita Sarkar, Dr. Katherine Rush, Dr. Seth Wiley, and Kelly Deng, for so much support throughout the years and the wonderful friendships. Also thank you to the current lab students in the lab Kareem Aboulhosn, Claire Griffith, Juan Blume la Torre, and Emerson Ducasse. I look forward to what you all will accomplish in this world.

Finally, thank you to my friends and family. My sister Stacey Pandit who I cannot express how much love I have for. Thank you for so much in my life and helping me navigate my life without our parents. Thank you to Sachin Pandit, my brother-in-law, and Ruby Pandit, my niece. Thank you to my Aunt Terri, Aunt Mary Alice, and my Uncle Mike for the constant checkups throughout my time here and my entire family. I would not be here without any of you. My childhood friends outside of science Gabrielle Davis, Matthew Coggins, and Alex King for

all the laughs and support while going through this time. I cannot imagine not having you all in my life.

Lastly, I want to express how important mental health is while going through graduate school. Thanks to everyone above, especially my mentor Steve for being respectful of my mental state while being here. Many students develop mental illness through this pathway. It's important to understand the struggles of graduate students and to limit the mental anguish many students go through.

Acknowledgements

For this work, I would like to acknowledge the Kern, Yano, and Yachandra lab at Berkley, California who I had the pleasure of spending 4 months in that beautiful area up on the hill. I want to thank Jan Kern, Junko Yano, and Vittal Yachandra for supporting me and guiding me through my DOE award. Thank you all so much for the friendships created and teaching me many fantastic scientific endeavors you are all taking. I want to thank the contributions of this group from, Medhanjali Dasputa, Philipp Simon, Asmit Bhowmick, Stephen Keable Hiroki Makita, Margaret Doyle, Isabel Bogacz, Miao Zhang, Isabella Nangca, and Nicholas Croy. Medhanjali Dusgupta and for my training and our wonderful friendship through the writing of out JIB manuscript. Phillip and Hiroki for their hands-on hard work and fun times. Asmit for helping me with my latest structure that I refined over 150 times. Stephen Keable for being my anaerobic partner at Berkeley. Isabel, Margaret, Miao, Isabella, and Nick for the companionship and making me feel comfortable in a new place.

Thank you to Dr. Flora Meilluer for the guidance in the neutron diffraction studies. Thank you to Dr. Darya Marchany-Rivera and Dr. Aina Cohen for their wonderful efforts in our anaerobic crystallography experimentation. These two made our time spent at SLAC so much fun and such a rewarding experience. I look forward to the next time I will get to see you both this year.

Table of Contents

List of Tables

List of Figures

List of Appendices

Abstract

Methyl-Coenzyme M Reductase (MCR) catalyzes the forward and reverse reactions of methane biosynthesis and anaerobic methane oxidation, respectively. MCR employs radical chemistry via the catalytic Ni cofactor F430, where in the low Ni(I) valence state leads to the CH_3-S bond cleavage of methyl-coenzyme M (CH_3SCoM) generating a methyl radical. The methyl radical abstracts a hydrogen atom from coenzyme-B (HSCoB) to form the heterodisulfide (CoBSSCoM) and the inert, high-energy molecule, methane. Due to MCR's low redox-potential of the Ni(I)/Ni(II) states, MCR is one of the most oxygen sensitive enzymes on the planet as well as one of the hardest enzymes to harvest and purify in the active-Ni(I) state. In the Ragsdale lab, we can purify and activate MCR. Therefore, we can monitor the catalysis of this enzyme in two strategies, structural biology and synthetic radical trapping. Structural biology in MCR has been hindered due to MCR's oxygen sensitivity, as only inhibited inactive-Ni(II) structures have been found. Due to plausible radiation damage of the CH_3-S bond of CH_3SCoM, only inhibitor bound coenzyme M (CoM) forms of the Ni(II) have been elucidated. Also, the radical mechanism proposed for MCR has lacked evidence due to the reactivity of the proposed methyl radical H-atom abstraction resulting in $CoBS^{\cdot}$, which has never been seen. Herein, we have solved these gaps of knowledge by (1) utilizing synthetic chemistry to make radical trapping HSCoB analogues and characterize the reaction with spectroscopy and (2) elucidating the structure of active-Ni(I) using X-ray Free Electron Laser (XFEL) femtosecond serial crystallography. In a synthetic approach, we synthesized a HSCoB analogue containing an aryl thiol to delocalize the

radical intermediate, thus, sharpening the thiyl radical peak via EPR. Furthermore, we employ XFEL serial crystallography to obtain what may be the first Ni(I) active structure revealing a very dynamic structure with high b-factors as well as novel Ni coordination distances. This knowledge will further the fields of methane mitigation with an understanding of the active Ni(I) MCR structure and biofuel production, and biocatalysis by further proving the radical mechanism by which this enzyme participates in CH functionalization.

Chapter 1 Introduction to Methanogenesis and Methyl Coenzyme Reductase

1.1 The Janus Face of Methane and The Methane Cycle

Methane is very powerful greenhouse gas related to climate change. While CO_2 is more abundant in the atmosphere, methane is 23 times more efficient in absorbing heat radiation, but over a 20 year span it is estimated that the social cost of methane emissions is 50-100 times greater than CO_2 [1]. Methane is known as a short-lived climate pollutant with an atmospheric lifetime of about a decade before being removed through oxidation by hydroxyl radicals in the troposphere as well as anaerobic and aerobic methanotrophs. Climate change brought about by an increase in methane (and CO_2) emissions is evident through the increased frequency of severe events including droughts, forest fires, heavy rainfall, coral bleaching, tropical cyclones, and ocean acidification [2,3]. Due to these extreme shifts in weather there are irreversible losses in open marine ecosystems, local losses of species, loss of kelp forests, and animal migration events [2]. The human ecosystem suffers as well. Extreme heat events have caused human mortality and morbidity and have caused increases in vector, food, and water-borne diseases, as well as zoonosis events [4]. Additionally, exposure to wildfire smoke, aeroallergens, and atmospheric dust play major roles in cardiovascular and respiratory diseases brought about by climate change [5]. Even humanitarian crises from climate change have displaced humans in all regions, especially islands, and have brought food insecurity and malnutrition in Africa [3,6]. Furthermore, sustainability of the human species is at great risk from methane emissions. Methane may not only drive climate change due to increasing temperatures. Methane also contributes to ground

level ozone, subjecting the human population to an estimated 500,000 premature deaths due to respiratory and cardiovascular diseases and reducing crop yields. Methane is thought to be responsible for a reduction of 7.1% of wheat, 12.4% of soybeans, 6.1% of maize, and 4.4% of rice yields [7–9].

The emission of methane can be categorized into two subsets called anthropogenic, and natural sources. Anthropogenic methane is considered human-induced and comes from sources such as landfills, rice paddy fields, burning of fossil fuels, and agriculture. Humans have greatly impacted the amount of methane before pre-industrial times attributing about 60% of global methane [5]. Furthermore, anthropogenic methane is expected to increase 15% by 2030 [10]. Three sectors to blame for this increase in methane are fossil fuels, waste, and agriculture. Of these sectors, the major contributions in the fossil fuel sector are attributed to oil and gas use. In agriculture, livestock are the largest contributors to methane due to biologic methane emitting microbes in the rumen of cattle. Similarly, in the waste sector, methanogenic microbes in landfills are the major contributor [5].

Natural sources of methane are found through several ecological areas where there is decomposition of organic material, such as the largest contributor wetlands. Natural sources of methane can be grouped into three categories: pyrogenic, thermogenic, and biogenic. Pyrogenic sources come from incomplete combustion from burning of organic matter. Thermogenic sources are through geological processes, like hydrothermal vents, and marine/terrestrial seeps. Biogenic methane is produced by biological sources, specifically microbes called methanogens [11]. Methanogens are thought to produce about 1 gigaton of methane per year by methanogenesis [12].

Methane levels in the atmosphere, thus, are controlled by its various sources including industrial and natural sources in equilibrium with methane sinks in the form of methanotrophic

bacteria and archaea as well as oxidization by hydroxyl radicals in the atmosphere. Large amounts of anthropogenic methane coincide with the increase of global warming because natural sources of methane in the preindustrial era was found to be in a state of equilibrium due to the methane cycle. With the increase of methane that humans cultivated, the methane sources have led to a buildup of methane in our atmosphere. Studying the methanotrophic organisms and the mechanisms of methane formation and oxidation may allow us to reduce methane build up. Furthermore, understanding the biologic methods of methane production can aid us creating biofuels, revealing the other side of this Janus Face.

The second face of methane is its extreme importance in energy use on earth. Natural gas consumption in the United States is the second most utilized energy source encompassing 33% of the U.S.'s total primary energy consumption in 2022 [13]. The central component of natural gas is methane, encompassing around 80% of the total content of small alkanes [14]. The reason why natural gas is so widely used is due to methane's high heat combustion and high-energy output, 56 kJg^{-1}. The source of methane's power comes from the large amount of energy for both homo- and heterolytic cleavage of the C-H bond with a dissociation energy of ~104 kcal mol^{-1} [15]. Methane in natural gas can be made into electricity cleaner by reducing 50% of the carbon footprint and release of toxic emissions and less than one-tenth of the pollutant emission compared to coal [16]. Therefore, we may use methanogens to our advantage. By understanding how these microorganisms can create this clean energy compound, we may be able to harness renewable clean energy and biofuel.

1.1.1 Methane Releasing Archaea

Methanogens belong to the phylum *euryarchaeota* under the well-known kingdom of Archaea. Five orders were first distributed to classify methanogens: *Methanococcales,*

Methanobacteriales, Methanosarcinales, Methanomicrobiales, and *Methanopyrales* [17–19]. These methanogens are a diverse bunch that differ in natural or unnatural habitat, growth temperatures, physiological growth needs, and substrate uptake. Methanogens are wide spread in the gastrointestinal system of animals, insects, and humans, landfills, rice paddy fields, wetlands, geothermal systems, marine and fresh water sediments, and even permafrost [20–22]. *Methanopyrus kandleri* was found from a black smoker chimney in the Guaymas Basin in the Gulf of California [17]. *Methanohalophilus zhilinae* was cultured in the high salt Bosa Lake in Egypt [23]. *Methanolobus psychrophilus,* optimally grow at low temperatures of 18 °C and retains activity in freezing temperatures [24]. Conversely, methanogens are also hyperthermophilic, growing at temperatures up to 110 °C in *M. kandleri,* while many are characterized as thermophilic including *Methanothermobacter murburgensis*, the most studied methanogen [17]. Many methanogens are categorized as mesophiles and grow between moderate conditions of 20-45 °C are composed of the *Methanobacterium, Methanococcus,* and *Methanosarcina* [25].

Methanogens can be categorized based on the substrate to produce methane, primarily consisting of hydrogenotrophic methanogens where CO_2 is used as the substrate and electron donor H_2 as illustrated in Figure 1.1. Hydrogen gas first reduces an electron partner Ferredoxin. Ferredoxin then reduces CO_2 to a formyl group using the C-1 carrier methanofuran. The formyl moiety is then transferred to a second carbon carrier tetrahydromethanopterin and dehydrated to methenyl-tetrahydromethanopterin ($CH{\equiv}H_4MPT$) and is subsequently twice reduced by deazaflavin coenzyme $F_{420}H_2$ to methylene-tetrahydromethanopterin ($CH_2{=}H_4MPT$) and methyl-tetrahydromethanopterin (CH_3-H_4MPT). The reduced methyl group is then transferred to Coenzyme M (HSCoM) to result in Methyl-Coenzyme M (CH_3-SCoM). The final catalytic step of methane production is performed by Methyl-Coenzyme M Reductase with Coenzyme B

(HSCoB) to cleave the C-S bond of methyl-SCoM and release methane while producing a mixed disulfide called CoMSSCoB. Heterodisulfide Reductase (HDR) then reduces the disulfide bond to recycle HSCoM and HSCoB[26]. It has also been found that a few species of methanogens use formate as well as carbon monoxide (CO). This subset includes *M. marburgensis* and *Methanosarcina acetivorans.* In *M. marbergensis*, CO_2 can be made through CO oxidation using Carbon Monoxide Dehydrogenase (CODH) and successively reduced similar to other hydrogenotropic methanogens that use H_2 as reductant. Interestingly, *M. acetivorans* does not have a functioning hydrogenase system, and therefore, cannot use H_2 and CO_2 as its substrates for methanogensis. Instead, this methanogen using CO will produce high amounts of acetate and formate in the process of methanogenesis [27]. Not only can methanogenesis occur through hydrogenotropic means. but there are also other pathways these diverse organisms can create energy and emit one of the most detrimental gases to our atmosphere. These are acetoclastic methanogens present in *Methanosarcinales* and methylotrophic methanogenesis found in *Methanosarcinales*, *Methanomassiliicoccales*, and *Methanobacteriales*.

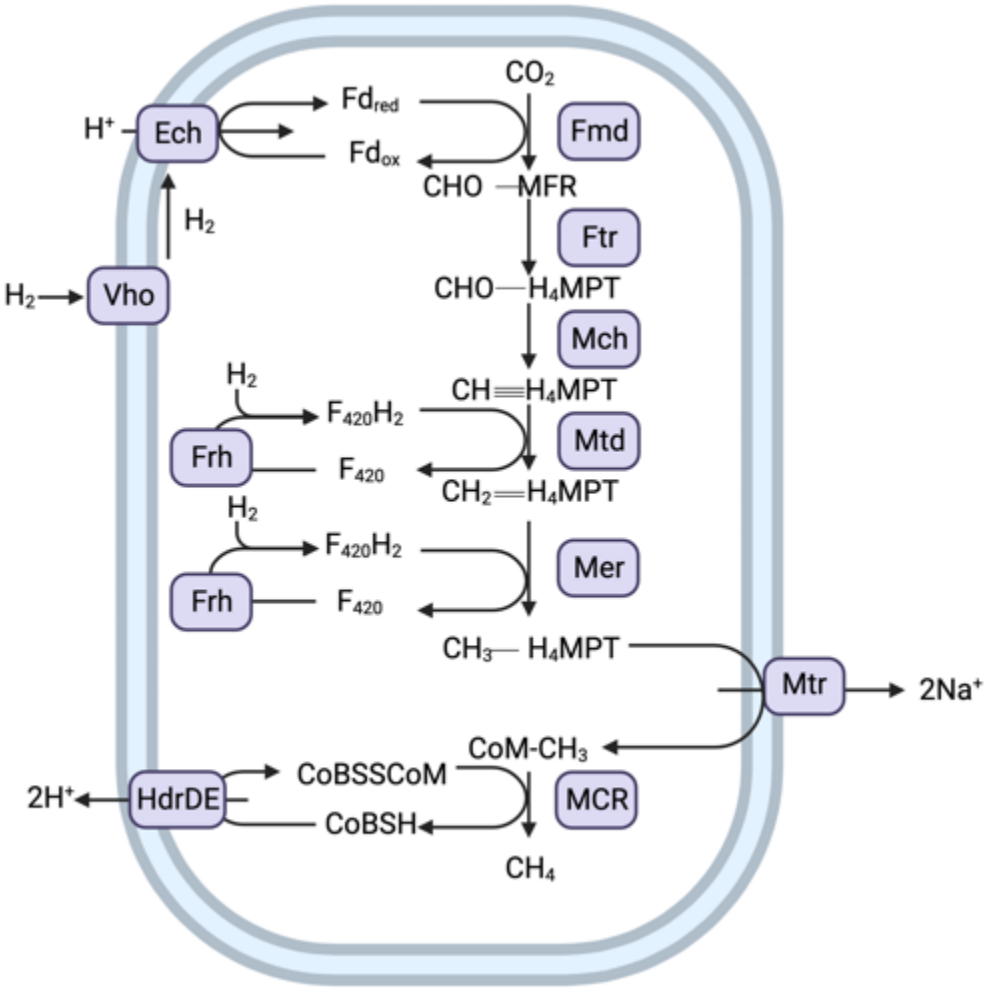

Figure 1.1 Pathway of Hydrogenotrophic Methanogenesis. Biosynthesis pathway of methanogenesis in *M. marburgensis*. Enzymes within the linked pathway are purple and membrane associated enzymes are in contact with the light blue membrane. A list of enzyme abbreviations are as follows: Vho, Methanophenazine-dependent hydrogenase; Ech, Ferredoxin-dependent hydrogenase; Fmd, Formylmethanofuran (CHO-MFR) dehydrogenase; Ftr, Formylmethanofuran-tetrahydromethanopterin (H_4MPT) formyltransferase; Mch, N^5,N^{10}-methenyl- H_4MPT dehydrogenase; Frh, F_{420}-dependent hydrogenase; Mtd, $F_{420}H_2$-dependent methylene- H_4MPT dehydrogenase; Mer, N^5,N^{10}- methylene-H_4MPT reductase;, Mtr N^5-methyl-H^4MPT:coenzyme M (CoM) methyltransferase; MCR, Methyl coenzyme M reductase; HdrDE, Heterodisulfide Reductase. Adapted from Timmers et. al. Created with BioRender.comAcetotrophic methanogens utilize acetate to make both CO_2 and methane as is outlined in Figure 1.2. This includes activation of acetate to acetyl-CoA by acetate kinase, phosphotransacetylase and acetyl-CoA synthetase. Acetyl-CoA is decarbonylated to produce two

C-1 appendages, a methyl group and CO [28]. Carbon monoxide oxidizes to CO_2 catalyzed by either flavodoxin or ferredoxin [29]. In tandem, methyl transfer occurs first to a C-1 carrier molecule tetrahydrosarcinapterin, a derivative of the hydrogenotropic pathway's tetrahydromethanopterin, to produce methyl-sarcinapterin. The methyl group is then transferred to HSCoM by a membrane bound methyltransferase (Mtr), and Methyl Coenzyme M Reductase (MCR) then catalyzes the reduction of the methyl group to methane and the formation of the mixed heterodisulfide CoMSSCoB. The cleavage and cycling of CoMSSCoB in aceticlastic methanogenesis is intriguing. Found in *Methanosarcina* are two distinct pathways for electron transport ultimately reducing and recycling the mixed heterodisulfide, one that is H_2 dependent and one that is H_2 independent. In the H_2-dependent pathway, found in *Methanosarcina barkeri* and *Methanosarcina mazei*, Vho hydrogenase oxidizes H_2 to perpetuate a proton gradient and electrons from this process are transferred to a modified Hdr, $HdrE_1D_1$ to reduce CoMSSCoB. In the H_2-independent pathway a novel Rnf complex replaces Vho by accepting electrons from a ferredoxin or flavodoxin and pumps Na^+ to drive ATP synthesis. Methylotrophic methanogens can operate similar pathways to demethylate methylated compounds, like methanol, methanethiol, choline, methionine, and dimethylethanolamine and transfer the methyl group to HSCoM and contribute to methanogenesis in an entirely new pathway comprising of a wide variety of substrates.

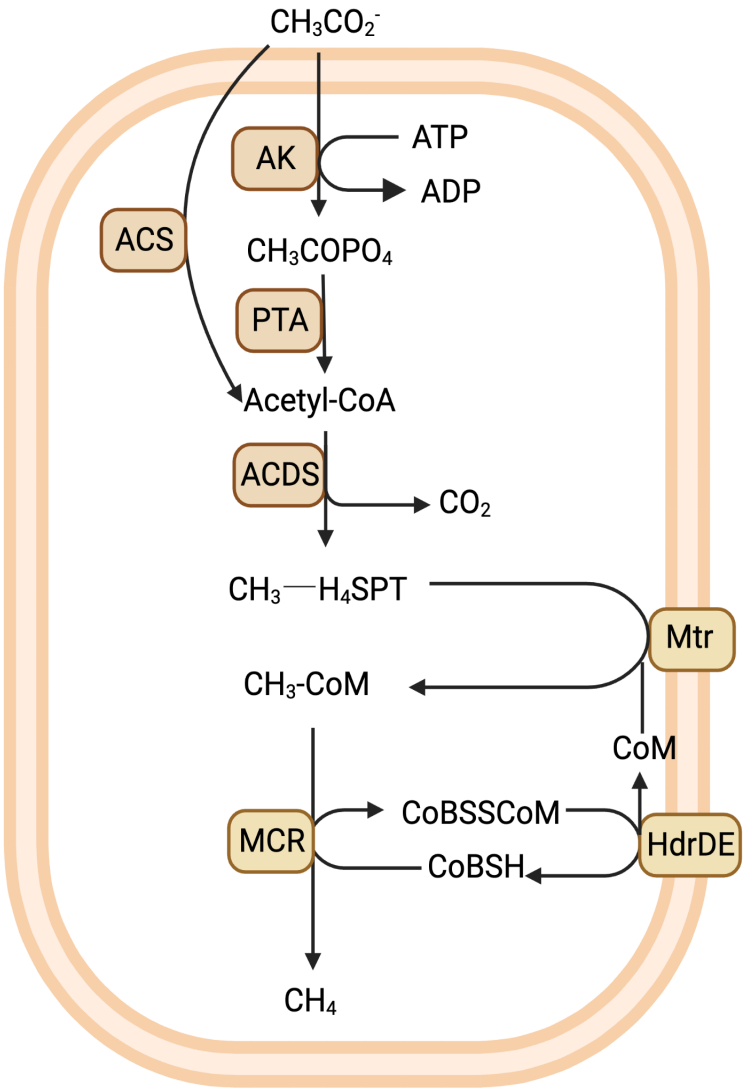

Figure 1.2 Proposed Pathway of Acetoclastic Methanogenesis. Biosynthesis of methane from acetate in aceticlastic methanogenesis involved in M. mazei. Enzymes involved in the pathway are designated as tan ovals. Abbreviations are as follows; AK, acetate kinase; ACS, acetyl coA-synthetase/carbon monoxide dehydrogenase complex; PTA, phosphotransacetylase; ACDS, acetyl-coA decarbonylase/synthase complex; Mtr, N^5-methyl-H^4MPT:coenzyme M (CoM) methyltransferase; MCR, methyl coenzyme M reductase; HdrDE, heterodisulfide reductase. Adapted from Smith and Ingram-Smith. Created with BioRender.com

1.2 Organisms of Methane and Alkane Production and Oxidation

1.2.1 Methanotrophic Archaea

Other Archaea have evolved the ability to live in ocean sediments and terrestrial environments where methane is in high abundance due to fecal release of aquatic beings, hydrothermal vents, and mud volcanoes [30]. ANerobic MEthane Oxidizers, or ANME, using this methanotrophy is accomplished by the use of direct reduction of inorganic ions or by syntrophic partnerships exchanging electrons [31,32]. These archaea belong to a group of ANME and consist of 3-clades: Methanosarcinales of ANME-2 and ANME-3, and *Candidatus methanophagales* of ANME-1 [19]. The mechanism of the oxidation of methane is thought to begin with the reverse reaction of the final and rate limiting step of methanogenesis, more will be discussed about this reaction later. Interestingly, the model methanogen *M. barkeri* has been found to oxidize methane through extracellular electron transfer [33]. Furthermore, the model organism *M. marburgensis* was also able to oxidize methane with a K_M of 10mM for methane [34]. In fact, methylotrophic methanogens already use this pathway where about 25% of the C-1 methyl compounds extracted from the substrate are oxidized to CO_2 to provide reducing equivalents. Studying methanogenesis may also reveal how these archaea are able to oxidize 80% of the methane in marine ecosystems [35].

1.2.2 Deviations of the Core Carbon Canon

Throughout the study of methanogenesis and methanotrophy, the central compound of substrates and products has been canonically C-1 centered. Recently, the oxidation and biosynthesis of alkyl compounds other than methane has been discovered and the core carbon canon has been dismantled. While oxidation of alkanes has been explored in bacteria, archaea have been found to be a largely unexplored subset based on metagenomic studies [36]. In 2016

Laso-Perez *et al.* published the discovery of a dense consortia of archaea and bacteria of which genomes encoding enzymes related to β-oxidation, carbon monoxide dehydrogenase, and methylotrophic enzyme were able to completely oxidize *n*-butane [37]. Furthermore, 16S rRNA of MCR was encoded within the genes of this proposed genus *Candidatus* Syntrophoarchaeum were also found in many of the consortia, leading researchers to believe that this mechanism is naturally widespread for many organisms to perform short chain hydrocarbon oxidation [37]. C-4 oxidation is far from the limit. Recently petroleum alkanes have been found to be oxidized in the Guaymas Basin hydrothermal vents ranging from C-5 to C-14 compounds breaking out of the C-1 paradigm and shifting the biochemistry of methanogens and methanotrophs to alkanogens and alkanotrophs [38]. These findings have spawned a divergent homolog to MCR called, Alkyl-Coenzyme M Reductase (ACR). Furthermore, bulky groups along the long chain alkanes of C-≤13 such as *n*-alkylcyclohexanes and *n*-alkylbenzenes were found to be oxidized by *Candidatus* methanoliparia in an anoxic environment 1,000 to 2,000 meters deep into the sludge and oil reservoirs of the Shengli oilfield in the Dong Ying, China. *C.* methanoliparia encode a unique combination of MCR-ACR and Mtr suggesting that this oxidation is accomplished in a non-syntrophic fashion, although more evidence is needed to be certain of this hypothesis [39].

1.2.3 Environmental Impact of Methanogens and Methane Oxidizers

Although the human disturbance of the methane cycle has had detrimental effects to the world and the human population, we may use nature's tactics for creating methane using methanogens. Methanogens can be utilized as a fuel source and uptake of methane from the atmosphere as well as other productions of relevant fuel and products.

The production of biogas is an enormous application for methanogens providing the fourth and final step of biogas synthesis by digestion of organic matter steps; hydrolysis,

fermentation, acetogenesis, and methanogenesis. With this microorganism consortium, organic matter can be degraded from waste processes like sewage water, manure, microalgae, and genetically modified plants for biogas production [26]. Furthermore, methane can be made not only by the uptake of H_2 and CO_2 characterized as hydrogenotrophic, but also by substrates acetate and many methylated compounds through the process of aceticlastic methanogenesis and methylotrophic methanogenesis, respectively [40,41].

1.3 She Who Lights the Fuse: Methyl Coenzyme M Reductase

1.3.1 Brief Introduction to MCR

Whether methane is created by hydrogenotrophic, aceticlastic, or methylotrophic methanogenesis, all pathways lead to methyl-SCoM and the rate limiting, final step catalyzed by a CH bond activation event from Methyl Coenzyme M Reductase, discovered by R.S. Wolfe in 1971 [42]. This reaction begins with substrates Methyl Coenzyme M (CH_3-SCoM), Coenzyme B (HSCoB), and a low valent cofactor containing a Ni(I) metallocentre and finishes with the potent greenhouse gas methane and a heterodisulfide (CoMSSCoB) as products. As previously stated, there have also been short chain alkanes that have been found to be oxidized as well as depicted in Figure 1.3.

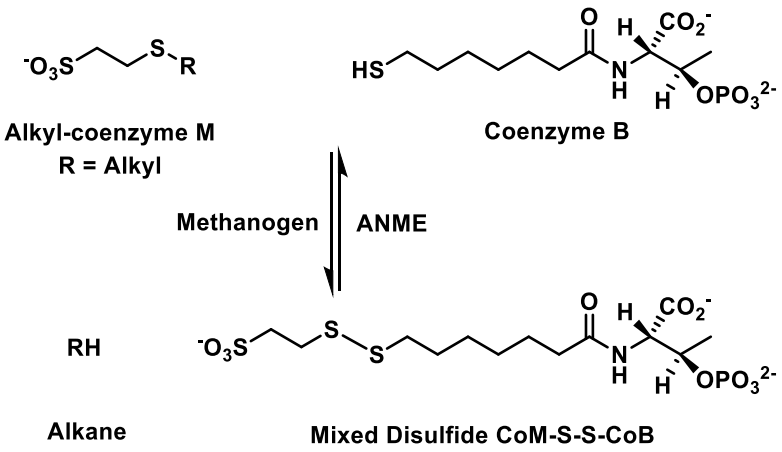

Figure 1.3 Methyl Coenzyme M Reaction. Alkyl-coenzyme M and Coenzyme B react to make an alkane and a mixed disulfide.The activation of the CH bond of HSCoM is accomplished with the Ni-Cofactor F430. This colorful cofactor was discovered in 1978 and found to harbor nickel in 1980 [43,44]. Similar to heme, cobalamin, and chlorophyll, the chromophoric Ni-Cofactor 430, illustrated in Figure 1.4 is a derived tetrapyrrole with a Ni center that can vary between three oxidation states, Ni(I), Ni(II) and Ni(III), where the active form is a forest green Ni(I) [45]. The cofactor F430 has two additional rings, a ɣ-lactam ring along ring B as well as a six membered ring with a carboxylate at ring D.

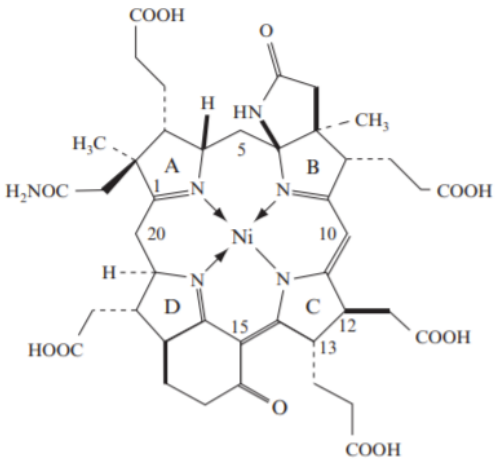

Figure 1.4 Structure of the Ni Cofactor F430. Depicted is the structure of the tetrapyrrole Nickel F430 with ring labeling, appendages, and carbons labelled. (With permission) The power of this cofactor lies in the Ni(I) to Ni(II) redox potential, estimated to be around -650mV in the

native organism [46]. Consequently, this low redox potential is also the enzyme's fatal weakness in aerobic conditions as it is one of the most oxygen sensitive enzymes on the planet. Not only is it a weakness for the active form of the enzyme, but it is what makes MCR incredibly difficult to study as air exposure degrades the enzyme in a matter of seconds, creating a 1 electron oxidation to a yellow Ni(II)-MCR.

1.3.2 MCR Gene Cluster

The MCR operon contains the genes *mcrABGCD. McrA, mcrB,* and *mcrG* encode the three subunits of MCR, which are discussed in the next section. *McrC* and *McrD* are thought to encode accessory proteins that are pivotal in the *in vivo* reduction of MCR and assembly of the Ni-cofactor F430, respectively [47–49]. In a recent paper published by Chadwick *et al.*, cryo-em revealed asymmetric binding of MCR∂ facilitating the accessibility of the active site of MCR for Ni cofactor F430 incorporation, cementing the hypothesis that the ∂ subunit of MCR aids in the assembly of the Ni-cofactor F430 [49].

Interestingly, there are two isoforms of MCR called MCR I and MCR II [50]. In our lab, MCR I expression is found to be increased when cells of *M. marburgensis* are harvested in stationary phase, while MCR II expression is increased with the log phase. The reason for this is unknown, but one could argue that MCR has evolutionarily encoded different MCRs to be expressed in different environments. Both MCR I and MCR II gene clusters encode for the three catalytic subunits, but MCR II lacks *mcrC*. Furthermore, there exists another isoform of MCR called MCR III exclusively found in *Methanococcales* [51]. The MCR operon does differ in ANME-1 where *mcrC* and *mcrD* are not present. A homolog of *mcrC* is found outside of the operon, while *mcrD* is not present within the genome. Additionally, ANME-2a is found to have

mcrD, but lacks *mcrC.* This begs the question of how the Ni cofactor F430 is assembled in the ANME-1 clad.

1.3.3 Difficulties of Heterologous Expression of MCR

Heterologous expression in MCR has been an incredibly difficult task, and still has many hurdles and has yet to provide an enzyme suitable for *in vitro* analysis due to incredibly low activity. The heterologous expression of MCR in *Escherichia coli* is difficult because *E. coli* does not contain the machinery to biosynthesize the Ni-cofactor F430 nor does it encode the enzymes, some cobalamin dependent radical S-adenosyl methionine (SAM) enzymes, that modify the post translational modifications (PTMs) of MCR. Furthermore, doubling times of methanogens and methanotrophs vary and many organisms, especially ANME clades, have doubling times that may take as long as months. Therefore, using other methanogens with the machinery capable of carrying out the Ni-cofactor F430 synthesis and the post translational modifications of MCR with significantly shorter doubling times has been the target for heterologous expression of MCRs from other organisms difficult to culture [52]. Leading the way for the heterologous expression of MCR is the lab of William Metcalf. In 1997 Metcalf, while in Ralph Wolfes lab, established a liposome-mediated transformation using *Methanosarcina* [53]. *Methanosarcina* is a great target for this task as it will grow on a large variety of substrates, such as acetate, methylated compounds, carbon monoxide, and cardon dioxide and hydrogen gas [54]. Developments for developing genetic tools have since included parental strains of a counterselectable marker *hpt* gene. Additionally, these strains contain the ΦC31 site specific recombinase gene and an *attP* site inserted at the *hpt* locus. With this strategy, site specific recombination can insert recombinant plasmids with the complement *attB* sequence into the host chromosome [54]. Recently, Dipti Nayak in the Metcalf lab, now an assistant professor at Berkeley,

developed the first Cas9-mediated genome-editing tool ever seen in archaea using *M. acetivorans*. With this method, insertions and deletions can be accomplished with precise efficiency by homology-directed repair. The speed of which to make these mutants has been reduced as well from an 8 week long process to make a mutant to 3 weeks [55]. Large strides are being made to accomplish heterologous expression so that host organisms are not the sole source for MCR and MCR homologs. Much needs to be done, especially from the *in vitro* side where no heterologously expressed MCR has been able to be purified in its active-Ni(I) form.

1.3.4 Post Translational Modifications

MCR has a significant feature where evolution has led to a slew of unusual post translational modifications as shown in Figure 1.5. In *M. marburgensis,* MCR contains six post translational modifications, a thioglycine, a *S*-methylcysteine, a 5-(*S*)-methylarginine, a 1-*N*-methylhistidine, and a 2-(*S*)-methylglutamine, all discovered by the first crystal structure of the enzyme in Ermler *et. al*. in 1997 and a didehydroaspate found via Mass Spectroscopy (MS) by Wagner *et. al.* in 2016 [56,57]. The function of each of these modifications is not entirely known. From genome analysis, many methanogens lack these PTMs, like *M. maripaludis*, *M. barkeri*, and *M. wolfeii* missing the *S*-methylcysteine, 2-(*S*)-methylglutamine, and didehydroaspartate, respectively [58,59]. Across all methanogenic and methanotrophic archaea, the three PTMs that are conserved are the 1-*N*-methylhistidine, 5-(*S*)-methylarginine, and thioglycine. The genes that encode these three PTMs were previously used as a methanogenesis marker due to its presence universally in methanogenic and methanotrophic archaea [60–62]. Due to the low occurrence of methylarginine and thioglycine in nature, it was thought that these two PTMs were essential for catalysis[58], but this seems to have been negated from MCR growth studies performed by Dipti Nayak *et al.* where deletions to genes encoding enzymes were made using the Cas-9 mediated

genome editing system. Several deletions were made to the cobalamin dependent radical SAM and other hypothesized gene loci to prevent the modifications to the *S*-methylcysteine, and the hypothesized catalytic methyl-arginine and thioglycine as well as the double and triple mutants. It was found in this study that deletion of *McmA*, the gene that encodes the SAM-dependent methyltransferase responsible for the *S*-methylcysteine, grew faster than the wild type at lower temperatures (29°C) and high temperatures (42°C) and thermal stability of the mutant was indistinguishable from the wild type. Based on this data, Nayak *et al.* suggest that the modification is related to catalysis rather than stability or structure of the enzyme. Furthermore, the 5-(*S*)-methylarginine was found to play a significant role in thermal stability of the enzyme, but the double mutant without the 5-(*S*)-methylarginine and thioglycine showed that the thioglycine deletion compensated to global stability of the enzyme without the methyl moiety of 5-(*S*)-methylarginine. Overall, the studies performed using the novel Cas-9 mediated genome editing tool are still done on either *in vivo* growth analysis, or *in vitro* Thermofluor assays of the inactive Ni(II) form of the enzyme. *M. acetivorans* does not contain a hydrogenase system, which is used for the *in vivo* activation of the enzyme. Therefore, catalysis is difficult to directly study with this system [63]. In methanotrophic archaea, there are two conserved PTMs, the 1-*N*-methylhistidine and thioglycine, but the contain two additional posttranslational modifications, 7-hydroxy-tryptophan and *S*-oxymethionine based on the first crystal structure of an ANME-1 clade by Shima *et. al.* in 2012. They suggest the new PTMs may be due to a compensation of the ANME-1 clade's lack of C-methylation machinery resulting in a lack of methylation in the modified arginine and glutamine [64].

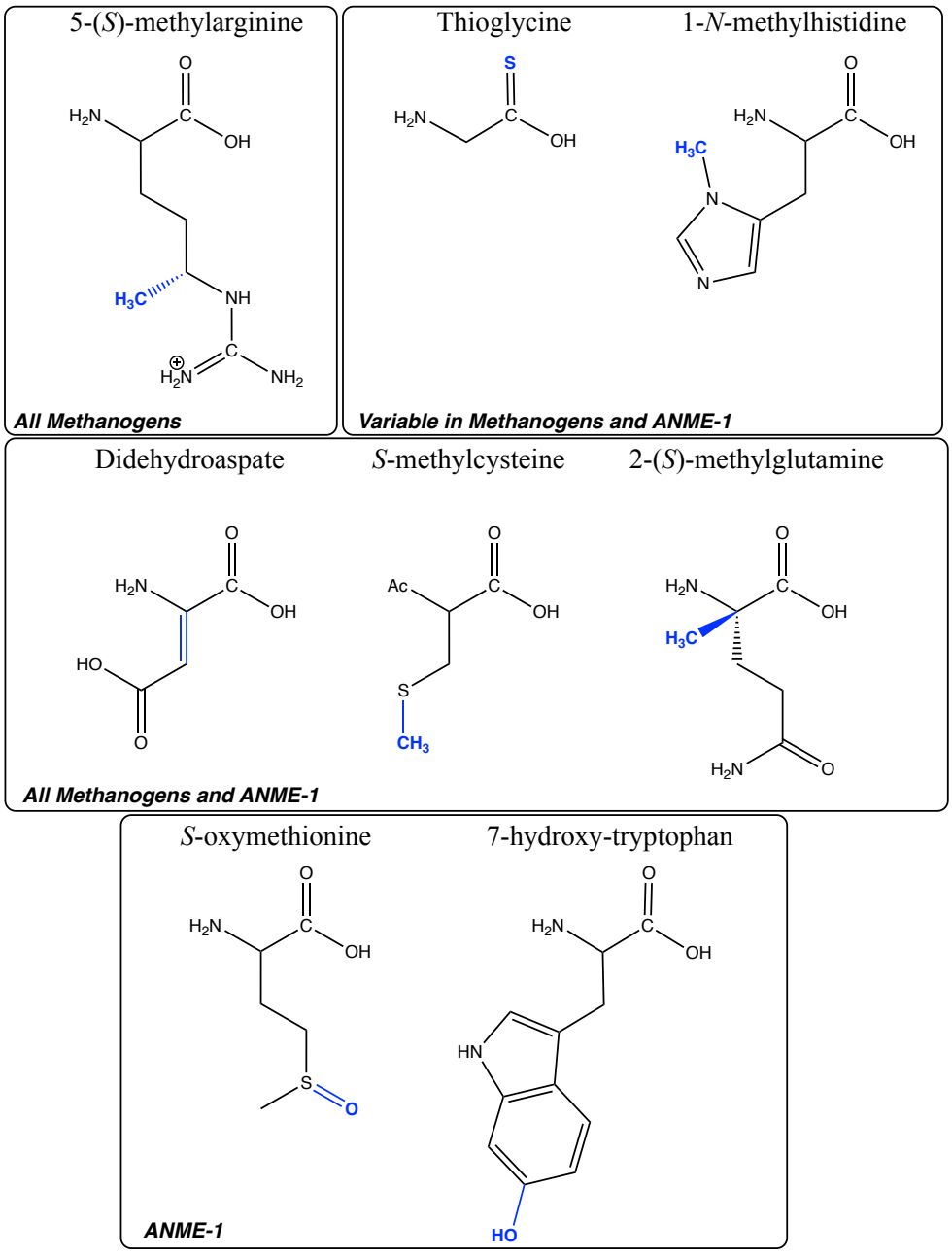

Figure 1.5 Modified Amino Acids Methanogens and ANME-1. Chemical Structures of the posttranslational modification found in MCR of various Methanogens and ANME-1 clades based on crystal structures and mass spectroscopy.***Introduction into the Competing MCR Mechanisms***

MCR is found to be a ternary complex that operates in an ordered bibi enzymatic mechanism, where first CH_3-SCoM enters the active site and is followed by HSCoB[65]. Once

MCR has catalyzed the production of methane, it is presumed that methane leaves the active with subsequent removal of the heterodisulfide CoMSSCoB as shown in Figure 1.6 [65]. Much of the speculation surrounding how MCR is able to catalyze the biosynthesis of methane is comprised of two schools of thought shown in Figure 1.7: (1) a two electron SN_2 mechanism involving a Ni(III) intermediate or (2,3) a one-electron mechanism resulting in a methyl radical and an EPR-silent intermediate Ni(II) Ni species.

In mechanism 1, the Ni(I) state acts as a nucleophile in an S_N2 reaction attacking the methyl group of CH_3-SCoM following the deprotonation of HSCoB to result in a methyl-Ni(III) species and HSCoM in step 1. This methyl-Ni(III) species has never been seen catalytically, but has been chemically generated with methyl-iodide[66]. This is very similar to the methyl transfer of the Ni-cofactor F430 sister metallo-tetrapyrrole cob(I)alamin. In step 2, one electron is then transferred to the methyl-Ni(III) to generate methyl-Ni(II), a thermodynamically difficult reaction, what many have argued to be the difference between the Ni-cofactor F430 and cobalamin. A one electron reduction from a methyl-Ni(III) to methyl-Ni(II) is much easier than the reduction of cob(III)alamin to cob(II)alamin, therefore evolution engineered the Ni-cofactor F430 for the catalysis of methane [67]. In step 3, the deprotonation of HSCoM by the methyl group produces methane and a heterodisulfide anion radical is formed. Finally in step 4, one electron to transferred to the Ni(II) and the heterodisulfide is removed with the completion of enzyme turnover.

In mechanism 2, step 1 starts with the homolytic cleavage of the S-C bond of CH_3-SCoM from a one electron push from the Ni(I) resulting in a methyl radical and a Ni(II) thiolate. The methyl radical then performs a hydrogen atom abstraction from HSCoB to produce •SCoB, a species never seen experimentally. In step 3, the •SCoB reacts with the Ni(II)-thiolate complex

to form the heterodisulfide radical anion, which then transfers to the Ni center to form the heterodisulfide and regenerates MCR to the Ni(I) state.

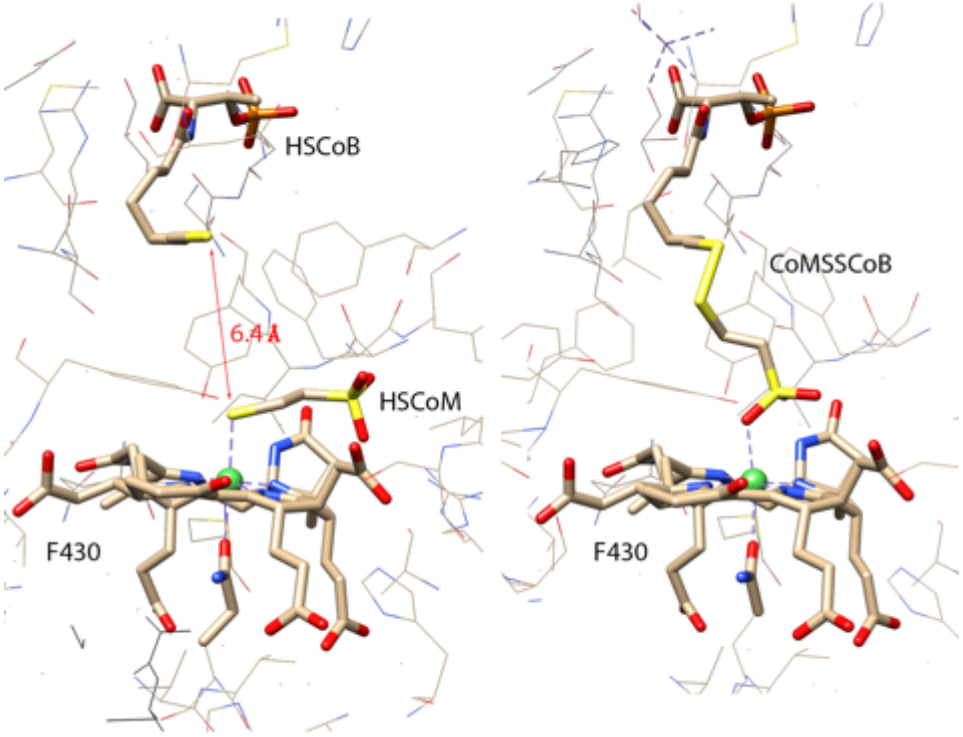

Figure 1.6 Crystal Structure snapshots illustrating hypothesized binding mode before and after catalysis. (Left, PDB: 1MRO) Crystal structure of bound HSCoM and HSCoB prompting the canonically proposed binding mode of a Ni-thiolate. For this binding mode to perform methane catalysis the enzyme must overcome a 6.4Å distance to make the heterodisulfide. (Right, PDB: 1HMB) Crystal structure of bound CoMSSCoB heterodisulfide. The sulfonate group of the CoM side of the heterodisulfide is coordinating the Ni center via an oxygen atom.Mechanism 3 is a recent proposal from Patwardhan *et al.* where the CH_3-SCoM is binding to the Ni metallocentre via the sulfonate group rather than a thiolate. This binding mode is derived from near infrared (NIR) d-d transitions and EPR spectroscopy of CH_3-SCoM bound MCR having similar spectroscopic characteristics of the product state,CoMSSCoB bound MCR, where the sulfonate group of the CoM partition is bound to the Ni center. This was also supported by DFT calculations. Uncovering this binding mode is incredibly important as the understanding of the 6.4Å spatial distance between the two substrates could be resolved.

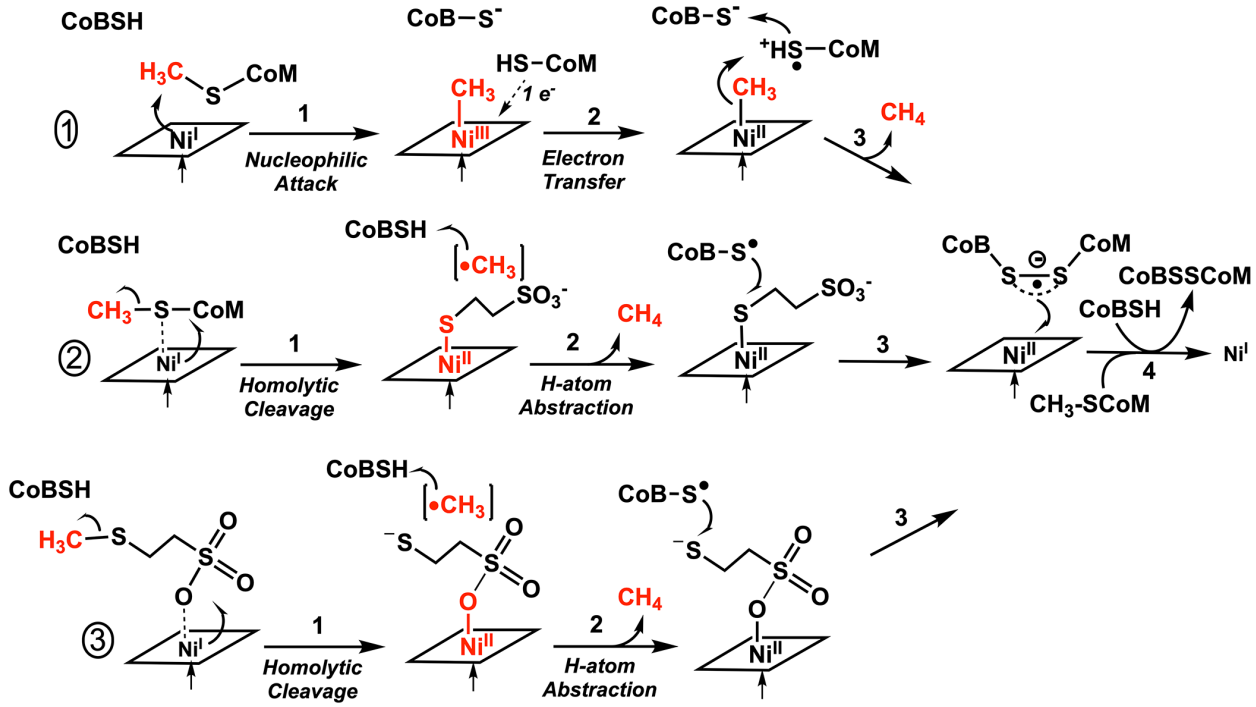

Figure 1.7 Proposed organometallic versus radical mechanisms MCR-catalyzed methane formation. (A) Organometallic mechanism involving nucleophilic attack on methyl-CoM to form a Ni(III)-methyl intermediate (B) Ni(I) promoted homolysis of the methyl-S bond of methyl. (With permission)

Wongnate *et al.* provided the magnetic circular dichroism and rapid freeze quench electron paramagnetic resonance (EPR) studies of the Ni(II) to disprove the SN_2 methyl-Ni mechanism in 2016 . Therefore, the one-electron methyl radical mechanism is found to be the most acceptable due to the experimental evidence provided by Wongnate *et. al.* The methyl radical mechanism and will be the one guiding this thesis.

1.4 Structure of MCR

1.4.1 Methanogenic MCR

The structure of MCR was first elucidated in 1997 by Ermler *et. al.* at the Max Planck Institute in Frankfurt Germany with one crystal structure including bound substrate HSCoB and inhibitor HSCoM, and another in which the heterodisulfide product is bound. We will first discuss the HSCoM- and HSCoB-bound structure.

Using *M. marburgensis* MCR, Ermler *et al.* were able to aerobically crystallize the inactive Ni(II) state of MCR at 1.45Å resolution. This crystal structure of this 300 kDa enzyme revealed a heterohexameric oligomer whose subunits form an α_2, β_2, γ_2 complex $(\alpha\beta\gamma)_2$. The overall structure of MCR shown in Figure 1.8. forms a series of tight α helicies where the subunits of the enzyme have long interfaces, particularly between subunits α and α' and subunits β and β'. Additionally, every subunit has contact to each subunit, except between γ and γ', which . In this structure, densities of the five posttranslational modifications of the thioglycine, *S*-methylcysteine, 5-(*S*)-methylarginine, 1-*N*-methylhistidine, and 2-(*S*)-methylglutamine were found. As previously mentioned, the didehydroaspartate was found later in 2016, but is included in Figure 1.9. The densities that modelled two Ni-cofactor F430s were found to lay sandwiched in α, β, γ, and α' and α', β', γ', and α. Into this alcove there is a 30Å long tunnel that extends to the surface of the protein, as shown in Figure 1.9. In the active site, the Ni-cofactor F430 binds via an axial glutamine side chain oxygen from the opposite protomer's subunit (the α subunit with most contacts in the Ni-cofactor F430 is axially ligated by the glutamine on α') around 2.1Å away. The corphinoid is provided stability by 21 hydrogen bonds, including 15 contacts with the amides from the peptide backbone. The crystal structure and all subsequent crystal structures have a bound inhibitor HSCoM that presumably remains from the purification process to stabilize MCR. The HSCoM is coordinated to the Ni center through its thiol creating a Ni-thiolate species that is, in most crystal structures, around 2.4 Å bond distance. Also interacting

with the S atom of HSCoM are two tyrosine residues both making a contact about 3 Å away. The sulfonate group of HSCoM is harbored by a closely associated arginine providing an ionic interaction that holds very tightly. About 3.3 Å and 6.3 Å away from the S atom of HSCoM, lies a water molecule and the S of HSCoB. This distance is the subject of the new binding mode of mechanism 3 discussed in the previous section. HSCoB is anchored into the active site by ionic interactions with its phosphate and carboxylate group by neighboring arginine residues as well as the post translationally modified 1-*N*-methylhistidine. The phosphate and carboxylate act like a bobber while the heptanoyl chain acts as the fishing line into the active site providing promiscuity that will later be discussed.

The global structure of the heterodisulfide product bound state of MCR very closely resembles the HSCoM- and HSCoB-bound state, but the contacts of the heterodisulfide CoMSSCoB drastically differ in the active site. CoMSSCoB is coordinated to the Ni center and proximal tyrosine residues via the sulfonate oxygen of the CoM side of the heterodisulfide. CoM has shifted from being parallel to the corphinoid ring to a perpendicular orientation. The HSCoB ionic anchor is unperturbed [56].

These two crystal structures have led to the conclusions that the binding mode of CH_3-SCoM acts similarly to the HSCoM inhibitor, but would displace the water molecule during catalysis. Two major problems with concluding this binding mode are that, 1) CH_3-SCoM is not and has never been found within the active site of MCR and 2) No active-Ni(I) structure of MCR has ever been elucidated. For these conclusions to be true, one must picture a large conformational change for either CH_3-SCoM to move 6.4Å to HSCoB for the formation of the heterodisulfide or HSCoB to dive deeper into the active site to produce the disulfide of which there is no evidence as of yet.

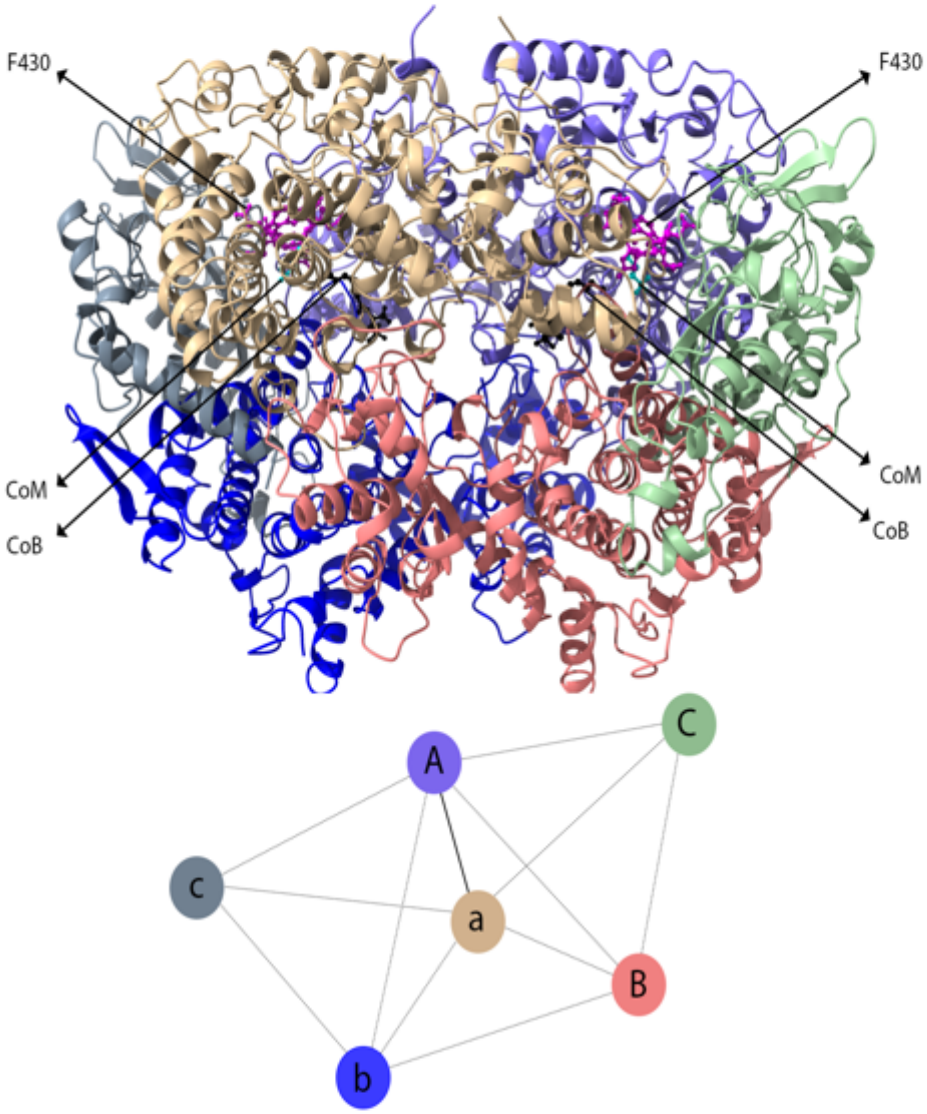

Figure 1.8 Structure of Methyl-Coenzyme M Reductase. (Top) The global structure of MCR (7SUC) where protomer 1 is comprised of subunits α (Purple), β (Salmon), ɣ(Green), while protomer 2 is comprised of α' (Tan), β' (Blue), ɣ'(Gray). HSCoM, HSCoB, and the Ni-F439 are illustrated in green, black, and magenta, respectively. (Bottom) The 12 contacts between the 6 subunits. (With permission) PDB:7SUC

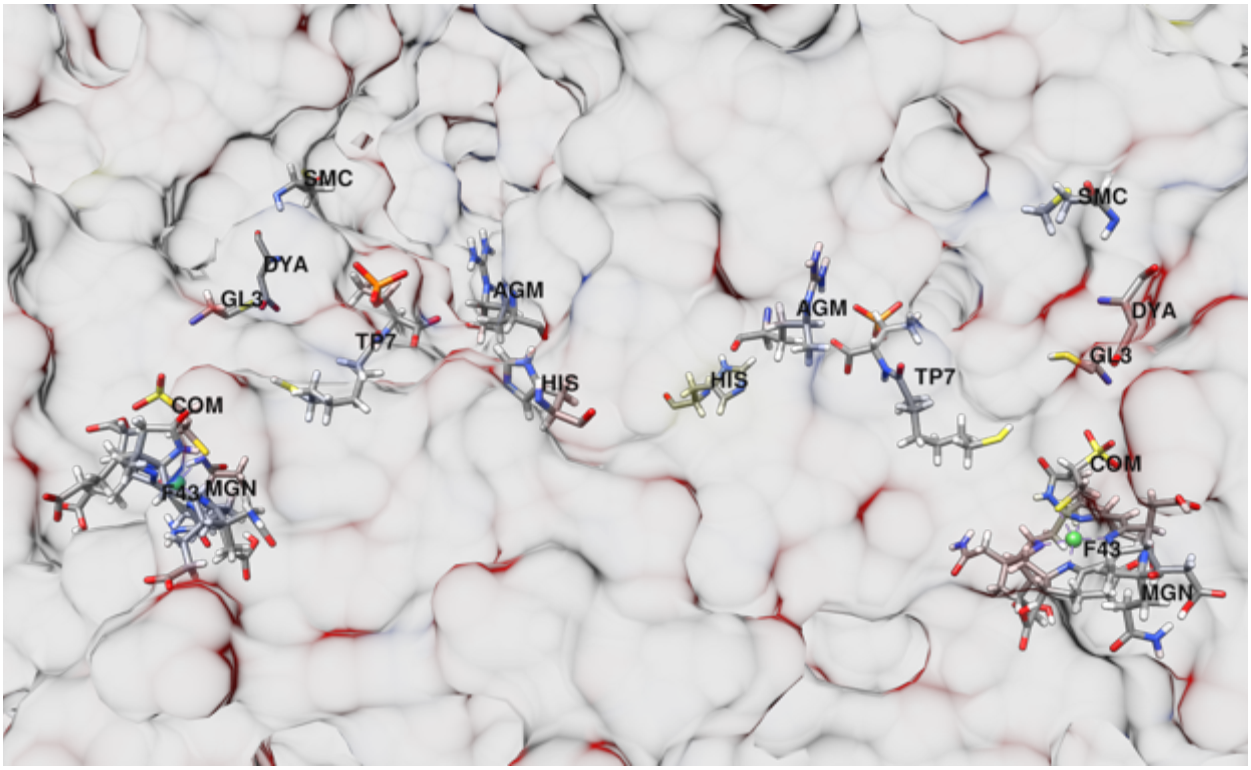

Figure 1.9 Structural location of the six post translational modifications found in MCR of M. marburgensis. Labels of the unnatural modified amino acids are as follows. GL3, thioglycine; SMC, S-methylcysteine; AGM, 5-(S)-methylarginine; HIS, 1-N-methylhistidine; MGN, 2-(S)-methylglutamine; DYA, didehydroaspartate. PDB:7SUC***Methanotrophic MCR***

The structures of methanotrophic MCRs are incredibly difficult to obtain due to their long doubling times. Shima *et al.* avoided this problem in 2004 by collecting large microbial mats of the Black Sea during a submersible exhibition of its anoxic northwestern waters. Rather than attempt to culture a specific ANME clade to make a heterogeneous sample, Shima *et al.* took a large mat of these anaerobic methane oxidizers and immediately lysed the cells using ultrasonication and purified the ANME proteins associated with this mat by salting out with ammonium sulfate and further purification on an anion exchange column. It was found that ANME-1 and ANME-2 clades could be separated via anion exchange chromatography, albeit very heterogeneous. The peak of the ANME-1 clade contained 6 different families of ANME-1. The heterogeneous sample of MCRs was still attempted to be crystallized, albeit not ideal. Three

years after setting up the crystal trays of this sample of ANME-1, two drops contained crystals. With these crystals, Shima *et al.* obtained the first crystal structure of an ANME-1 clad MCR in 2012. This structure of the ANME-1 clade is, unfortunately like all MCR structures, is found in the Ni(II)-inactive form, thus no enzyme activity of the reverse reaction could be measured. Despite the enzyme being purified inactively, many differences between the structure of methanogenic MCR from *M. marburgensis* and this ANME-1 clad were found. One difference of great note is a modification observed in the crystal structure and identified via MS is a methylthio functional group extending out of the $C17^2$ carbon of the Ni-cofactor F430. This addition to the Ni corphinoid ring is made possible due to a nearby residue replacement from a PTM methyl glutamine in methanogenic MCR to a valine in the ANME-1 structure. The post translationally modified methyl glutamine would collide with the methylthio arm of this modified corphinoid. Furthermore, ANME-1 contains five pronounced cysteine residues lining a path, but not a "tunnel" from the modified Ni-cofactor F430 to the protein surface. This chain of cysteines is proposed as a redox-relay system and could be used to activate the Ni center from a Ni(II) to a Ni(I) state, although this system is not found in methanogenic MCR. We could also assume a scavenging strategy is needed for methanogenic MCR as well that is not this redox-relay system. In the crystal structure of the ANME-1 MCR, a thioglycine PTM is present, although MS from the heterogeneous peak that the crystals were grown from show a lack of the thioglycine in 70% of the ANME-1 in the sample. Furthermore, a modified tryptophan is found to be hydroxylated in the 7C position, as described previously in the post translationally modified residue section. This modification is thought to compensate for a lack of the methyl-arginine postranslationally modified in the methanogenic MCR. The lack of methylations observed in the arginine, glutamine, and cysteine could be due to a lack of C-methylation

machinery in ANME-1. Overall, the structural differences of ANME-1 clade from the Black Sea mats may not affect the enzymatic processes, rather may be the result of a complex phylogenetic development and could be an indicator of different living conditions.

1.4.3 Alkyl MCR – Ethane Oxidation

Recent discoveries have shown that MCR homologs can oxidize short chain and long chain alkanes breaking the core carbon canon of what MCR was hypothesized to catalyze in the reverse and forward reaction of the biosynthesis of methane. Similar to ANME, many of these methanogens, or should we call them alkanogens, are very difficult to culture due to their higher doubling time. Luckily, a previous post-doc of Seigo Shima, Tristan Wagner set up his own lab at Max-Planck Institute. Working with Gunther Wegener, Cedric Hahn *et al.* found a new archaeal species was cultured from the Guaymas Basin in The Gulf of California. This species called *Candidatus* Ethanoperedens thermophilum was found to be involved in the large consortia of ethane-oxidizing archaea involved in a symbiotic relationship with other sulfate reducing bacteria known as *Candidatus* Desulfofervidus auxilii [68]. What has made this species incredibly important is its rate of growth. The doubling time of this archaea was found to be incredibly fast at only 7 days. Because of the increased doubling time, culturing the archaea and purification of the MCR homolog associated with ethane oxidation was conceivable and therefore able to be crystallized. Thus, the first crystal structure of an ethyl-coenzyme M Reductase (ECR) at 0.99Å resolution was found and published in 2021 by Hahn *et al.* As with the ANME-1 crystal structure, it was found that the Ni-cofactor F430 had modifications within the corphinoid ring, albeit different from both MCR from *M. marburgensis* and ANME-1. *Ca.* E. thermophilum contained a corphinoid with two methylation sites at C17 and $C17^2$, the second carbon position of the 6-carbon carboxylate ring. Furthermore, the axial glutamine that coordinates the Ni center

via oxygen atom is not present and is replaced with a methionine. The methionine's sulfur atom provides the coordination on the axial position of the Ni center, although this is not the case for other ethane oxidizers because the canonical axial glutamine is conserved in other ethane oxidizing archaea, *Cadidatus* Argoarchaeum ethanivorans for example. As with every MCR and MCR homolog structure, the crystal structure is of the Ni(II)-inactive state and HSCoM and HSCoB are bound in similar locations to *M. marburgensis* and ANME-1 structures of MCR. The active sites of all MCR and MCR homologs are all identical in nature, but this ECR has a slight increase in active site volume with a substitution of a tryptophan causing the aromatic face to point more outwards compared to the canonical phenylalanine. Hahn *et al.* believe that the dimethylated Ni-cofactor F430 can keep the correct position rather than moving into this additional active site volume. Furthermore, xenon pressurized studies of this structure found two sites occupied by Xe. One site was in between the thiols of HSCoM and HSCoB, while the other was found in a hydrophobic cavity between the active site and the protein surface. Using CAVER, Hahn *et al.* confirmed a novel 33Å tunnel connecting these two Xe locations to the outside of the enzyme. It is hypothesized that this tunnel is used for the diffusion of the hydrophobic gas, ethane. Unfortunately, this tunnel was never found in any crystal structure of MCR or other MCR homologs. Regarding PTMs, it was found that ECR contained several methylations along this tunnel including *S*-methylcysteine-354, 3-methylisoluecine-377, 2(*S*)-methylglutamine-445, and N^2-methylhistidine. All other PTMs found in MCR were found in this structure and detected via mass spectroscopy [69] .

1.4.4 Structural Studies Using HSCoB Analogues on M. marburgensis MCR

As previously discussed, the 6.3Å distance between the thiol of HSCoB and the sulfur of CH_3SCoM in the proposed binding mode based on previous crystallographic structures poses a

conundrum. It was thought at this time that the HSCoB induces a conformational change that moves CH_3SCoM closer to the Ni corphinoid and promotes the C-S bond cleavage creating this ordered bibi mechanism. A previous crystallographer in the Ragsdale lab aimed to use structure to uncover what the HSCoB binding might do to promote catalysis. Dey *et al.* synthesized four HSCoB analogues that range in length of the carbon chain of this substrate. Native HSCoB used by MCR contains a heptanoyl chain, therefore Dey synthesized a pentanoyl ($HSCoB_5$), a hexanoyl ($HSCoB_6$), an octanoyl ($HSCoB_8$), and a nonanoyl ($HSCoB_9$) chained Coenzyme B. With these HSCoB analogues, she then co-crystallized each of these substrates with MCR in the Ni(I)-active state under anaerobic conditions. With the help of Peter Cederval, Arwen Pearson, and Carrie Wilmot, crystal structures of each analogue were solved as well as a structure where HSCoB is depleted. Unfortunately, CH_3SCoM was not found within the active nor were the crystals structures of Ni(I)-active MCR. The structures presented were very similar globally to all solved MCR crystal structures. $HSCoB_5$ was found to place the thiol where the second carbon precedes the HSCoB thiol, unsurprisingly. In contrast, the $HSCoB_6$ analogue surprisingly adopts a slight change in its conformation to place the thiol in the same position as the native HSCoB. This analogue was found to slow the catalysis of MCR and bound very tightly to the enzyme with a K_i of 0.1 μM. $HSCoB_8$ shows a thiol that is 2.5Å closer to the thiol of HSCoM and $HSCoB_9$ positions the thiol in a very similar manner suggesting that the extended chains do not bind in an energetically favorable manner due to the hydrophobic nature of the active site pocket. Furthermore, it was found that a water channel is found when HSCoB is not present. This makes attempting to model a HSCoB and water channel a difficult task. Cederval *et al.* also claims to have solved a structure where only 50% of HSCoM is bound. They accomplish this by comparing the atomic displacement parameters (ADP) to the Ni-cofactor F430 and decrease the

occupancy if the ADP factors are higher than the B-factors of the Ni corphinoid. Then, waters are modelled to the extra density that may arise and found 4 waters placed in 50% occupancy of the position of the absent HSCoM. Overall, they found that the analogues did not lead to any significant conformational changes, therefore it may be that CH_3SCoM is what triggers the conformational change [70].

1.5 Bioinorganic Chemistry of MCR

1.5.1 Redox Properties of the Ni-cofactor F430

The Ni-cofactor F430's discovery by Gunsalus and Wolfe in 1978 from *Methanobacterium thermoautotrophicum* led to an immense contribution to the field of methanogenic biosynthesis of methane [43]. This was an exciting time in understanding Nature's method of C-H activation by finding incredibly unique coenzymes and cofactors that were only found in methanogenic archaea and not found anywhere else in Nature. Purification of MCR led to the identification of an interesting molecule with a distinct absorption at 430 nm that did not change under strong oxidizing or reducing conditions and lacked any observable fluorescence [43]. Later in 1980, Whitman and Wolfe in Urbana, Illinois purified the Ni-cofactor F430 from *Methanobacterium bryantii* and used neutron activation and atomic absorption spectroscopy to reveal that Ni was the sole metal associated with the cofactor, while Diekert *et al.* in Marburg, Germany showed that growth of *M. marburgensis* was dependent on Ni [44,71]. To understand whether the oxidation state of the Ni-cofactor F430 changes during catalysis, Jaun and Pfaltz studied a pentamethyl ester form of the Ni-cofactor F430 called F430M. F430M was easier to purify as well as more stable than the native pentacarboxylic acid. Cyclic voltammetry of F430M in tetrahydrofuran or dimethylformamide revealed a reversible one electron wave at -1.32V *vs.*

Fc^{+}/Fc (SHE vs NHE), but EPR or UV-Vis performed with preparative electrolysis failed. However, addition of a drop of 0.1% sodium amalgam to degassed F430M reduced the compound at room temperature for UV-Vis and EPR studies. The UV-Vis spectra of this F430M compound gave a large absorption peak at 382 nm and a broad peak at 754 nm. The EPR spectrum of the F430M compound gave g-values at 2.0036, and strong hyperfine splitting of the perpendicular g component that correlated linearly to the UV-Vis 385nm and 754nm peaks. This work was pivotal to understanding that the Ni(I) monovalent state is catalytically relevant [72]. About 7 years after this discovery, Holliger *et al.* provided EPR, UV-Vis, and Electron Spin Echo Envelope Modulation (ESEEM) spectroscopy of the pentacarboxylic acid in aqueous solution using Titanium-(III) citrate resulting in a tetragonally distorted octahedral geometry with an $S = ½$ spin and g values of $g_{II} = 2.44$ and $g_{\perp} = 2.061$. Additionally, the UV-Vis spectrum was very similar to the F430M where peaks were observed at 378 and 715 of the reduced Ni-cofactor F430. They found reduction only had occurred in alkaline conditions and the reduction potential was calculated to be -0.65 V *vs.* NHE for the Ni(II)/Ni(I) couple. The spectroscopic and redox properties of the Ni(I)-cofactor F430 are similar in the active site of the enzyme.

1.5.2 Spectroscopic Properties of MCR

UV-Visible (MCRred1, MCRred1silent, MCRox1)

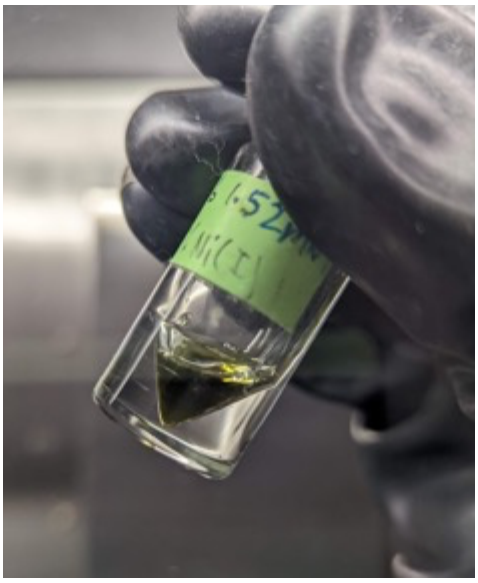

Figure 1.10 Color of MCRred1. MCRred1 exhibiting a dark forest green color indicative of the active-Ni(I) metallocentreMCR has a wealth of different states associated with distinct

spectroscopic properties, related to the Ni oxidation state, coordination number, geometry, and ligand binding. The plethora of MCR states is shown in Figure 1.12 on a separate page to view individually. The state of MCR can take many paths, but the first is related to harvesting conditions. If *M. marburgensis* is harvested under H_2 or harvested with H_2/CO_2 and activated *in vivo* by carbon monoxide the enzyme can be purified in the MCRred1 state. MCRred1 can be maintained if the enzyme is kept under anaerobic conditions and stored at 4° C [73,74]. The active Ni(I) state can also be generated by reducing the MCRox1 form with Ti(III)-citrate [75]. These methods generate what is called the "active" state where the Ni metallocentre is in the 1+ oxidation state. MCRred1 exhibits a very large peak like the free cofactor of 385nm and 750nm in the Ni(I) state. MCRred1 is a beautiful forest green as seen in Figure 1.10. MCRred1 is a d^9 paramagnetic species and can therefore be characterized via EPR spectroscopy. EPR of MCRred1 exhibits hyperfine coupling due to the Ni interacting with four *S*=1 nitrogen ligands of

the corphin ring. The geometry of the Ni(I) metallocenter is characterized with a g_{II} tensor of

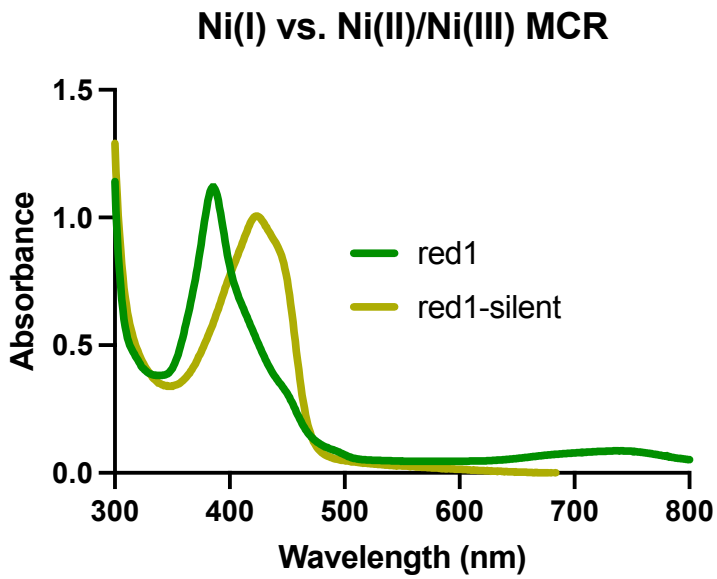

Figure 1.11 UV-Vis Spectra of MCRred1 and MCRred1silent. UV-Vis spectrum of MCRred1 (Green) with the Ni(I)-oxidation state displaying a large 385nm peak with a broad increase in the 750nm. MCRred1silent (Yellow) exhibiting the shifted oxidation state of the Ni to a 2+ and provided a large shift from 385nm to 420nm upon oxygen exposure. The Ni(II) spectra of MCR is similar Ni(III) MCR. 2.245 and two g tensor values associated with g⊥ of 2.065 and 2.057 illustrating axial geometry where g_z is larger than g⊥ compared to a Cu(II) standard [76]. At the MCRred1 state the enzyme must be kept under strict anaerobic conditions as the MCRred1 will degrade into a Ni(II)-MCR form called MCRred1silent. As we dive into the later portions of this thesis and for future nomenclature, oxygen exposure of any form will irreversibly result in formation of the silent form of the enzyme. The Ni(II)-MCR also has an incredibly distinct UV-Vis feature as a large 420 nm peak with a slight shoulder along 450 nm. Both UV-Vis spectra of the MCRred1 and MCRred1-silent forms are shown in Figure 1.11. Due to the one electron oxidation, MCRred1silent is not paramagnetic and the EPR signal becomes nonexistent, hence the "silent" specifier in the nomenclature.

A perplexing state of MCR is called MCR-ox1, which is generated by harvesting cells on a non-reducing gas mixture of N_2/CO_2. Assignment of the oxidation state of the nickel metallocentre has been ambiguous. The signal associated with MCR-ox1 exhibited an EPR signal of g_1 of 2.229, g_2 of 2.166, and g_3 of 2.148 [77]. This geometry is technically axial, like MCRred1, but g_2 and g_3 are much closer than in MCRred1. Furthermore, it was found that this state is completely inactive; however, reduction with a strong reductant Ti(III) citrate was needed to transform this inactive state to the active MCRred1 state[75]. Therefore, this MCR-ox1 was labelled the moniker "ready state". Because of a paramagnetic EPR active form, it was believed this state did not harbor the Ni(II) oxidation and must be a Ni(III) due to needing a strong reducing agent to convert MCR-ox1 to the Ni(I) MCRred1 [78]. This theory was tested with EPR spectra exhibiting an odd-electron $d_{x^2-y^2}$ ground state and falls within a configuration similar to a d^9, while a d^7 Ni(III) should exhibit a d_{z^2} ground state for an octahedral metallocentre. The state of MCR-ox1 based on DFT calculations has been hypothesized to be a thio radical d^9 Ni(II) species and Ni(III) thiolate in equilibrium [79]. The UV-Vis of MCR-ox1 closely resembles the UV-Vis spectra associated to the Ni(II)-silent forms of the enzyme, with a peak at 420 nm [80].

MCRred1c, MCRred2, MCRred1m.

MCRred1 is the active form of the enzyme and substrates that bind to this enzyme will change spectroscopic properties of MCR. For example, upon binding of inhibitor HSCoM, MCRred1 becomes a subset of the active form called MCRred1c. In MCRred1c, the HSCoM enters the active site in some way, but interaction with the Ni(I) is not observed. X-ray Absorption Spectroscopy (XAS) reveals that no binding occurs within 2.5Å of the Ni [81]. In this state, EPR can be observed with g tensors similar to those of MCRred1 state, suggesting axial geometry of the metallocentre, albeit less intense hyperfine couplings. In the MCRred1c state,

HSCoB may bind to make what is called the MCRred2 state. MCRred2 state exhibits a unique EPR spectra where the g values are found to be g_1=2.287, g_2= 2.231, and g_3=2.175 [82]. Because of the three distinct EPR signals, we conclude that the geometry of the metallocentre is rhombic where g_x, g_y, and g_z are not equal. Another interesting observation of MCRred2 is that UV-Vis and EPR studies have never observed an both active sites in the MCRred2 state. UV-Vis spectra were taken with changes in temperature, and it was found that at higher temperatures there was a 50% change to an MCRred2 state where there were two distinct peaks of an MCRred1 385nm peak and MCRred2 420nm peak. This lead Goenrich *et al.* to a hypothesis of MCR being a "dual stroke" motor where MCR exhibits half-sites reactivity. Upon binding of CH_3SCoM, MCRred1 becomes a subset called MCRred1m. EPR of this state reveals a very distinct increase in the hyperfine coupling of the interactions of the metallocentre and the corphin nitrogens. This is hypothesized to happen due to the decreased amount of microheterogeneity of the Ni position to a mostly planer orientation. Patwardhan *et al.* provides evidence of the sulfonate binding mode of CH_3SCoM. This is exemplified by d-d transitions in NIR absorption where a red shift occurs from 700nm to 750 nm. This red shift is observed with heterodisulfide CoBSSCoM, which from crystal structures is bound by the sulfonate moiety. Furthermore, a thiol absent analogue of CH_3SCoM, butane sulfonate was also found to exhibit this exact red shift without a thiol to bind to the Ni. Therefore, we believe that CH_3SCoM may bind in a manner that does not match the Ni(II) crystal structures that have been relied upon.

1.5.3 Need for Low Valent Ni(I) To Light the Fuse

Research in understanding MCR catalysis was incredibly difficult for several years. In 1991, Rospert *et al.* found a correlation between activity of the enzyme and spin concentrations that were associated with the MCRred1 signal in cell extracts, but purified MCR gave activity

less than 1% compared to the cell extracts [74]. In 1997, Goubeaud *et al.* found that the MCR-ox1 state from M. *marburgensis* could be converted to MCRred1 via titanium(III) citrate reduction at 60°C similar to that of the free cofactor [75]. With this conversion it was found that UV-Vis of the Ni center of MCR mimicked the Ni(I) state of the free cofactor, with the distinct 385nm increase. Furthermore, specific activity also increased with the conversion to MCRred-1 and this activity correlated with the spin concentration of the MCRred1 state Furthermore, Becker and Ragsdale just shortly after found another way to increase the amount of MCR-ox1 in *Methanosarcina thermophila* by adding sodium sulfide to the growth medium prior to harvest as well as the Ti(III) reduction of MCR-ox1 to MCRred1 [83]. This need for Ni(I) relies in its reduction potential. As stated previously, the redox potential of the Ni(I)/Ni(II) of the Ni-cofactor F430 is around -600mV. Therefore, the ease of oxidation of this Ni(I) metallocentre is directly related to its nucleophilicity. The Edwards equation is described below

$$\log(k/k_0) = aE^\circ + bH$$

where E^0 is the redox potential or the ease of electron loss and H as the proton basicity [84]. Therefore, having a low redox potential will most likely initiate a nucleophilic attack from the Ni(I) in a more likely scenario than a Ni(II) attacking to form a Ni(III).

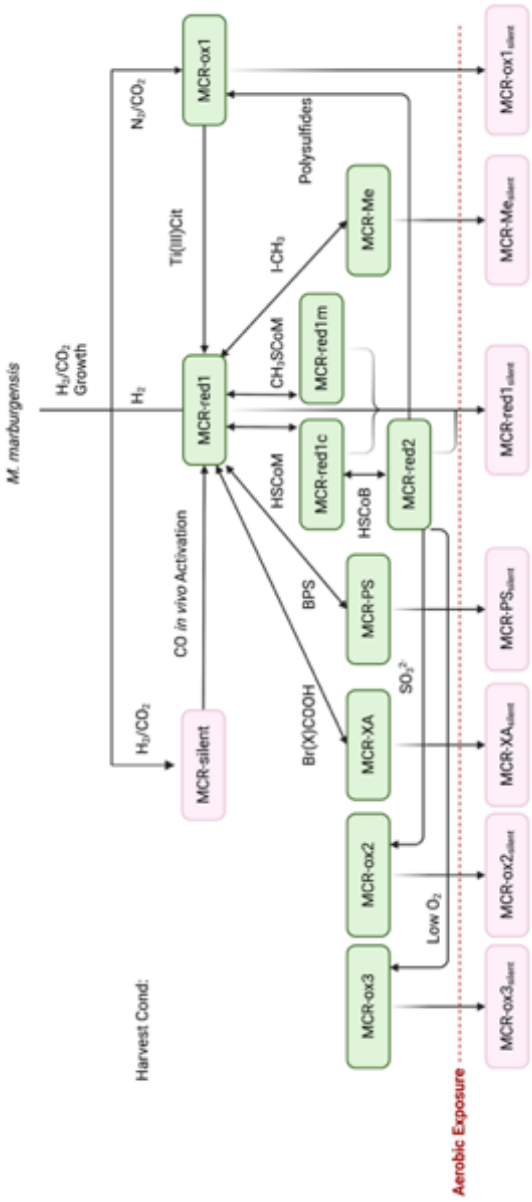

Figure 1.12 MCR Characterized States. Schematic of the various states of MCR where green and red labels resemble EPR active states and inactive state, respectively. Made with BioRender.com

1.5.4 Catalytic Mechanism of MCR – Supporting Evidence

When considering the mechanism of MCR, we must set out a series of rules. 1) There is unequivocal evidence that the MCR mechanism starts with the Ni(I) oxidation state [75]. 2) There must be stereo configurational inversion during the reduction of CH_3SCoM based on isotope labelling studies done with ethyl-CoM [85]. 3) HSCoB must be involved in the mechanism facilitating a ternary complex. Finally, 4) The rate limiting step is the breakage of the C-S bond of CH_3SCoM. The three mechanisms discussed in 1.3.5. all allow fall under the rules set out for the MCR mechanism. Due to how often this figure will be referenced in this section, the catalytic mechanism from Figure 1.4 is placed as Figure 1.13.

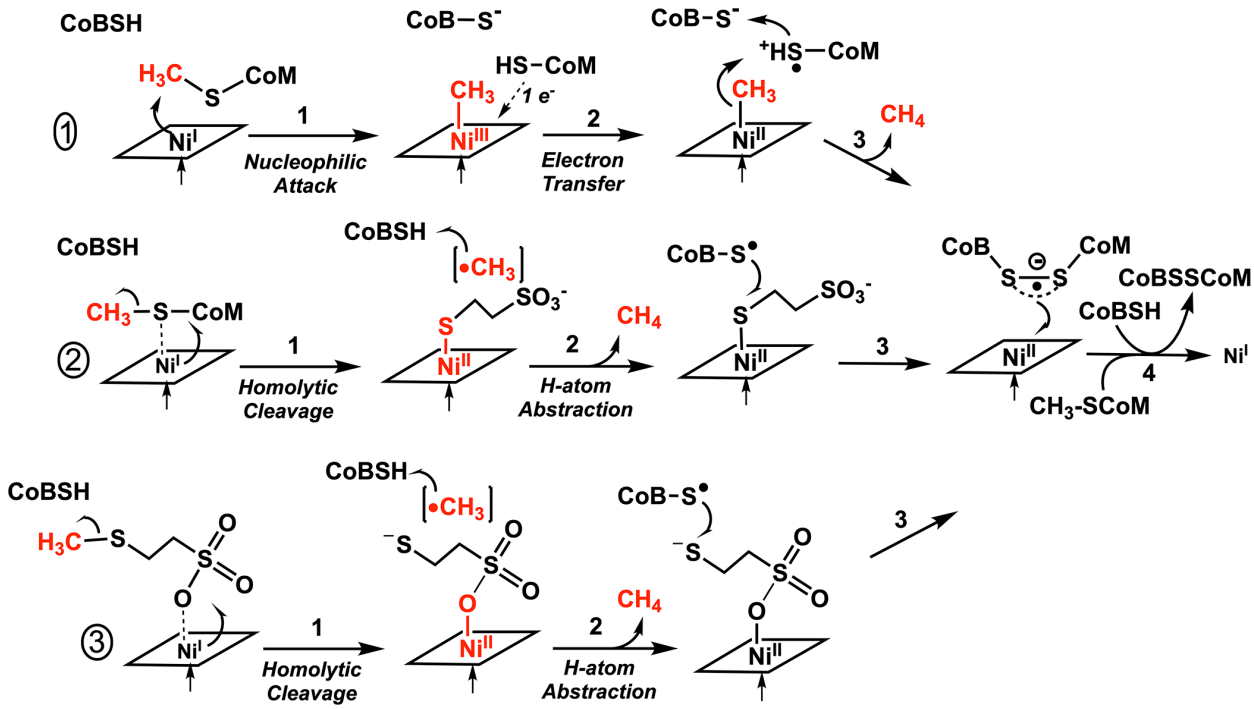

Figure 1.13 Proposed organometallic versus radical mechanisms MCR-catalyzed methane formation. (A) Organometallic mechanism involving nucleophilic attack on methyl-CoM to form a Ni(III)-methyl intermediate (B) Ni(I) promoted homolysis of the methyl-S bond of methyl-CoM to form a methyl radical and Ni(II)-thiolate of CoM. (C) Ni(I) promoted homolysis of the methyl-thioether bond of methyl-SCoM bound through long-range electron transfer from a Ni-sulfonate bond to generate a methyl radical and Ni(II)-sulfonate (as proposed by Patwardhan et al.). (With permission)Mechanism 1 seems reasonable because many metalloenzymatic systems act in a two-electron mechanism. SN2 reactions are some of the most common

mechanisms among transition metal complexes and also satisfy the criteria of rule 2 [84]. Furthermore, methyl halide reactions occur making a stable Me-Ni(III) as well as alkyl-Ni(III) using inhibitor 3-bromopropane sulfonate [86]. Mainly, the downfall of the two electron SN2 lies in DFT calculations of rule 4 considered by Pelmenschikov *et al.*. The S-C bond cleavage is suggested to then form the weak Me-Ni bond, but the energy activation barrier for this to overcome is 45 kcal/mol and would thus be endothermic. This is considered to not be very thermodynamically feasible. Pelmenschikov of the Siegbahn group then provided a new mechanism.

Mechanism 2 from the Siegbahn group involves the one electron attack of the Ni(I) to homolytically cleave the C-S bond, the rate limiting step. In DFT calculations where the active site tyrosines and lower axial ligand Gln147 are included, Pelmenschikov and Siegbahn further explored these calculations and found that the energy barrier for this step is around 10 kcal/mol, which is more favorable than that (20 kcal/mol) for the methyl-Ni state. To justify this hypothesis, they claim that the Ni-corphin may not have a large degree of flexibility, but the Gln147 interaction is significantly increased, which could increase the barrier for releasing the sulfur ligand [87]. One flaw of mechanism 2 is that whether the free rotation of the methyl radical would break rule 2, but Siegbahn provided an alternative. A methyl radical that, after formation, immediately contributes to the hydrogen atom abstraction and, therefore, created a transition state that effectively removes methyl radical rotation and, in the same paper, provided a computational diagram for the theoretical energy profile of the radical mechanism in which both the forward and reverse are plausible. Additionally the SN_2 mechanism fails to be thermodynamically favorable in either direction in these studies [88]. In 2016, Wongnate *et al.* provided the first spectroscopic evidence for the radical mechanism. Using a HSCoB inhibitor,

$HSCoB_6$, stopped flow kinetic studies were carried out. $HSCoB_6$ has been found to profoundly slow the kinetics of the reaction by removing one carbon from the heptanoyl chain. This simple analogue is beautiful for this experiment because structurally the thiol is placed in the same location as the HSCoM and reacts slowly meaning that the analogue does not hinder the ordered bi-bi ternary complex mimicking the MCR mechanism found with native substrate HSCoB. Monitoring the uptake of radiolabelled $^{14}CH_3SCoM$, the reaction exhibited a rate constant for removal of methane that matched the rate of decay of the Ni(I) 385nm peak to form either Ni(II) or Ni(III) peak at 420nm. This observation supports the transition state theory proposed by the Siegbahn group as the Ni(I) nucleophilic attack and subsequent rate limiting step of the S-C bond cleavage is a uniform rate constant. Mechanism 1 involves an additional step due to the stable methyl-Ni(III). Furthermore, rapid freeze quench EPR was performed on the reaction to see if either an EPR active Ni(III) intermediate, either a Me-Ni(III) or a Ni(III)-thiolate, would be seen. The experiment showed a conversion to a completely EPR-silent Ni(II) intermediate, providing more evidence for mechanism 2. Magnetic Circular Dichroism was also performed on this reaction, and the spectra gave similar features to MCR-ox1silent, the proposed intermediate of the reaction [89]. Similar studies using DFT calculations similar to the Seigbahn group were also used to show that mechanism 2 is more thermodynamically favorable.

Recently, it has been speculated that even the binding mode of CH_3-SCoM differs from that of the crystal structure represented by the Ni(II)-inactive Ni-thiolate, where the sulfonate group of CH_3-SCoM is what truly coordinates to the Ni(I) and involves a long range through space or bond electron transfer in mechanism 3. The two previous mechanistic proposals must overcome a large spatial distance of 6.4 Å for the •SCoB to form the S-S bond of CoMSSCoB. Patwardhan *et al.* has challenged the Ni-thiolate binding mode seen in all inactive-Ni(II) crystal

structures. By EPR, it was found that the CH_3-SCoM-bound enzyme exhibits intensified hyperfine splitting similar to the binding of CoMSSCoB and a CH_3-SCoM analogue butane-sulfonate, where the thiol is replaced with the carbon. This was proposed to bind in a manner that causes the Ni to shift into the plane of the Ni-F430. Furthermore, binding of CH_3-SCoM to MCR was monitored by near-infrared (NIR) absorption and shows effective d-d transitions around 700 nm, which are similar to those of CoMSSCoB and butane sulfonate, and distinct from those observed upon incubation of MCRred1 with f HSCoM.

1.5.5 Kinetic Characterization of the MCR Mechanism

For MCR to accomplish methane synthesis, it has been found that MCR and its substrates, CH_3SCoM and HSCoB. must be in a ternary complex [90]. Based on the crystal structure of the enzyme, the 50Å long tunnel is populated and closed with the phosphate head group of HSCoB bound at the top of the tunnel. This indicates that the more buried substrate CH_3SCoM is most likely set in the active site before binding of HSCoB. Furthermore, we have observed the product state crystal structure with no methane bound [56]. This finding has supported that the most likely mechanism for MCR is the ternary ordered bi-bi rather than a ping pong mechanism as represented in Figure 1.14. This was made evident in 2001 by Horng *et al.* where HSCoB was found to initiate the cleavage of the S-C bond in the first reported pre-steady-state kinetic studies of MCR. Wongnate *et al.* was set to do the first transient kinetic study using EPR, stopped flow, and fluorescence to tease out this mechanism in 2016. Using fluorescence, the binding of either CH_3SCoM and/or HSCoB to MCRred1 was explored. It was found that binding of HSCoB to MCRred1 occured before addition of CH_3SCoM with a K_d of 96 μM but resulted in

an inhibitory complex

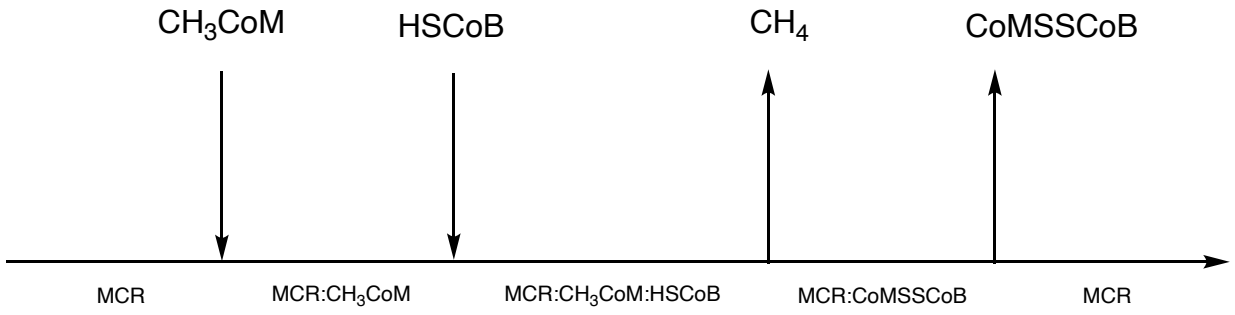

Figure 1.14 Cleland diagram of methane biosynthesis via MCR. The proposed ordered bi-bi mechanism of MCR in which CH_3SCoM first binds to MCRred1 followed by binding of HSCoB. Binding of HSCoB provides the ternary complex to facilitate catalysis removing methane followed by the release of the heterodisulfideunable to initiate catalysis once CH_3SCoM binds. Using hydroxocobalamin to catalyze reduction of the heterodisulfide product (thus relieving product inhibition), Wongnate *et. al.* conducted steady-state and presteady state analyses of the reaction. The stopped flow kinetic measurements followed the absorbance of the 385nm and 420nm peaks of Ni(I) and Ni(II) states, respectively, with varying concentrations of CH_3SCoM and HSCoB. Additionally, depletion of $^{14}CH_3SCoM$ was monitored via liquid scintillation counting and formation of methane was observed via gas chromatography. It was found that MCRred1 bound CH_3SCoM 7 times more tightly than HSCoB with a K_{d1} of 17 μM vs. HSCoB binding of 96 μM. The MCR:CH_3SCoM complex would then bind HSCoB with a K_{d2} of 79 μM. This reaction was found to contain 4 distinct kinetic phases, one of which the Ni(I) is regenerated from enzyme turnover. Quantification of sotope-labelled $^{14}CH_3SCoM$ depletion and generation of $^{14}CH_3$ demonstrated the reaction occurs at a rate of 20 s^{-1}. Furthermore, simulations using Berkeley Madonna were found to match the experimental model and is represented in Figure 1.15.

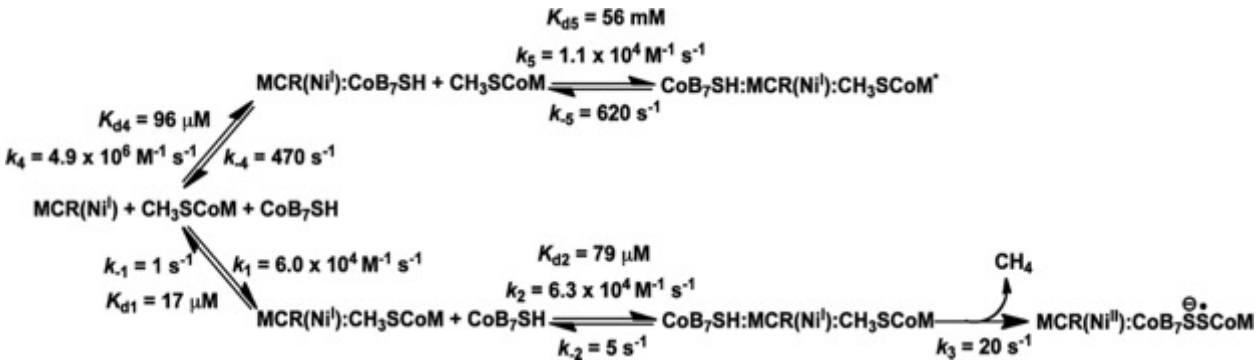

Figure 1.15 Reaction of MCR with both CH_3SCoM:MCR and HSCoB:MCR complexes. Kinetic parameters found by Wongnate and Ragsdale for the ternary complex promoting methane catalysis and the inhibitory complex. (With permission)Interestingly, the inhibitory complex of a bound HSCoB:MCR complex was found to be highly disfavored in which a mechanism is proposed and supported by the kinetic evidence that the presence of CH_3SCoM promotes the dissociation of HSCoB from the MCR active site [65].

1.5.6 Radicals within the MCR Catalytic Cycle

This section discusses the most probable mechanism to date, mechanism 2. In this mechanism, three radicals that must be considered. The Ni(I) nucleophilic attack to the thioether sulfur group forms the first radical, the methyl radical. As stated before, this radical is proposed to be in a non-rotational transition state that will immediately abstract the hydrogen of HSCoB. This state was validated by Wongnate *et al.* matching the rate of Ni(I) decay to methane formation [89]. It was found that the S-C bond cleavage was rate limiting and, therefore, very difficult to trap the proposed methyl radical [91]. Through isotope labelling studies, Scheller *et al.* found that when completing the reaction cycle with MCR in D_2O, about 2% of deuterated CH_3SCoM was discovered. Leading the group to hypothesize a microstate in which the methane is trapped and does not leave the active site fast enough, and therefore, can participate in the reverse reaction. Therefore, conserved methane pocket was hypothesized.

After the methyl radical performs the hydrogen atom abstraction, a ·SCoB thiyl radical is formed and is our second radical of the mechanism. Wongnate *et al.* describes a very low amount of accumulation of a radical in the EPR studies, but claims the thiyl radical may not be easily observed or too broad. This would be an ideal radical to trap as the methyl radical is very short-lived. Chapter 2 attempts trap the ·SCoB thiyl radical with the synthesis of a HSCoB analogue that will make the thiyl radical more visible by delocalization of the radical along a phenyl ring.

Once the thiyl radical combines to the Ni-thiolate, the second transition state is formed, the disulfide anion radical. The disulfide anion radical of the pathway is interesting because disulfide anion radicals are seen as super reductants in biology with redox potentials between -1 V and -2 V [92] and is needed to provide the electron transfer to the Ni(I) and outcompete the -600mV redox potential of the Ni(I)/Ni(II) couple. Unfortunately, this redox potential will make the disulfide anion radical very difficult to trap.

1.6 Gaps and Conundrums

While MCR has been studied for decades, the full extent of research on the enzyme was hindered for years due to activation difficulties of sub-minimal reactivity. Even after the full conversion from MCR-ox1 to MCRred1, irreversible oxidation from the Ni(I)-active to the Ni(II)-inactive state has hindered the understanding of the structural implications of the active Ni(I) form. Below I will highlight the gaps and conundrums of MCR and what this thesis aims to uncover.

1.6.1 Unresolved MCR Structural Questions

Most structural characteristic and binding modes are reliant on the current crystallographic studies of this enzyme, but to this date, there are no current Ni(I)-active MCR

crystal structures found. MCR is one of the most oxygen sensitive enzymes on the planet, and crystallography methods nor any of the world's beamlines have not been able to keep the Ni(I)-active state. Even anaerobically crystallized and cryo-frozen crystals of this enzyme are found in the Ni(II) form when data has been collected [70]. Furthermore, anaerobic tactics utilizing propane icicles have also been performed to no avail. Obtaining the Ni(I)-active structure of MCR is an incredibly difficult task even with anaerobic methods in place. With the low redox potential of the Ni(I)/Ni(II) couple, it has been thought that x-ray exposure may photo-oxidize the enzyme, resulting in a Ni(II) state after the diffraction has been completed. To combat this, this thesis aims to solve the Ni(I) structure by using serial femtosecond x-ray crystallography using an x-ray free electron laser (XFEL) in tandem with X-ray emission spectroscopy as well as serial anaerobic capillary experiments to understand why the Ni(I) crystal structure is so elusive and to solve the structure and finally obtain the snapshot of the Ni(I) active site of MCR. Additionally, this problem of anaerobicity with MCR leads to questions of other previous anaerobic crystal structures. Thus, this thesis aims to attempt new strategies of tandem oxidation state monitoring with X-ray diffraction.

The native substrate CH_3SCoM has never been found in a crystal structure of the enzyme leaving the binding mode of the native substrate in question. This could be for two reasons. Ermler *et al.* hypothesizes that radiation damage may play a role in the S-C bond cleavage of CH_3SCoM resulting in an HSCoM bound structure [56]. Another could be that the Ni(II) MCR prevents the removal of HSCoM or binding of CH_3SCoM. Therefore, by using XFEL the diffraction before destruction strategy can be utilized to obtain the CH_3SCoM bound form of the enzyme [93].

1.6.2 Trapping of Intermediates in the MCR Radical Mechanism

Wongnate *et al.* provided spectroscopic evidence of the radical mechanism of MCR. The evidence was used to disprove mechanism 1, but very little accumulation of a radical character of the pathway was observed. A major intermediate of this pathway has not been trapped and elucidated. Of which, the radical formation of ·SCoB is an excellent target intermediate to trap. To uncover this intermediate we must rely on the low level of accumulation of the Wongnate *et al.* study. Thiyl radicals are very difficult to uncover due to the short-lived nature of the radical and the broad EPR spectrum that is attributed to it. To sharpen this peak, we will use an HSCoB analogue equipped with a phenyl thiol to delocalize the thiyl radical along the conjugated ring, and thus stabilize the radical.

Chapter 2 Investigation of Radical Intermediate CoBS· with Synthetic Thiyl Radical Trapping Analog, CoBphSH.

2.1 Introduction

There is a an intermediate detected in low accumulation in the radical mechanism presented by Wongnate *et al.* This is presumed to be the CoBS· radical. The competing mechanisms of the SN2 two electron mechanism and the radical mechanism have been controversial in the MCR field for several decades. The SN2 reaction of MCR was thought to occur due to the large amount of transition metal mechanisms that use this approach. Rudolf Thauer supported this mechanism for a long time believing that MCR's Ni(I) metallocentre would act as a nucleophile similar to Cob(I)alamin, where MCR reduction of the methyl-Ni(III) is much easier to reduce to methyl-Ni(II) than cob(III)alamin to cob(II)alamin. Furthermore, methionine synthase was used as a model for this reaction where the reversible mechanism of methionine synthesis could mimic the mechanism of MCR. Not only Rudolf Thauer believed this to be the case. The Ragsdale lab in the 2000s, Ryan Kunz and Mishtu Dey were a driving force uncovering that alkyl-Ni(III) compounds could be made using a methyl halide, hypothesizing a reaction intermediate mimic. Additionally, it was discovered that introduction of CoMSH to a Me-Ni(III) MCR could catalyze the formation of CH_3SCoM and regenerate the MCRred1 state. Unfortunately, the methyl-(III) intermediate was never observed and could only be chemically made with a methyl halide. The main drawback of this mechanism was published by the Siegahn

group where DFT calculations illustrated that the SN2 mechanism transition state was not thermodynamically favorable. This led the Siegbahn lab to propose a new mechanism, one that comprised of the second most abundant mechanism of transition metals, a radical mechanism [84].

Based on DFT calculations, the Siegbahn group hypothesized the now most probable mechanism, denoted mechanism 2, where Ni(I) acts as a nucleophile attacking the sulfur group of CH_3SCoM resulting in a homolytic cleavage of the S-C bond of CH_3SCoM. This cleavage creates a non-rotational methyl radical transition state that immediately abstracts the H atom from HSCoB creating a postulated conserved methane pocket and a ·SCoB radical intermediate. The ·SCoB radical then attacks the sulfur of the Ni-thiolate creating a heterodisulfide anion radical, the proposed second transition state. The disulfide anion radical then regenerates the Ni(I) and the heterodisulfide CoMSSCoB leaves the active site.

Providing evidence of this intermediate is crucial to solidify that MCR is based on a one electron radical mechanism. Thus far, kinetic, spectroscopic, and computational evidence of the methyl radical transition state exists, but only a small amount of radical was found in EPR spectroscopy [89]. The target for this project is the ·SCoB intermediate is highlighted below in Figure 2.1.

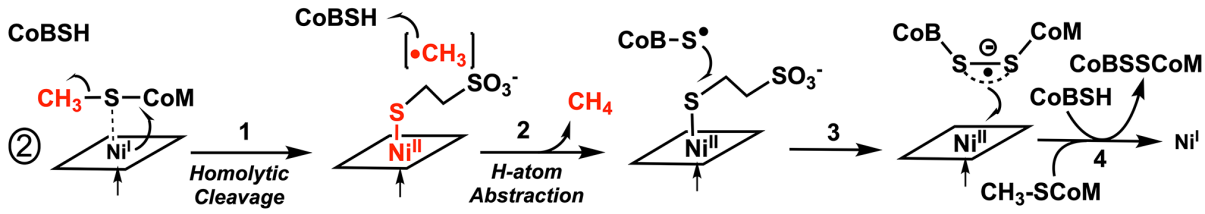

Figure 2.1 The Radical Mechanism of MCR. The radical based mechanism of MCR that we call mechanism 2, with a highlight on the ·SCoB radical.**Materials**

1,2-ethanedithiol, copper sulfate hexahydrate ($CuSO_4$), potassium hydroxide (KOH), sodium acetate (NaOAc), copper iodide (CuI), TCEP, N,N'-dicyclohexylcarbodiimide (DCC), N-hydroxysuccinimide (NHS), 1-[Bis(dimethylamino)methylene]-1H-1,2,3-triazolo[4,5-b]pyridinium 3-oxid hexafluorophosphate (HATU), dimethyl sulfoxide (DMSO), methanol (MeOH), ethyl acetate (EtOAc), petroleum ether (PET), silica gel, dichloromethane (DCM), Sulfur Powder (S_8), diisopropylethanolamine (DIPEA), and dimethyl formamide (DMF) chemicals were purchased from Sigma Aldrich. Hydrochloric acid (HCl), acetic acid (AcOH) and magnesium sulfate anhydrous ($MgSO_4$) was purchased from fisher scientific. 3-(4-iodophenyl)propanoic acid was purchased from Synthonix. 1,4-dioxane was purchased from Agros Sciences. Argon gas was purchased and supplied by cryogenic gases.

2.2.1 Copper Sulfate Mediated Aryl Thiol Synthesis

5mmol of 3-(4-iodophenyl)propanoic acid, 0.25mmol of $CuSO_4 \cdot 5H_2O$, and 25mmol of KOH into a two neck round bottom flask with a condenser attachment and septa. The flask is flushed with argon and an inert argon gas balloon is added. To this solid mixture, 10mls of anaerobic DMSO is added via syringe flushed with argon, as well as 1ml of anaerobic water added in the same fashion. 1,2-ethanedithiol (10mmol) is added via syringe to the flask and heated to 100°C for 20 hours. The organic layer is extracted with 5% HCl and EtOAc 3 times each then washed with water and brine. The liquid is dried over $MgSO_4$ and rotovaped to concentrate. Dioxane is added to dissolve the compound and silica is used to dry load a silica column equilibrated with 95% EtOAc, 4% PET, and 1% AcOH, the mobile phase. Fractions were collected and run via TLC to determine the correct Rf value. Fractions were collected and evaporated.

2.2.2 Synthesis of methyl 3-(4-iodophenyl)propanoate

3-(4-iodophenyl)propanoic acid (44.4mmol) is placed in a round bottom flask in 75ml of methanol. Sulfuric acid (2.2mls) is added with a reflux condenser with an argon gas balloon. The solution is allowed to reflux at 75°C for 15 hours. The solution is then evaporated in a rotovap and the organic is extracted with DCM. The organic is washed with water, sodium bicarbonate, and sodium chloride. The liquid is dried over $MgSO_4$ and rotovaped to concentrate. The yield of this reaction is 96%.

2.2.3 Copper Iodide Mediated Diaryl Disulfide Synthesis with Weak Base NaOAc

3-4(Iodophenyl)propanoic methylester (22.5mmol), S_8 (22.5mmol), CuI(1.5mmol), and NaOAc (45mmol) is placed in a round bottom flask. The solids and flask are flushed with argon and an inert gas balloon is attached. Anaerobic DMF (30mls) is added via syringe and the mixture is heated to 100°C for 26 hours. DMF is blown off on an air line. The product is solubilized with EtOAc and dry loaded using silica gel in 100% PET in a 300ml silica column. The compound is eluted with 80%PET/20%EtOAc and monitored via TLC.

2.2.4 Methyl Ester Hydrolysis of Dimethyl 3,3'-(disulfanediylbis(4,1-phenylene))dipropionate.

Dimethyl 3,3'-(disulfanediylbis(4,1-phenylene))dipropionate (1mmol) is placed in a conical flask and 7.5mls of 75% H_2SO_4 is added and stirred at room temperature. The reaction is monitored via TLC (Mobile phase 95% EtOAc/5% PET) by placing a small amount of the reaction, quenching with chilled water, and extracted with EtOAc. The reaction is diluted with chilled water and extracted with ethyl acetate. The organic is washed with KOH and water several times. The compound is in the aqueous phase and crashed with H_2SO_4 and filtered.

2.2.5 HATU Peptide Cross Couple

3,3'-(disulfanediylbis(4,1-phenylene))dipropionic acid (1mmol), HATU (4mmol), DIPEA (6mmol) and 5ml of DMF is reacted to deprotonate the carboxylic acid for 30min. Separately, O-phospho-l-threonine (2.4mmol) is dissolved in 2mls DMF, 2.5mls water, and 300µl of DIPEA. The two solutions were mixed and stirred at room temperature for 2 hours. The reaction mixture is diluted with water and rotovaped to create an azeotrope between water and DIPEA. This step is repeated until no DIPEA is seen via HPLC. The rotovaped material is diluted in acid water and purified via reverse phase PoraPak column purchased from Waters with a water/methanol gradient.

2.2.6 TCEP Cleavage Resulting in CoBphSH

2,2'-((3,3'-(disulfanediylbis(4,1-phenylene))bis(propanoyl))bis(azanediyl))bis(3-(phosphonooxy)butanoic acid) (62µmol) is dissolved in 1ml of 50mM Trizma Base. TCEP is added in 3 molar excess (186µmol) and cleavage is monitored by HPLC using anaerobic HPLC vials. The reaction mixture is then loaded onto a reverse phase PoraPak column in the anaerobic chamber and purified using a water/methanol step wise gradient. The fractions that contained the target compound were lyophilized and stored in the anaerobic chamber to prevent thiol oxidation.

2.2.7 UV-Vis and EPR Spectroscopy

Absorbance spectra were recorded inside of an anaerobic chamber <2ppm O_2 using a Cary UV/Vis equipped with a xenon lamp with a dual out of plane monochromator. EPR spectra were recorded on a Bruker EMX spectrometer (Bruker Biospin Corp., Billerica, MA), equipped with an Oxford ITC4 temperature controller, a Hewlett-Packard model 5340 automatic frequency counter, and Bruker gaussmeter. The EPR spectroscopic parameters included the following:

temperature, 77 K; microwave power, 10 milliwatt; microwave frequency, 9.37 GHz; receiver gain, 6.32 × 10^4; modulation amplitude, 9.37 G; modulation frequency, 100 kHz. Spin concentration was determined by double integration of the sample spectrum obtained under nonsaturating conditions and comparison to that of 1 mm copper perchlorate standard. All samples for EPR spectroscopy were prepared in 50 mm Tris-HCl, pH 7.6, in a Vacuum Atmospheres anaerobic chamber.

2.2.8 pKa Titrations

pKa measurements of the various substrates were carried out using acid–base titrations with 0.1 M standard sodium hydroxide solution (Sigma) to obtain titration curves. pKa values were found by identifying the equivalence points, the max ΔpH/Δml derivate plot maxima, and obtaining the pKa value at half-equivalence point.

2.3 Results

2.3.1 Design of Radical Trapping Analogues of HSCoB

To design the radical traps associated with MCR, we must look toward previous attempts for radical trapping in other biological systems. Many groups will use small molecule radical spin traps like 2,2,6,6-tetramethyl-1-piperidinyloxy (TEMPO), dimethyl-5,5-pyrroline-N-oxide (DMPO), or α(4-pyridil-1-oxide)-N-tert-butylnitrone (POBN). These traps would need to be placed in the active to trap the MCR radical. A radical clock could be used, pursuing a chemical perturbation such as a methyl group addition from a termination product like a radical cyclization or ring opening [94]. Additionally, some may use a chemical approach to attach a functional group that may stabilize a radical such as a resonance delocalizing aryl group.

Of these techniques, radical capture experiments from our lab have been performed using small molecule radical spin traps, but to no avail. Thus, designing the radical spin traps must be thought of as a method that is able to bind into the active site while still providing the ternary complex needed to initiate catalysis. Therefore, we thought of three different HSCoB analogues. 1) An aryl thiol HSCoB to stabilize the thiyl radical and detect via EPR. 2) An α- phenyl-N-tert-butyl nitrone (PBN)-derived nitrone spin trap analogue to HSCoB where components of HSCoB are available to provide the ternary complex, but with a PBN arm to create a spin adduct. And finally, 3) a vinyl radical clock that will attach the methyl due to a homolytic cleavage of the vinyl bond (Figure 2.3).

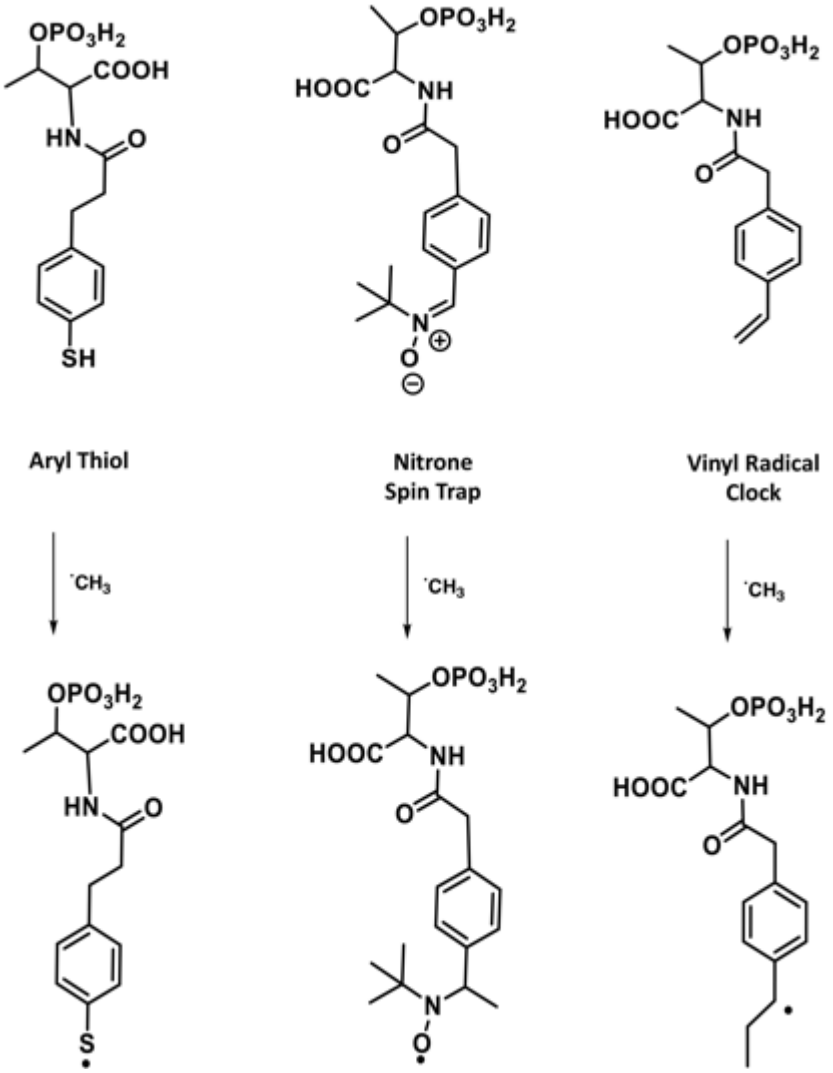

Figure 2.2 Three HSCoB analogue designs for the detection of the radical intermediate. The aryl thiol analogue that we will call CoBphSH once upon seeing the methyl intermediate will provide the hydrogen atom abstraction leading to a CoBphS·. The PBN derived nitrone spin trap, called CoB_{PBN}, will create a spin adduct upon methyl radical exposure. The vinyl radical clock, called CoB_{Vin}, will attach the methyl radical creating a new compound to visualize. It is of note that a termination event will occur, most likely via an H atom.While we have designed three molecules for this purpose, this project will focus on the synthesis and characterization of CoBphSH.

2.3.2 Docking Studies for CoBphSH

Before we synthesize the compound CoBphSH, we must validate whether MCR will have a promiscuous active site for the binding of phenyl ring. The active site of MCR can bind many different chained analogues of HSCoB, $CoB_{5\text{-}9}SH$, therefore it is likely that MCR. Based on hydrophobic active site residues that harbor the heptanoyl chain of HSCoB, we would not expect to see a charged or polar associated repulsion of the phenyl ring. Therefore, we visualized the CoBphSH molecule using docking studies via GOLD against the slow substrate $HSCoB_6$.

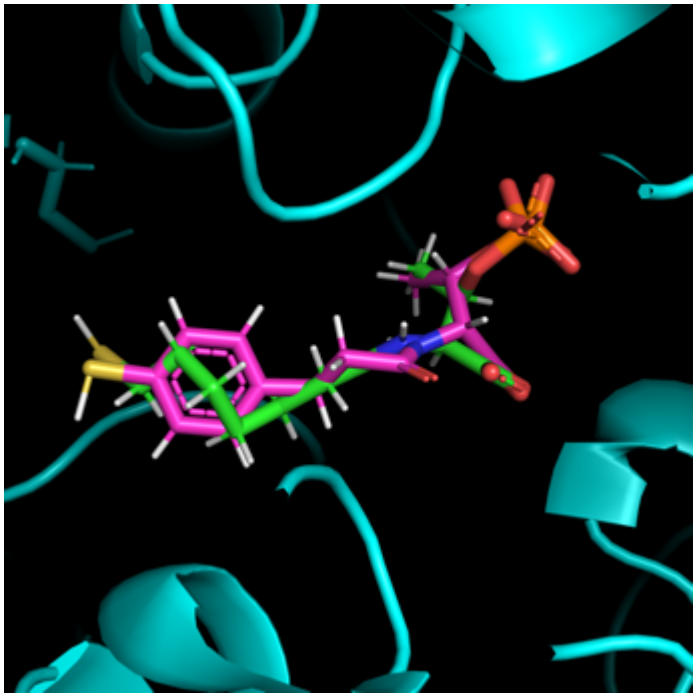

Figure 2.3 Docking Representation of CoBph against CoB_6. Using GOLD docking software, we can visually see CoBph inside of the active site in a similar conformation as HSCoB analogue $HSCoB_6$. CoBph is represented in magenta, while $HSCoB_6$ is illustrated in greenThe docking study illustrates that the phenyl ring can migrate into the active site while the placement of the phosphate head group nestles tightly via ionic interactions, most likely stimulating the ternary complex (Figure 2.4). Furthermore, the thiol positioning of CoBphSH is very similar to the $HSCoB_6$ and thus will similarly react to the methyl radical and participate in the first transition state. However, the hydrogens of the model are placed in a different direction which hopefully

will position this hydrogen in a precise location for H atom abstraction upon conformation change of the ternary complex

2.3.3 Synthesis of CoBphSH

To target this intermediate, we have developed a thiyl radical visualization tool in the form of a HSCoB analogue that is equipped with an aryl thiol. The aryl thiol will delocalize the sulfur radical around the ring once the radical is formed. The radical will be captured via EPR spectroscopy. The synthetic route of the compound is represented in Figure 2.2. We first start the synthesis with molecule 1 (3-(4-iodophenyl)propanoic acid). To ease purification of later steps, a methyl group is added to the carboxylic acid to make a non-polar methyl ester molecule **2** (methyl 3-(4-iodophenyl)propanoate). From molecule **2**, we will use copper iodide and weak base sodium acetate in dimethyl formamide to attach a diaryl dithiol (Ar-S-S-Ar) product molecule **3** (dimethyl 3,3'-(disulfanediylbis(4,1-phenylene))dipropionate) and purify via silica column. We then remove the methyl ester, after silica column purification, using concentrated sulfuric acid. With molecule **4**, 3,3'-(disulfanediylbis(4,1-phenylene))dipropionic acid, we employ a 1-(Bis (dimethylamino) methylene) -1H-1,2,3-triazolo (4,5-b) pyridinium 3-oxide hexafluorophosphate, or HATU, mediated peptide couple with o-phospho-l-threonine to result in molecule **5**, 2,2'-((3,3'-(disulfanediylbis(4,1-phenylene))bis(propanoyl))bis(azanediyl))bis(3-(phosphonooxy)butanoic acid). Purification of this compound is then run using a reverse phase tabletop column. The disulfide of molecule **5** is then cleaved using tris(2-carboxyethyl)phosphine, TCEP, in aqueous media. **CoBphSH** is then purified inside of an MBraun anaerobic chamber using a reverse phase porapak column and kept under N_2. From this point on the compound can be dissolved readily in water or Tris for experiments with MCR.

CoBphSH will be a newly synthesized HSCoB analogue to allow the capture of the thiyl radical. This compound was synthesized and binding assays using UV-Vis, NIR, and fluorescence of the molecule were performed to understand what the extend of binding. With this information, rapid freeze quench EPR studies will be performed to attempt to trap the elusive thiyl radical and provide clear evidence of this intermediate, attributing to new insight of how this enzyme catalyzes the formation of methane. Thus, this project will aid in understanding C-H activation to produce methane through Nature's enzymatic process. This could aid in the design of small molecules to act as a biological methanogenesis inhibitors in cattle as well as, though the process of enzymatic micro reversibility, understand how MCR may work in reverse for the uptake of methane.

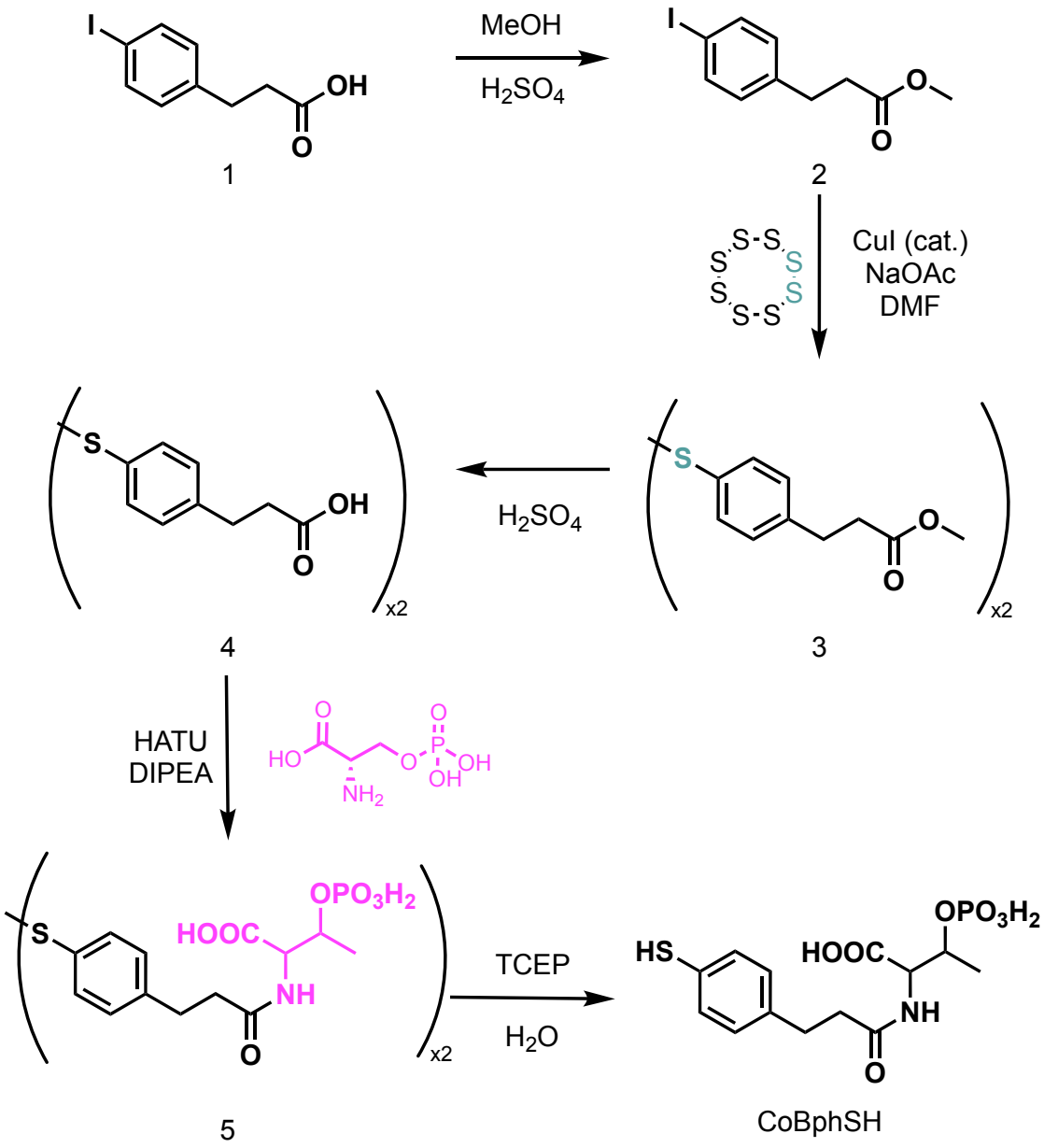

Figure 2.4 Synthetic route to 2-(3-(4-mercaptophenyl)propanamido)-3-(phosphonooxy)butanoic acid (CoBphSH). Full synthesis route from molecule 1, 3-(4-iodophenyl)propanoic acid to CoBphSH, 2-(3-(4-mercaptophenyl)propanamido)-3-(phosphonooxy)butanoic acid or CoBphSH. The following abbreviations are used in this figure: MeOH, Methanol; H_2SO_4, Sulfuric Acid; CuI, Copper Iodide; NaOAc, Sodium Acetate; DMF, Dimethyl Formamide; HATU, 1-(Bis(dimethylamino)methylene)-1H-1,2,3-triazolo(4,5-b)pyridinium 3-oxide hexafluorophosphate; DIPEA, N, N-Diisopropylethylamine; TCEP, tris(2-carboxyethyl)phosphine.

2.3.4 Titration of CoBphSH for pKa Determination

Characterization of CoBphSH pKas was carried out by dissolving CoBph in water and titrating the mixture with a standard 0.1N sodium hydroxide solution while monitoring the pH of the solution inside of the chamber (Figure 2.5). The titration data suggests at least 3 pKas were found to exist. The three functional groups to highlight for this study would be the phenyl thiol, the carboxylic acid, and the phosphate protons on CoBphSH. Native HSCoB's pKa of these protons on the phenyl thiol, carboxylic acid, and phosphate protons are found to be 9.1, 4.4, and 2.4, respectively [81]. Based on the titration data, a distinct pKa is observed for the thiol at 6.77, which is typically the pKa for several phenol thiols. The increase at 1.8 in the derivative plot will result in a 2nd pKa at 4.14 for the carboxylic acid and a 1.8 for the phosphate protons as a collective group. While this is expected, it does pose a situation in which the thiol present at pH of 7.6, the typical pH for studied enzymatic reactions, to be 90% deprotonated. Whether the active site of MCR adjusts this pKa is up for debate.

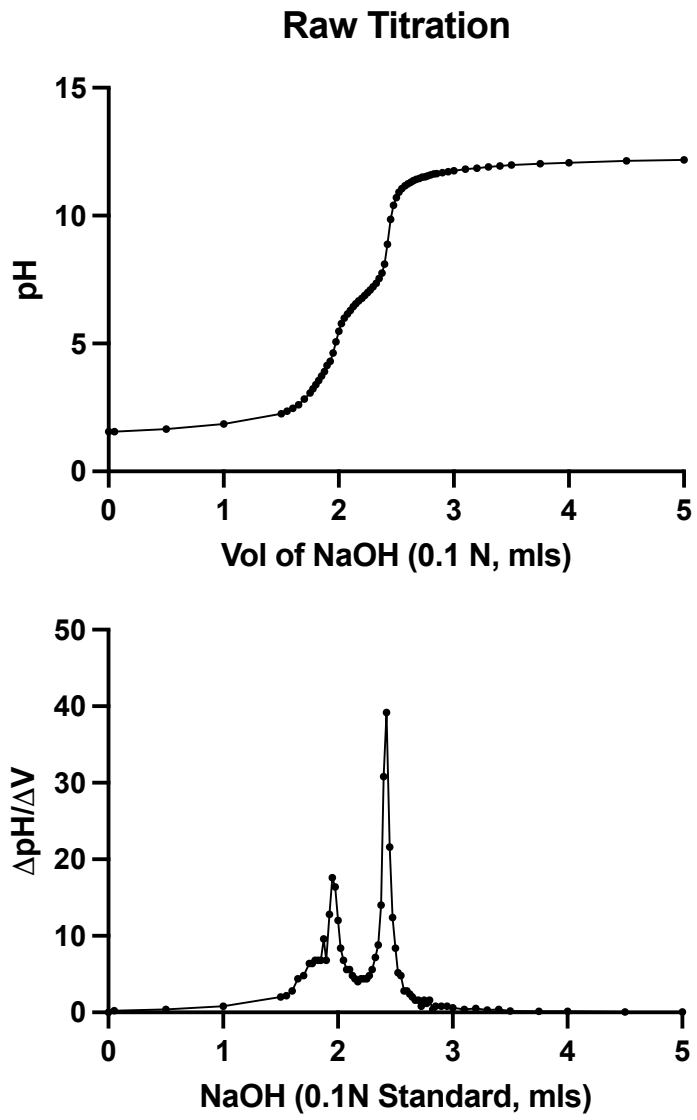

Figure 2.5 pKa Determination of CoBphSH. (Top) Titration of CoBphSH with a starting pH of 1.6 with small incremental additions of NaOH standard. (Below) Derivative of the raw titration used for pKa determination.

2.3.5 UV-Vis Binding Assay of CoBphSH to MCRred1c

Binding of a HSCoB derivative is intricate. UV-Vis for MCR can hone in on very slight changes in either the 380-450nm range for charge transfer between either the Ni(I)/Ni(II) state or how the Ni(I)/Ni(II) interact with the corphinoid macromolecule. This technique seems

promising, but it is likely that an HSCoB analogue alone may not stimulate a charge transfer. Furthermore from Patwardhan *et al.*, we may attempt to see absorption through a d-d transition, like the sulfonate O-Ni bond in the CH_3SCoM or product heterodisulfide [81]. Therefore, a binding assay was performed with CoBphSH, where MCRred1 was buffer exchanged against 10mM HSCoM making this MCRred1c (see Figure 1.12). Binding of CoBphSH hopefully would illicit some type of change of the UV-Vis spectra of MCRred1c. This experiment is shown in Figures 2.6-2.9.

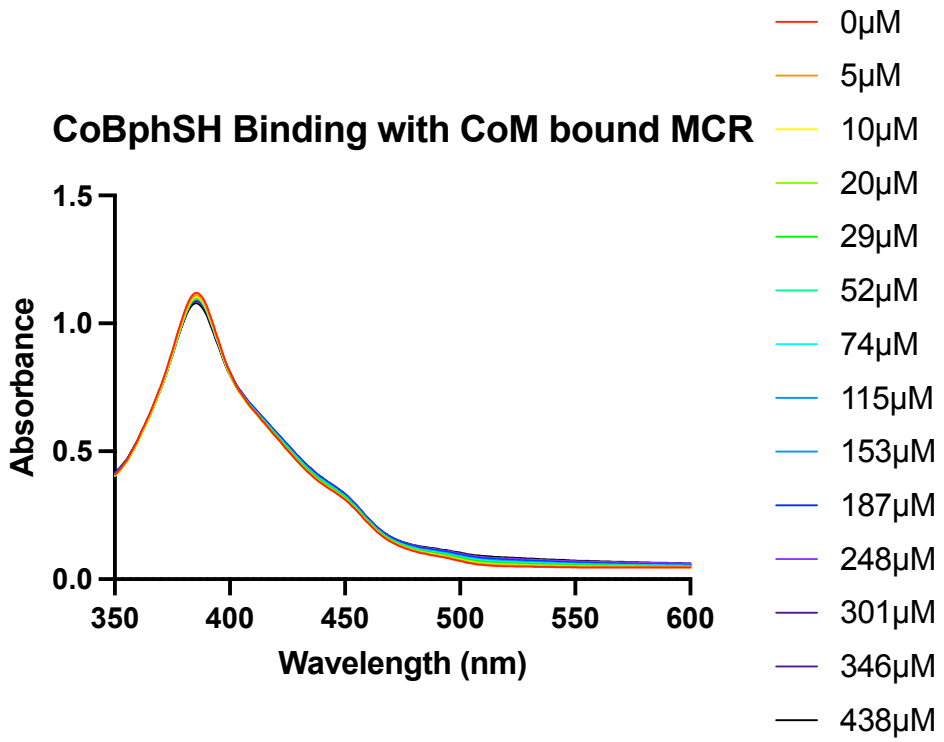

Figure 2.6 Binding Assay of CoBphSH with HSCoM Bound MCRred1. UV-Vis spectra of 50μM MCRred1c upon additions of CoBphSH in μM.

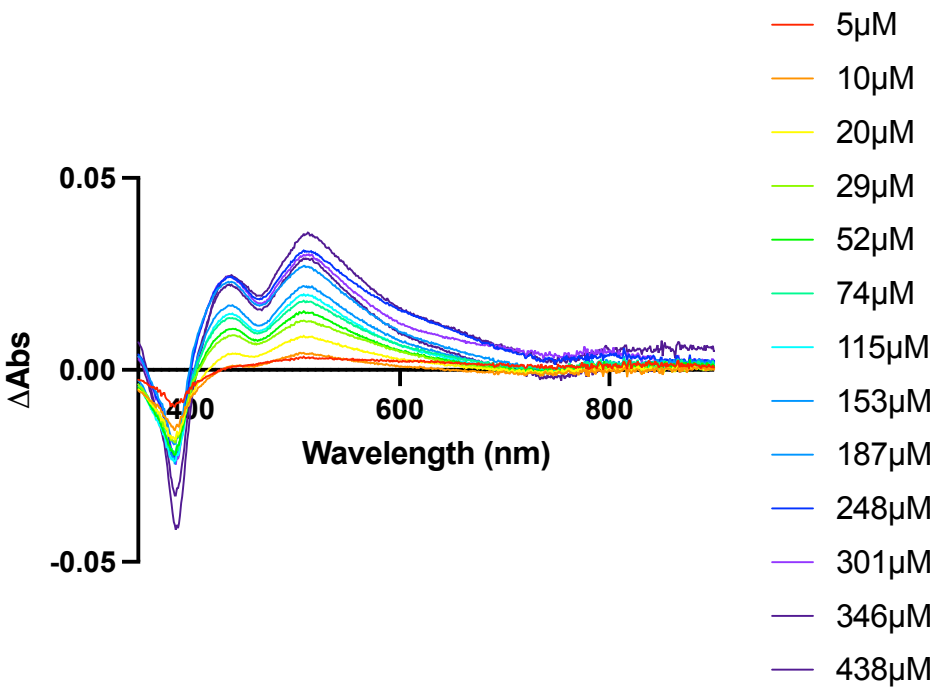

Figure 2.7 Difference Spectra of Figure 2.6. UV-Vis spectra of 50μM MCRred1c upon additions of CoBphSH in μM substracted with MCRred1c spectra.The binding assay revealed a change in spectra at 385, 420, 436, and 510nm as shown in Figure 2.23. The 385 peak corresponds to the Ni(I) state of the enzyme, but whether catalysis is being performed or oxygen damage is occurring is unknown. Additionally, this is similar to a difference for the 420nm peak albeit for the status of the Ni(II) state of the enzyme. The novel changes associated with binding of CoBphSH are illustrated in peaks 436 and 512nm.

In Figures 2.23 and 2.24, the absorbance with an MCRred1c subtraction increased up to 436 μM. The data followed a one site specific binding equation that resulted in a Kd of 88.33 μM, compared to HSCoB's binding affinity of 78 μM. Similarly, an additional novel absorbance difference was found at 436nm. This peak also followed a one site specific binding equation that resulted in a Kd of 102.6μM. This does not seem to follow the charge transfer transitions of the 385 and 420 of which the hypothetical Kds are 11.49 and 132.9, respectively.

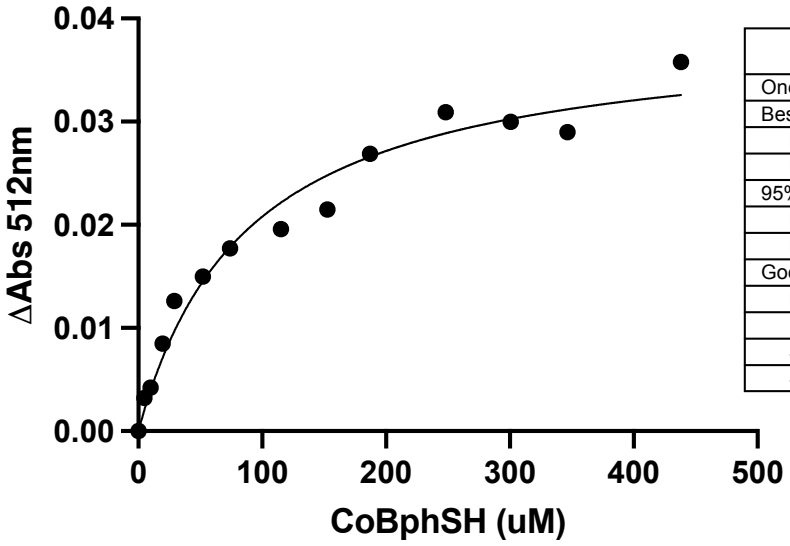

One site -- Specific binding	
Best-fit values	
Bmax	0.03915
Kd	88.33
95% CI (profile likelihood)	
Bmax	0.03436 to 0.04564
Kd	57.96 to 136.1
Goodness of Fit	
Degrees of Freedom	12
R squared	0.9713
Sum of Squares	4.889e-005
Sy.x	0.002018

Figure 2.8 Binding of CoBphSH via 512nm Wavelength Absorbance. Difference spectra maxima at 512nm from Figure 2.7 plotted against concentration of CoBphSH fitted with a one-site specific binding equation using Graphpad Prism.

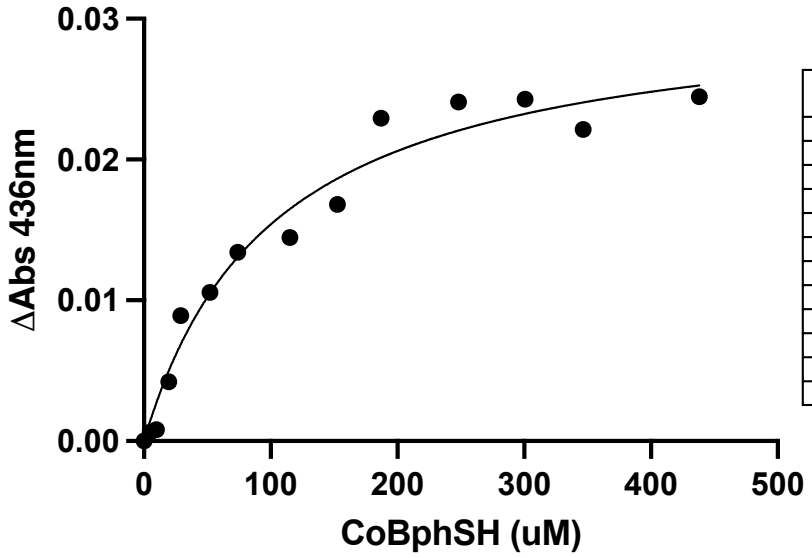

One site -- Specific binding	
Best-fit values	
Bmax	0.03117
Kd	102.6
95% CI (profile likelihood)	
Bmax	0.02709 to 0.03677
Kd	67.52 to 158.0
Goodness of Fit	
Degrees of Freedom	12
R squared	0.9704
Sum of Squares	3.399e-005
Sy.x	0.001683

Figure 2.9 Binding of CoBphSH via 436nm Wavelength Absorbance. Difference spectra maxima at 436nm from Figure 2.7 plotted against concentration of CoBphSH fitted with a one-site specific binding equation using Graphpad Prism.

2.3.6 UV-Vis Characterization of the Ternary Complex and Catalysis Initiated by CoBphSH

To test whether CoBphSH is an inhibitor or substrate of MCR, UV-Vis was performed to monitor Ni(I) character upon formation of the ternary complex. For an inhibitor one would expect minimal change of the characteristic 385 nm peak of Ni(I) MCR. On the other hand, if catalysis is initiated a decay of the in the Ni(I) 385nm peak would be visualized while observing an increase in a 420nm peak indicative of a Ni(II) or Ni(III) F430 as result of nucleophilic attack by the metallocenter. In Figure 2.10, MCRred1 was incubated CH_3SCoM (600μM) and reacted with either CoBphSH (120μM) or inhibitor HSCoM (120μM). A decrease in the Ni(I) 385nm peak and increase in the Ni(II)/Ni(III) 420nm peak is observed when CoBphSH is introduced, initiating catalysis (Figure 2.10A and 2.11A). The reaction progress is compared to inhibitor HSCoM where the change in 385nm and 420nm peaks are ten-fold less (2.10B and 2.11B). Surprisingly, this change occurs in a 60-minute timeframe reacting about ten-fold slower than CoB_6SH.

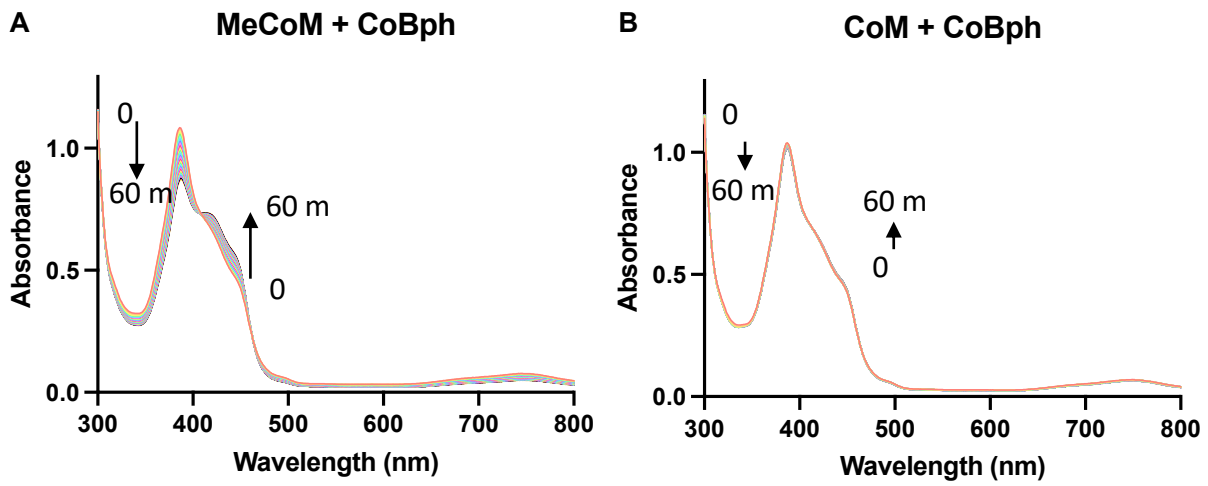

Figure 2.10 MCR Catalysis Monitored via UV-Vis with CoBphSH and HSCoM. MCRred1 was incubated CH_3SCoM (600µM) and reacted with either CoBphSH (A, 120µM) or inhibitor HSCoM (B, 120µM) and time points up to 60min were collected. Arrows indicate the decrease in absorbance at peak 385nm and decrease at peak 420nm.

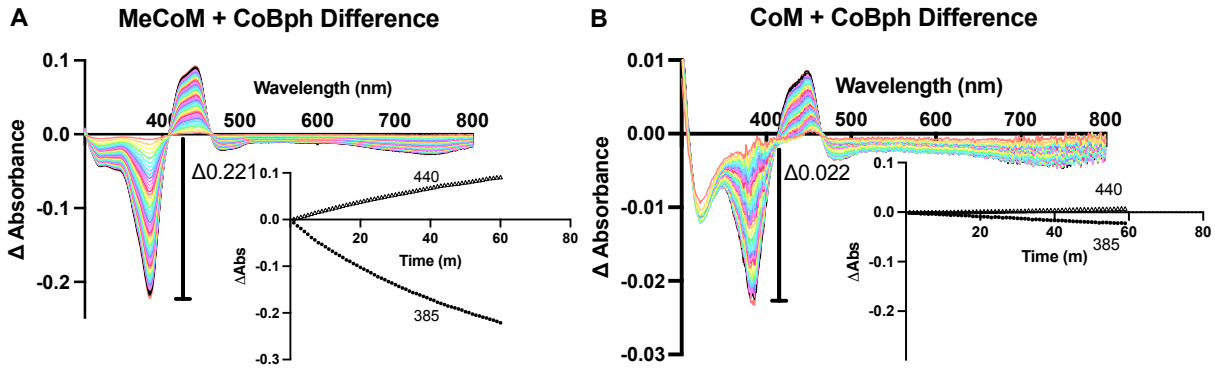

Figure 2.11 Difference Spectra of MCR Catalysis Monitored via UV-Vis with CoBSH and HsCoM. Difference spectra of Figure 2.10 illustrating the changes of Ni(I) characteristic peaks. A) Difference spectra of ternary complex initiated by CoBphSH resulting in a 0.221nm difference in the Ni(I) 385nm peak. The peak difference is also plotted against time (inset) along with another distinct change in the 440 shoulder peak associated with the Ni(II)/Ni(III). B) Difference spectra of CoBphSH binding to inhibitor HSCoM bound MCRred1 resulting in a 0.022nm difference in the Ni(I) 385nm peak. The peak difference is also plotted against time (inset) along with another distinct change in the 440 shoulder peak associated with the Ni(II)/ Ni(III) showing a minute increase.

Upon binding of the HSCoB analogue CoBphSH with the productive CH_3SCoM bound MCRred1 state, we initiate catalysis visualized via UV-Vis in a similar fashion that Wongnate *et*

al. describes of the MCR reaction with HSCoB in 2015 [65]. Wherein, a significant decrease in Ni(I) is observed with a decrease in 420nm and 440nm shoulder illustrating the Ni oxidation state change from a Ni(I) to what was found to be an EPR silent Ni(II) MCR. Therefore, CoBphSH upon binding of MCRred1 can light the fuse for catalysis and can be considered a slow substrate. The low speed at which CoBphSH can initiate catalysis is hypothesized to be a consequence of the plausible deprotonation of the phenyl thiol low pKa. However, enzymes often adjust the pKa of the substrate with their active site microenvironment. Consequently, the slow reaction speed could perhaps be spatial rather than due to protonation state.

2.3.7 EPR Analysis of MCRred1 Incubated with CoBphSH

To understand whether the Ni(I) signal decrease results in a Ni(II) signal, EPR studies were performed on MCRred-1 with various substrates illustrated in Figure 2.12.

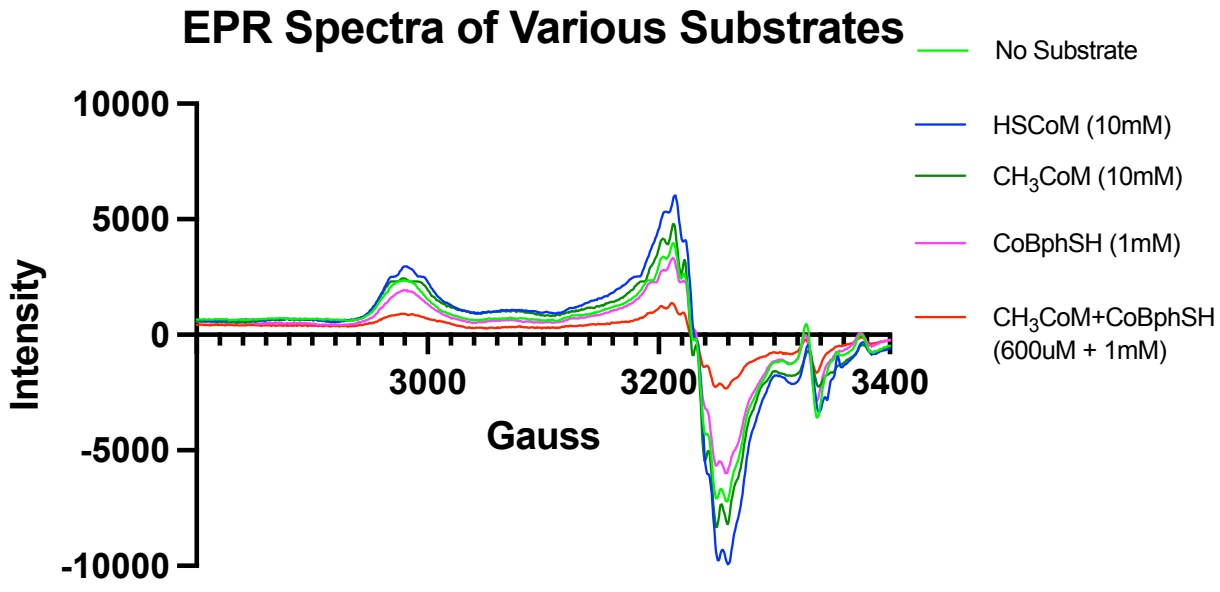

Figure 2.12 EPR Spectra of Various Substrates with MCRred1. EPR spectra taken with 49µM MCRred1 with 10mM HSCoM, 10mM CH_3SCoM, 1mM CoBphSH, and 600µM CH_3SCoM incubation with a 1mM addition of CoBphSH. EPR analysis reveals that the predominant form of MCR with these various substrates stays in the MCRred1 form with a

significantly lower g⊥ compared to an MCR-ox1. The MCR-ox1 signal may be slightly present with a first derivative rise and fall around 3099 gauss, but not significant to make a proper conclusion. From this data, we can dismiss that CoBphSH does not change the Ni(I) metallocentre of MCRred1 to a differenct EPR active form of the enzyme, a Ni(III) MCR. Additionally, we can see a difference in the MCRred1 intensity with the addition of CH_3SCoM and CoBphSH, meaning the binding of both substrates does change the Ni(I) to some form of silent Ni(II). Based on Wongnate *et al.* proposed mechanism, this could be an MCR-ox1silent species or oxygen damaged MCRred1-silent. This observation is illustrated when calculating the spin percentages of these samples as shown in Figure 2.13.

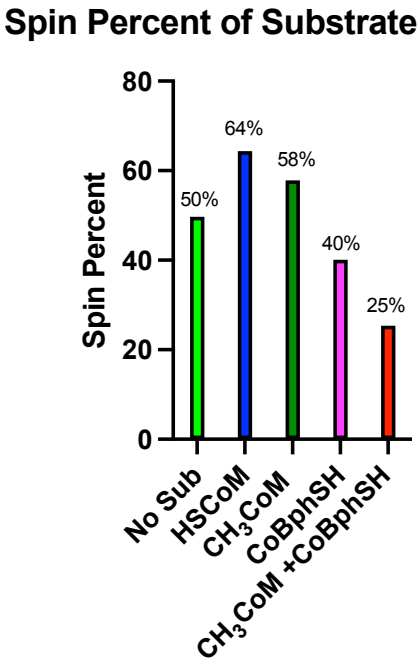

Figure 2.13 Spin Percentages of Samples from EPR Study. EPR spectra taken with 49µM MCRred1 with 10mM HSCoM, 10mM CH_3SCoM, 1mM CoBphSH, and 600µM CH_3SCoM incubation with a 1mM addition of CoBphSH spin percentages found via integration of EPR.

The addition of CH_3SCoM and CoBphSH reduces the amount of MCRred1 significantly from a no substrate 49.69% to a 25.39% decrease in Ni(I). Furthermore, addition of CH_3SCoM

and CoBphSH exhibits an increase hyperfine intensity illustrating that the sulfonate of CH_3SCoM is decreasing microheterogeneity of the Ni(I) in relation to the corphin ring. By taking spin percentages and normalizing the EPR spectra, we illustrate this claim in Figure 2.14 bb. The difference of intensity is minute, but still prevalent. The two samples that observe this increase are CH_3SCoM and CH_3SCoM with CoBphSH where a slight increase in intensity is observed compared to HSCoM, no substrate, and CoBphSH bound samples.

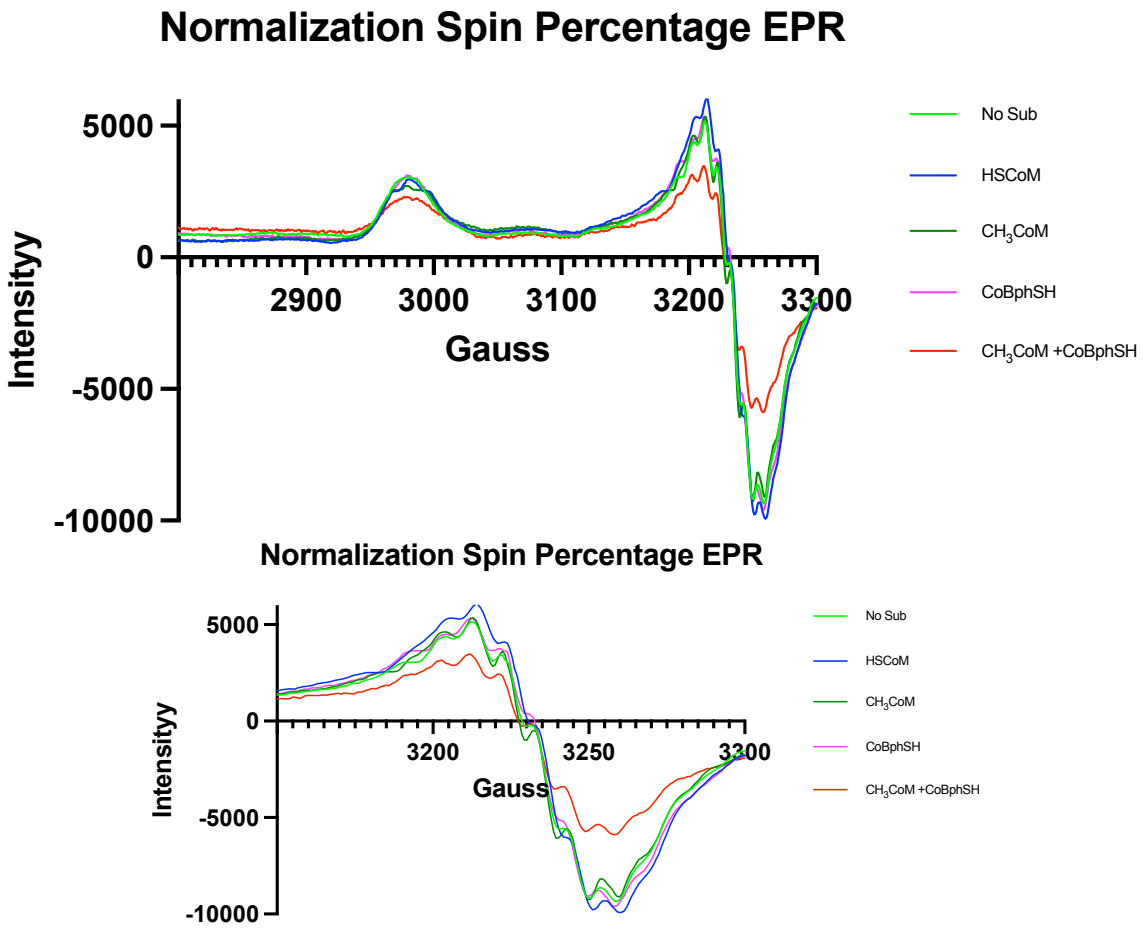

Figure 2.14 EPR Spectra of Various Substrates with MCRred1. (Top) EPR spectra taken with 49µM MCRred1 with 10mM HSCoM, 10mM CH_3SCoM, 1mM CoBphSH, and 600µM CH_3SCoM incubation with a 1mM addition of CoBphSH with a normalization factor to equate spectra with the same spin percentage. (Bottom) Inset of the $g_{\perp}$ to accentuate the hyperfine coupling intensity.

2.4 Discussion

Uncovering the intermediates of MCR is crucial to identifying how this complex enzyme catalyzes what is considered the chemistry "holy grail" of C-H bond activation of methane. By capturing the intermediates, we may gather insight to the chemistry available to make methane for biofuels as well as understand how MCR provides the reverse reaction for the oxidation of methane.

CoBphSH has been shown to bind the enzyme and cause a decrease in the MCRred1 signal via UV-Vis and EPR with no resulting new EPR active species. This finding is consistent with the 2016 Science paper by Wongnate *et al.* whose mechanism involving the radical production with an EPR silent MCRox1-silent intermediate [89]. With the pKa of the compound being 6.7 with a pH 7.6 of the reaction, it is possible that this compound may not react with a deprotonated $CoBphS^-$ and therefore decrease the reaction rates substantially. This hypothesis may work in our favor to slow the reaction rate to detect the radical, that theoretically should sharpen the radical peak seen in Wongnate *et. al*[89]. If the compound does not provide the sustained and identifying EPR signal, the next steps for this project are the synthesis of the PBN derived nitrone spin trap, and the vinyl radical clock synthesis. If the reaction of the PBN derivative does take place, the nitrone spin trap has been designed to provide the nitrone radical needed for identification. Furthermore, the vinyl radical clock will be chemically perturbed attaching a methyl group and homolytically cleaving the double bond vinyl. With these molecules soon to be synthesized, we will trap or find the evidence of a radical indicative of the radical mechanism described in Wongnate *et al.*[89].

Chapter 3 XFEL Serial Crystallography Reveals the Room Temperature Structure of Methyl-Coenzyme M Reductase

This chapter was previously published as

*Ohmer, C. J. et al. XFEL serial crystallography reveals the room temperature structure of methyl-coenzyme M reductase. J Inorg Biochem **230**, 111768 (2022).*

3.1 Abstract:

Methyl-Coenzyme M Reductase (MCR) catalyzes the biosynthesis of methane in methanogenic archaea, using a catalytic Ni-centered Cofactor F_{430} in its active site. It also catalyzes the reverse reaction, that is, the anaerobic activation and oxidation, including the cleavage of the C-H bond in methane. Because methanogenesis is the major source of methane on earth, understanding the reaction mechanism of this enzyme can have massive implications in global energy balances. While recent publications have proposed a radical-based catalytic mechanism as well as novel sulfonate-based binding modes of MCR for its native substrates, the structure of the active state of MCR, as well as a complete characterization of the reaction, remain elusive. Previous attempts to structurally characterize the active MCR-Ni(I) state have been unsuccessful due to oxidation of the redox- sensitive catalytic Ni center. Further, while many cryo structures of the inactive Ni(II)-enzyme in various substrates-bound forms have been published, no room temperature structures have been reported, and the structure and mechanism of MCR under physiologically relevant conditions is not known. In this study, we report the first room temperature structure of the MCRred1-silent Ni(II) form using an X-ray Free-Electron Laser (XFEL), with simultaneous X-ray Emission Spectroscopy (XES) and X-ray diffraction

(XRD) data collection. In celebration of the seminal contributions of inorganic chemist Dick Holm to our understanding of nickel-based catalysis, we are honored to announce our findings in this special issue dedicated to this remarkable pioneer of bioinorganic chemistry.

Keywords: Methanogens, Nickel, X-ray Free-Electron Laser (XFEL), Serial Femtosecond Crystallography (SFX), X-ray Diffraction (XRD), X-ray Emission Spectroscopy (XES)

3.2 Introduction:

Methane is ~25 times more potent as a greenhouse gas compared to carbon dioxide, and it has been estimated that it has contributed to about 20% of earth's warming since the industrial revolution [95]. Methanogenic microbes are responsible for producing about 100 billion tons of methane per year [96]. Although methanogenesis is the primary source of methane in the atmosphere, anaerobic methane oxidizing archaea found in marine ecosystems and aerated and dry soils use methane as an energy source [97]. Additionally, methane oxidation via hydroxyl radicals is the primary sink for atmospheric methane [98]. This generation and depletion of methane is a major contributor to the global carbon cycle and is critical for maintaining the earth's temperatures. Within the last 200 years, the concentration of methane in the atmosphere has more than doubled due to increased agricultural ruminants, mining of natural gases, and landfill seeps [99,100]. The global carbon cycle has been thrown out of sustainable equilibrium causing extreme droughts throughout Africa and the Mediterranean, heat, and precipitation [101]. Despite its global warming effect, methane, having the highest energy content of any carbon-based fuel, is very important for energy production, and accounts for 22% of U.S. energy consumption, with half of homes using natural gas as their heating fuel. Therefore, understanding the mechanism

and energetics of methane formation will enable more efficient biofuel production, providing us with a more sustainable source of energy while decreasing our dependence on fossil fuels and natural gas.

The nickel enzyme Methyl Coenzyme M Reductase (MCR) is responsible for the synthesis of methane in methanogens. MCR catalyzes the conversion of methyl-coenzyme M (CH_3-SCoM) and coenzyme B (HSCoB) to the heterodisulfide CoMSSCoB and methane [102]. Interestingly, MCR can also catalyze the reverse reaction, that is, the anaerobic oxidation of methane in a syntrophic process coupled to sulfate reduction [103]. This activation and subsequent cleavage of the very strong alkane C-H bond in methane occurs at its active site Ni(I)-F_{430} cofactor without utilizing any reactive oxygen species. Moreover, the reverse reaction of methane oxidation catalyzed by MCR in anaerobic methane oxidizing archaea (ANME) is one of the major biological sinks for atmospheric methane [104]. The specifics of the mechanism of MCR catalysis, however, still remain elusive.

Thus, a complete understanding of the structure and any potential physiologically relevant conformational dynamics in MCR is important. A variety of catalytic intermediates, including the formation of a Ni-alkyl intermediate shown in Fig 1A, have been proposed over the years based on various biochemical investigations and computational studies [105]. On the other hand, computational work proposed that the Ni-alkyl mechanism is too high in energy and provided evidence for a methyl radical-based mechanism of methane formation [106]. In 2016, based on computational, spectroscopic, and rapid kinetic studies, Wongnate *et.al* provided evidence supporting the formation of a methyl radical and disfavoring the Ni-alkyl mechanism [107].

The binding mode of substrates in all proposed mechanisms has been mostly based on their orientations within a 50 Å substrate channel as observed in the Ni(II) crystal structures [108–112]. As described in the canonical mechanism of Fig 1B, it is proposed that CH_3-SCoM binds to Ni(I) through a Ni-S interaction with HSCoB tethered above the F_{430} catalytic center. In Step 1, homolytic cleavage of the S-C bond of CH_3-SCoM results in a methyl radical. The methyl radical then abstracts a hydrogen atom from HSCoB, forming methane and a CoBS radical. In Step 3, the CoBS radical then reacts with the Ni thiolate complex forming a heterodisulfide anion radical intermediate, which transfers an electron into the Ni(II) to form CoBSSCoM and regenerate the active-Ni(I) state. In these mechanistic proposals, the CoBS radical must overcome an apparent 6.4 Å gap, as seen in various crystal structures of the Ni(II)-MCR-substrate-complex, to form the S-S bond of CoMSSCoB. Recent studies by our group have challenged the canonical binding mode of MCR [81]. Near-infrared, X-ray absorption spectroscopy, and electron paramagnetic resonance (EPR) studies have described a Ni-sulfonate coordination of the sulfonate group of CH_3-SCoM, shown in Fig 1, rather than the thiolate as previously suggested [109]. This binding mode places the two sulfurs (of SCoB and SCoM) within bonding distance. However, it implies a long-distance electron transfer mechanism from Ni(I) to cleave the C-S bond of CH_3-SCoM.

Further studies are required to discriminate between the various proposed mechanisms and gain insight into how the C-H bond of methane is enzymatically formed and activated. A critical limitation to that is the challenge of crystallizing MCR in its active reduced Ni(I) form. Due to the extremely low Ni(II)/(I) redox potential, the Ni(I) form is highly sensitive to oxidation during handling [111], even under highly anoxic conditions; These are significant challenges to structural elucidation of the active form of MCR. Thus, all structures of MCR so far have

captured the inactive Ni(II) forms, MCRred1-silent and MCRox1-silent, formed upon air exposure from MCRred1 and MCRox1, respectively [110]. Even dark green MCRred1 crystals grown and harvested within an anaerobic chamber at <1 ppm O_2 undergo oxidation to the yellow MCRred1-silent state by exposure to even small amounts of ambient oxygen present during X-ray data collection [111]. Moreover, no room-temperature structure currently exists for any state of MCR. Cryo-crystallography has yielded many MCR structures, but it has some limitations. Damage to the crystals from rapid freezing, the need for optimization of cryoprotectants, and ice ring interference are all problems that must be overcome with cryo structures [113]. Most importantly, cryo-crystallography provides limited insight into physiologically relevant protein dynamics. Room temperature (RT) crystallography gives us the opportunity to overcome this issue and study MCR conformational dynamics at more physiologically relevant conditions [114].

This present study provides a glimpse of the first room-temperature crystal structure of MCR. This structure was obtained using the X-ray Free Electron Laser (XFEL) at Linac Coherent Light Source (LCLS) and describes the Ni(II)-MCRred1-silent state of the well-studied MCR from *Methanothermobacter marburgensis.* The rationale for pursuing XFEL rather than synchrotron measurements for this room-temperature structure of MCR is based on the limitations of cryo structures described above. For example, the S-C bond in CH_3-SCoM has been suggested to break due to radiation-induced damage during data collection [110]. This may explain why CH_3-SCoM has not been observed in any synchrotron-based crystal structures [108–112]. In this report of the room-temperature crystal structure of MCR, we aim to provide a snapshot into its active site architecture and reveal potentially functionally relevant conformational dynamics. We also present a structure of MCR Ni(II) pressurized with xenon gas in an attempt to map gas channels within this fascinating enzyme, with the continuing goal of using these

methods to map potentially important gas channels in the active Ni(I) MCR enzyme undergoing catalysis.

3.3 Materials and Methods:

3.3.1 Purification and crystallization of MCRred1-silent:

MCRred1 from *M. marburgensis* (catalog OCM82) was purified and handled in an anaerobic chamber (Vacuum Atmospheres, Inc. or MBRAUN) containing <1ppm of O_2, as previously described [81,111]. We removed the Ni(I)-enzyme from the chamber to convert the enzyme to the inactive Ni(II)-state, also known as MCRred1-silent. To be noted, this is different from the MCRox1-silent state where MCRox1 is air exposed [110]. UV-Vis spectroscopy following purification and oxidation of the MCR protein shows the catalytic Ni to be in the +2 oxidation state (SI Fig 1), indicating conversion to the MCRred1-silent form.

The concentration of MCRred1-silent used for crystallization was quantified using UV-Vis spectrophotometry with extinction coefficients of 22.0 and 12.7 $mM^{-1}cm^{-1}$ at 420 and 385 nm, respectively, using a multi-wavelength calculation as previously described [115]. All crystallization of MCRred1-silent was carried out at a concentration of 150mM (40 mg/ml) in 50 mM Tris, pH 7.6. The crystallization buffer used in both crystal drops and the well reservoir is composed of 18% PEG 400, 150 mM magnesium acetate hexahydrate, and 100 mM HEPES Sodium, pH 7.5. Hanging drop vapor diffusion was used with 1:1 ratios of protein solution and crystallization buffer, respectively, to produce crystallization solutions ranging from 2-10 µL with a well solution containing 0.5mL crystallization buffer. Crystals of MCRred1-silent grew overnight, but the crystals were too large (~100-200 µm sized) to be appropriate for XFEL analysis. Crushing big MCR crystals by vortexing for 5 minutes with a Teflon bead (0.5mm) fragmented the crystals but damaged diffraction quality which was demonstrated during

screening at the Advanced Light Source (ALS, beamline 8.2.1), Berkeley. We grew slightly smaller MCRred1-silent crystals (40- 80 μm) by adjusting the seed stock concentration in our hanging drop trials and used these microcrystals for our RT XFEL measurements. They belong to space group $P2_1$ (a=83.08±0.09 Å, b=119.78±0.16 Å, c=123.21±0.15 Å, α=90°, β=91.7°, γ=90°) with two MCR dimers per asymmetric unit as reported previously [111] (Fig 2A).

3.3.2 Sample Delivery, X-Ray Diffraction (XRD) and X-ray Emission Spectroscopy (XES) data collection at LCLS:

XFEL diffraction data were collected at the Macromolecular Femtosecond Crystallography (MFX) instrument of LCLS, (SLAC National Accelerator Lab, Menlo Park, CA) [116] at 300 K on a RAYONIX MX340-HS CCD detector, using the previously established Drop-On-Tape (DOT) [117] approach (SI Fig 2). The X-ray beam photon energy was 9.5 keV with a pulse energy of 1 mJ, a pulse length of 35 fs and a beam size on the sample of 4 μm x 4 μm (Full Width Half Max, FWHM). Data collection statistics are available in SI Table 1. X-ray emission data were collected in tandem with diffraction data using a multicrystal wavelength-dispersive hard X-ray spectrometer based on the von Hamos geometry [118]. Due to the change of polarization direction of the hard X-ray undulator of LCLS our previously used setup [117,118] was modified to place the analyzer crystals above the X-ray interaction point and the position sensitive detector at 90 degrees from the beam direction in the horizontal plane. An array of three Si(620) analyzer crystals was placed 250 mm above the interaction point with the center of the crystals at 74.80 degrees respect to the interaction point, collecting both Ni Kα lines on an ePix 100 detector with its center located 136 mm side wise of the X-ray interaction point (SI Fig 2). To calibrate the spectrometer geometry, spectra from $[Ni(H_2O)_6]^{2+}$ were collected and compared

to a synchrotron reference. The XES data was also pedestal corrected to account for differences in noise of the detector pixels.

3.3.3 XRD Data Reduction, Processing, and Refinement:

The collected dataset was reduced and processed using *cctbx.xfel* and DIALS [119,120]. We performed joint refinement of the crystal models against the detector position for each batch to account for small time-dependent variations in detector position [120]. We also corrected for the Kapton tape shadow as in [117]. Data were scaled and merged to 1.9 Å based on previously established resolution cutoff criteria (~10x multiplicity, where the values of I/σ(I) do not uniformly decrease any more [117], and where $cc_{1/2}$ values stop decreasing monotonically [121], indicating no useful information is contained in resolution shells beyond that point), using *cctbx.xfel.merge* with errors determined by the ev11 method [122]. Data statistics are available in SI Table 1. Structure determination was done using Phenix [123] starting with molecular replacement using the model PDB ID: 3M1V. [111] as the reference model [124]. For all subsequent refinements with Phenix, we turned off automatic linking within the chain, as well as NCS restraints, and instead defined the interactions between the Ni-OE1(Q147) and Ni-S1(CoM) by supplying custom coordination restraints as parameter (phil) files. We used Coot [125] for model building with multiple iterations of refinement using phenix.refine [123,126,127] with the aforementioned settings. Comparisons of the cryogenic MCRred1 models with the room temperature model were performed using the SSM function in Coot [128]. All figures for this paper were generated using Chimera [129] and Chimera-X [130].

3.3.4 Xe-pressurized cryo-crystallography:

MCR was crystallized using the sitting drop crystallization method in an In Situ-1 Crystallization Plate (MiTeGen) under aerobic conditions in an MBraun Chamber at room temperature. 1 μL of 24 mg/mL MCR was mixed with 1 μL of well solution (27% (w/v) PEG400, 0.18 M magnesium acetate, 0.25 M sodium chloride, and 0.10 M HEPES pH 7.5) to make a 2-μL sitting drop in a sealed well with 30 μL well solution. Yellowish green rod MCR crystals grew in two to four hrs. The entire crystallization plate was shipped to Advanced Light Source Beamline 8.2.2 for Xe- pressurization and data collection. The crystals used to determine Xe-derivatized structure were transferred from the sitting drop into 2-5 μL of paraffin oil briefly and then sealed in a steel chamber pressurized with xenon at 180 psi for 10 mins. The Xe-derivatized crystals were flash-cooled in liquid nitrogen for data collection immediately. Data were collected at ALS 8.2.2 on an ADSC Q315R CCD detector using the inverse beam method with wavelength at 1.5498 Å. The dataset was indexed and scaled in HKL2000 [131] with Bijvoet pairs treated independently. cc1/2 ~ 0.75 was used as the high-solution cutoff criteria. Data statistics are listed in SI Table 2. The structure of Xe-derivatized MCR was determined to 2.5-Å resolution by rigid body refinement from previously published MCR structure (PDB ID: 3M1V) using Phenix.refine [126]. The model contains a dimer of heterotrimers in the asymmetric unit (Fig 2A). The atomic coordinates and B-factors were iteratively refined in Phenix Refine with manual adjustment of the model in Coot [125,126,128]. Two-fold non-crystallographic symmetry (NCS) restraints were used throughout refinement. Water molecules were added manually using Fo-Fc density contoured to 3.0σ as criteria. Xenon sites were assigned using anomalous difference density contoured to 5.0σ as criteria. Occupancies of xenon atoms were adjusted such that the B factors of xenon atoms are similar to atoms nearby. Restraints for cofactors and modified amino acids were generated with Phenix.eLBOW[126]. A composite-omit electron density map was

calculated using Phenix to verify the model. The refinement statistics are listed in SI Table 2. Software used to process Xe- derivatized MCR dataset was provided by SBGrid [132].

3.3.5 Identification of potential "Gas Tunnels" in MCRred1-silent and its ethane-oxidizing homolog ethyl-coenzyme M reductase (ECR):

Caver [133] was used to identify potential tunnels in our RT MCRred1-silent structure. Key amino acid residues were identified in our structure by a sequence alignment with identified ECR (7B1S) residues around the gas tunnel via Clustal-W [134].

3.4 Results

3.4.1 Comparison of the first XFEL structure of MCRred1-silent at 1.9 Å resolution with cryogenic structures

We collected a 1.9 Å resolution X-ray diffraction dataset for the (Ni-II) MCRred1-silent state using microcrystals at the X-Ray Free-Electron Laser (XFEL) source at LCLS. Although several cryo structures of MCRred1-silent currently exist, this new structure is important as it provides us with the exciting opportunity to study physiologically relevant MCR dynamics and/or any functionally significant conformational shifts that are permitted only at temperatures above freezing. In our presented structure, MCRred1-silent exists as a dimer of trimers (Chains A, B, C and a, b, and c) with 12 contacts across the six chains (Fig 2A), forming the 50Å long substrate tunnel leading to the catalytic Ni-F_{430} (SI Fig 3B). Both trimers exhibit similar overall B- factors (Fig 2B), as observed in previously published cryo models of MCRred1-silent (SI Fig 3A).

3.4.2 Modified amino acids:

We have identified the six previously reported modified amino acids in 5AY0 [109], namely, 2-Methyl-glutamine (MGN), S-Methyl-cysteine (SMC), 5-Methyl-arginine (AGM), Di-dehydro-aspartic Acid (DYA), Thioglycine (TG) and N1-Methyl-histidine (MHS) (Fig 3) in the chain A/a of our new XFEL MCRred1-silent structure as well. Difficulties in purifying active MCR from organisms where a genetic system has been developed have hindered the understanding of the structural or catalytic role(s) of these modified amino acid residues. Thus, we are only able to assign the function of any substituted amino acid based on comparisons of growth rates, which are limited by biosynthesis, not by methanogenesis [135]. Substitution of the thioglycine with a glycine residue in *Methanosarcina acetivorans* did not reveal any growth defects except at elevated temperatures and with substrates that have low free energy yields [136]. It was proposed that the thioglycine residue is not involved directly in catalysis, but in stabilizing the protein secondary structure; however, as just mentioned, the growth rate would not be limited by enzymatic activity of the variant(s), unless it is severely reduced. It is important to complement such studies with activity measurements of the wild-type versus variant proteins. Therefore, we used structural analysis of the *M. marburgensis* enzyme to see if these residues are dynamic in room temperature crystallography. In this study, we find no evidence of dynamics in these six modified amino acids at room temperature. A structural comparison with previously published cryogenic MCRred1-silent models 3M1V and 5A0Y, reveal that the modified amino acids do not exhibit any significant changes in structure or in B-factors across these three models (Table 1, SI Fig 4). However, out of all the modified amino acids, N1-Methylated Histidine (MHS) shows highest mobility across all three models tested, and among all the reported modified amino acids. However, we require more studies with the active Ni(I) MCR structure to understand the physiological functions of these unique modifications.

3.4.3 Active site:

Superimposition of the cryogenic MCRred1-silent structures (3M1V and 5AY0) with our room temperature structure reveals most of the active site architecture to be conserved structurally (Fig 4, SI Table 2). However, the distance between the oxygen atom of Glutamine 147 and the catalytic Ni in our RT XFEL MCRred1 structure is observed to be 2.27Å ± 0.05 and 2.28Å ± 0.04 in protomers 1 and 2, respectively (Fig 4B). This indicates a 0.07 ± 0.05 Å and 0.03Å ± 0.04 Å decrease in the Ni/F430-OE1-(Q147) bond in protomer 1 and 2 respectively of the XFEL structure, compared to the cryogenic model 3M1V (SI Table 2). The accuracy of these positional assignments was determined by perturbation of the structure factors (±[F_{obs}-F_{model}]) of the model using the END RAPID method [137] which allows us to assign coordinate errors to individual atoms. We randomly perturbed the structure factors in the target model in 100 trials, followed by re-refinement of each of the perturbed datasets using Phenix. This generated the standard deviations of the reported positions. Although this distance shrinking in the RT MCR model is exciting, it must be noted that at his current data resolution this observation is within the error limits and hence it is not possible to draw further conclusions from this observation

Another distinction between the structures is a 0.24Å ± 0.09 expansion in the distance between the two thiolates of CoM and CoB in protomer 1 (negligible change in protomer 2) with respect to the cryogenic model 3M1V.

3.4.4 Substrate analog CoM (Coenzyme M) & native substrate HSCoB:

We see the substrate analog CoM (100% occupancy) as well as the native substrate HSCoB (~ 90% occupancy) bound to the active site of our room temperature XFEL MCRred1-silent structure, with visible 2Fo-Fc electron density at 1.5 sigma (SI Fig 5B). CoM and HSCoB

thiolates are at about 2.4Å and 8.8Å distances respectively from the catalytic Ni (SI Table 3). Retention of CoM and CoB is a little surprising, given that the purified protein had been subjected to seven rounds of buffer exchange; however, CoM and HSCoB are also found in the cryogenic structures of this form of MCR [109,111]. The thiol of HSCoB is only coordinated by a nearby (~2.6Å away) N481 (Chain A/a) and a water (~3Å away); however, CoB interacts strongly with several nearby residues via its threonine phosphate end (SI Fig 6). This CoB-phosphate coordination is also intact in the cryogenic MCRred1-silent structures (3M1V and 5A0Y), which makes the retention of CoB following oxidation and several rounds of buffer exchange in our study, quite logical. The retention of CoM within the crystal active site can be potentially explained owing to its coordination via its thiolate group to the Ni atom and three other active site residues, namely Y333-OH, Y367-OH, Ni, and a water (SI Fig 7).

These observations point to a potential mechanistic feature of MCR wherein it assumes a "locked-in" state as soon as the catalytic Ni is oxidized. This hypothesis is further bolstered by the overall similarities observed in the active site architecture of the RT XFEL structure compared to previously published cryogenic structures of MCRred1, although this requires further exploration. Furthermore, CoM is positioned as in the cryo structures, with the sulfur of CoM located near the Ni center (SI Fig 7). It should be noted that CH3-CoM is not present in our structure, as it was not present in our crystallization solution. However, previous attempts in the field to crystallize MCR with CH_3-SCoM have yielded several synchrotron cryo structures that lack the methyl group of CH_3-SCoM [111]. Grabarse *et al.* suggest radiation damage-induced conversion of the CH_3-SCoM to CoM at synchrotron sources [110]. This observation highlights the need to use XFEL to record damage-free structures of MCR co-crystallized with CH_3-SCoM and track its fate within the active site.

Interestingly, we notice significant 2Fo-Fc electron density roughly halfway between the thiol groups of CoM and CoB (SI Fig 5), at about 1.7 sigma in protomer 1 and 1.4 sigma in protomer 2. This "mystery" 2Fo-Fc electron density has also been reported previously in cryogenic structures of both MCR and ECR, wherein a water molecule was fit in to explain the density in MCR. However, there is debate about the identity of this molecule. While some favor water, others suggest the density might be explained best by a molecule having one or two heavier atoms in MCR and ECR, respectively [138]. We placed a water molecule between the two substrate thiol groups in both protomers of MCRred1-silent (Fig 4C). This water has an average B factor of ~32 $Å^2$ in our room-temperature structure. Furthermore, there is no significant B factor elevation within a radius of ~20Å centered on this active site water in both protomers in our room-temperature structure or in the cryo structures of 3M1V or 5A0Y [109,111]. These factors support the assignment of this density to a "conserved" and well-ordered water molecule that remains coordinated to the active site of MCRred1-silent (SI Fig 5). While this water molecule appears to be well conserved in the Ni(II) state of the MCR enzyme, it is unlikely to be present during catalysis [108]. We suggest that the water molecule in this "locked-in" Ni(II) MCR structure acts as a placeholder for the methyl radical during the transition state.

There is one major difference between the coordination environment of the assigned water molecule in our structure versus those of the cryogenic structures (SI Fig 6). In protomer 1 of the RT structure, the water molecule is not coordinated to the CoB thiol but instead only weakly coordinated to the thiolate of CoM (3.05Å away) unlike in the cryogenic structures (3M1V and 5A0Y) where it associates with the CoB thiol, 2.8Å and 2.96Å away, respectively. The distance between the water and the CoM thiolate in the cryogenic models 3M1V and 5A0Y are expanded to 3.5Å and 3.3Å compared to the 3.05Å in the RT structure. This distance

elongation in the cryogenic structures could potentially indicate evidence of radiation damage or partial motion of the water molecule at room temperature. However, in protomer 2 of the RT structure, this water-CoB sulfur thiolate coordination is intact (distance between the water and sulphur of CoB is 2.99Å), like in the cryogenic models. Moreover, this water molecule is close to two active site tyrosines nearby, namely Y333 and Y367 (~3.0Å away from both hydroxyl groups of the tyrosines), which might coordinate it by weakly by donating H bonds via their OH groups (SI Fig 5A) during catalysis. It will be interesting to further explore the active site water coordination environment as shown in SI Fig 5, and its dependence on data collection temperatures to see whether this has a significant impact on the enzyme's catalysis.

3.4.5 Simultaneous collection of Ni XES for the MCRred1-silent form:

We collected Ni Kα X-ray emission spectroscopy (XES) simultaneously with XRD data (Fig 5). These data provide a real-time handle to monitor both oxidation state and electronic structure during serial femtosecond crystallography [139,140]. The oxidized MCR data was compared against those of two water-soluble nickel(II) standards, $[Ni(H_2O)_6]^{2+}$ and $[Ni(bpy)_3]^{2+}$ (bpy = 2,2'-bipyridine), which were also collected in solution at room temperature at the XFEL using the DOT sample delivery system. The XES spectrum of the Ni center in the oxidized MCR is significantly shifted from both molecular standards. That such a clear difference is observed between complexes in similar oxidation state, but with changes only in the coordination environment implies that XES will be a useful tool to monitor subtle changes to the electronic structure of the Ni center in MCR during future experiments in which we will collect simultaneous XRD and XES snapshots of the catalytic cycle by SFX.

3.4.6 Identification of potential "Gas Tunnel" residues in MCR-Ni(II):

Recently, the crystal structure of an MCR homolog, ECR, isolated from the ethane oxidizing organism *Candadatus* Ethanoperedens thermophilum, was reported by Hahn *et. al*. via xenon pressurized cryo-crystallography [138], wherein a 33 Å long gas tunnel was discovered, leading from the substrate binding cavity to the surface [138], as shown in Fig 6. When the same technique was performed on the MCR purified from the methane producing *M. marburgensis*, six Xe atoms were found in each protomer, all at the surface of the enzyme, leading Hahn *et al.* to suggest that the gas tunnel is specific to ethane oxidizers [138]. Our independent xenon pressurized cryo-crystallographic structure of the *M. marburgensis* MCR revealed four xenon binding sites (Fig 6). Of these four sites, Xe1 and Xe2 are found near the surface of the B subunit, Xe3 at the surface of the A subunit, and Xe4 in the B subunit 22 Å from the catalytic Ni (Fig 6, SI Fig 8). To validate Hahn *et al'*s observation of no methane transport tunnel present in MCR, we superimposed our Xe- pressurized MCR structure with ECR (PDB 7B1S). We noticed that Xe3 is ~11 Å away from the ECR gas tunnel (Fig 6), but found no indication of a "tunnel" in MCR by computational analysis using Caver [133] or by Xe pressurized crystallography, as previously shown by Hahn *et al*, who proposed that this tunnel exists specifically for ethane oxidizers [138].

To perform a more extensive investigation into the difference between methane and ethane oxidizers, we performed sequence alignment of MCR from *M. marburgensis* with ECR (PDB 7B1S) via Clustal-W [134] and identified several common residues in both enzymes that line the putative ECR gas tunnel (SI Fig 9). Out of these residues, three hydrophilic residues of *M. marburgensis* (namely K351, E355, and E487 in chain A of 3M1V) align to *Ca.* E. thermophilum hydrophobic residues (namely A392, M398, and G532 respectively; 7B1S numbering), highlighted in red in SI Fig 9. The first two of these residues in ECR are located at the opening of this ethane gas tunnel, while the latter is located in the middle of the tunnel. A comparison of these residues in the ECR 7B1S structure with the MCR cryogenic 3M1V structure yields no significant differences in structure or B factors. Moreover, in all the models

(cryo ECR, cryo MCR and RT MCR), the side chains of K351 and E355 have the highest B factors compared to their surrounding residues (within ~15 Å). It will be interesting to use the room temperature DOT and XFEL methods to further investigate the possibility of a gas tunnel in MCR by tracking structural differences and B factor changes in these conserved tunnel residues after adding substrates (and analogs/inhibitors like CoM) to MCR.

3.5 Discussion

While previous crystallography studies have provided the foundation for understanding the mechanism of MCR catalysis [108–112], capturing the structure of the enzyme in the active Ni(I) state is still a goal to be achieved. Therefore, the elucidation of MCR's active structure and visualization of conformational dynamics along the reaction cycle will depend on the evolution of techniques in structural biology. In this study commemorating Dick Holm and his contribution to the field of Ni complexes, we demonstrate the feasibility of using our DOT sample delivery approach to perform simultaneous XRD and XES data collection on the Ni- dependent MCR protein system. This approach will be critical in characterizing the structural, as well as electronic state progression of the catalytic Ni as MCR undergoes catalysis. Herein, we present the first room temperature structure of MCRred1-silent Ni(II) state using the X-Ray Free-Electron Laser (XFEL) source at LCLS, SLAC.

Comparison of the room temperature and cryogenic MCR structures reveals mostly similarities, but some differences are of note. While we observed an apparent ~0.07Å shortening of the bond between the lower axial glutamine (Q147) and the Ni(II) in protomer 2 of our RT structure relative to the cryogenic MCR structure (3M1V) (0.03Å bond shortening in protomer 1), high resolution data is needed to confirm if this is significant. A second distinction pertains to

the loss of coordination of the water molecule in our RT structure with the thiol of CoB in protomer 1 (this coordination is retained in both cryogenic structures 3M1V and 5A0Y in protomer 1). Third, we notice that the distance between the thiolate of CoM and the thiol of CoB expands by an average of ~0.24Å in one of the protomers in the RT structure compared to the cryogenic structure, 3M1V, with no changes in these distances in the other protomer. These last two variations observed in the room-temperature structure represent small changes in the locations of CoM and CoB relative to those seen in previous cryo structures. While these subtle differences are interesting and warrant additional investigations, we require higher quality datasets at RT to better resolve them, which is our continuing goal.

We had hoped that our room temperature structure might reveal evidence supporting a proposal, based on electron paramagnetic resonance and UV-visible spectroscopic studies of the active Ni(I) enzyme, that MCR exhibits half-of-sites reactivity. This hypothesis envisions that the two MCR active sites are structurally connected such that one active site can undergo catalysis, like the motion of a "dual stroke motor" [45]. However, in our room-temperature Ni(II) structure, we observe similar B-factors between the related protomers, even near the active site. Therefore, if this model is correct, it appears that the dynamical differences may be observed only in the structure of the Ni(I) form of MCR, further underlining the need for capturing the structure of the active state of this enzyme, especially at room temperature. Furthermore, these overall structural similarities between the RT and cryogenic structures, as well as the retention of HSCoB in the active site of our RT MCRred1-silent structure point to a potential "locked-in" state of the Ni(II) MCR enzyme's catalytic cavity.

Due to the lack of movement in the "locked-in" state of Ni(II) MCR, to observe any important conformational dynamics relevant to its catalysis, we require a complete structural

characterization of the active Ni(I) MCR form as it turns over at physiologically relevant temperatures. While previous solution XAS studies of MCRred1 have revealed the local coordination environment of the Ni center in various states [81], the overall crystal structure of MCR and its catalytic intermediates is a challenge that we hope can be met by future XFEL studies. This active MCR structure will provide a clear visual representation of the active site, substrate binding modes, and methane localization as it lights the fuse for methane production and oxidation.

Obtaining the structure of the Ni(I) form of MCR is challenging because the most reliable methods of activation are by sparging cell cultures with H_2 [141] or, as used in this study, CO [73]. Moreover, oxidative damage irreversibly converts the active enzyme to a Ni(II) form. We are currently working on resolving some of these obstacles by batch co-crystallizing MCR with reducing agents and developing protocols for anaerobic data collection. We will screen these co-microcrystals for shifts in unit cell parameters from MCR Ni(II), potentially indicating a change in oxidation state. We hope to take advantage of MCR's strictly ordered catalytic mechanism [107] to synchronize the turnover process in all the microcrystals. To maintain this synchronicity in each crystal, we will co-crystallize the Ni(I) enzyme with the native substrate, CH_3-SCoM, and use the Drop-On-Drop-On-Tape sample delivery system to deliver HSCoB in order to trigger catalysis [142].

In conclusion, this current study serves as a good starting point that demonstrates i) the feasibility of using our Drop-On-Tape (DOT) sample delivery technique to capture the electronic state of the catalytic Ni atom via XES, while simultaneously collecting a complete 1.9 Å XRD dataset in less than one hour. ii) While we do not see large structural differences between our XFEL and published cryogenic MCRred1-silent structures, we do see indications that the active

site “locks” in place following Ni(I) oxidation, thereby retaining the CoM analog and native CoB substrates. In the future, we want to build on this demonstrated simultaneous XRD and XES technique to trigger and track damage free catalysis in active Ni(I)-MCR *in crystallo* using anaerobic sample delivery and data collection at XFEL sources.

3.6 Abbreviations

MCR, Methyl-Coenzyme M Reductase; CH_3-SCoM, Methyl-Coenzyme M; DOT, Drop-On-Tape; ECR, Ethyl-coenzyme M Reductase; HSCoB, Coenzyme B; LCLS, Linac Coherent Light Source; RT, Room Temperature; XES, X-ray Emission Spectroscopy; XFEL, X-ray Free Electron Laser; XRD, X-ray Diffraction

3.7 Acknowledgements

We thank staff from LCLS and ALS (BL 5.0.2, 8.2.1 and 8.3.1) for their support. P.Y.-T.C. and C.L.D. thank Dr. Corie Ralston and Dr. Steven E. Cohen for helping with Xe-pressurized cryo- crystallography. C.L.D. is a Howard Hughes Medical Institute investigator and a Fellow of the Bio- inspired Solar Energy Program, Canadian Institute for Advanced Research. This work was supported by the Director, Office of Science, Office of Basic Energy Sciences (OBES), Division of Chemical Sciences, Geosciences, and Biosciences of the Department of Energy (DOE) (J.Y., V.K.Y., J.F.K.) for X-ray methodology and instrumentation and spectroscopy and crystallography data collection and analysis, by National Institutes of Health, National Institute of General Medical Sciences (NIH NIGMS) grants 1P41GM139687 (R.A.-M.), GM55302 (V.K.Y.), GM110501 (J.Y.), GM126289 (J.F.K.), GM117126 (N.K.S.). R35 GM126982 (C.L.D.). PO1GM063210 (N.W.M). Vetenskapsrådet 2017-00356 (T.F.), and the Air

Force Office of Scientific Research grant FA8655-20-1-7010 (T.F.) are acknowledged for support. This work also was supported by the Physical Biosciences Program within the OBES at DOE by contract DE-FG02-08ER15931 (S.W.R.). Beamlines 5.0.2, 8.2.1, 8.2.2 and 8.3.1 of the Advanced Light Source, a DOE Office of Science User Facility under Contract No. DE-AC02-05CH11231, are supported in part by the ALS-ENABLE program funded by the NIH NIGMS, grant P30 GM124169-01. Use of the LCLS, SLAC National Accelerator Laboratory, is supported by the US DOE, Office of Science, OBES under contract DE-AC02-76SF00515. The Rayonix detector used at LCLS was supported by the NIH NIGMS grant S10 OD023453. This research used resources of the National Energy Research Scientific Computing Center, a User Facility supported by the Office of Science, DOE, under contract DE-AC02-05CH11231.

3.8 Author Contributions

Conceptualization; J.Y., J.F.K., S.W.R. Sample Purification and Crystallization: C.J.O., A.P. XFEL setup design for XES and XRD: R.A.-M., F.D.F., H.M., P.S.S. Data collection at LCLS: M.D., S.M.K., C.K., I.B., H.M., P.S.S., L.B.G., R. A.-M., F.M., F.D.F., Al.B., U.B., V.K.Y., J.Y., J.F.K. SR Data collection: M.D. R.C., P.Y.-T.C., C.L.D., XRD Data Analysis: M.D., P.Y.-T.C., C.L.D., A.B, A.S.B., D.W.P., N.K.S. XES Data Analysis. C.K., I.B., H.M., M.D.D., R.M., T.F., U.B. Structure Refinement: C.J.O., M.D., P.Y.-T.C., S.M.K., N.W.M. C.L.D. Writing – Original Draft: M.D., C.J.O., S.W.R. Writing –Review and Editing, all authors. Supervision: C.L.D., V.K.Y., J.Y., J.F.K, S.W.R.

Competing Interests: The authors have no competing interests to declare.

3.9 Tables

	RTXFEL (Å²)	CRYO 3M1V (Å²)	CRYO 5A0Y (Å²)
2-Methyl Glutamine (MGN400)	22.4, 22.3	7.2, 6.9	8.0, 7.2
5-Methyl Arginine (AGM271)	22.5, 21.7	6.8, 6.5	6.6, 6.6
1-Methylated Histidine (MHS257)	35.1, 32.0	18.0, 15.2	12.8, 11.9
S-Methyl Cysteine (SMC452)	23.7, 24.4	7.8, 8.0	8.5, 8.5
ThioGlycine (TG445)	23.0, 22.9	6.8, 6.5	7.6, 6.7
DI-Dehydro Aspartic Acid (DYA450)	23.4, 22.6	7.9, 8.2	8.4, 8.3

Table 3.1 B factors of modified amino acids in RT vs. Cryo MCRred1-silent structures.

(average calculated B factors for MCRred1-silent protomers, separated by commas).

3.10 Figures

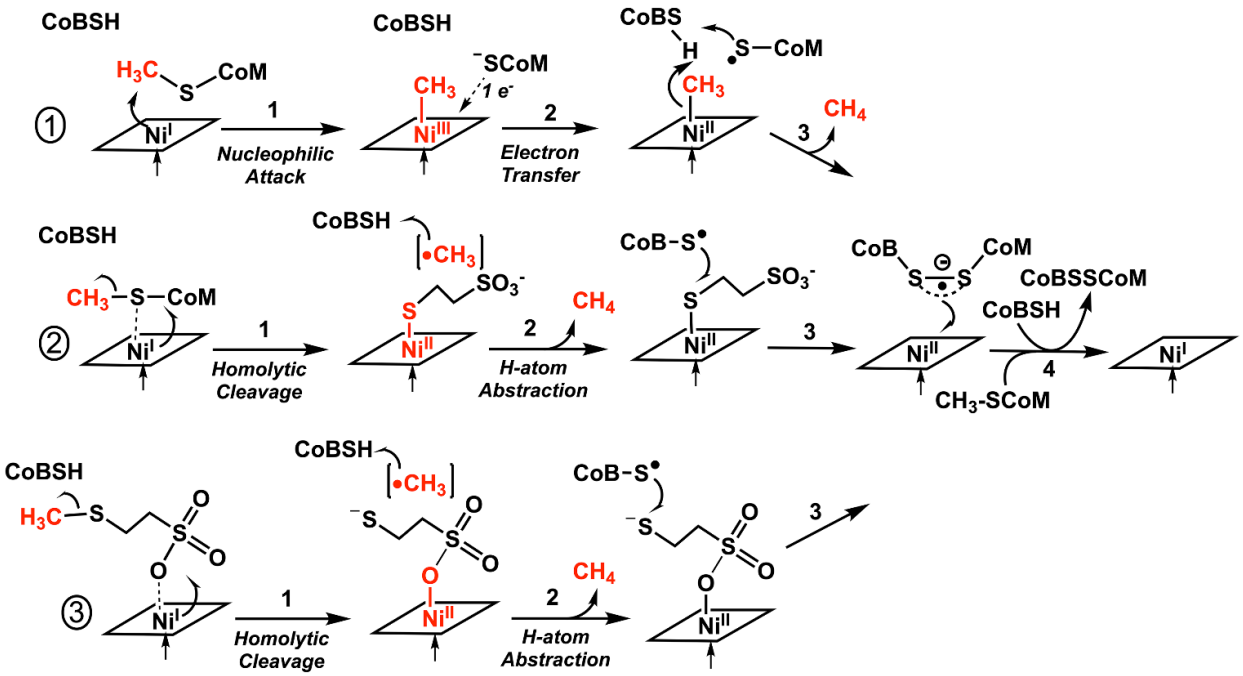

Figure 3.1 Proposed organometallic versus radical mechanisms MCR-catalyzed methane formation. (A) Organometallic mechanism involving nucleophilic attack on methyl-CoM to form a Ni(III)-methyl intermediate (B) Ni(I) promoted homolysis of the methyl-S bond of methyl-CoM to form a methyl radical and Ni(II)-thiolate of CoM. (C) Ni(I) promoted homolysis of the methyl-thioether bond of methyl-SCoM bound through long-range electron transfer from a Ni-sulfonate bond to generate a methyl radical and Ni(II)-sulfonate (as proposed by Patwardhan et al. [81]).

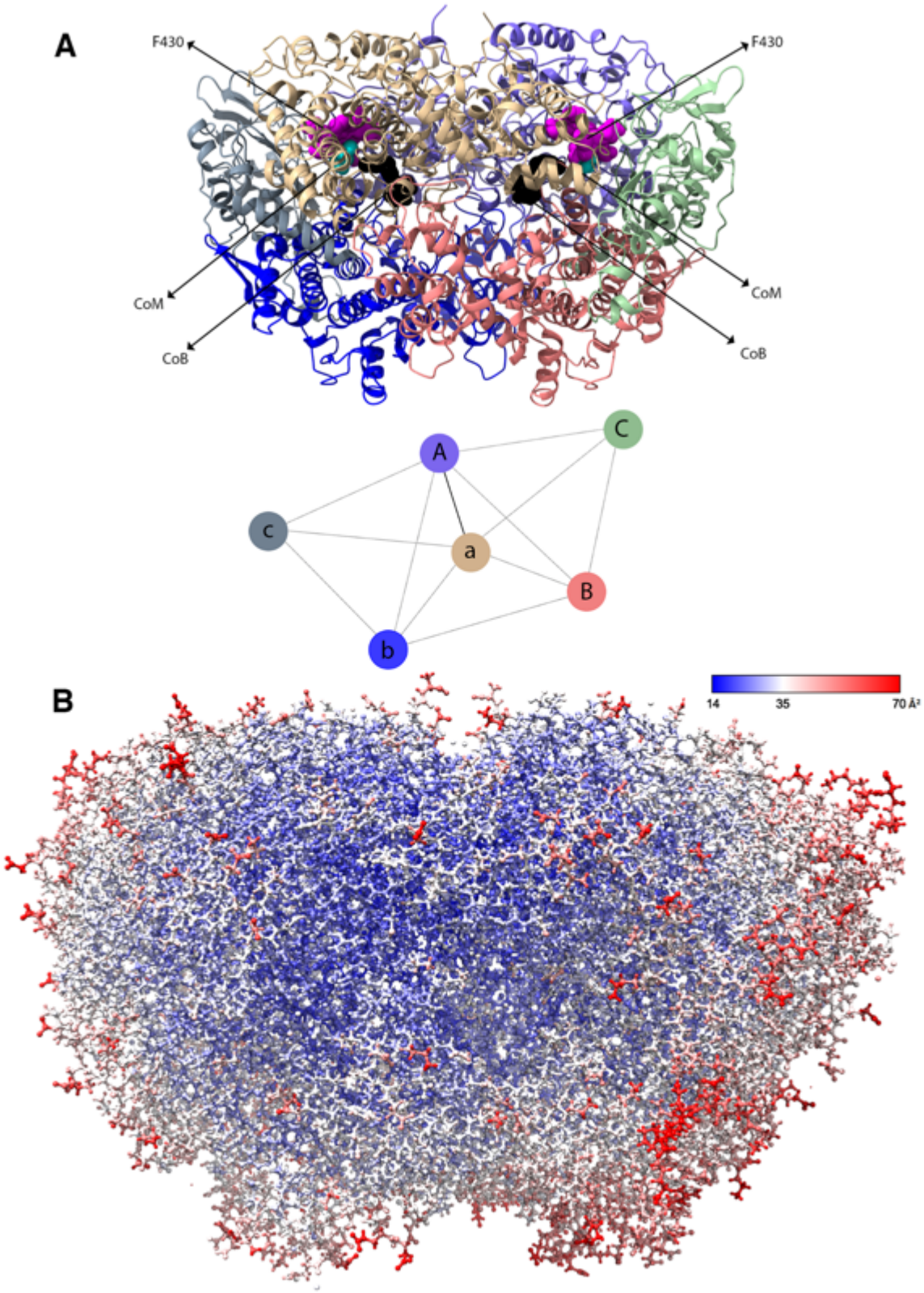
A
F430
F430
CoM
CoM
CoB
CoB
C
A
c
a
B
b
B
14
35
70 Å²

Figure 3.2 Room Temperature structure of MCRred1-silent (A Top): The global structure of MCRred1-silent at room temperature shows two trimers per asymmetric unit; trimer 1 is comprised of chains A (Purple), B (Salmon), C (Green) and trimer 2 is comprised of chains a (Tan), b (Blue), c (Grey). CoM (red with green outline), CoB (Black) and Ni-F430 (Magenta) are shown as sphere representations and are labeled. (Bottom) shows the 12 contacts between the 6 chains. (B) B factor analysis across the entire structure of MCRred1-silent shows overall similar B factors across both trimers (low B factors towards the core of the protein and higher B factors towards the surfaces, as expected). Figure made with Chimera-X(1.3).

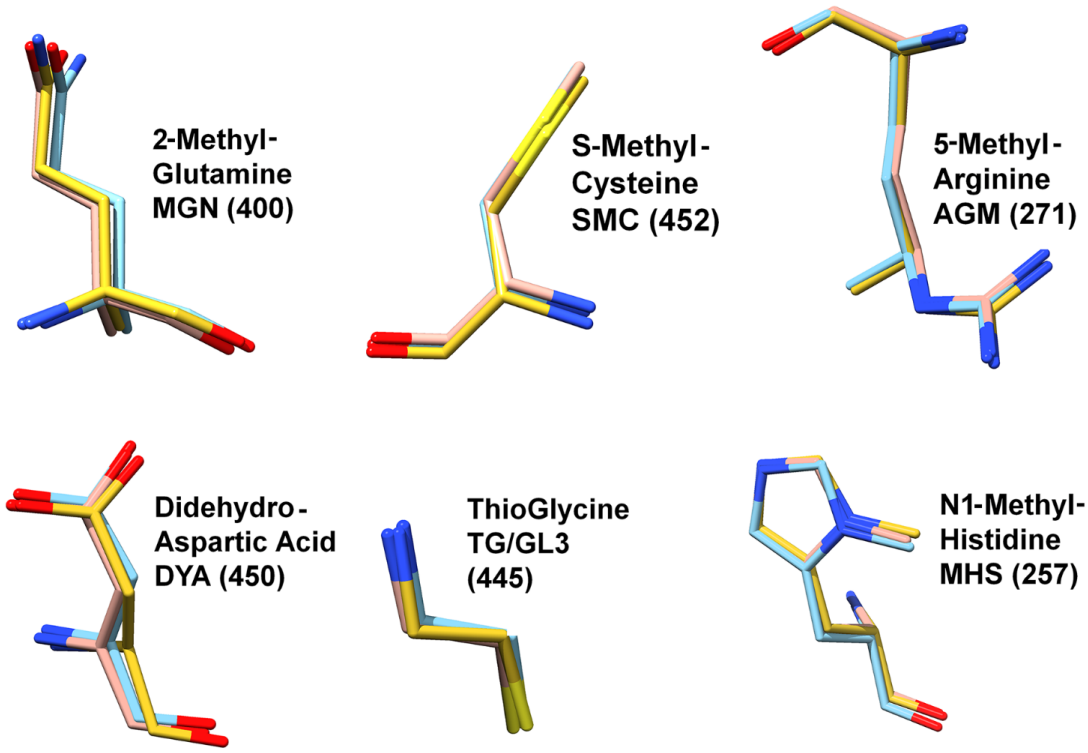

Figure 3.3 Modified amino acids in the active site of MCR. In this room temperature structure, these modified residues, namely 2-Methyl-glutamine (MGN), S-Methyl-cysteine (SMC), 5-Methyl-arginine (AGM), Di-dehydro-aspartic Acid (DYA), Thioglycine (TG) and N1-Methyl-histidine (MHS), in MCRred1-silent (yellow) compared with previously collected cryo MCRred1-silent structures (cyan 3M1V, pink 5AY0) show no major structural variations nor fluctuations in B factors across all three structures (Inset & Table 1). B factors normalized according to equation one in a study published by Johnson et. al. [143]. Figures made with COOT, Chimera and Chimera-X [125,129,130].

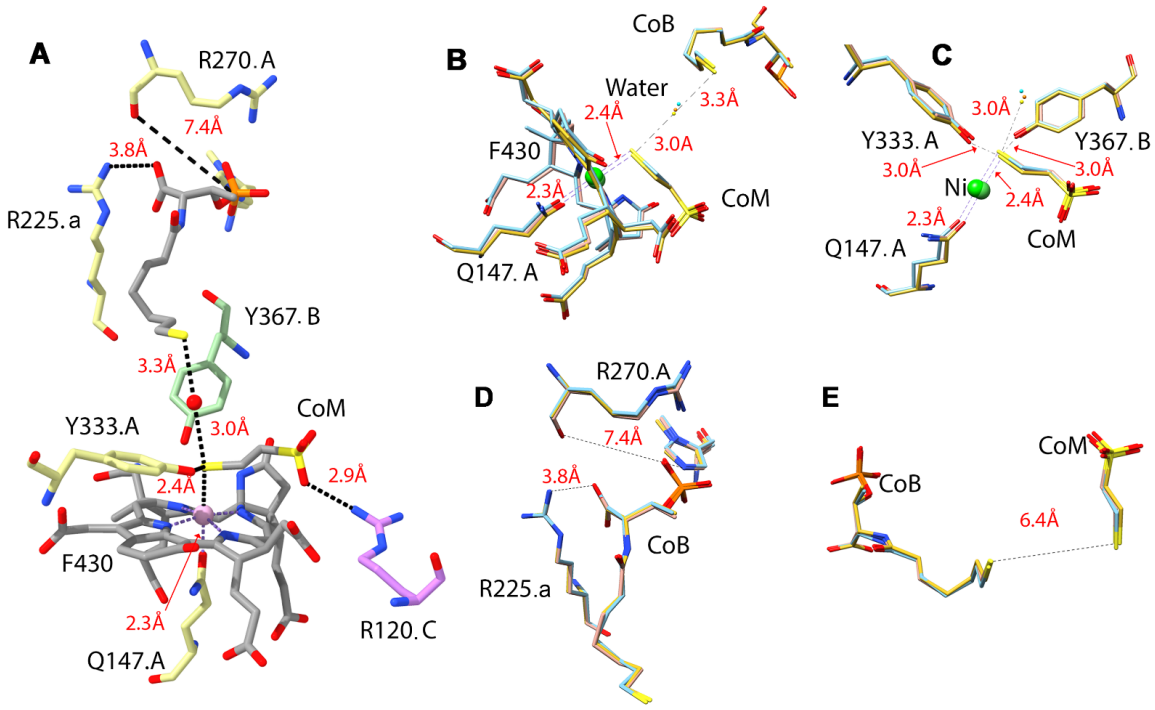

Figure 3.4 Active Site Environment of MCRred1-silent (A) Active site of MCRred1-silent shows conserved water (shown as red sphere) located halfway between CoM and CoB substrates. (B-E): Different views of key active site residues in previously collected cryo MCRred1-silent structures (cyan 3M1V, salmon 5AY0) superimposed on our RT structure (yellow) show that these structures have similar active site organization.

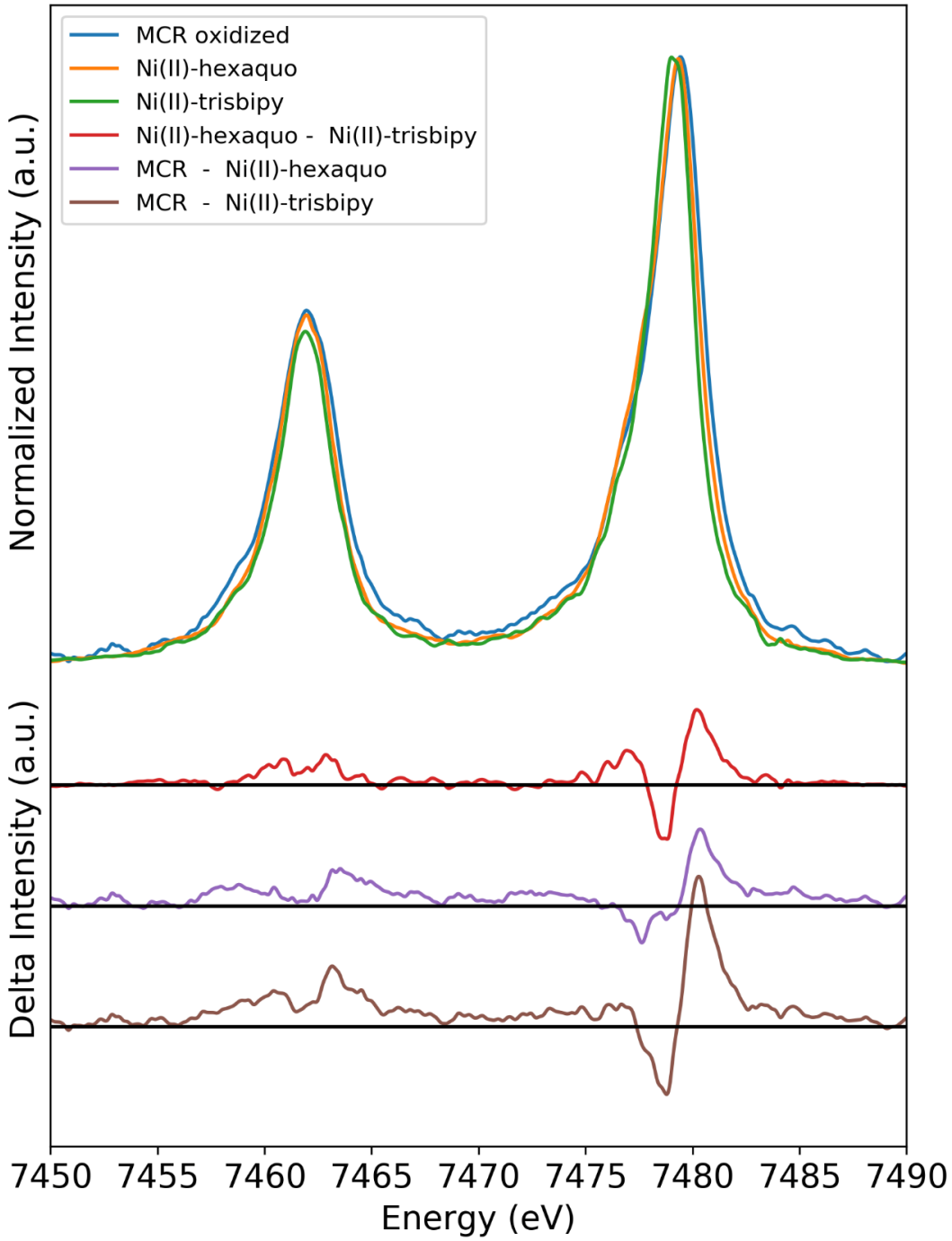

Figure 3.5 XES of MCRred1-silent. Ni Kα XES spectrum of the MCRred1-silent crystals collected simultaneously with the XRD data at the XFEL. Spectra of solutions of two molecular standards, [Ni hexaquo, $Ni(H2O)6]^{2+}$ and [Ni(II)-trisbipy, $Ni(bpy)3]^{2+}$ collected at the XFEL are also shown. Difference spectra between the MCR and the molecular standards are presented.

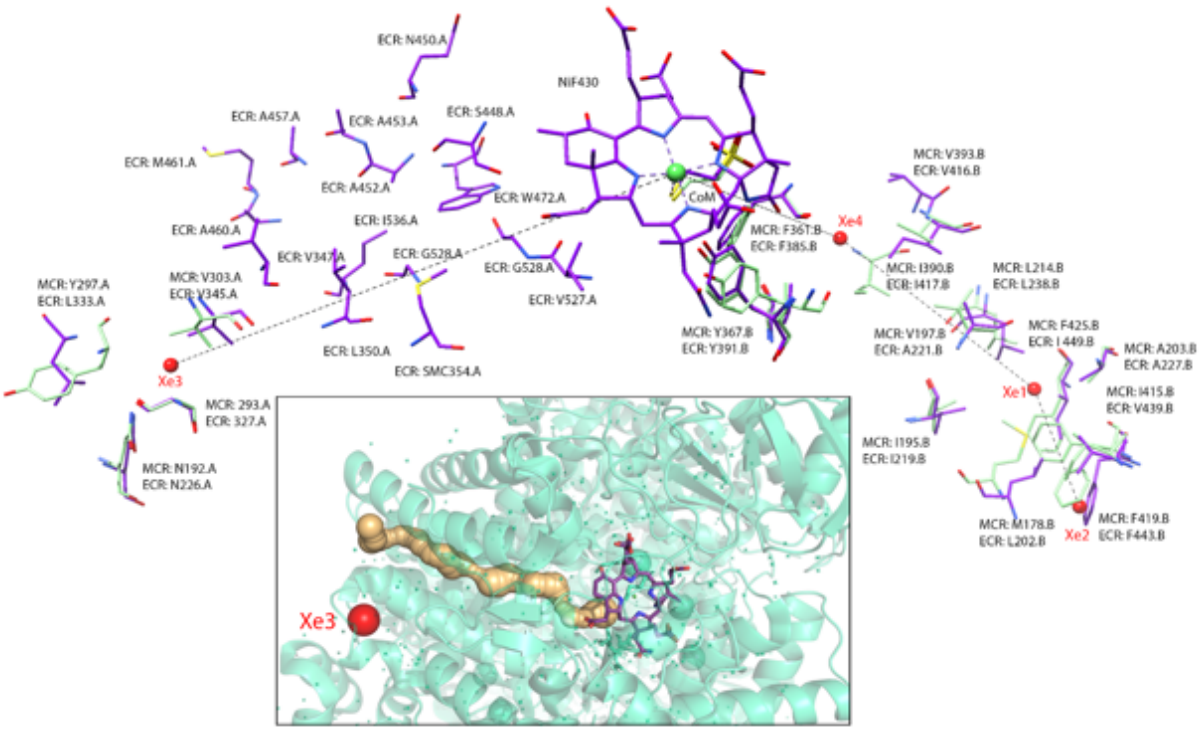

Figure 3.6 Using xenon to map gas channels in MCR and ECR. (A) An overall view of the four Xe locations in MCR. Xe 3 is located close to (~11Å away from) the putative ECR gas tunnel. (Inset) Caver analysis of ECR to visualize the gas tunnel in relation to Xe3 in the MCR pressurized cryo structure (B) Location of Xe1, 2 and 4 and the surrounding residues in the MCR Xe pressurised cryo structure (green) superimposed with the corresponding ECR (PDB ID 7B1S) residues (purple). Inset: Location of MCR Xe 3 and superimposed key surrounding residues in MCR (green) and ECR (purple)

3.11 Attributions

Christopher J. Ohmer[a,j], Medhanjali Dasgupta[b,j], Anjali Patwardhan[a], Isabel Bogacz[b], Corey Kaminsky[b], Margaret D. Doyle[b], Percival Yang-Ting Chen[c,i], Stephen M. Keable[b], Hiroki Makita[b], Philipp S. Simon[b], Ramzi Massad[b], Thomas Fransson[d], Ruchira Chatterjee[b], Asmit Bhowmick[b], Daniel W. Paley[b], Nigel W. Moriarty[b], Aaron S. Brewster[b], Leland B. Gee[e], Roberto Alonso-Mori[e], Frank Moss[e], Franklin D. Fuller [e], Alexander Batyuk[e], Nicholas K.

Sauter[b], Uwe Bergmann[f], Catherine L. Drennan[c,g,h], Vittal K. Yachandra[b], Junko Yano[b], Jan F. Kern[b], Stephen W. Ragsdale[a]

[a] Department of Biological Chemistry, University of Michigan Medical School, 1150 W. Medical Center Dr., 5200 MSRBIII, Ann Arbor, MI 48109-0606, USA.

[b] Molecular Biophysics and Integrated Bioimaging Division, Lawrence Berkeley National Laboratory, Berkeley, CA 94720, USA.

[c] Department of Chemistry, Massachusetts Institute of Technology, 77 Massachusetts Avenue, Cambridge, MA 02139, USA.

[d] Department of Theoretical Chemistry and Biology, KTH Royal Institute of Technology, Stockholm, Sweden.

[e] LCLS, SLAC National Accelerator Laboratory, Menlo Park, CA 94025, USA.

[f] Department of Physics, University of Wisconsin-Madison, Madison, WI 53706, USA

[g] Department of Biology and the Howard Hughes Medical Institute, Massachusetts Institute of Technology, 77 Massachusetts Avenue, Cambridge, MA 02139, USA

[h] Canadian Institute for Advanced Research, Bio-inspired Solar Energy Program, Toronto, ON M5G 1M1, Canada

[i] Current Address: Morphic Therapeutic, 35 Gatehouse Drive, A2, Waltham, MA 02451, USA

[j] These authors contributed equally

Corresponding authors: Stephen W. Ragsdale, sragsdal@umich.edu; Junko Yano, jyano@lbl.gov; Jan F. Kern, jfkern@lbl.gov.

Chapter 4 Development of Methods for the Determination of the Active Ni(I) State Crystal Structure of Methyl-Coenzyme M Reductase

4.1 Introduction

MCR is a very difficult enzyme to study. Due to the complex nature of activation of MCR as well as its irreversible oxidative damage, crystallographic data on active-Ni(I) form of the enzyme is entirely absent. We have developed methods to crystallize and mount crystals of the active Ni(I)-MCRred1 state. However, Ni(I)-MCR crystals that have been cryofrozen inside of an anaerobic chamber and stored under cryogenic conditions reveals a Ni(II)-inactive form once exposed to the X-rays by the X-ray diffractometer [70]. Even propane icicles have been utilized to prevent oxygen exposure to no avail. Until this thesis, the cause of this oxidation event was unknown. We have two hypotheses to explain why we have only obtained structures of the Ni(II) EPR-silent state of MCR . 1) The anaerobicity of the collection environment is not suitable for data collection. While cryo conditions have been primarily used over MCR's history for crystallographic structure determination, this does not sufficiently protect from the oxygenated environment of the beamline, even including a significant cryo stream of inert gas enveloping the sample. With MCR, it is obvious when oxidation occurs because the color of the crystal changes from green to yellow, reflecting the shift in the UV-visible absorption maximum from 390 to 420 nm. It appears that the inert gas stream does not sufficiently protect the crystal for structure determination of the active Ni(I) state of MCR. 2) Another rationale for Ni(I) decay to Ni(II) during data collection might be the metallocentre's sensitivity for radiation. Ermler *et al.* has previously claimed that radiation damage may be the culprit for the inability to observe the

CH_3SCoM which was incubated with MCR crystals. Perhaps the X-rays may lead to S-C bond cleavage generating CoM which is observed with a typical 2.2 Å Ni-thiolate bond. Furthermore, radiation damage may also be the culprit for the oxidation of the metallocentre. X-ray photoreduction is typically seen in many metalloenzymes such as heme containing horse heart metmyoglobin, ribonucleotide reductase, and a lytic polysaccharide monooxygenase [144–146]. While photoreduction from Ni(II) to Ni(I) has not been observed with MCRred1 [70], there is substantial evidence that hydroxyl radicals can form from solvent during X-ray irradiation, and thus can provide the conditions necessary for oxidation of the sensitive metallocenter [147]. Therefore, we must be aware of these two challenges when planning data collection experiments.

Despite the 20 years that crystallography has been used to obtain a sizable amount of MCR and homologous MCR structures, we must take steps to improve the environment in which these crystallography experiments take place. This is very clear in the crystallographic studies of MCR, making the enzyme a great model for all anaerobic redox metalloprotein crystallographic methods. This thesis chapter will not only serve as a possibility of solving the Ni(I)-MCR structures but highlight the methods needed to solve the structures of other oxygen-sensitive enzymes, especially metalloproteins. Illustrated in this thesis are several methods of room temperature anaerobic data collection such as, sealed capillary room temperature crystallography, neutron diffraction, anaerobic graphene devices, and XFEL serial crystallography.

The methods needed to solve these structures must have another simultaneous or tandem method to confirm the oxidation state of the metallocentre. Groups have attempted to use dyes or including oxygen-scavenging enzymes in the solution to protect the enzyme. Others have assumed that they can remove the frozen or room-temperature crystals from an anaerobic

enviroment and retain the redox state. MCR is a very important test of these concepts because it has a single metal ion with very clear diagonistic colorimetric and spectroscopic changes to indicate its redox state, whereas most proteins have only minor changes that can be monitored. Furthermore, metalloenzymes have different echelons of oxygen sensitivity. Therefore, for MCR we have created collaborations with groups seeking to improve on the methods of anaerobic crystallography. As MCR is one of the most oxygen sensitive enzymes on the planet with a complete void of any active structure of the enzyme, MCR may serve as a model for all radiation and oxygen sensitive enzymes.

4.2 Materials and Methods

4.2.1 Purification and crystallization of MCRred1:

MCRred1 from *M. marburgensis* (catalog OCM82) was purified and handled in an anaerobic chamber (Vacuum Atmospheres, Inc. or MBRAUN) containing <1ppm of O_2, as previously described [81,111]. The concentration of MCRred1 and MCRred1-silent used for crystallization was quantified using UV-Vis spectrophotometry with extinction coefficients of 22.0 and 12.7 $mM^{-1}cm^{-1}$ at 420 and 385 nm, respectively, using a multi-wavelength calculation as previously described [115]. The enzyme Ni(I) percentage for this chapter were found to be around 60-70%, however recent developments have achieved 80% consistently. All hanging drop vapor diffusion crystallization of MCRred1-silent was carried out at a concentration of 150 μM in 50 mM Tris, pH 7.6. The crystallization buffer used is composed of 18% PEG 400, 150 mM magnesium acetate hexahydrate, and 100 mM HEPES Sodium, pH 7.5. Hanging drop vapor diffusion was used with 1:1 ratios of protein solution and crystallization buffer with seed, respectively, to produce crystallization solutions ranging from 2-10 μL with a well solution containing 0.5mL crystallization buffer. Microcrystals were made using a batch method in which

a concentrated solution of MCRred1 at 1.5mM was added to the previously described crystal buffer in a 1:9 ratio of concentrated protein to crystal buffer with an anaerobic MCRred1 seed stock, respectively. This would result in a crystal slurry of 20-80 μm sized crystals in a total volume of 100-500 μL where the crystals would make up around 10% of the slurry.

Preliminary counter diffusion crystallography was carried out with 300 μM MCRred1-silent taken via into a capillary via capillary action. In a falcon tube, 8 mls of crystal buffer is pipetted along with a 1 ml of 0.4% agarose to float on the top. Once the agarose solidified, protein capillaries were sealed with bees wax and inserted into the agarose layer and stored in 4° C. Crystals form in the capillaries 1-2 days.

4.2.2 Sample Delivery, X-Ray Diffraction (XRD), X-ray Emission Spectroscopy (XES), and UV-Vis data collection at SLAC:

XFEL diffraction data were collected at the Macromolecular Femtosecond Crystallography (MFX) instrument of LCLS, (SLAC National Accelerator Lab, Menlo Park, CA) [116] at 300 K on a RAYONIX MX340-HS CCD detector, using the previously established Drop-On-Tape (DOT) [117] approach. The X-ray beam photon energy was 9.9 keV with a pulse energy of 2-2.2 mJ, a pulse length of 35 fs and a beam size on the sample of 4 μm x 4 μm (Full Width Half Max, FWHM). Data collection statistics are available in Appendix B. X-ray emission data were collected in tandem with diffraction data using a multicrystal wavelength-dispersive hard X-ray spectrometer based on the von Hamos geometry [118]. Due to the change of polarization direction of the hard X-ray undulator of LCLS, our previously used setup [117,118] was modified to place the analyzer crystals above the X-ray interaction point and the position sensitive detector at 90 degrees from the beam direction in the horizontal plane. An array of three Si(620) analyzer crystals was placed 250 mm above the interaction point with the center of the crystals at 74.80

degrees respect to the interaction point, collecting both Ni Kα lines on an ePix 100 detector with its center located 136 mm side wise of the X-ray interaction point. To calibrate the spectrometer geometry, spectra from $[Ni(H_2O)_6]^{2+}$ were collected and compared to a synchrotron reference. The XES data was also pedestal corrected to account for differences in noise of the detector pixels.

XRD data collection at Beamline 9-2 at SSRL was paired with a UV-Vis microspectrophotometer. A 5-axis pico-motor stage aligned the microspectrophotometer objective with a Hamamatsu light source with deuterium and halogen lamps, UV solarization-resistant optical fibers, Newport Schwardchild objective, and an Ocean Optics QE65000 Spectrum Analyzer.

4.2.3 XRD Data Reduction, Processing, and Refinement:

The collected XRD dataset was reduced and processed using *cctbx.xfel* and DIALS [119,120]. We performed joint refinement of the crystal models against the detector position for each batch to account for small time-dependent variations in detector position [120]. We also corrected for the Kapton tape shadow as described [117]. Data were scaled and merged to 1.85, 1.75, and 2.14 Å for MCRred1 Unit Cell 1, MCRred1 Unit Cell 2, and MCRred1-silent based on previously established resolution cutoff criteria (~10x multiplicity, where the values of I/σ(I) do not uniformly decrease any more [117], and where $cc_{1/2}$ values stop decreasing monotonically [121], indicating no useful information is contained in resolution shells beyond that point), using *cctbx.xfel.merge* with errors determined by the ev11 method [122]. Structure determination was done using Phenix [123] starting with molecular replacement using the reference model PDB ID: 7SUC[148] [124]. For all subsequent refinements with Phenix, we turned off automatic linking within the chain, as well as NCS restraints, and instead defined the interactions between the Ni-

OE1(Q147) and Ni-S1(CoM) We used Coot [125] for model building with multiple iterations of refinement using phenix.refine [123,126,127] with the aforementioned settings. Occupancies were found by manual b factor changes based on the average b factor of the same heteroatom with a 5 Å range. Occupancy refinement is then performed, and waters are modelled to resolve Fo-Fc density. This is repeated until b factors of the molecule and waters match the surrounding residues with Fo-Fc densities resolved.

4.2.4 Synthesis of CD_3SCoM

CD_3SCoM was prepared with 1.26 mmol of HSCoM with 1.26mmol of CD_3I in 5 ml of concentrated anaerobic NH_4OH. The reaction proceeded overnight at 4° C and evaporated. CD_3SCoM was precipitated using aqueous acetone and filtered through a Büchner funnel.

4.3 Results

4.3.1 Neutron Diffraction Method Development and Controlling Crystal Sizes

What separates neutron crystallography from X-ray crystallography is the bombardment of neutrons as opposed to diffraction of X-rays upon collisions with electrons. Because of this technique, H atoms that are not very prevalent in non-sub-atomic resolution X-ray crystallography because scattering intensity associated with X-ray diffraction is proportional to the number of electrons the atom possesses. In neutron crystallography the coherent scattering lengths of H and D atoms are comparable to protein backbone atoms in magnitude. Therefore, H-atom placement and water orientations can be examined at resolutions of 2.5Å and lower [149]. While this could be beneficial for finding the methyl group of CH_3SCoM, X-ray crystallography should be able to detect the methyl group. However, what makes Neutron Diffraction an ideal method for this and other systems where photoinduced damage is prevalent is that neutron

diffraction does not cause observable radiation damage to the crystal [150]. Furthermore, neutron crystallography uses a room temperature capillary to house the crystal, making anaerobicity of the sample a possibility if the crystal is mounted/harvested inside of an anaerobic chamber. Therefore, we are collaborating with Dr. Flora Meilleur at Oak Ridge National Laboratory to prepare their beamline for anaerobic crystallography as well as prep MCR crystals suitable for neutron diffraction.

There are two requirements for growing suitable crystals for neutron diffraction: 1) crystals must be grown larger than 0.1mm^3 and 2) protons must be exchanged with deuterium. Large crystals need to be grown due to the low flux from neutron sources compared to the high brilliance of X-ray sources. Additionally, H atoms provide a negative coherent scattering and high incoherent scattering. To have a protein with fully populated protons with no exchange, the background noise during data collection would be insurmountable [149]. Therefore, we must grow very large deuterium exchanged crystals for suitable neutron diffraction studies.

Growing large crystals takes a lot of time and finding the right conditions can be a very tedious process. Crystallization of MCR was started aerobically to optimize crystal growth using a buffer recipe developed by Dr. Mishtu Dey [70]. The crystal buffer is comprised of 18-24% polyethylene glycol 400 (PEG 400), 150 mM magnesium acetate tetrahydrate ($MgSO_4$) and 100 mM HEPES sodium (HEPESNa). A 1:1 mixture of 150 μM MCR and crystal buffer, was used in sitting and hanging drop vapor diffusion. What first appeared was an amalgamation of crystals where no possible single diffraction could be seen as shown in Figure 4.1.

Figure 4.1 Crystal Aggregation of MCR. Optimization of crystal formation starting progress.

While the crystals could not be used for any sort of diffraction, one could use it as a seed stock. Therefore, a crystal of this fashion was vortexed with a polytetrafluoroethylene bead to break the crystal into microscopic seeds in crystal buffer. Seeds were diluted and used in place for the crystal buffer with the same protein to crystal buffer ratio. What appeared was single crystals with sharp edges where size of the crystal seemed to be governed by nucleation sites, unsurprisingly. The less numerous the nucleation sites, the larger the crystals and vice-versa, therefore the protein would grow crystals based on non-crystallized protein concentration in a very controlled approach as seen in Figure 4.2.

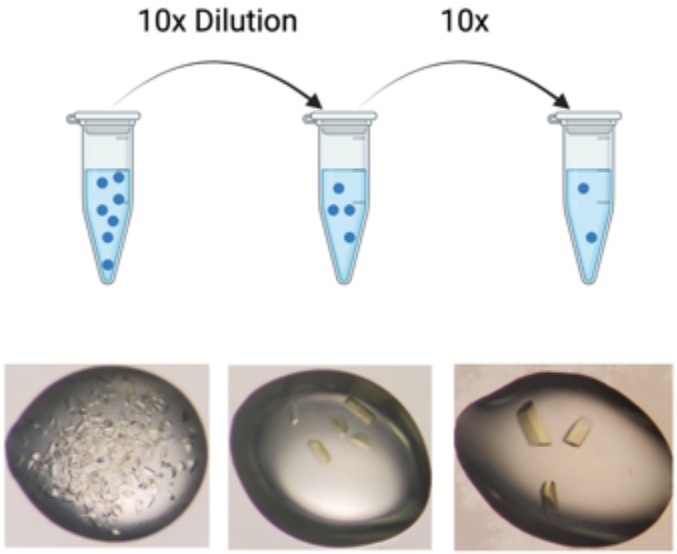

Figure 4.2 Seed Stock Dilution Controls Crystal Size. Crystals of MCR vary in size by the amount of nucleation sites in the crystal buffer. Created with BioRender.com

With this method, we scaled up the crystal conditions necessary to product large crystals with sitting drop method with a 9 well glass plate in sandwich trays (schematic in Figure 4.3). This set-up acts as a traditional sitting drop tray where one well is scaled up from 0.5 ml to 14 ml and the drop size can be increased from 10 µL to 800 µL. The sandwich tray acts as a well where the crystal buffer for vapor diffusion is placed and large drop sizes of the protein and crystal buffer may be used to increase the amount of protein and therefore make larger crystals.

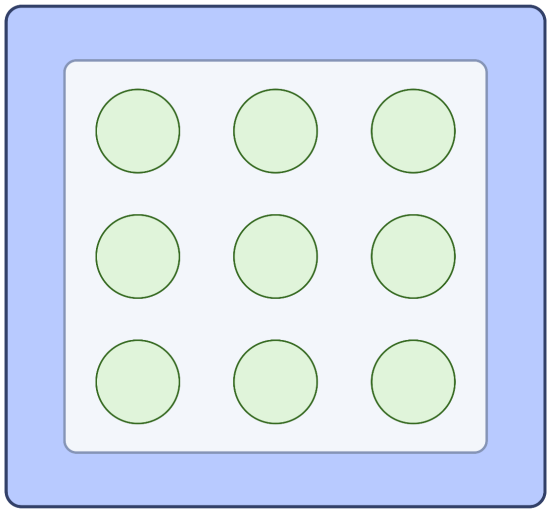

Figure 4.3 9-Well Sandwich Tray Setup. Crystal buffer is placed into the sandwich tray in blue of around 14 ml. Crystal drops are placed up to 800 µL and allowed to crystallize up to one month. Created with Biorender.com.

What resulted from this study is that MCR crystals would form after an estimated 2 weeks but could grow for up to one month where large crystals would be found in low seed stock concentration crystal conditions. After a month of growth, crystals suitable for neutron diffraction could be found with dimensions of 0.5 mm x 0.5 mm x 1 mm and 0.25 mm^3 volume (Figure 4.4) . Succeeding this development of large crystal growth, we must now exchange protons with deuterium.

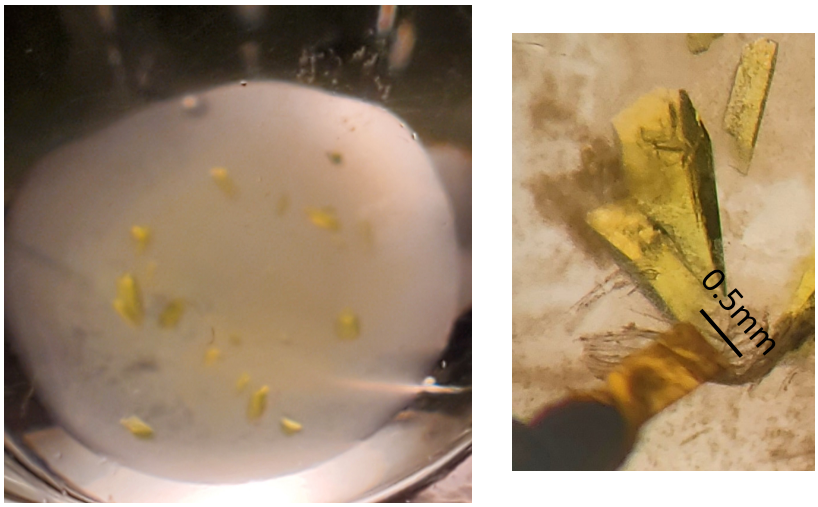

Figure 4.4 Large Crystal Growth Result. (Left) Illustration of a 200 µL crystal well as seen by eye. (Right) Individual crystal dimension measurements under microscope show large crystals of growth suitable for neutron diffraction.To minimize incoherent and negative coherent scattering, deuterium exchange of crystals can be accomplished in many ways. Crystals can be grown in deuterated crystal buffers, a mother liquor of deuterated buffer can be supplied for vapor diffusion of D_2O within the capillary used for data collection, or the crystals can be soaked in deuterated crystal buffer. Some groups go to extremes of expressing the enzyme in media containing D_2O for full incorporation of deuterium [149]. For MCR, because the crystallization method provides large crystals without extraneous methods, it was decided to exchange MCR in deuterated protein buffer (50 mM Tris) and deuterated crystal buffers.

Growing crystals in deuterium has some challenges, e.g., the slightly higher viscosity of D_2O relative to H_2O, making crystallization re-optimization an absolute necessity. Upon using the same vapor diffusion strategy employed for growth of the large crystals but in deuterium, immediate widespread precipitation had occurred immediately after the solution was made. This optimization led to a decrease in $MgSO_4$ and protein concentration to 125 mM and 125 µM, respectively, to prevent precipitation. Unfortunately, after reaching volumes around 0.05 mm^3, the crystals would crack and have difficulties in neutron diffraction experiments, reaching only

3.0 Å resolution diffraction spots. Therefore, more optimization was needed to prevent cracking and increase the resolution. What was found to help prevent cracking was a drop ratio of 1:3 for protein:crystal buffer (Figure 4.5).

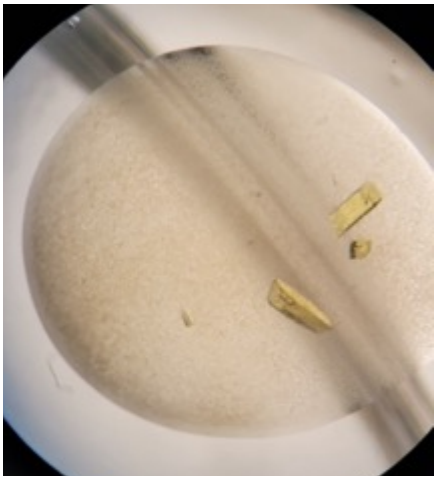

Figure 4.5 Crystal Growth of MCRred1-silent in Deuterium Oxide. Crystals were grown using a 1:3 ratio of protein to crystal buffer with a crystal buffer composition of 18% PEG 400, 125 mM $MgSO_4$, 100 mM HEPESNa

Having deuterated crystals is an important step in getting neutron diffraction to work for our anaerobic crystallography of MCR, but the hydrogens for our substrate CH_3SCoM must also be exchanged. If the protons of CH_3SCoM are still present, we may introduce noise into the most crucial position for study of the MCRred1m state. CD_3SCoM was synthesized using HSCoM and iodomethane-d_3 and ammonium hydroxide (Figure 4.6). CD_3SCoM was then soaked with the deuterium crystal and harvested inside of a capillary with mother liquor and sealed with beeswax. Unfortunately, this did not result with a structure as the ligand soaking seemed to completely dissolve the crystal shown in Figure 4.7.

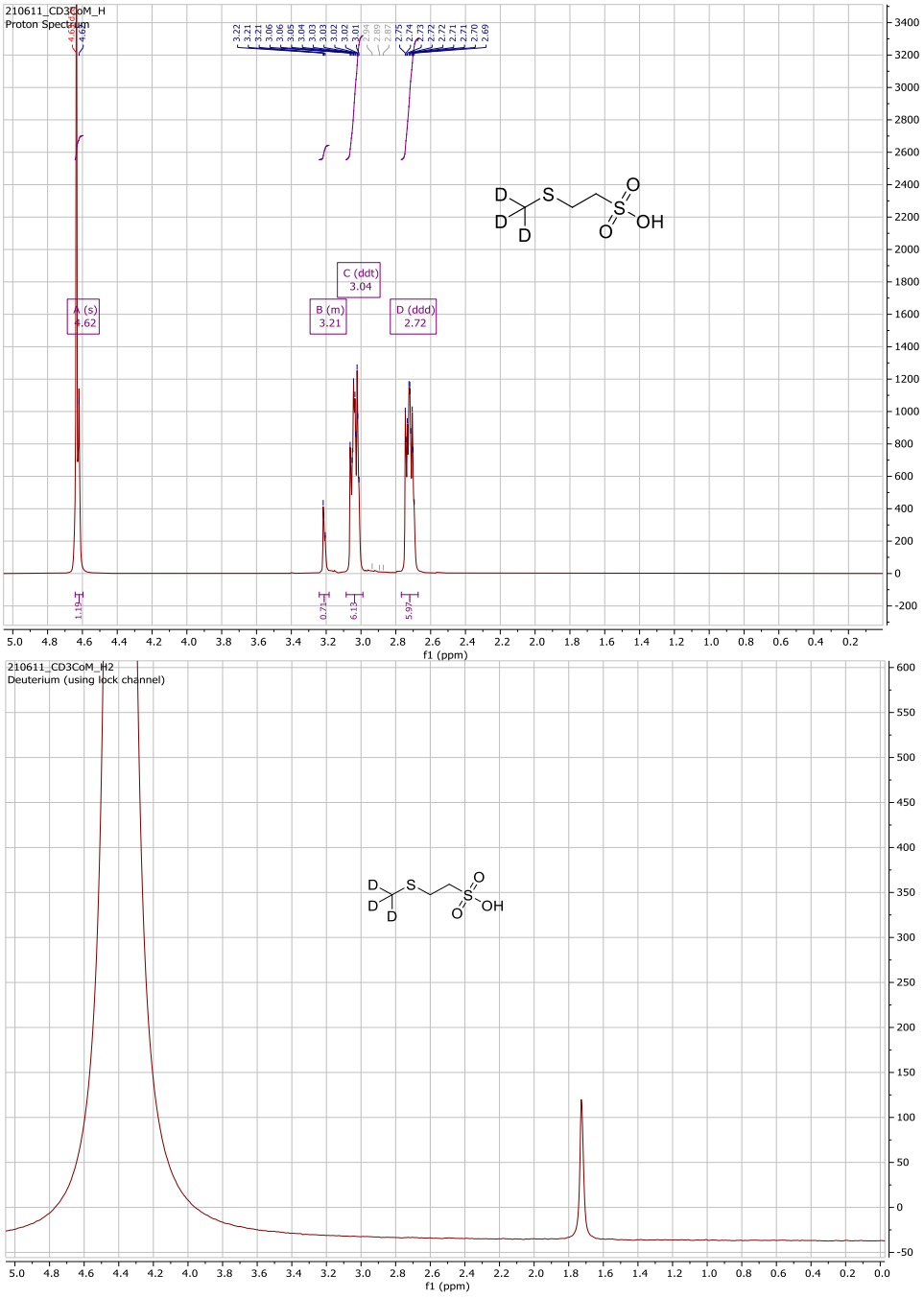

Figure 4.6 NMR Spectroscopy of CD_3SCoM. (Top) HNMR spectroscopy of CD_3SCoM. (Bottom) ^{2}HNMR spectroscopy of CD_3SCoM

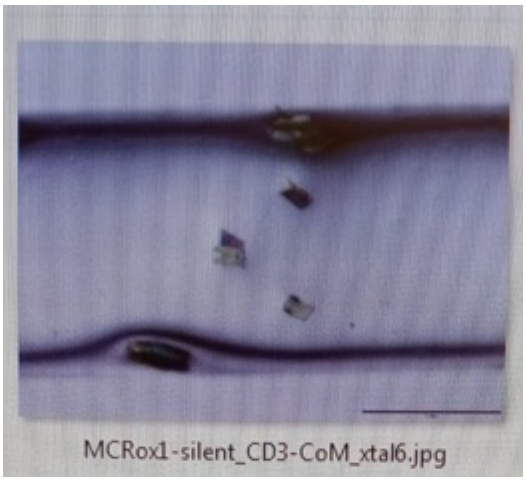

Figure 4.7 Ligand Soaking Result. Dissolved MCRox1-silent crystals upon ligand soaking

Unfortunately, the beam for neutron diffraction has been entirely closed until the summer of next year and therefore, we will pick up this portion of the project when the beam at Oak Ridge is functional.

4.3.2 Graphene Device Testing

Making an environment suitable for anaerobic crystallography is a strenuous task because no beamline in the world is housed inside of an anerobic box, to my knowledge. This makes only crystallographers who have experience in anaerobic enzymology suitable to attempt these experiments due to the sensitive nature of metalloenzymes. For these studies, we collaborated with Dr. Sarah Perry at the University of Massachusetts Amherst and Dr. Aina Cohen at SSRL to develop a microfluidic crystallography device that could house a crystal inside of gas impermeable graphene. With the development of 3D printing, these devices could be used commercially to make anaerobic crystallography much easier to accomplish. Furthermore, these graphene devices could easily be made for either serial crystallography for X-ray sensitive enzymes or for growing crystals where the device acts as a well to house the crystal making a no-handling procedure for fragile crystals.

The microfluidic device has a base layer of polyester with a poly(methylmethacrylate), PMMA, layer that houses the graphene "well". On this graphene layer can be set a drop or a slurry of crystals or act as a crystal well for microbatch techniques. Once the crystals or crystal solutions are placed on the graphene layer, another polyester layer with PMMA and graphene can sandwich the crystals or crystal drop and sealed with epoxy and vacuum grease. The device is then attached to a mount suitable for the goniometer and attached with epoxy and a tightening screw as shown in Figure 4.8.

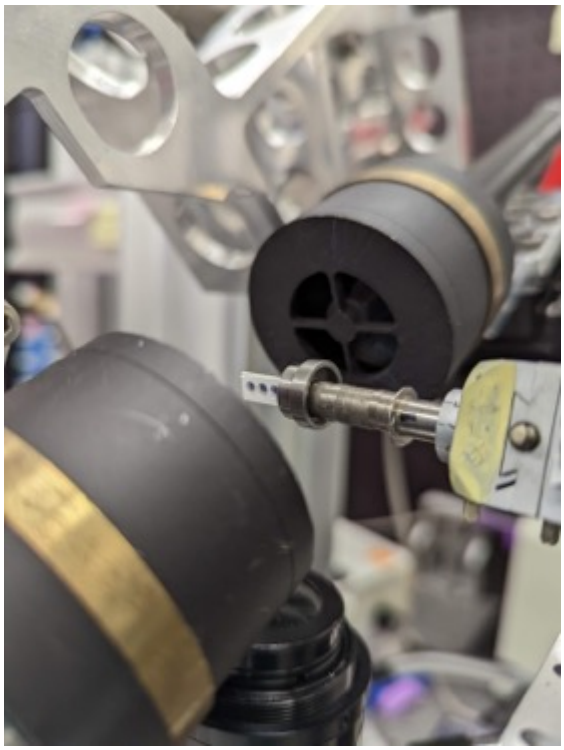

Figure 4.8 Microfluidic Graphene Device. The graphene device placed on an auxiliary goniometer magnet and visualized in a microUV-Vis spectrophotometer.

At beamline 9-2 at Stanford Synchotron Radiation Light Source (SSRL), we prepared methyl viologen as an oxygen indicator, in which the solution will undergo a violet color change when reduced but will turn colorless upon oxygen exposure. Into the graphene wells was placed a 50 μL amount of methyl viologen and sealed inside of an anaerobic chamber (MBraun). The device was then brought out and visually inspected to test the anaerobicity of the device.

Unfortunately, we can see the methyl viologen turn more colorless between 9 and 20 minutes (Figure 4.9). The redox potential of methyl viologen is -0.446V [151]. Therefore, MCRred1 with a Ni(I)/Ni(II) couple at -0.650V would likely not survive for very long in a device at the current state. Whether the oxygen is seeping into the epoxied sides or the graphene barrier is unknown, therefore optimization of this graphene design will be accomplished in the next iteration of these experiments where we will house MCRred-1 in this device paired with a microUV-Vis spectrophotomer.

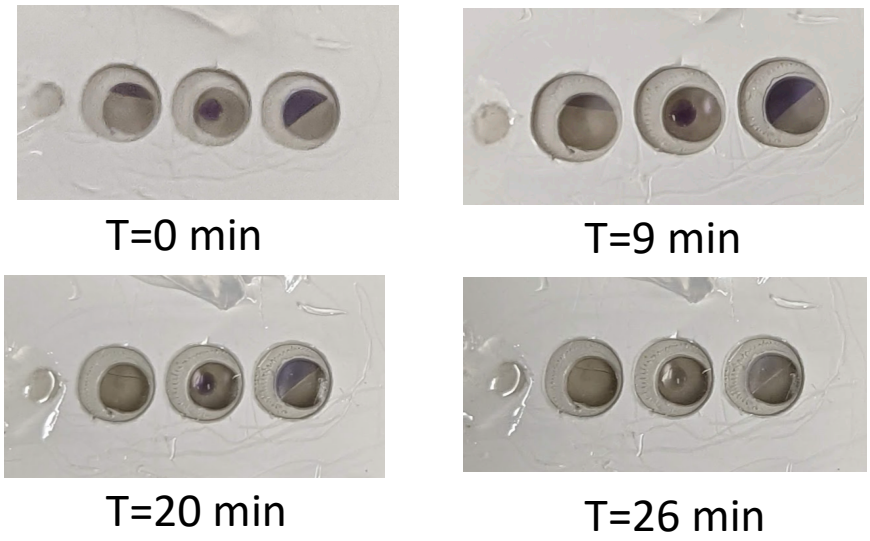

Figure 4.9 Test of Anaerobicity for Graphene Devices Using Methyl Viologen. Utilizing the oxygen indicator methyl viologen we can see how long the graphene device can withstand oxygen. Violet color of methyl viologen is in its reduced state, while colorless methyl viologen has been oxygenated.

4.3.3 Anaerobic Capillary XRD Paired with UV-Vis Capabilities

Even after we have successfully developed the methodology to produce and stabilize the active form of MCR, it is crucial to verify the oxidation state of the enzyme. UV-Vis crystal capabilities have been done previously but only after the data collection took place revealing the Ni(II) MCR state [70]. It is essential to have the UV-Vis capabilities to analyze the oxidation state

of the Ni(I) corphin during XRD data collection. Only then can we diagnose if Ni(II) generation results from radiation damage from the beam line source or oxygen exposure and to validate that the structure is indeed of the active ni(I) state. . To validate the oxidation state of MCR during XRD measurements, we formed a collaboration with Dr. Aina Cohen and Dr. Darya Marchany-Rivera at beam line 9-2 at SSRL. Beamline 9-2 was developed by Dr. Aina Cohen with a built in microspectrophotometer than can collect UV-Vis data in tandem with XRD. The development of this beamline is exceptional for studying crystallography of MCR4.

Custom anaerobic capillaries were made by cutting long 1.5 mm diameter capillaries and sealing them to a pin using epoxy with a coat of vacuum grease. We then added a solution of 10 mM of oxygen scavenger Ti(III)Cit to the base of the capillary to remove any oxygen that may be introduced into the capillary environment. We first set up a methyl viologen dye in the capillary to understand if the experiment would even be feasible. Additionally, a control capillary was snapped outside of the chamber to expose the solution to air. After 10 minutes the capillary control open to oxygen had turned colorless. After 30 minutes, as shown in Figure 4.10, the methyl viologen had not changed within the sealed capillary with Ti(III)Cit. Furthermore, the solution was left overnight and still did not change color until 3 days had passed. We believe that 3 days of showing no observable oxygenated methyl viologen illustrates the feasibility of this method to gather data on MCR without worry about the anaerobicity of the crystal.

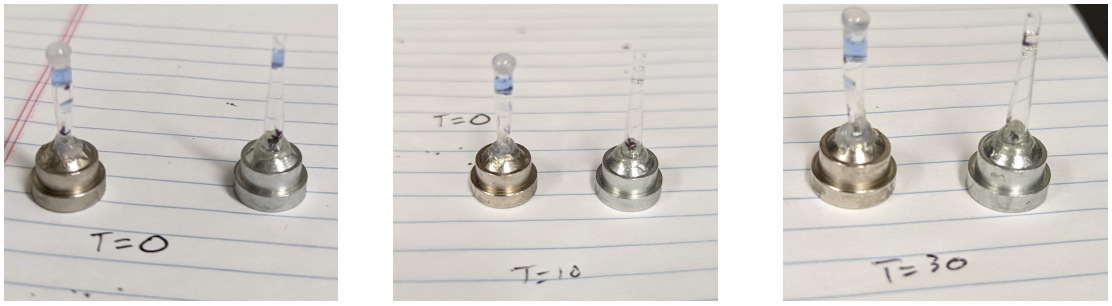

Figure 4.10 Feasibility of Custom Capillary Mounts. A time trial of sealed capillary containing methyl viologen oxygen indicator with a snapped capillary exposed to oxygen as a control. Once the capillaries were brought out of the anaerobic chamber, we snapped our control at T=0 min. After 10 min our control turned colorless, but the methyl viologen solution stayed violet in the sealed capillary over 3 days.

MCRred1 crystals were grown inside of an anaerobic chamber using the microbatch method where a ratio of 1.5 mM protein:crystal buffer in a 1:9 ratio is placed inside of an Eppendorf tube and allowed to crystallize. This sample was co-crystallized with 2 mM Ti(III)Cit to keep the redox potential of the drop around -403.9 mV [152]. The crystal slurry was placed inside of a capillary, epoxied to the mount, and exported out of the chamber in an anaerobic

vessel to the beamline. Upon adding the crystal containing capillary, we measured the UV-Vis spectrum of a single crystal (Figure 4.11), revealing the distinct 385 absorption band of Ni(I) - MCRred1. In this crystal, the Ni(I) content the crystal was around 45%.

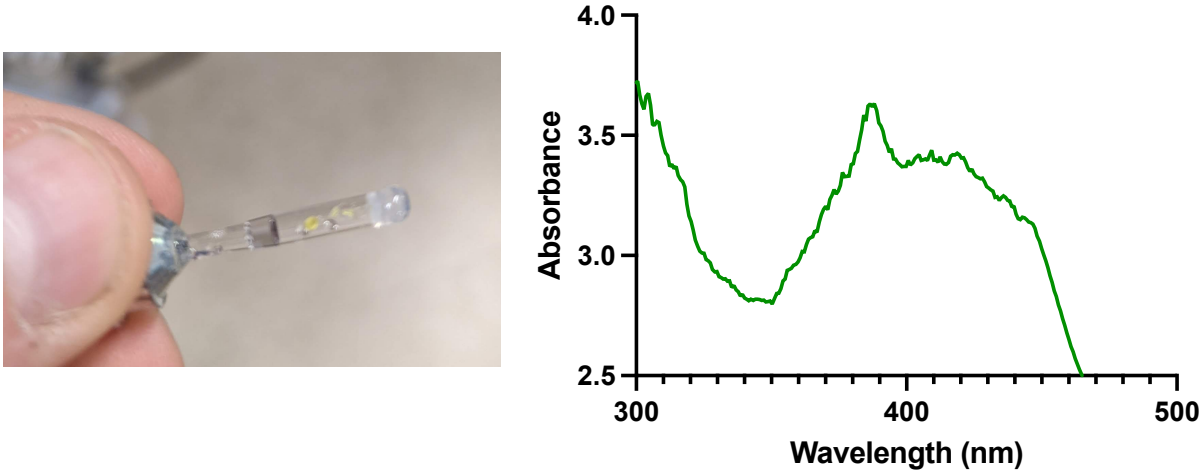

Figure 4.11 Single Crystal UV-Vis Characterization of MCRred-1. (Left) MCR crystal housed in an anaerobic epoxied capillary with 2 mM Ti(III)Cit. (Right) UV-Vis spectrum of single crystal MCRred-1 exhibiting the characteristic MCRred-1 Ni(I) at 385 nm peak

A radiation dose scan was then measured to understand the X-ray beam's influence on the sensitive metalloprotein. By centering the microspectrophotomer around the optimal phi angle to obtain an identifiable UV-Vis spectrum, we can have a constant point to produce a UV-Vis spectrum of a single crystal with minimal deviations. As shown in Figure 4.12, as MCR meets the beam during a specified number of frames we see a decrease in the Ni(I) signature of 385 nm. This crystal saw damage at 100 frames, but after 200 frames the Ni(I) signal has decreased significantly demonstrating that the beam causes photooxidized of MCRred1's Ni(I) center to Ni(II). Therefore, serial crystallography paired with UV-Vis microspectroscopy is required to ensure that we are cognizant of the percentage Ni(I) is present during the XRD data collection. Unfortunately, the beam at 9-2 was shut down for an indiscernible amount of time starting in January. Therefore, other methods were explored in this time.

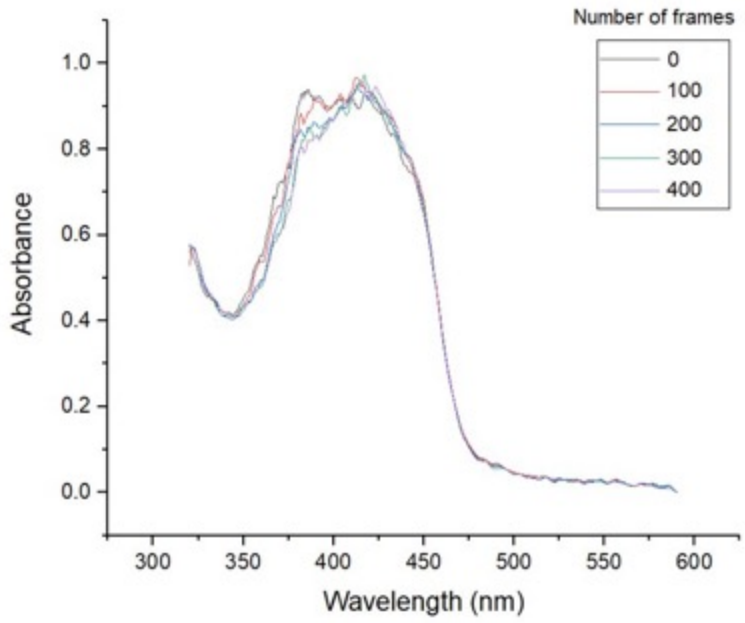

Figure 4.12 Radiation Damage of MCRred1 Conversion to MCRred1-silent. UV-Vis spectra of a single crystal during beam collection showing Ni(I) oxidation within 200 frames.

To explore the best experimental set up for serial crystallography paired with single crystal UV-Vis, the method of counter diffusion was considered. Counter diffusion experiments take place inside of a capillary. Thus, crystals can be grown in the capillary that is used for XRD collection minimizing the harvesting of precious crystals. Furthermore, crystals in 0.1 – 0.3mm diameter capillaries can be frozen on the cryo-stream with no discernable defects [153]. Therefore, if it is possible to freeze crystals without oxidation of the Ni(I) corphin, the radiation damage can hopefully be minimized by preventing movement of radiation induced radicals within the active site.

Counter diffusion utilizes capillary action to introduce crystal buffer to protein slowly via diffusion through an agarose plug against gravity. This slow movement aids in slowing down crystal growth, making a wide range of protein to crystal buffer ratios, different sized crystals throughout the capillary, and providing the vessel for XRD experiments for a transfer free crystal

harvest. Optimization of counter diffusion led to promising crystals, but one large drawback impeded single crystal growth. The protein that is placed inside of the capillary must contain crystal seed. Unfortunately, crystals that are placed in the 50 mM Tris pH 7.6 protein buffer completely dissolve. Therefore, counter diffusion was attempted using the batch prep used in Chapter 3 to grow the crystals as shown in Figure 4.13. Furthermore, the 0.1 mm to 0.3 mm OD capillaries must be less than 20 mm long to fit in the beam path, therefore a minimized counter diffusion assembly was accomplished shown in Figure 4.14. We have tested capillary freezing at the Center for Structural Biology (CSB) in the Life Sciences Institute (LSI), but a clear capillary suitable for XRD and UV-Vis was not attainable. This could be due to the CSB's cryostream being set at a 45° angle from the capillary causing temperature differentials that result frost build up.

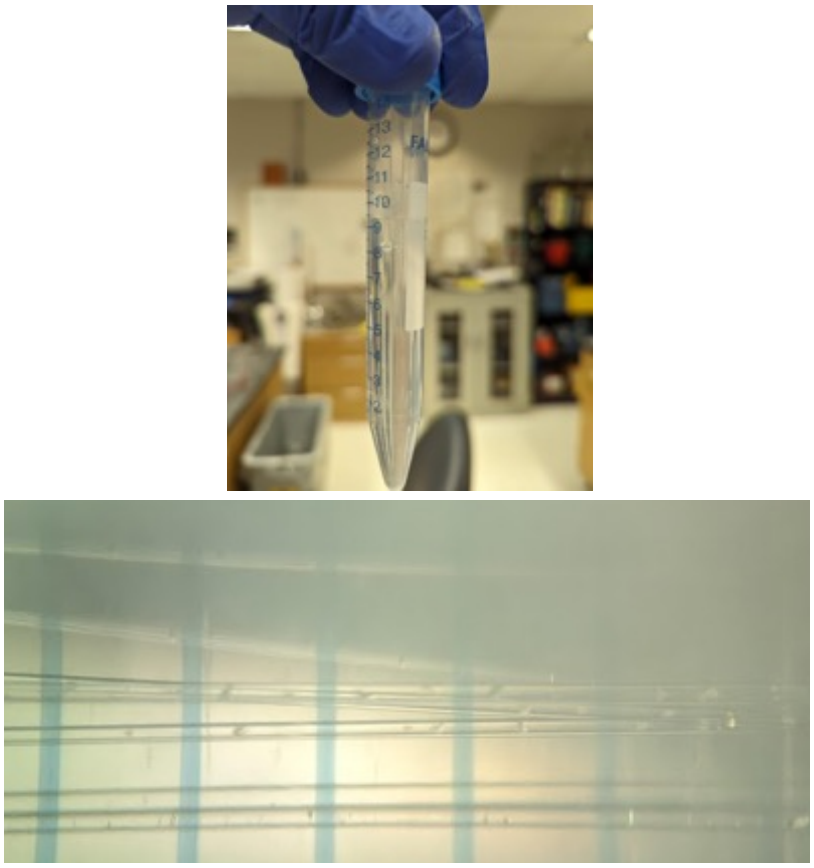

Figure 4.13 Counter Diffusion Assembly and Crystal Growth. (Top) Counter diffusion assembly comprised of crystal buffer in the bottom with an agarose plug (in between 8 ml and 9 ml markings with long capillaries fulled with 150 µM MCRred1-silent. (Bottom) Result of this experiment with several individual crystals along the length of the capillary

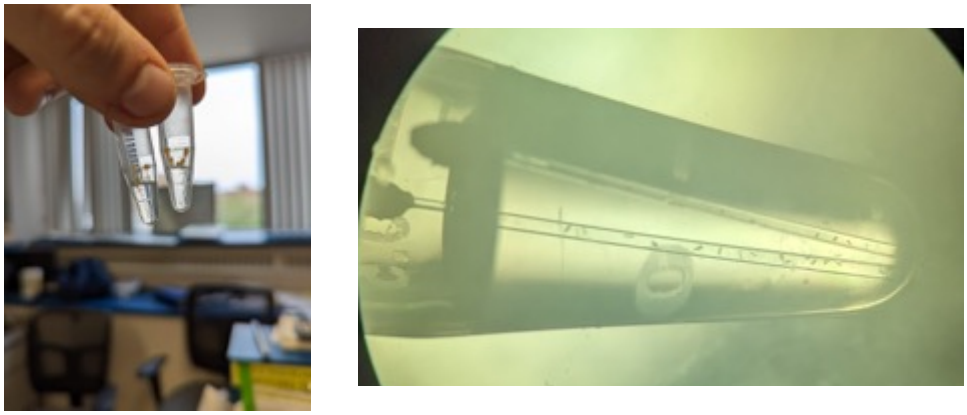

Figure 4.14 Minimized Counter Diffusion Assembly. Set up as shown in Figure 4.13 with 20 mm and 0.3 mm OD capillaries.

4.3.4 XFEL Serial Crystallography of Ni(I)-MCRred1

Radiation damage from X-ray sources is now a major hurdle to overcome, but serial x-ray femtosecond crystallography can bypass this problem. To put briefly (see Chapter 3 for more information,) serial femtosecond crystallography is a technique that relies on the "diffraction before destruction" technique where individual crystals undergo a high-brilliant x-ray pulses that destroy the crystal upon impact but diffract to a detector before radiation damage occurs. To collect a full data set, hundreds of thousands of crystals are needed where each provides an image of diffraction. These images can be merged into one data set from which the structure of the enzyme can be solved. Therefore, theoretically, this method is radiation free. Furthermore, in collaboration with Dr. Jan Kern, Dr. Junko Yano, and Dr. Vittal Yachandra at U.C. Berkeley, this all can be done inside of an anaerobic chamber filled with helium (N_2 causes diffraction of the X-rays). Next, spectroscopic data can be simultaneously collected by XES and UV-vis microspectrometry can be measured in tandem to determine the oxidation state of the enzyme right before the X-ray pulse hits the crystal. All methods presented in Chapter 3 are preliminary methods to achieve our goal for collecting a Ni(I) MCRred1 data set. Here, I will discuss how crystallization for this method was achieved as well as present what may be the first Ni(I) structure of MCRred1.

Previously, generation of many vapor diffusion trays were initiated to make the hundreds and thousands of crystals, but that method is incredibly labor intensive. Therefore, a method was optimized for creating microcrystals within a stationary Eppendorf tube. It was discussed in section 4.3.1 how the crystal seed stock was able to grow large crystals by limiting the amount of nucleation sites with diluted seed. The converse is also true. When the seed stock is highly populated, growth of small microcrystals of about 20 um – 80 um can be grown in a controlled

fashion. It was found that the protein buffer 50 mM Tris dissolved MCR crystals and was limited to only keeping the enzyme stable. MCRred1-silent at 150 μM enzyme was used in a 1:9 drop of protein: crystal buffer containing seed. The increase of the enzyme concentration allowed numerous crystals to form in the span of 12 hours, Figure 4.15.

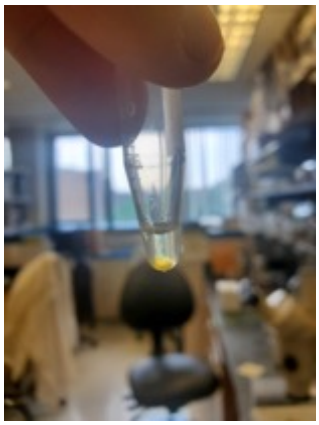

Figure 4.15 MCRred1-silent Micro Crystal Formation with Batch Method. The yellow MCRred1-silent crystals are shown in the bottom of the Eppendorf tube after a 12-hour growth at 4°C.

Using this method with MCRred1 was incredibly easy as no tray set up is needed, nor any handling with the large anaerobic chamber gloves. MCRred1 crystals behaved very similarly to MCRred1-silent, as expected. An issue with previous crystal structures in the past is Ni(II) generation. To keep the Ni(I) state of MCR in the crystal as long as possible, the redox potential of the solution must be examined. Even MCRred1 left cold inside of an anaerobic chamber will degrade when a low redox potential is not maintained. Therefore, a range of Ti(III)Cit was used as a component of the crystal buffer to reduce the redox potential. We found that Ti(III)Cit concentrations higher than 2 mM would result in precipitation of either Ti(III)Cit or enzyme, but 2 mM gave reproducible results and successfully reduced the redox potential of the crystal solution to -403.9 mV [152].

With this set up, crystals of about 40% Ni(I) MCRred1 crystals were collected and screened at the XFEL. As shown in Figure 4.16, this sample resulted in diffraction patterns that

contained two different unit cell parameters. Furthermore, the new unit cell was estimated to be proportional to the amount of Ni(I) found in the same before crystallization, 20% Ni(I), but the samples of Ni(I) and Ni(II) had to be combined.

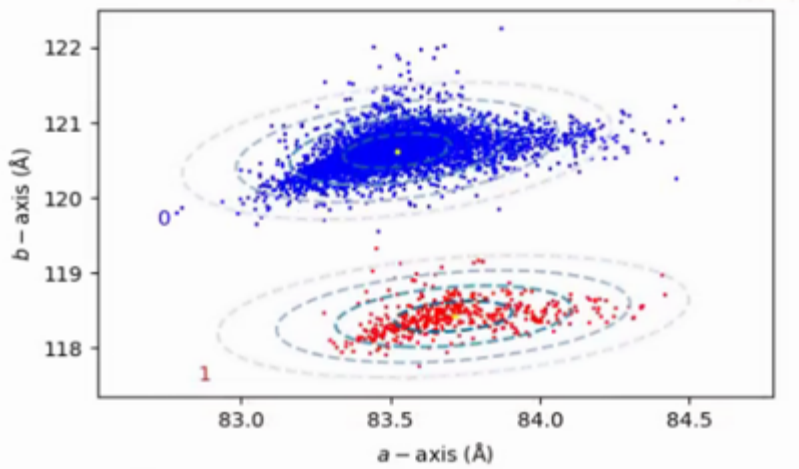

Figure 4.16 Trial of MCRred1 Exhibits a Novel Unit Cell Dimension Proportional to the Percentage of Ni(I). Results showing the unit cell dimension split providing a new unit cell dimension of estimated percentage of Ni(I) content. In blue is the unit cell dimensions of the predominant unit cell found in most MCR structures, and in red is the novel unit cell.

The result of this data lead us to hypothesize that this new unit cell dimension is the slight perturbation of the enzyme architecture in the Ni(I) state changing the unit cell. Unfortunately, the diffraction only went to 2.5 Å resolution. Therefore, we optimized the crystal growth procedure, finding the higher concentrations of MCRred1 not only resulted in better diffraction, but also yielded more crystals. The best diffraction data during optimization was found with very concentrated enzyme of 1.5 mM MCRred1.

With the new optimized growth method, XFEL was run on 3 different samples of MCRred1, MCRred1 co-crystallized with 10 mM HSCoM, and MCRred1 co-crystallized with 10 mM CH_3SCoM. Unfortunately, HSCoM influenced the viscosity of the sample and disrupted the acoustic droplet injector. Also, MCRred1 co-crystallized with CH_3SCoM did not result in data that was complete enough for an accurate data set. We finished the run with a structure of

MCRred1 without co-crystallization of ligands. The unit cell difference of the 61% MCRred1 produced the novel unit cell found previously, but at a much higher unit cell percentage of 47.1%. Figure 4.17 shows the unit cell distribution of MCRred1. Fortunately, there were enough spots to be able to separate out both unit cell distributions into separate structures. The structures of these two along with another structure of 100% Ni(II) MCRred1-silent was also solved. The new unit cell will be called MCRred1 Unit Cell 1, while the unit cell found in most MCR structures will be called MCRred1 Unit Cell 2.

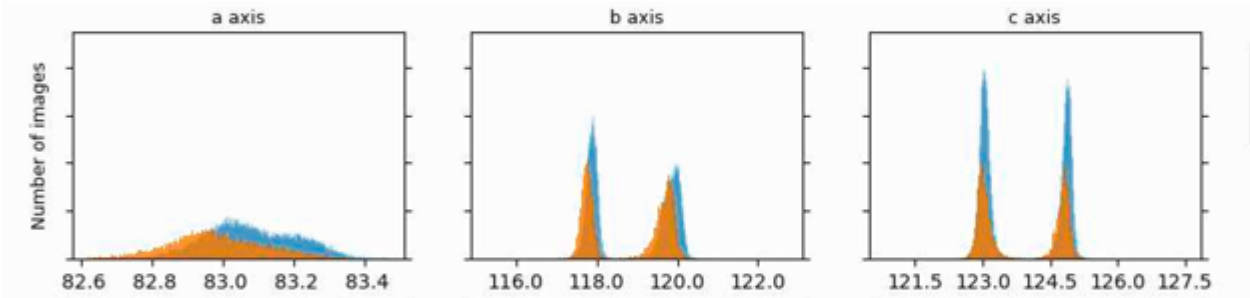

Figure 4.17 Unit Cell Distribution of MCRred1 Without Ligand Co-crystallization. Unit cell distribution by axis. The first run of this sample is shown in blue, while the second run is displayed in orange. The novel unit cell in question is 83.1, 117.8, 124.0, while the unit cell found for the MCRred1-silent in Chapter 3 is 83.0, 119.8, and 123.

MCRred1 Unit Cell 1 was solved at 1.85 Å resolution with R-work and R-free values of 0.1620 and 0.2129, respectively. MCRred1 Unit Cell 2 was solved at 1.75 Å resolution with R-work and R-free values of 0.1411 and 0.1730, respectively. MCRred1-silent was solved at 2.17 Å resolution with R-work and R-free values of 0.1660 and 0.2410, respectively. An overlay of these structures is exhibited in Figure 4.18. The global structures of these three MCR's are very similar, only allowing slight perturbations along loop regions of the β subunit on each protomer. With a difference in unit cell, this is surprising. Surprisingly, MCRred1 Unit Cell 1 shows much higher B-factors than either MCRred1 Unit Cell 2 or MCRred1-silent. This could indicate that this structure is indeed of Ni(I) MCRred1, given its dynamic nature compared to "locked-in" state of Ni(II) MCRred1-silent.

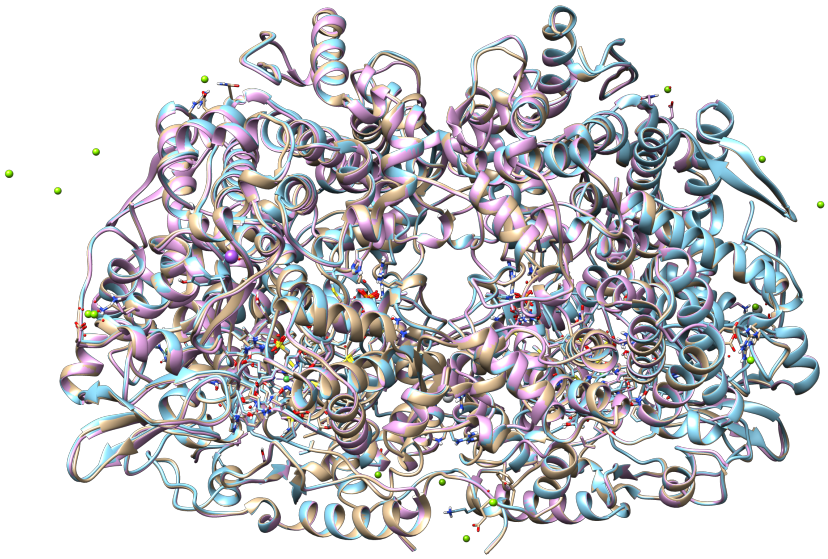

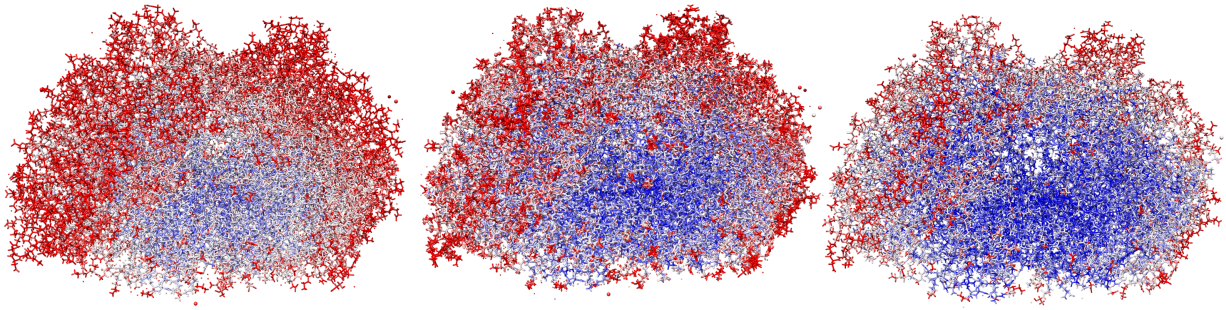

Figure 4.18 Superimposition of MCRred1 Unit Cell 1, MCRred1 Unit Cell 2, and MCRred1-silent. Overlay of the three crystal structures all collected during the same beamtime. (Above) MCRred1 Unit Cell 1 in pink, MCRred1 Unit Cell 2 in blue, and MCRred1-silent in tan all portray a similar global structure. (Below) B-factor representation of each structure globally where a gradient from blue to white to red represents b-factors 20 to 40 to 60, respectively. (Left) MCRred1 Unit Cell 1, (Middle) MCRred1 Unit Cell 2, and (Right) MCRred1-silent.

The modified amino acids as previously mentioned in Chapter 1 and Chapter 3 do not differ structurally between the three protein models, but the ADB, or B-factors, of these residues differ substantially. For instance, the 1-*N*-methylhistidine (MHS257) in the active site tunnel B-factors are much higher in the Unit Cell 1 structure compared to the other two structures as shown in Figure 4.19. Other B-factors of the modified amino acids are slightly higher as well illustrating some dynamics at room temperature (Table 4.2). It is of note that the MHS275 is positioned in the substrate opening and therefore would most likely have a higher b-factor than other points of the enzyme. The other modified amino acids are higher in MCRred1 Unit Cell 1 compared to MCRred1 Unit Cell 2 and MCRred1-silent, but not to this extent.

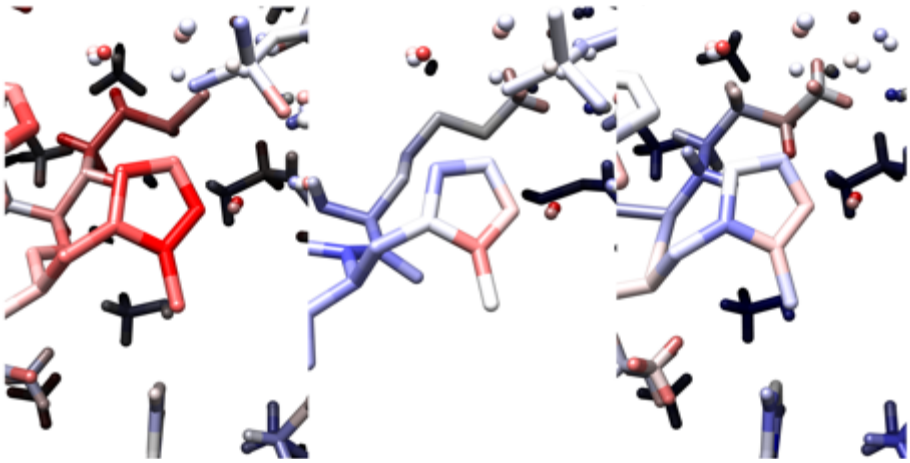

Figure 4.19 1-N-methylhistidine B Factor Comparison. B factor representation where Blue is 20, White is 40, and Red is 60 in a gradient. (Left) MCRred1 Unit Cell 1 MHS B-factors show large atom B-factors. (Middle) MCRred1-Unit Cell 2. (Right) MCRred1-silent.

	MCRred1 Unit Cell 1 (Å2)	MCRred1 Unit Cell 2 (Å2)	MCRred1-silent (Å2)
2-Methyl Glutamine (MGN400)	34.1, 36.0	27.1, 26.0	26.2, 29.6
5-Methyl Arginine (AGM271)	38.9, 36.0	27.0, 27.6	28.8, 28.8
1-Methylated Histidine (MHS257)	57.9, 54.0	39.1, 40.8	40.9, 38.2
S-Methyl Cysteine (SMC452)	40.0, 40.1	28.8, 27.3	27.4, 30.0
ThioGlycine(TG445)	37.3, 36.7	25.7, 26.5	27.0, 21.0
DI-Dehydro Aspartic Acid (DYA450)	34.3, 36.1	26.7, 26.3	21.9, 21.5

Table 4.1 B-factors of Modified Amino Acids in MCRred1 Unit Cell 1, MCRred1 Unit Cell 2, MCRred1-silent Structures. Average calculated B factors for MCRred1Unit Cell 1, MCRred1 Unit Cell 2, and MCRred1-silent XFEL structures.

The active sites of the MCRred1 Unit Cell 1 structure are greatly perturbed compared to the MCRred1 Unit Cell 2 and MCRred1-silent structures as shown in protomer 1 in Figure 4.20. The measured Ni-SCoM bond has increased in MCRred1 Unit Cell 1 to 2.75 and 2.68 Å in protomer 1 and 2, respectively. This distance is too long to be called a "bond" and thus the complex is effectively square pyramidal N_4O complex lacking a Ni-S bond. In contrast, the Ni-S distance for protomers 1 and 2 of MCRred1 Unit Cell 2 are 2.48 and 2.47 Å, while those of MCRred1-silent are 2.51 and 2.50 Å. Furthermore, in MCRred1 Unit Cell 1 the distance between the oxo of Gln147 and the Ni is shortened to 2.07 and 1.96 Å in protomers 1 and 2, respectively

compared to that in MCRred1 Unit Cell 2 (2.29 and 2.30) and MCRred1-silent (2.39 and 2.38) for protomers 1 and 2, respectively(Table 4.1).

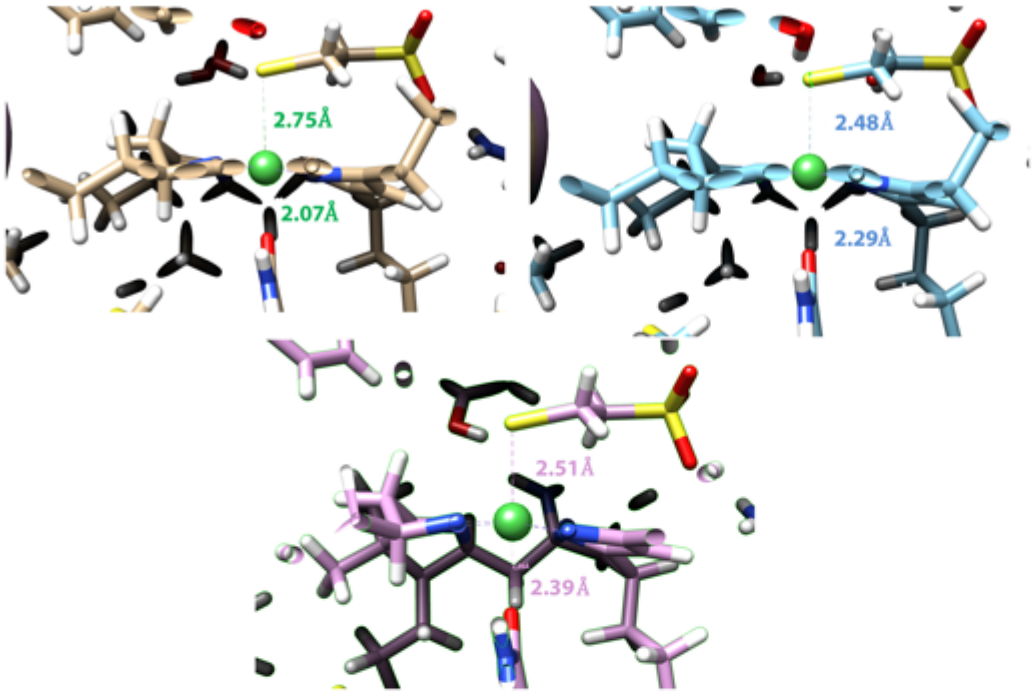

Figure 4.20 Ni Coordination of Ni Metallocentre is Perturbed in MCRred1 Unit Cell 1. MCRred1 (Tan) illustrates an elongated coordination from the Ni to the S atom of HSCoM and a decrease in coordination distance of the Ni-OGln bond of the MCRred1 Unit Cell 1. (Blue)

	MCRred1 Unit Cell 1	MCRred1 Unit Cell 2	MCRred1-silent
Ni-SCoM	2.75, 2.68	2.48, 2.47	2.51, 2.50
Ni-OGln	2.07, 1.96	2.29, 2.30	2.39, 2.38

Table 4.2 Comparison of Ni Coordination Distances. MCRred1 Unit Cell 1 shows a significant perturbation, deviating from both structures found at the same beam time.

Unfortunately, the XES for this run was inconclusive and the microspectrophotometer set-up had not yet been developed for the XFEL experiment. Therefore, while we do not have an

unambiguous indicator of the oxidation state of the enzyme in this structure, we may look to recent XAS literature for a comparison between the Ni(I) and Ni(II) active site structures. In Patwardhan *et al.*, XAS was used to understand the Ni coordination in a variety of substrates. Specifically, two structures should be highlighted. Via XAS, Ni(II) MCRred1c-silent HSCoM containing was found to have a Ni-S(CoM) coordination distance of 2.42Å and a Ni-OGln distance of 2.20. On the other hand, the Ni(I)-MCRred1 structure is pentacoordinate, exhibiting 2.03Å Ni-OGln bond and undetectable Ni-S(CoM). Furthermore, incubation with HSCoM with Ni(I)-MCRred1 results in an undetectable Ni-S(CoM) bond in the state MCRred1c. The detection limit of XAS is around 2.50Å. Thus, the XAS data suggest that the structure of the MCRred1 sample in this new unit cell is indeed of the Ni(I) state. Furthermore, upon oxygen damage, the Ni-OGln bond length appears to extend from 2.03Å to 2.20Å and the Ni-S to contract to ~2.42Å. This data correlates to our MCRred1 Unit Cell 1 structure and could possibly be concluded as the Ni(I) MCRred1c. If MCRred1 was incubated with HSCoM, XAS could not detect the sulfur atom of HSCoM, resulting in a pentacoordinated metallocentre.

Interestingly, each crystal structure contains one atom of titanium where previous structures have shown other cations such as calcium or magnesium [57,70]. It is unknown how Ti(III)Cit is able to reduce the Ni metallocenter redox potential or reduce MCRox1. While this is an interesting finding, it is 26.2 Å away from the Ni, it is located at the interface between α and α' subunits. Whether the Ti atom influences structure between the two protomer active sites is an interesting question, but more for this must be explored for this answer to be elucidated.

Interestingly, HSCoM and substrate HSCoB remain in all three structures, but seemingly at different occupancies. Removal of the substrates has been setback in crystallography of MCR. In Chapter 3, I described our hypothesis that the Ni(II)-silent state is "locked in" due to

occupancy of HSCoM and HSCoB being 100% in most structures, except in Cederval *et al.* where, to determine occupancy, b factors were matched with the Ni cofactor F430. When b factors were considered higher than the corphin, occupancy was decreased by 10% and waters were modelled to visualize a water chain replacing HSCoB.

Because the Ni cofactor F430 is very tightly bound compared to HSCoM and HSCoB, we used a different strategy to determine occupancy. Each atom of HSCoM and HSCoB was attributed a B-factor based on the average b factors of surrounding molecules with a cutoff of 5Å. Refinement was run on the structure with constant B-factors while the refinement would change the occupancy. We attributed that to be the occupancy of HSCoB and HSCoM. It is of note, that this b factor vs occupancy comparison strategy can be easily manipulated and should not be considered an absolute. From this strategy, we find that HSCoB inhabits around 40% (40%, 34%, and 47% for MCRred1 Unit Cell 1, MCRred1 Unit Cell 2, and MCRred1-silent, respectfully) of each structure. HSCoM is found in 100% occupancy for MCRred1 Unit Cell 1, while 93% is found in MCR Unit Cell 2. Surprisingly, the MCRred1-silent structure has an average of 73% HSCoM. This may be explained by the method to make this sample. The MCRred1-silent sample was made with MCRred1 through 7 rounds of 10x buffer exchange. Unfortunately, the centrifuge for this sample was not refrigerated. MCR will oxidize to a silent species more readily if not kept at 4° C. After the 7 rounds of 10x buffer exchange, the enzyme fully converted to MCRred1-silent. It is possible temperature had a significant effect on removal of HSCoM, but it is with great risk that the enzyme will degrade if using this strategy. For the future, to remove HSCoM from the enzyme may be important in allowing us to visualize the binding site for methyl-SCoM. Perhaps by varying the temperature of buffer exchange (in the

presence of methyl-SCoM) we may be able may remove more HSCoM without damaging the enzyme.

4.4 Discussion

Since MCR's discovery in the 1970's, scientists spent 20 – 30 years to find the first crystal structure of the enzyme published by Ermler *et. al.* in 1997 [56]. It is now 2023, 26 years later, and the Ni(I) active structure of MCRred1 has never been solved. The reason for this is the redox and oxygen sensitivity of the Ni cofactor F430, with its low redox couple of -0.65 V, making the enzyme one of the most oxygen sensitive enzymes on the planet. Moreover, the Ni in the enzyme and CH_3-SCoM could undergo radiation damage, oxidizing any Ni(I) cleaving the S-C bond of CH_3SCoM generating the inhibitor HSCoM bound to and stabilizing Ni(II) [56]. Thus, several methodologies have been introduced to help determine the structure of the active site of MCR. Many of these methods supplied information to the MCR structural field. Anaerobic capillary XRD paired with microUV-Vis was employed to uncover photooxidation of Ni(I) to Ni(II) . Moreover, XFEL serial femtosecond crystallography produced a plausible Ni(I) MCRred1 structure. We observed that the current simultaneous XES experiment must be improved, since it was unable to resolve Ni(I) from Ni(II) and provide a validation of the oxidation of the MCRred1 sample. Therefore, we are working with Philipp Simon in the Kern, Yano, Yachandra lab to build a microspecUV-Vis for tandem XFEL serial femtosecond XRD and UV-Vis analysis of MCRred1.

Chapter 5 Conclusions, Future Directions, and Broad Impact

5.1 Investigation of Radical Intermediate CoBS· with Synthetic Thiyl Radical Trapping Analog, CoBphSH

5.1.1 Conclusions

The mechanism of MCR has been disputed for decades. What was thought based on stereo configurational inversion to be an SN2 mechanism involving formation of methyl-Ni(III) was challenged by computational studies to rather occur by a radical mechanism. First experimental evidence was found for the radical mechanism by Wongnate *et. al.* in 2016, but the EPR signal for the radical intermediate found was too broad for clear determination. To capture and stabilize this radical intermediate proposed by Wongnate *et al.*, an analogue of HSCoB was synthesized replacing the heptanoyl chain with an aryl moiety, which should delocalize the the proposed thiyl radical intermediate along the ring. Based on pH titrations, I found that the pKa of the phenyl thiol was 6.7, compared to 9.4 of the thiols found in HSCoB. This pKa may provide a kinetic variation of the catalytic mechanism. Binding of the newly synthesized substrate analogue was discovered to have an estimated affinity of Kd = 88.3 μM. Furthermore, EPR analysis of MCRred1 incubated with CoBphSH and CH_3SCoM decreased the spin percentage of MCRred1 indicating that the reaction of MCRred1 with CH_3SCoM and CoBphSH elicits a reaction. This will be followed up using steady-state and presteady-state kinetics along with further binding studies. Furthermore, reaction by tracking a radiolabelled $^{14}CH_3SCoM$ uptake would let us know the kinetics of MCR utilizing CoBphSH rather than HSCoB.

5.1.2 Future Directions

First, CoBphSH must be confirmed to bind MCR and form the ternary complex needed to start this ordered bi-bi mechanism, as previously mentioned. This could be confirmed by measuring the reaction of MCR with radiolabeled $^{14}CH_3SCoM$ and CoBphSH (in comparison with CoB). Similarly, UV-Vis could be used to see a decrease in the Ni(I) at 385 nm and expected increase in Ni(II) at 420 nm. We will be careful to discriminate between this being a reaction versus uncoupled oxidation of the Ni(I)MCRred1. If CoBphSH binds but does not undergo reaction (or perhaps a slower reaction), the compound could be used as an inhibitor for the decrease in methane production. Therefore, the catalytic nature of CoBphSH must be identified. Furthermore, crystallography of MCRred1 co-crystallized with CoBphSH may also help identify an active site structure of the either slow or inhibitory complex. Luckily, my time here is extended for another year as a postdoctoral associate, so this will be done very shortly.

Additionally, there are two other HSCoB analogues that can be synthesized to provide evidence of the radical mechanism, the PBN derived nitrone spin trap and the vinyl radical clock. These compounds can be used to either visualize the nitrone radical upon methyl radical generation or synthesize a methyl group onto the substrate for MS identification.

Another major conundrum is understanding the reverse reaction of MCR. Stopped flow kinetic experiments with MCRsilent (MCR bound with CoMSSCoB) would enable real time kinetic characterization of the disulfide anion radical via NIR and UV-Vis. Furthermore, the backwards reaction with *M. marburgensis* is found to be much slower than the forward mechanism. Thus, by studying the reverse reaction we should, theoretically, be able to capture the remaining intermediates of MCR catalysis. EPR of this species performed by Anjali Patwardhan has perceived an MCRox1 like spectra with CoB_6SSCoM, but not CoB_7SSCoM.

Trapping this possible MCRox1 and disulfide anion radical would help complete the proposed radical reaction scheme.

5.2 Development of Structural Methods to Determine the Active Ni(I) Methyl-Coenzyme M Reductase Structure

5.2.1 Conclusions

The active Ni(I) MCR structure remains elusive since the first inactive Ni(II) MCR structure solved in 1997 [56]. Methods of anaerobic crystallography thus far have not been able to prove the oxidation state of metallocentre of many anaerobic enzyme structures. Therefore, we have worked with many collaborations to develop structural methods reliable for anaerobic crystallography and tandem spectroscopy to ascertain the oxidation state of MCR. With Dr. Flora Meilleur at Oak Ridge National Lab, we have worked to develop MCR crystals suitable for neutron diffraction as well as worked to create an anaerobic chamber to house the crystal during collection. Additionally with Dr. Aina Cohen and Dr. Darya Marchany-Rivera, we have determined a proper method to collect MCRred1 crystals using a UV-Vis microspectrophotometer to ascertain the oxidation state during data collection on beamline 9-2. We have provided the first evidence of photooxidation of MCR upon X-ray radiation. Moreover, we have collected what we consider the first active Ni(I) MCR structure via XFEL in collaboration with Dr. Jan Kern, Dr. Junko Yano, and Dr. Vittal Yachandra displaying high b factors attributing to the proposed dynamic structure of the active MCRred1 structure. The coordination of the metallocentre in this structure also reflects previous XAS data of a 5 coordinate MCRred1 incubated with HSCoM.

5.2.2 Future Directions

While we may have the active Ni(I) MCR structure in our hands, it is difficult to be undoubtably certain unless we have spectroscopic evidence of the Ni(I) metallocentre. Unfortunately, XES in tandem with XRD did not accomplish this task, and thus another method must be used. Furthermore, we have shown that photooxidation occurs on the metallocentre and that serial capillary room temperature XRD in tandem with single crystal UV-Vis could be a reliable method. However, SLAC was shut down in January 2023 with an estimated opening in September. Consequently, capillary crystallography and XFEL have been halted until the facility reopens. During this time, we have worked with Philipp Simon at LBNL to develop a microspectrophotometer for the anaerobic set up for XFEL as well as developed an oxygen scrubber for the XFEL set up during my time at Berkeley National Lab. Furthermore, counter diffusion crystallography has been utilized to ease handling of crystals for anaerobic capillary on beam line 9-2 as well as provide a freezing strategy with small 0.1 mm to 0.3 mm OD capillaries for quality freezing.

5.3 Impact

With methanogens producing more than 1 billion tons of methane annually, as well as having populations that serve as methane sinks for the reverse reaction of the enzyme, understanding how MCR catalyzes methane is critical. Methane has two incredible roles, existing as a Janus Face molecule, in that on one hand it is a widely used energy source as well as a potent greenhouse gas. Understanding MCR, which catalyzes both the forward and reverse reactions, i.e., the production and oxidation of methane can benefit the human species in two ways. 1) To use methane as a fuel source and 2) by removal or prevention of methane imparting its greenhouse gas potential on the earth. We are in a climate crisis and, thus, understanding how Nature has bioengineered an enzyme for the production and oxidation of this inert molecule can take us leaps and bounds toward a greener future. Furthermore, the functionalization of inert C-H

bonds is dubbed to be one of the holy grail reactions of chemistry because of the abundance of synthetic applications for creating C-C bonds and functional group attachment [154]. Understanding how biology has developed a biocatalyst such as MCR to carry out this reaction will have critical applications in synthetic and bio- catalysis.

Specifically, solving the structure of active Ni(I) MCR will be a definitive glimpse into the inner working of this biocatalysis. With this knowledge, groups after us will be able to produce potent, or non-potent and non-lethal, inhibitors for the agricultural industry, a massive contributor to anthropogenic methane. After heterologous expression of MCR is widely developed, many scientists will be able to modulate the active site of the enzyme based on the active Ni(I) structure. This pairing of knowledge will be extremely impactful to modify MCR to oxidize methane, to create a human made methane sink, as well as producing copious amounts of biofuel by utilizing methanogenic processes. We are in a specific time with global warming on a rise for methane research and I believe that this project and future projects that may stem there from will create a better, more inhibitable world for our kids and future generations.

Appendix A: Supplemental Materials for Chapter 2

Synthetic Methods and Spectroscopy

Synthetic route improvement

Before the proposed schematic presented in the introduction section was found to synthesize CoBphSH, we first started with synthesizing molecule **3** and a completely different synthetic route outlined in Figure SI 2.1. The first reaction attempted for the synthesis of this diaryl disulfide was attempted from starting at molecule **1** and using catalyst copper sulfate, $CuSO_4$, and 1,2-ethanedithiol to produce a thiol version of molecule **3** called 3-(4-mercaptophenyl) propanoic acid, or what we will call molecule **1a**[155]**.** From molecule **1a**, we would follow the published synthesis for HSCoB which involves an N-hydroxysuccinimide (NHS) addition using coupling agent N,N'-Dicyclohexylcarbodiimide (DCC) to make 2,5-dioxopyrrolidin-1-yl 3-(4-mercaptophenyl)propanoate, molecule **1b**. With **1b** having a very good N-succinimidyl ester leaving group, we may perform a peptide couple using Diisopropylethanolamine (DIPEA) and o-phospho-l-threonine to make CoBphSH. This synthetic pathway had many faults, one of which started with the synthesis of molecule **1a.**

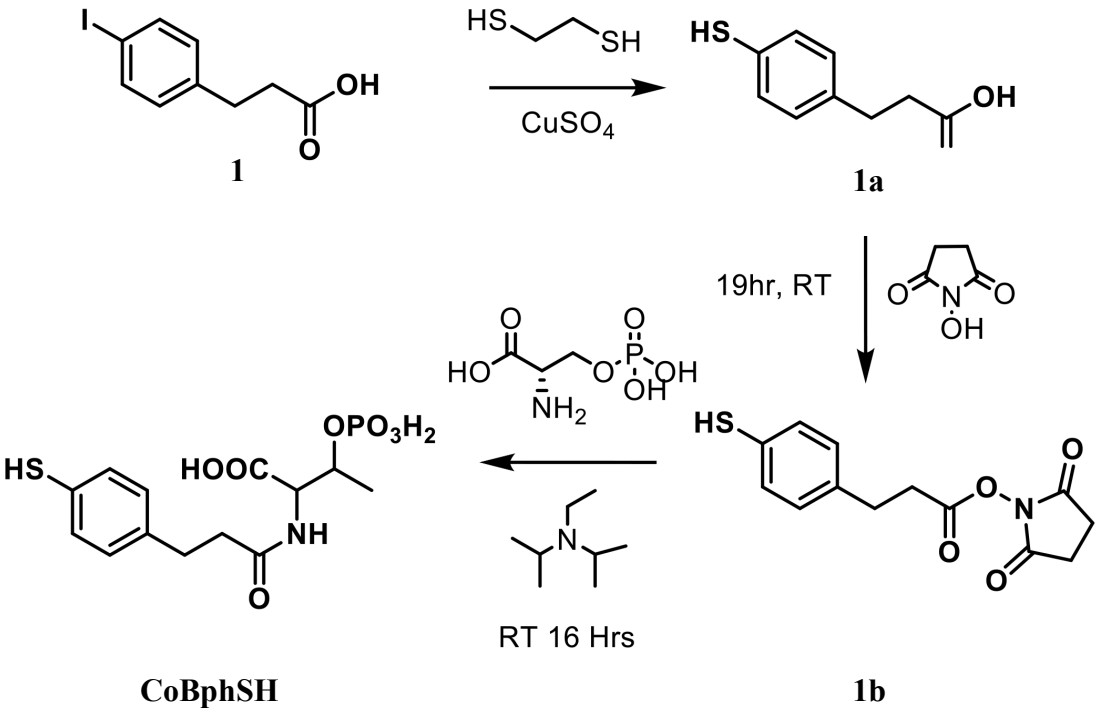

Figure A1 Premature Synthetic Route to CoBphSH. Synthesis starting at molecule **1** where the route to CoBphSH is progressed through a thiol compound along with a two-step peptide coupling using DCC, NHS to make molecule **1b** and a subsequent reaction involving o-phospho-l-threonine and DIPEA. RT refers to room temperature.

This reaction using 1,2-ethanedithiol from a paper published by Liu *et al* in 2014. This paper was able to obtain 32 different compounds using this method [155]. This reaction was set up under inert argon gas attached with an inert argon gas balloon to prevent catalyst damage. This is shown in Figure 2.6. This method first resulted in a slight amount of disulfide product (not **1a** but molecule **3**) of about 2% yield after purification on a silica column and running MS, but many other biproducts were made. After attempting to further increase yield, only about 8% was able to be purified. Much of the difficulty in purification was due to a large amount of what seemed to be polysulfides identified by MS. Furthermore, the carboxylic acid moiety's polarity made purification on silica challenging. In Figure SI 2.2, we can see a large amount of the compound streak and have difficulties with purification. Therefore, we sought to improve this

synthesis by adding a methyl ester to the compound as well as attempt to get the disulfide rather than the oxygen sensitive molecule **1a.** This disulfide reaction seems to be quite difficult with an aryl-halide, but Hsing-Ying *et al.* in 2013 used the strength of the base to control whether a diaryl disulfide or a diaryl thioether would be predominantly synthesized [12]. This reaction used sulfur powder, or S_8, as the sulfur donor, CuI, and NaOAc as a weak base to make the diaryl disulfide. Therefore, we set out to attempt this round of synthesis.

Figure A2 Copper sulfate mediated synthesis with 1,2-ethandithiol. Inert gas balloon was used to attach the round bottom to avoid oxidative damage to the catalyst while all compounds were degassed on a Schlenck line.

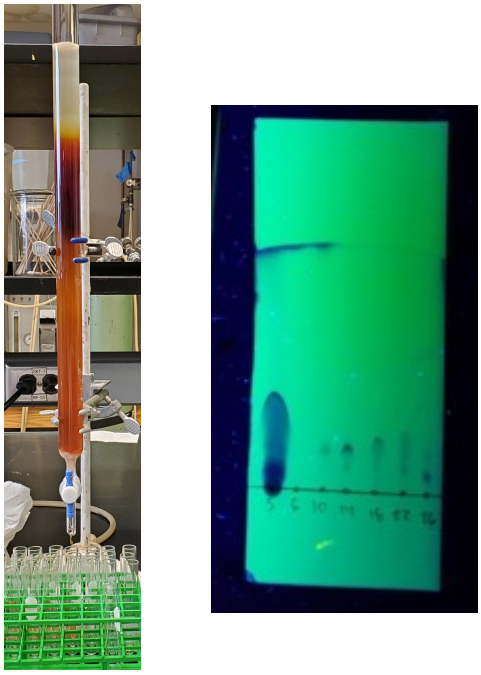

Figure A3 Streaking associated with COOH appendage. From both the TLC and silica column, streaking was observed decreasing purity of the purified samples

Synthesis of molecule 2

The synthesis of molecule **2** is a simple reaction in which a methyl is attached to a carboxylic acid to form a non-polar methyl ester (Figure 2.8). This is accomplished with a simple reaction using sulfuric acid and methanol allowed to reflux for 15 hours in an acid catalyzed methyl ester synthesis. Spectroscopy can be found in Figure 2.9.

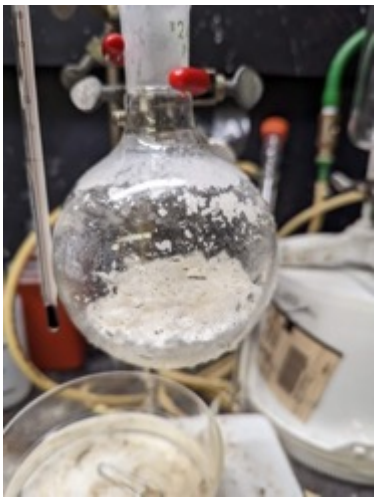

Figure 4 Synthesis of molecule 2. (Left) Methyl ester synthesis using sulfuric acid and methanol. (Right) molecule **2** after rotary evaporation.

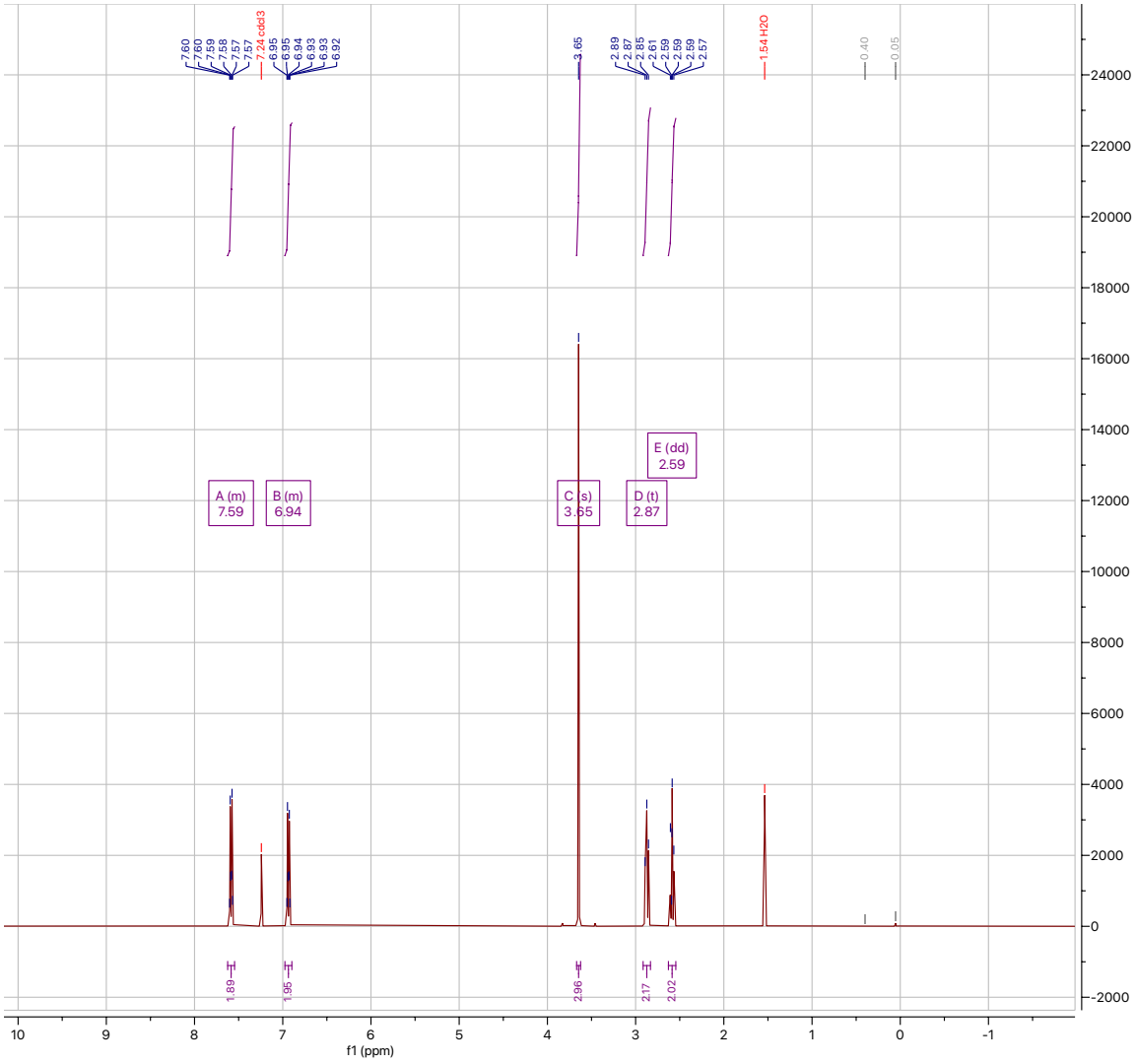
7.60
7.60
7.59
7.58
7.57
7.57
7.24 cdcl3
6.95
6.95
6.94
6.93
6.93
6.92
3.65
2.89
2.87
2.85
2.61
2.59
2.59
2.57
1.54 H2O
0.40
0.05
A (m) 7.59
B (m) 6.94
C (s) 3.65
D (t) 2.87
E (dd) 2.59
1.89
1.95
2.96
2.17
2.02
f1 (ppm)

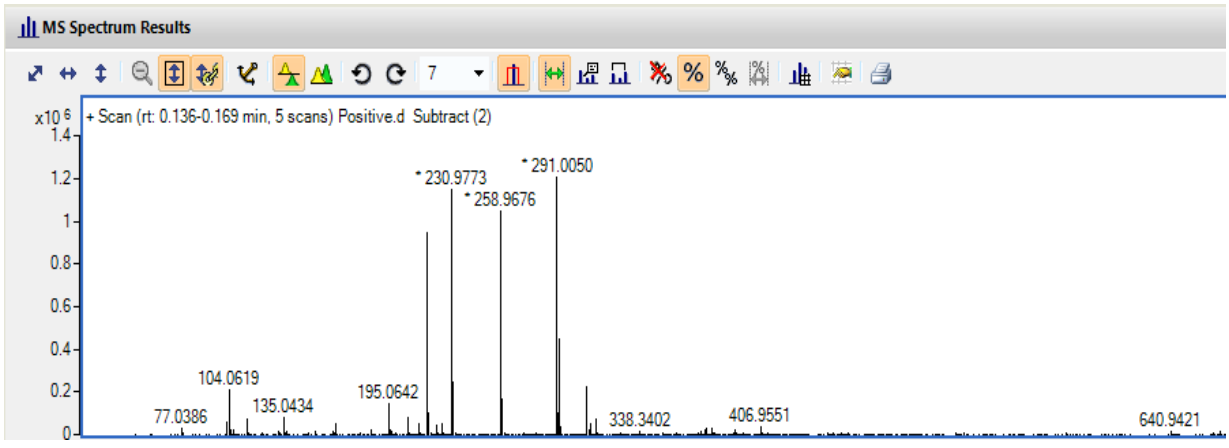
MS Spectrum Results
+ Scan (rt: 0.136-0.169 min, 5 scans) Positive.d Subtract (2)
x10 6
* 230.9773
* 291.0050
* 258.9676
104.0619
77.0386
135.0434
195.0642
338.3402
406.9551
640.9421

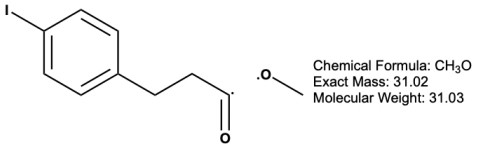
Chemical Formula: CH3O
Exact Mass: 31.02
Molecular Weight: 31.03

Chemical Formula: C9H8IO
Exact Mass: 258.96
Molecular Weight: 259.07

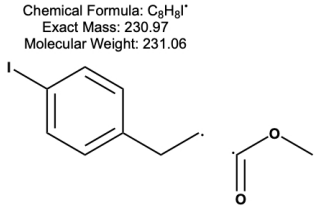
Chemical Formula: C8H8I
Exact Mass: 230.97
Molecular Weight: 231.06

Figure A5 Spectroscopy of molecule 2. (Above) NMR spectroscopy illustrating the correct molecule with proper integrations and splittings (Below) Mass Spectroscopy revealing the correct mass at 291 m/z with two additional peaks due to fragmentation of the compound around the carbonyl.

Synthesis of Compound 3 and Polysulfide Remediation

We explored using a weak base to control the selectivity of the polysulfide production to hopefully obtaining diaryl disulfides. This reaction must be kept under inert conditions due to the Cu^0 catalysts sensitivity to oxygen and moisture. Therefore, all solutions were degassed on a vacuum line and the headspace was exchanged with N_2 before addition with an argon washed syringe. The solution is made in dimethyl formamide as a solvent up to 100°C and run for 26 hours for optimal conversion to mostly disulfide. The purification of the molecule **3** worked ideally with the addition of the methyl ester moiety and new base-controlled reaction, transforming the previous 8% to 68% yield (Figure SI 2.6). Unfortunately, there were several other polysulfide species shown in the NMR and MS (Figure SI 2.7 and SI 2.8).

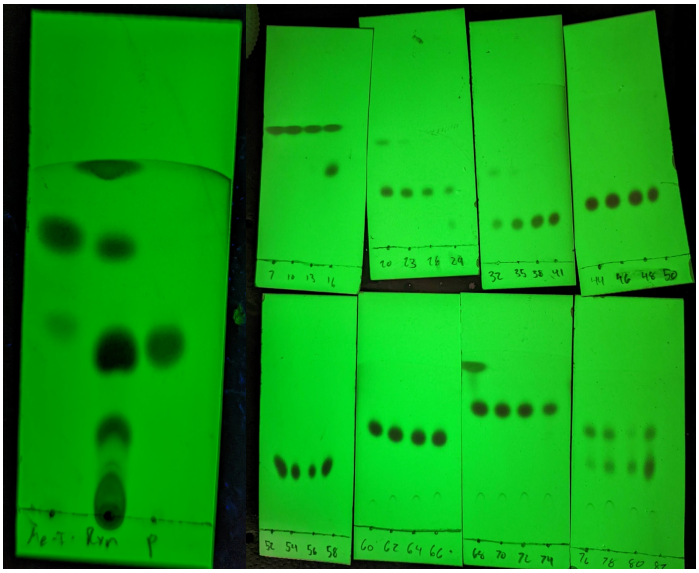

Figure A6 Column Purification Improvements. (Left) Overall purification visualized via Thin Layer Chromatography (TLC) at a UV of 320nm. Me-I is the starting material of molecule **2**, Rxn is after the 26 hour reaction time, and P is product purified after column of molecule **3**.

(Right) TLC of the full column purification where the numbers below indicate the fraction where pure compound was found in fractions 35–74.

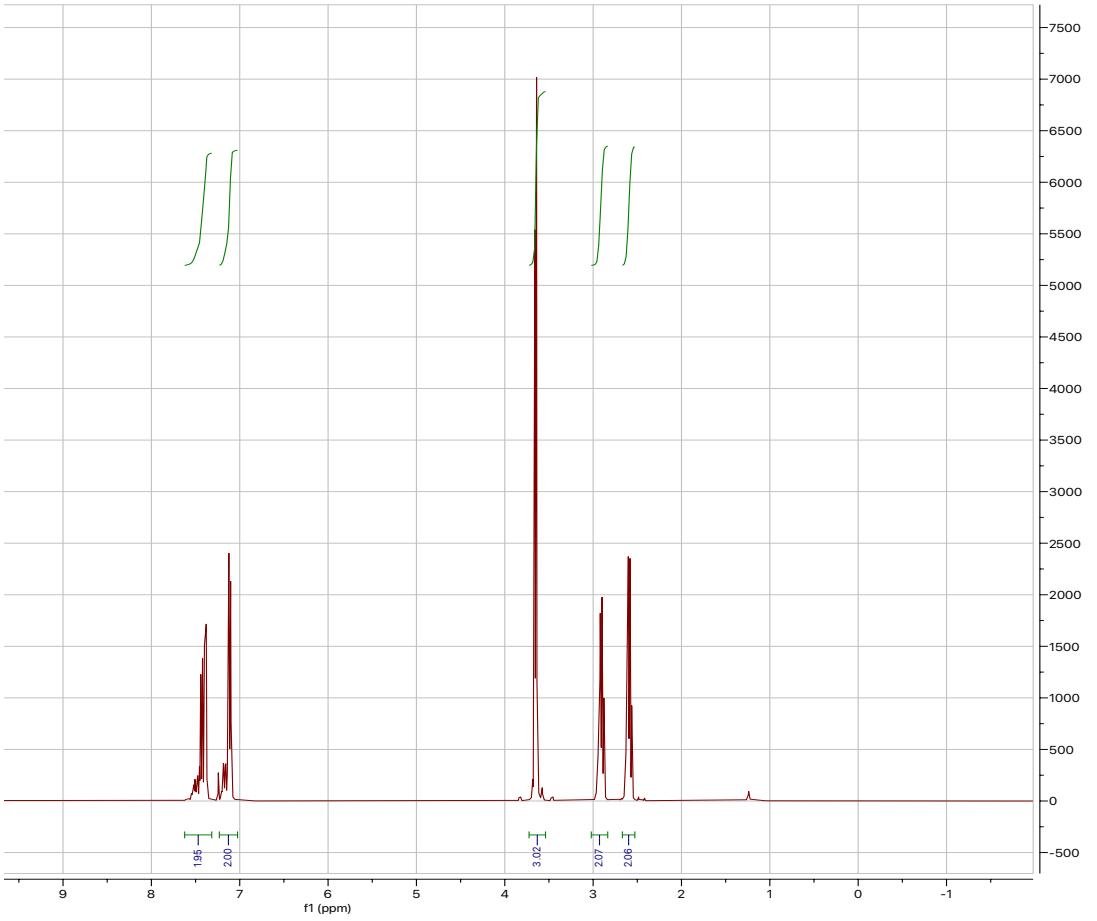

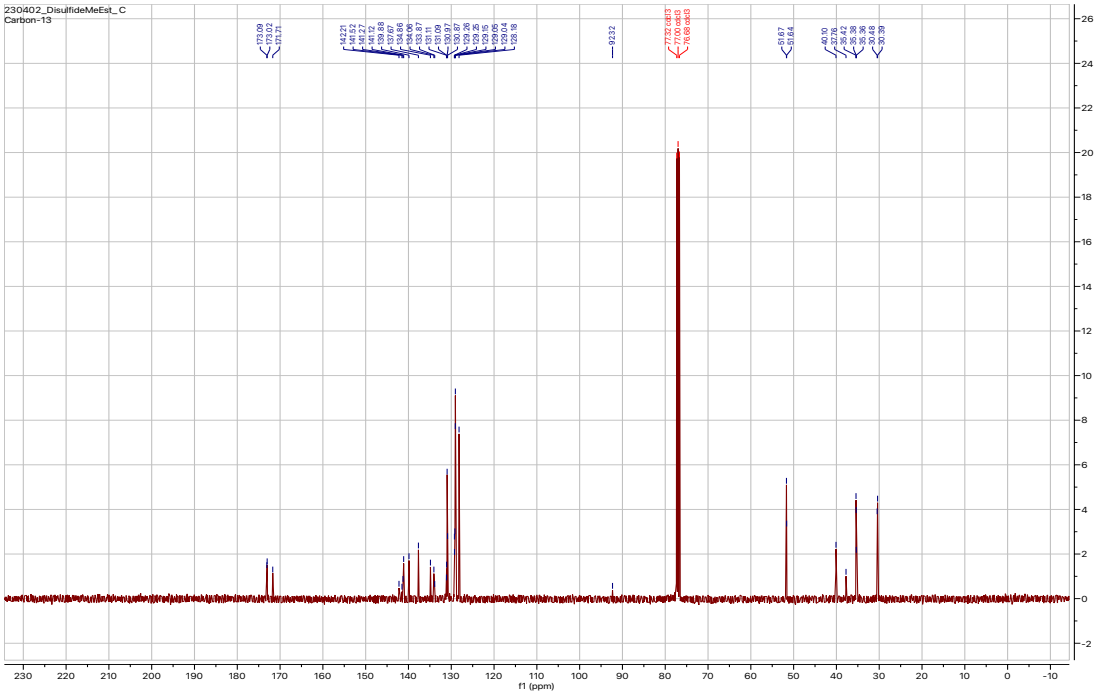

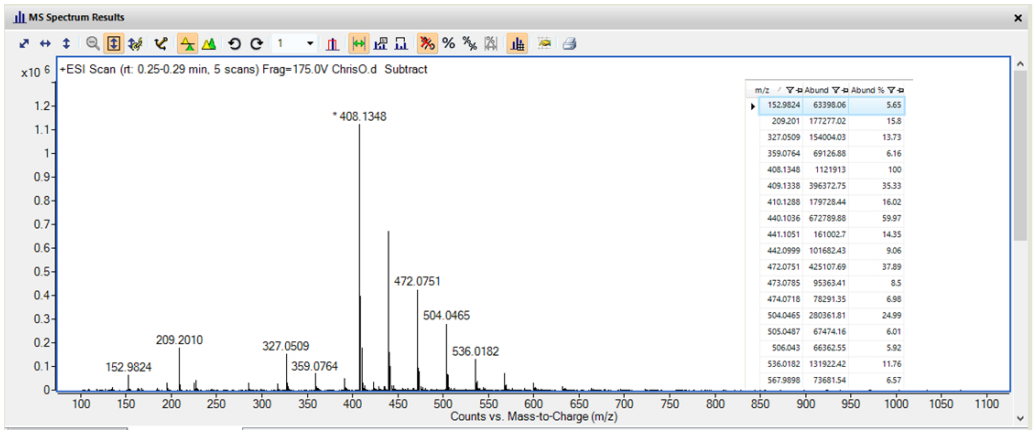

Figure A7 Column Purification Improvements. (Left) Overall purification visualized via Thin Layer Chromatography (TLC) at a UV of 320nm. Me-I is the starting material of molecule **2**, Rxn is after the 26 hour reaction time, and P is product purified after column of molecule **3**. (Right) TLC of the full column purification where the numbers below indicate the fraction where pure compound was found in fractions 35–74.

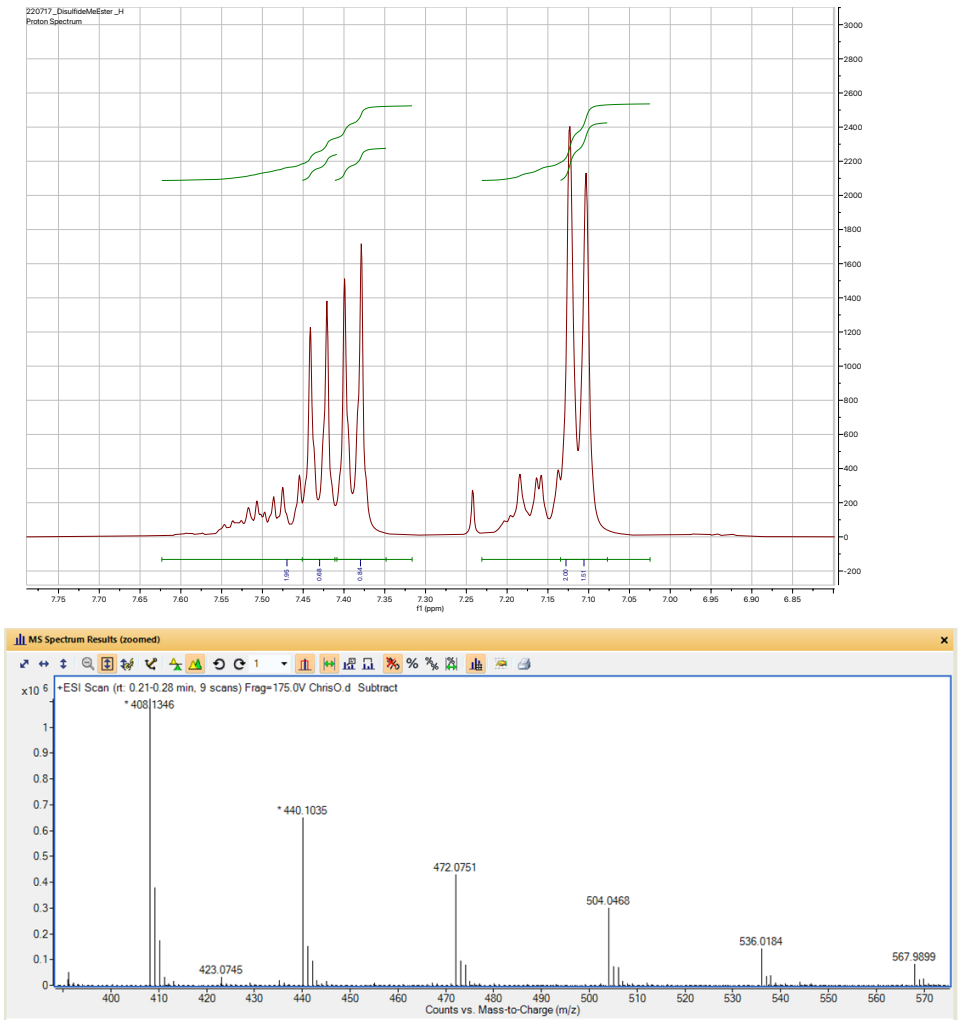

Figure A8 Spectroscopy of molecule 3 reveals additional polysulfides. (Above) In the ppm range related to the aryl protons shows a doublet shifts correlating to additional polysulfides

where the downfield aromatic protons show a large downfield shift due to deshielding from additional sulfur appendages. (Below) Mass Spectroscopy showing m/z values with differences of 32 m/z for several peaks, showing evidence of 7 different polysulfides.

The addition of the polysulfides makes this reaction very difficult to purify even with the methyl ester appendage. Silica gel columns do not separate the polysulfides from the disulfide. Therefore, we relied on cleavage of the disulfides later in the reaction. In 2013 Cumnock *et al.* found that TCEP was able to reduce trisulfides making a P=S double bonded phosphine in the process[156] (Figure SI 2.9). Luckily, with a disulfide for our product, we must cleave the disulfide using TCEP, therefore we can use an excess amount of TCEP to take our polysulfides to disulfides. Then, with another molecule of TCEP, cleave off the disulfide to give us our target CoBphSH.

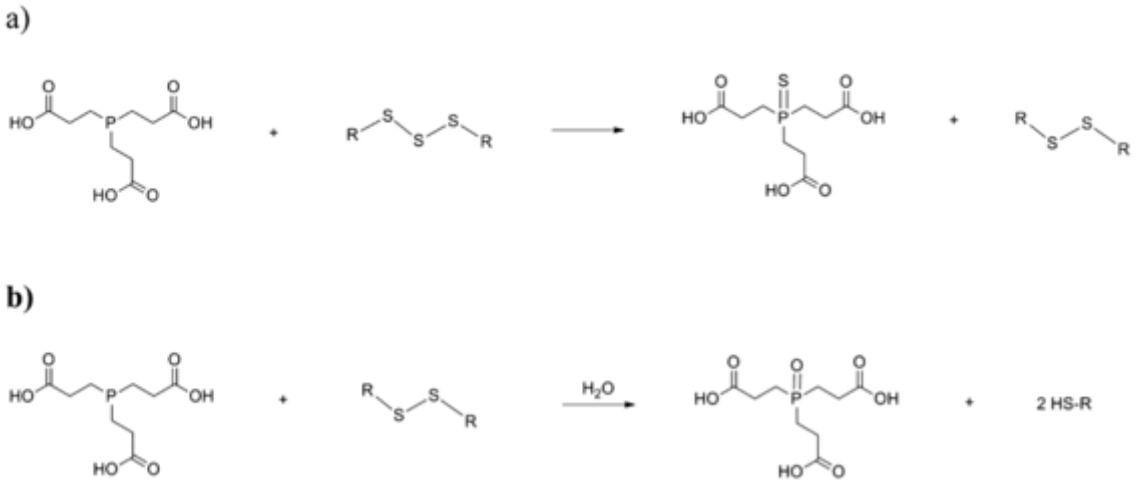

Figure A9 TCEP reduction from trisulfides to thiol. A) Trisulfide reaction with TCEP to form thiophosphene and disulfide. B) Reaction with TCEP, disulfide from previous reaction, and water resulting in oxidized TCEP with stoichiometric thiol.

Synthesis of Molecule 4

Synthesis of molecule **4** removes the methyl ester back to a carboxylic acid now that silica-based purification strategies are no longer needed. The methyl removal is performed with

an acid catalyzed hydrolysis method. Even in concentrated sulfuric acid, the disulfide on molecule **3** did not cleave and instead through acid-catalyzed hydrolysis, cleaved the methyl ester. Thus, we attempted the acid catalyzed hydrolysis of the methyl ester using 75% sulfuric acid. The hydrolysis yielded on average 60% with successful purification of molecule **4** (Fig SI 2.10, SI 2.11**).**

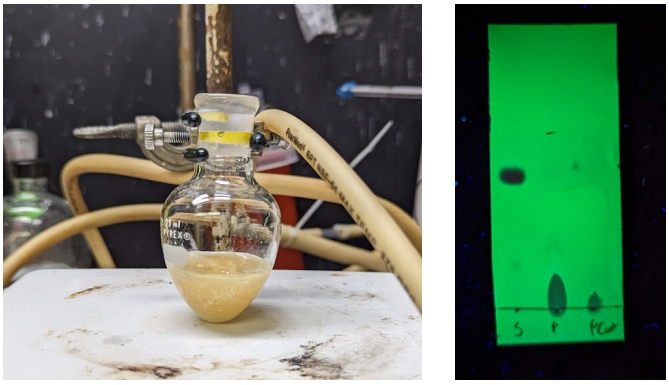

Figure A10 Reaction set up for synthesis of molecule 4 and TLC. (Left) Reaction of molecule **4** in a conical vial. (Right) TLC of Starting material control "S", purified product from reaction "P" and product control "Pcont".

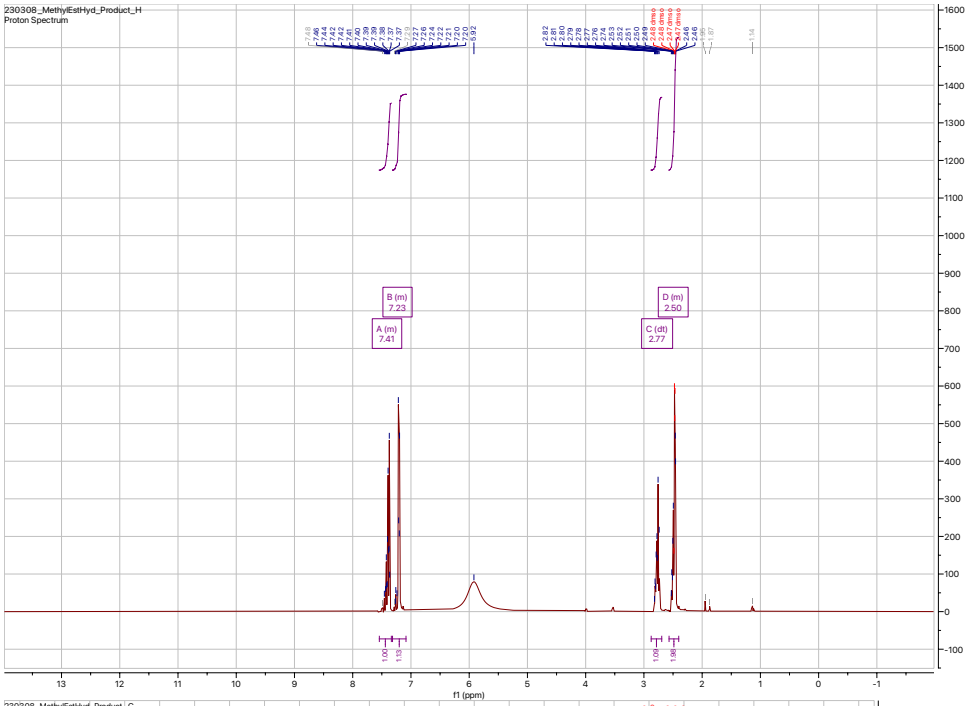
230308_MethylEstHyd_Product_H
Proton Spectrum
B (m)
7.23
A (m)
7.41
D (m)
2.50
C (dt)
2.77
f1 (ppm)

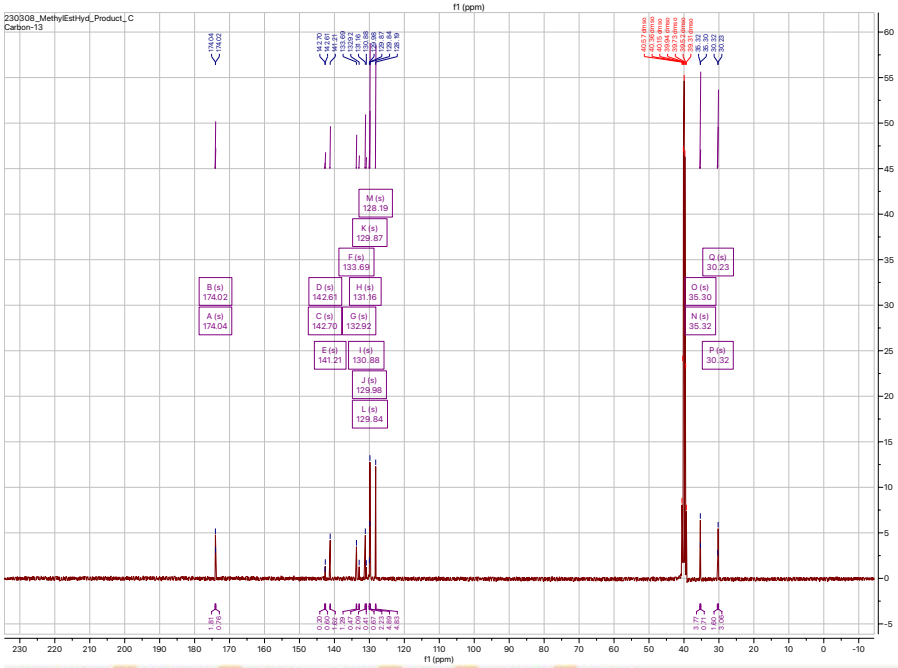
230308_MethylEstHyd_Product_C
Carbon-13
M (s)
128.19
K (s)
129.87
F (s)
133.69
B (s)
174.02
D (s)
142.61
H (s)
131.16
A (s)
174.04
C (s)
142.70
G (s)
132.92
E (s)
141.21
I (s)
130.88
J (s)
129.98
L (s)
129.84
Q (s)
30.23
O (s)
35.30
N (s)
35.32
P (s)
30.32
f1 (ppm)

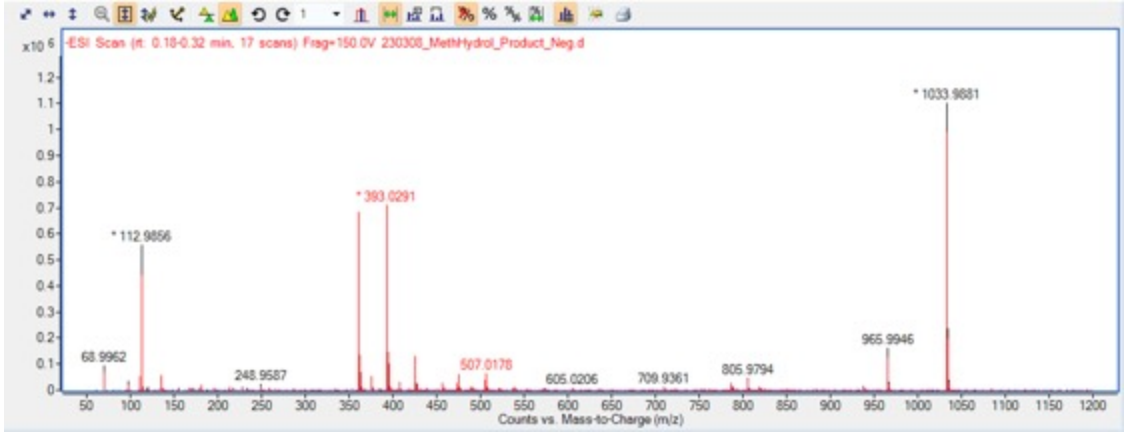
-ESI Scan (rt: 0.18-0.32 min, 17 scans) Frag=150.0V 230308_MethHydrol_Product_Neg.d
x10 6
* 1033.9681
* 393.0291
* 112.9856
68.9962
248.9587
507.0178
605.0206
709.9361
805.9794
965.9946
Counts vs. Mass-to-Charge (m/z)

Figure A11 Spectroscopy of molecule 4. (Above) HNMR spectroscopy with the correct molecule with proper integrations and splitting. (Middle) CNMR Spectroscopy showing correct C placement, although polysulfides have cause a few extra peaks due to the more upfield polysulfides (Below) Mass Spectroscopy revealing the correct mass at [M-H]= 361 and additional polysulfide mass [M+S-H]=393 and [M+2S-H]=425

Synthesis of Molecule 5 and Peptide Couple Rework

Previous peptide couple was intended to be done with N-hydroxysuccinimide and DCC to provide a proper leaving group such as an N-hydroxysuccinimidyl ester for peptide coupling. We run this reaction when making the native HSCoB, thus we used this method first. We had clear evidence that the peptide couple was not working on both ends of the molecule and would synthesize half reacted molecules in the first step, which lead to half synthesized molecules in the o-phospho-l-threonine addition. We would, therefore, see collection of molecules with combinations of carboxylic acid, N-hydroxysuccinimidyl ester, and o-phospho-l-threonine tails as shown in Figure SI 2.12.

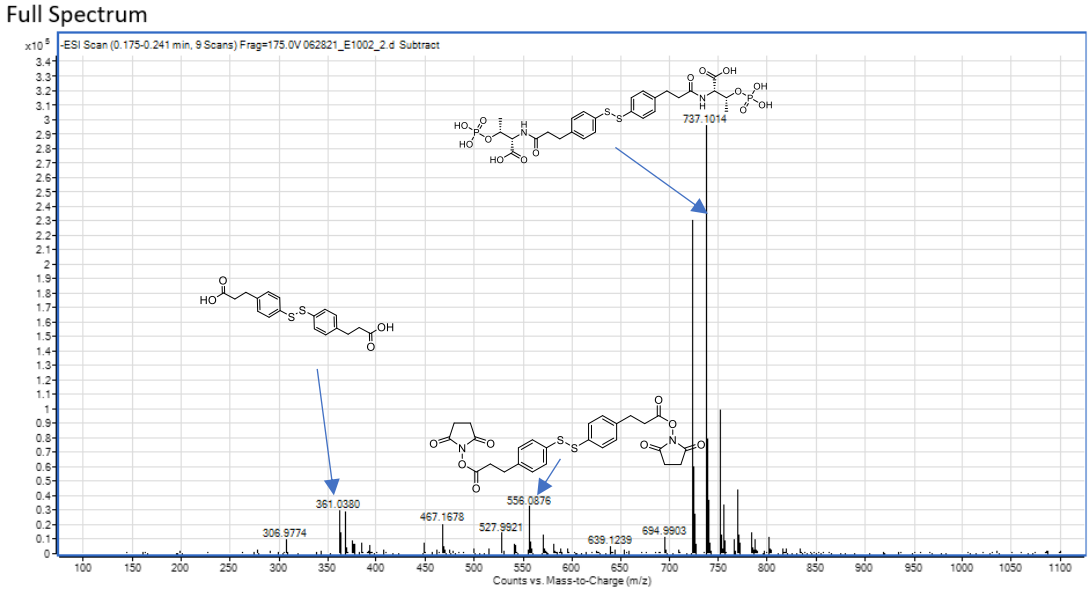

Figure A12 Mass Spectroscopy of NHS and DCC peptide coupling with o-phospho-l-threonine. After peptide coupling of the carboxylic acid to o-phospho-l-threonine to make molecule **5** several species of the molecule were present including starting material molecule **4**, the unreacted NHS intermediate, and molecule **5**.

If this mixture was carried to the final step of cleavage with TCEP followed by a reverse phase column, NMR results would have trace amounts of product detectable via MS, but the NMR would show no resemblance of the aromatic signature protons.

After several attempts of this method, it was decided that a new peptide coupling method would be attempted. Thanks to Dr. Timothy Cernak for consultations, it was decided to use a one-pot reaction with Hexafluorophosphate Azabenzotriazole Tetramethyl Uronium (HATU) and weak nucleophile DIPEA. In this reaction, DMF is used as solvent as it will dissolve both the HATU and our compound. Unfortunately, it was found that o-phospho-l-threonine was not soluble in DMF. Furthermore, the o-phospho-l-threonine also was not soluble in water. Only when all three solutions/solvents were combined did the o-phospho-l-threonine dissolve. Because of this solubility issue, o-phospho-l-threonine was dissolved separately using minimal water to solubilize the amino acid derivative. This reaction occurs within the span of two hours, and purification relies on a reverse phase PoraPak column with a water/methanol gradient. We found that the compound did bind to the Porapak and we obtained purified compound **5**. Albeit at a low 14% yield, this is still enough of a yield to obtain the product for EPR and binding studies (Figures SI 2.13).

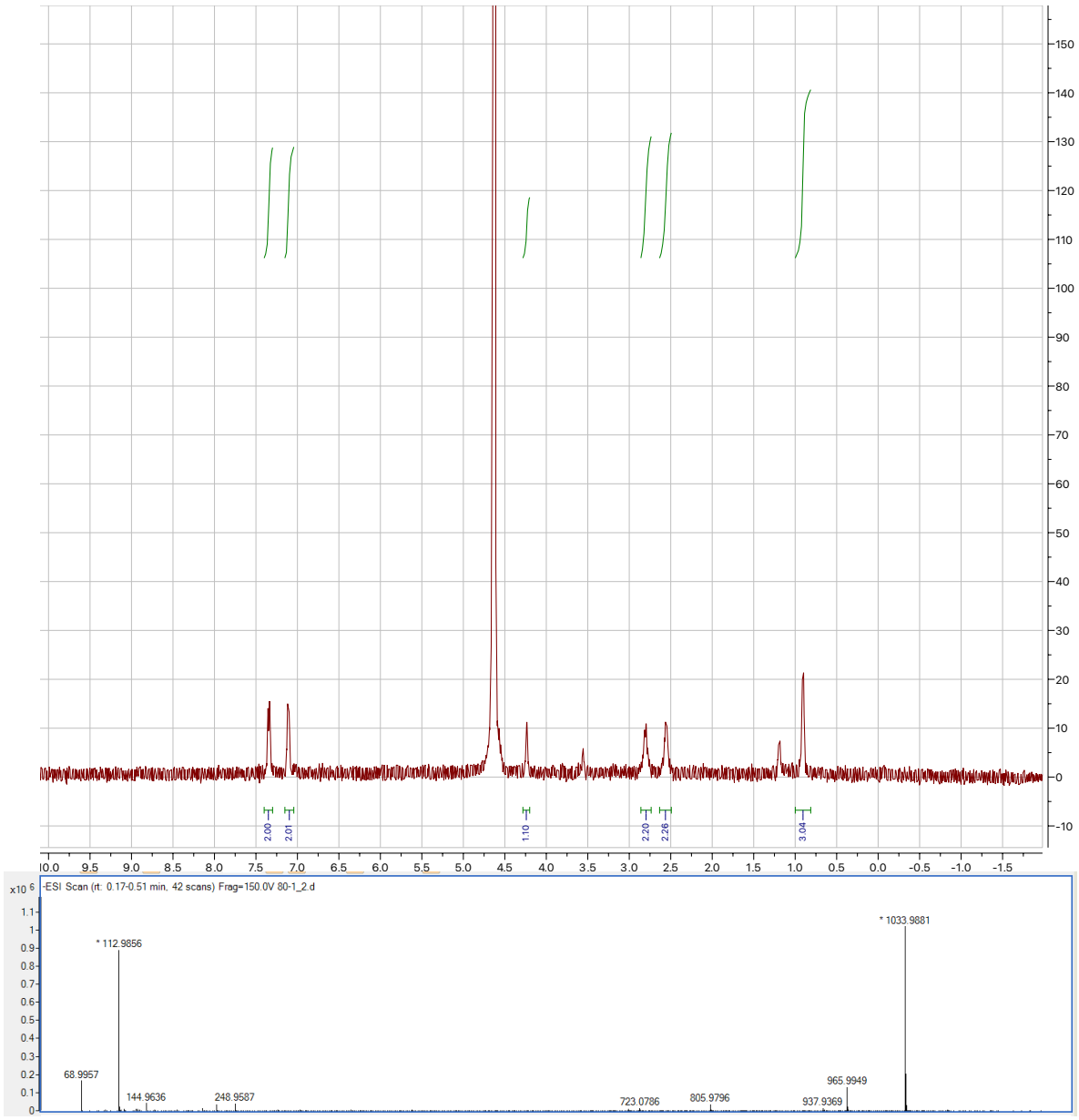

Figure A13 Spectroscopy of molecule 5. (Above) HNMR spectroscopy with the correct molecule with proper integrations and splitting. (Below) Mass Spectroscopy revealing the correct mass at [M-H]= 723. References are 112.9 and 1933.9 m/z.

Synthesis of CoBphSH

Synthesis of CoBphSH is carried out with TCEP to cleave the disulfide bond of molecule **5**. The concern with this reaction is the oxidation of the free thiols in open air. Therefore, the reaction is done and purified with a Porapak column in an anerobic chamber below <1 ppm O_2. The reaction is very fast if excess TCEP is used, therefore 3:1 molar equivalents of TCEP and

molecule **5** were reacted and monitored by High Pressure Liquid Chromatography (HPLC). After 3.5 hours, TCEP cleaved 100% of the reaction giving rise to a new compound with a retention time of 21.184min (Figure SI 2.14). Spectroscopy and MS of CoBphSH are shown in Figure SI 2.15.

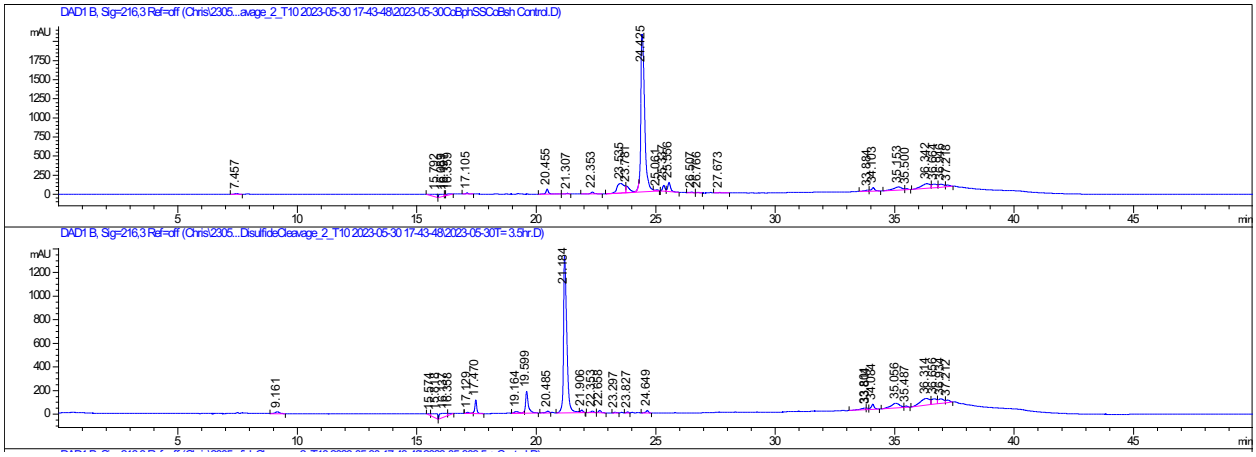

Figure A14 HPLC of synthesis of CoBphSH. HPLC traces showing complete disulfide cleavage of molecule **5** using a Phenomenex RP Fusion Column. (Top) Molecule **5** standard at a retention time of 24.425. (Bottom) Reaction progress after 3.5hrs showing a novel peak at 21.184.

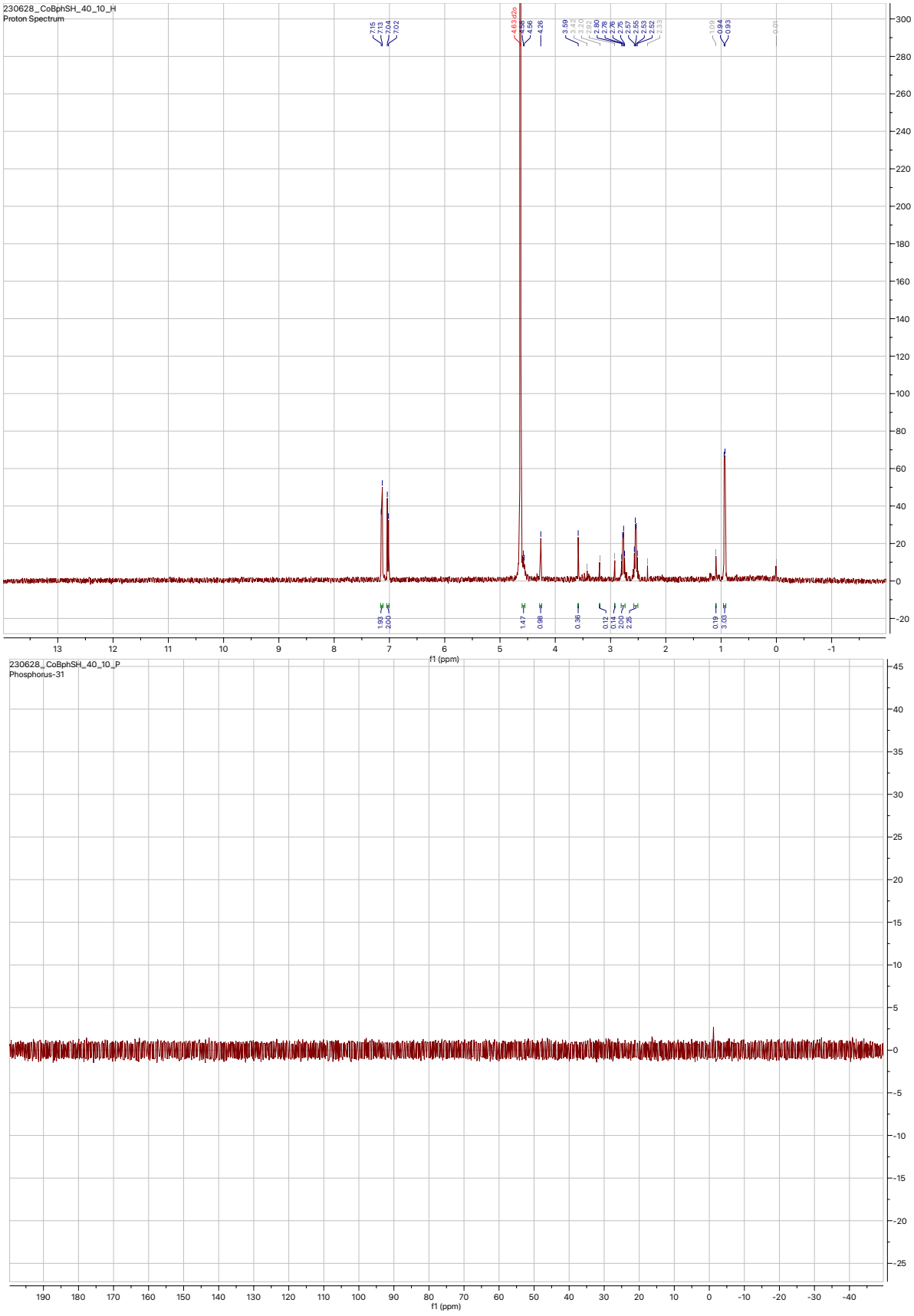
230628_CoBphSH_40_10_H
Proton Spectrum
f1 (ppm)
230628_CoBphSH_40_10_P
Phosphorus-31
f1 (ppm)

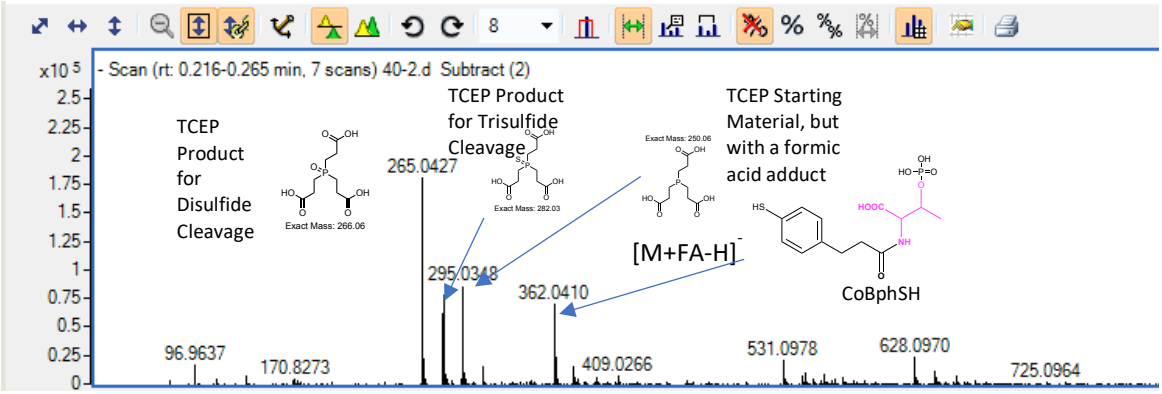

Figure A15 Spectroscopy of CoBphSH. (Above) HNMR spectroscopy with the correct molecule with proper integrations and splittings with no TCEP product contamination. (Middle) PNMR Spectroscopy showing correct P placement of the phosphate without any indication of TCEP phosphines(Below) Mass Spectroscopy revealing the correct mass at [M-H]= 362, although there is evidence of several TCEP products in MS, but both NMR either did not show evidence of these products. Therefore, we can conclude there would be only trace amounts.

Appendix B: Supplemental Materials for Chapter 3

Supporting Information From XFEL Serial Crystallography Reveals the Room Temperature Structure of Methyl-Coenzyme M Reductase

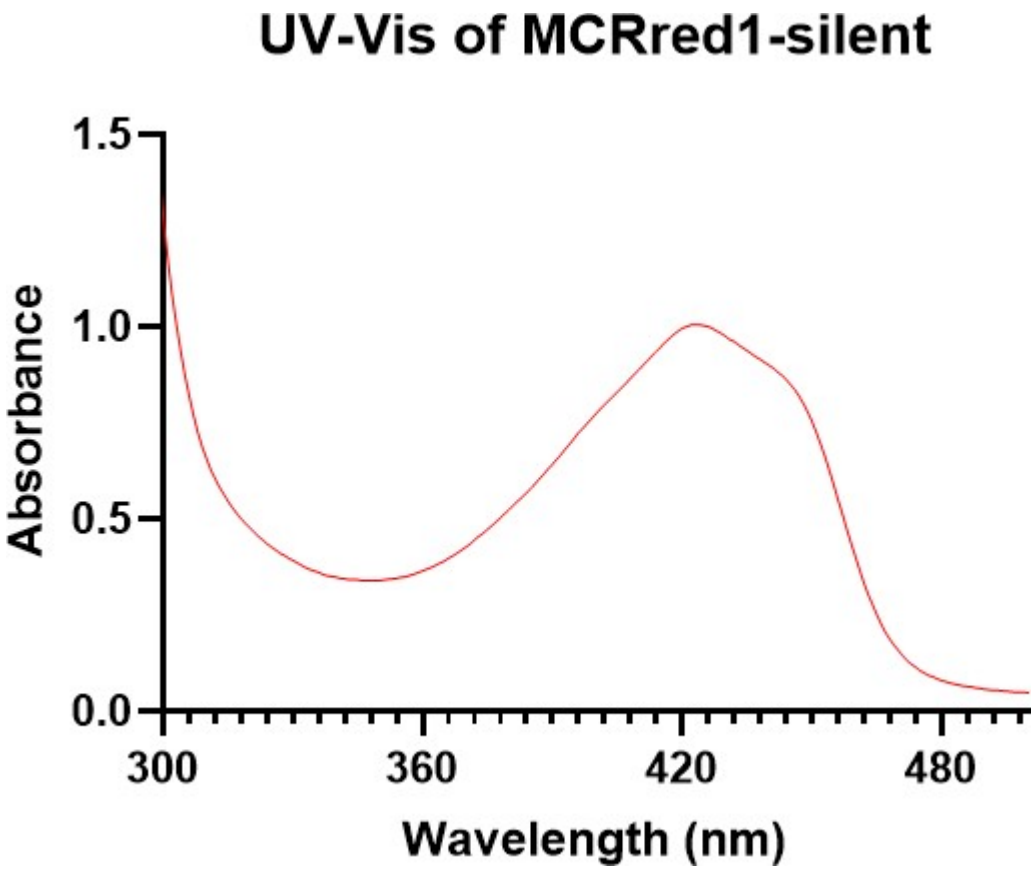

Figure B1 UV-Vis spectrum of purified MCR protein shows the Ni(II) absorption at 420nm. Spectrum was measured in 50 mM Tris pH7.6 on a Shimadzu UV-2600 UV-Vis spectrophotometer.

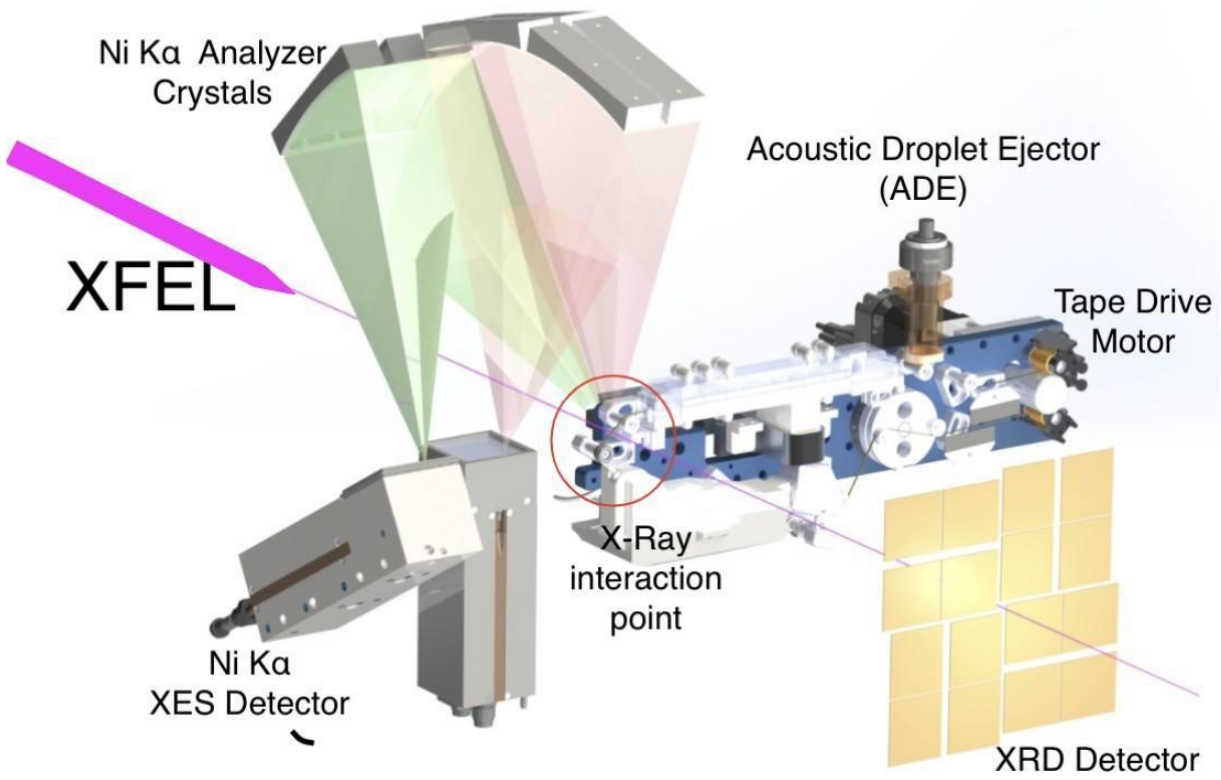

Figure B2 A cartoon depiction of our Drop On Tape (DOT) sample delivery setup with simultaneous XRD and XES data collection at MFX, LCLS (SLAC, Menlo Park, CA) enables us to collect both structural as well as metal oxidation state information in MCR in-crystallo .Shown in this picture is a two-metal (Ni and Fe) XES setup which permits measurements of both either simultaneously or only one of them without chaining the entire setup, depending on the enzyme system studied (Fe, Ni, or Fe+Ni).

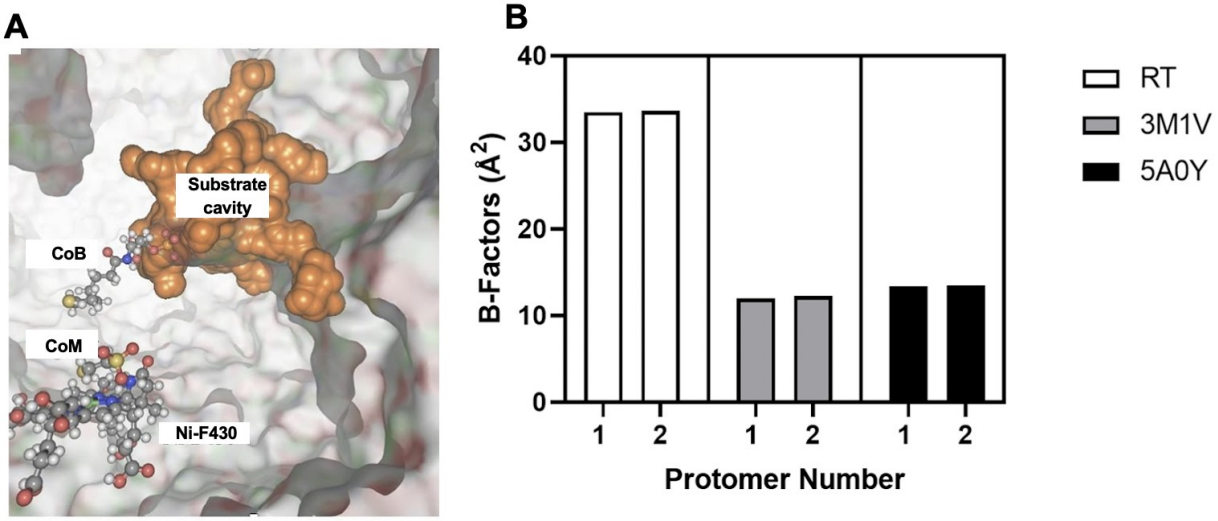

Figure B3 (A) Caver [43] cavity analysis shows the substrate channel found in all structures of MCR to date (substrate channel in our RT structure shown as orange surface) in the active

site, with the Ni-$F_{430}$and the CoB and CoM coenzymes shown in ball and stick representation. (B) B factor analysis shows similar flexibilities in both protomers of MCRred1-silent independent of data collection temperatures.

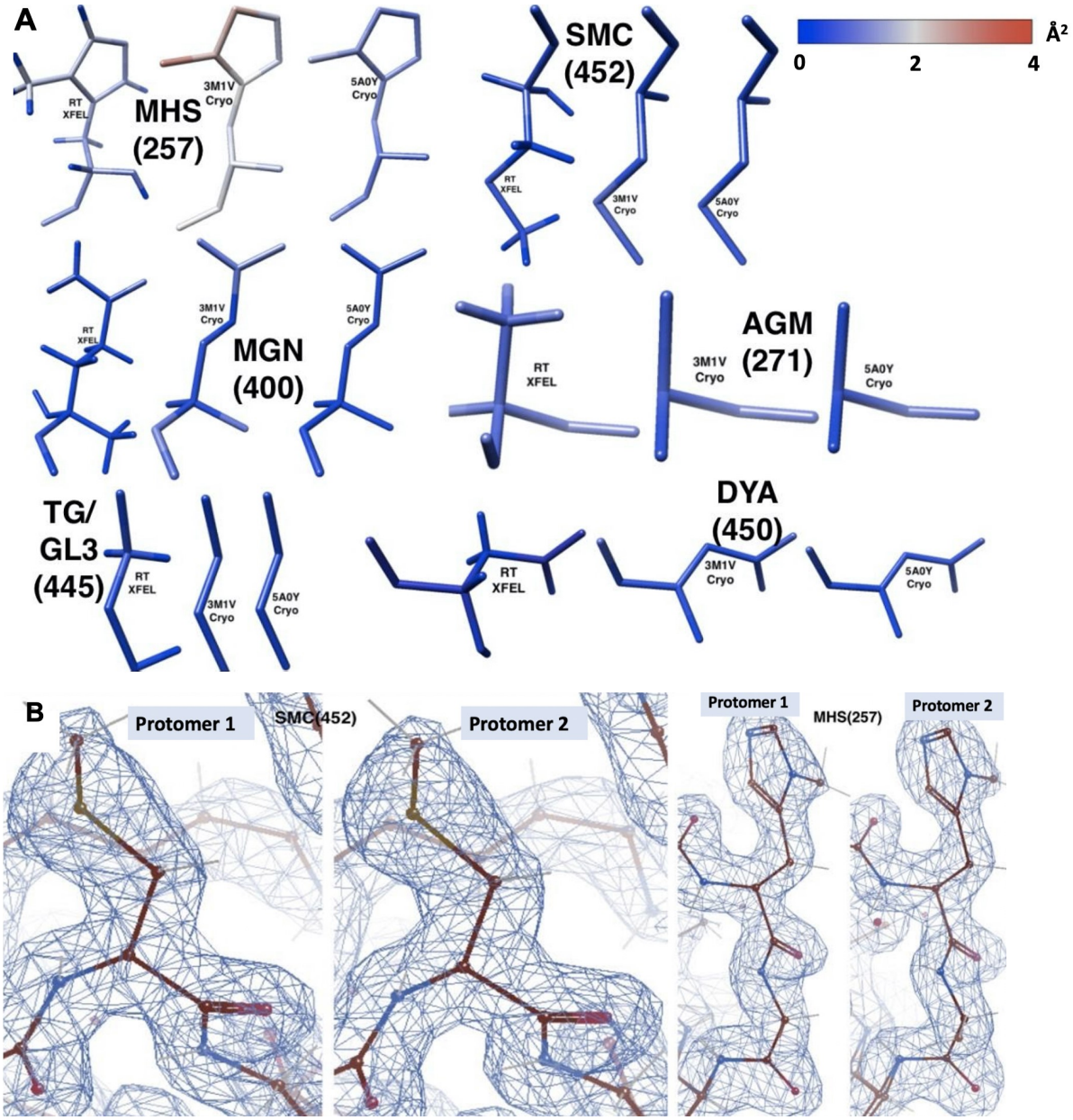
A
RT XFEL
MHS (257)
3M1V Cryo
5A0Y Cryo
SMC (452)
0
2
4
Å²
MGN (400)
AGM (271)
TG/ GL3 (445)
DYA (450)
B
Protomer 1
SMC(452)
Protomer 2
MHS(257)

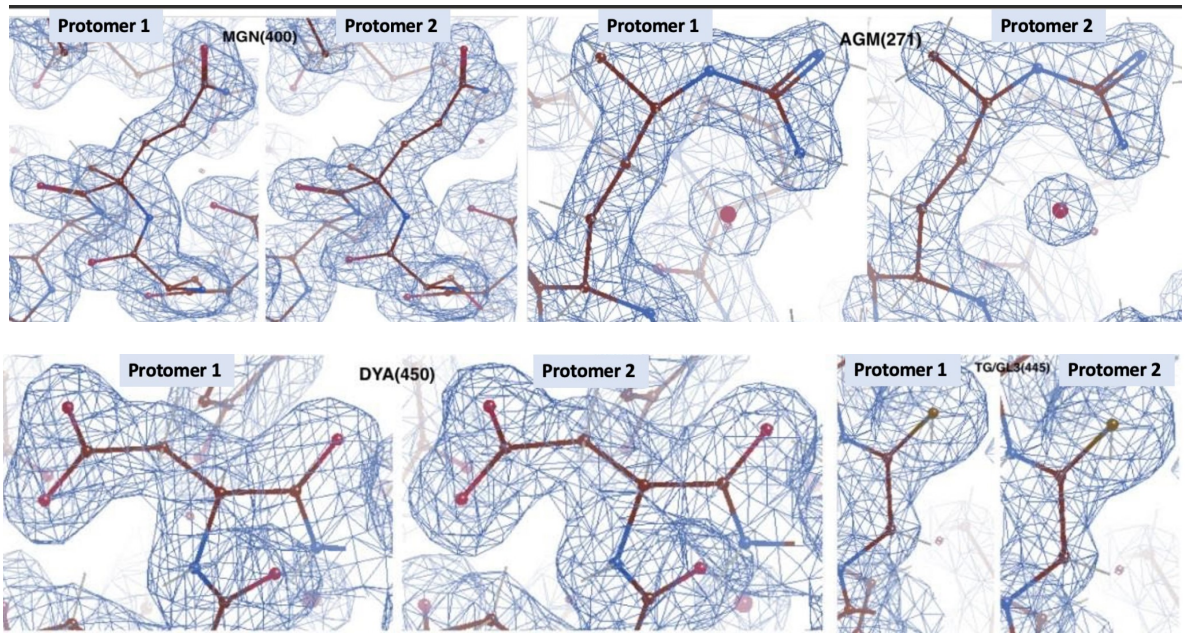

Figure B4 Densities of Modified Amino Acids (A) From Top Left Clockwise: Modified amino acids, N1-Methylated Histidine (MHS), S-MethylCysteine (SMC), 5-Methyl Arginine (AGM), Di-Dehydro Aspartic Acid (DYA), Thioglycine (TG/GL3), and 2-Methyl Glutamine (MGN), colored by B factors of the individual atoms in MCRred1-silent structures collected at room temperature at SLAC during LCLS beamtime proposal LX45, and under cryogenic temperatures (3M1V,5A0Y). The normalized b-factors were subtracted by the lowest normalized B-factor residue to give normalized B-factors greater than 0 for figure visualization in Chimera and Chimera-X. (B) 2Fo-Fc electron densities for the modified amino acids in our RT MCRred1-silent structure contoured at 1.5 sigma.

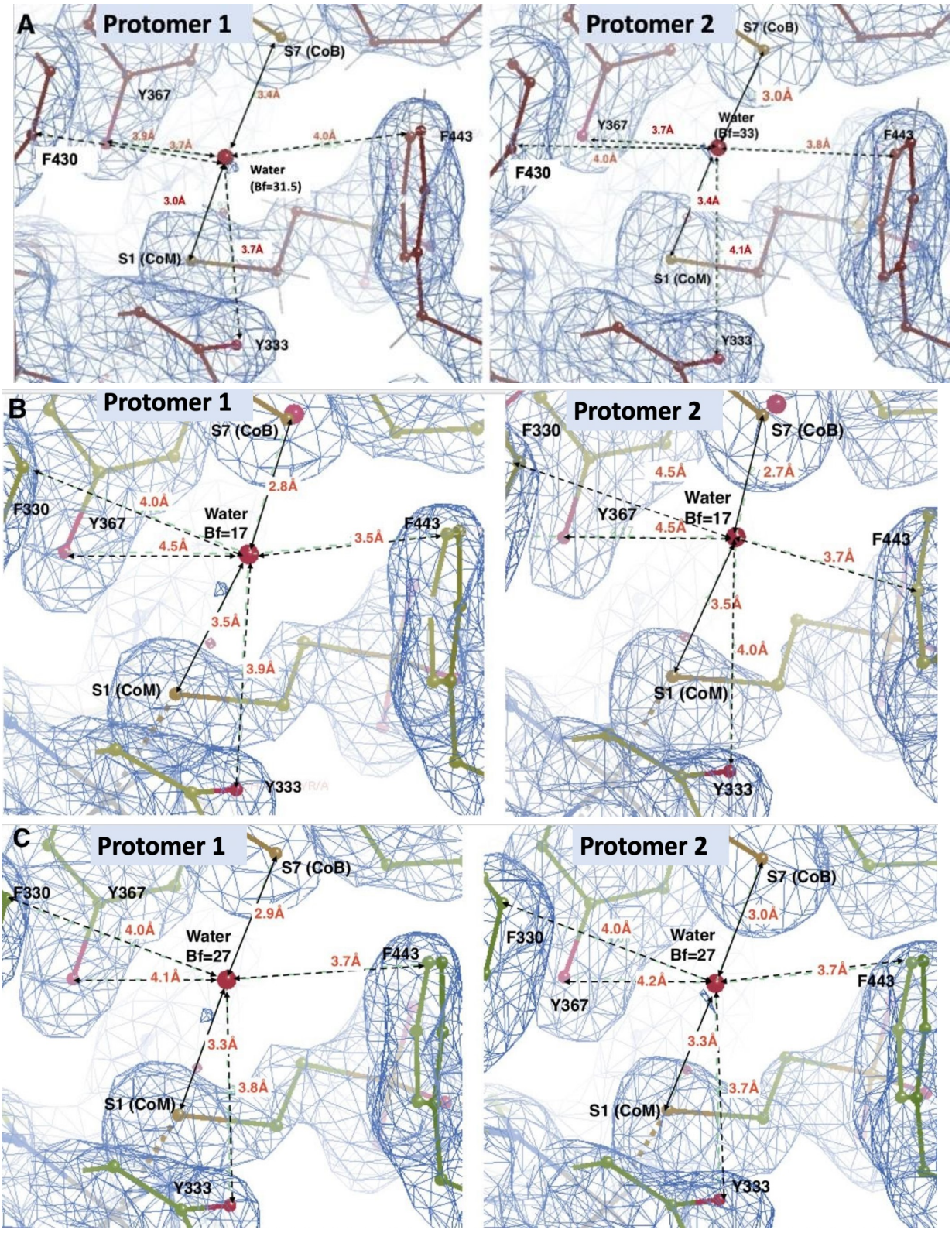

Figure B5 Densities of Active Sites 2Fo-Fc density shows up around 1.8 sigma in between MCRred1-silent substrates, CoM and CoB in protomer 1, and around 1.4 sigma for the second protomer. (Distances between water and substrates, CoM and CoB shown as a straight black

arrow, distances between nearby amino acid residues shown as dotted arrows). (A) We have modeled a water molecule in that density with 100% occupancy in both protomers (B factor of the water is ~32 Å^2) in our RT XFEL structure, indicating this is not a very "mobile" water. These waters seem to be conserved across the MCR cryogenic structures (B, 3M1V and C, 5A0Y),although there are clear differences in the coordination environment of the waters in the respective models.

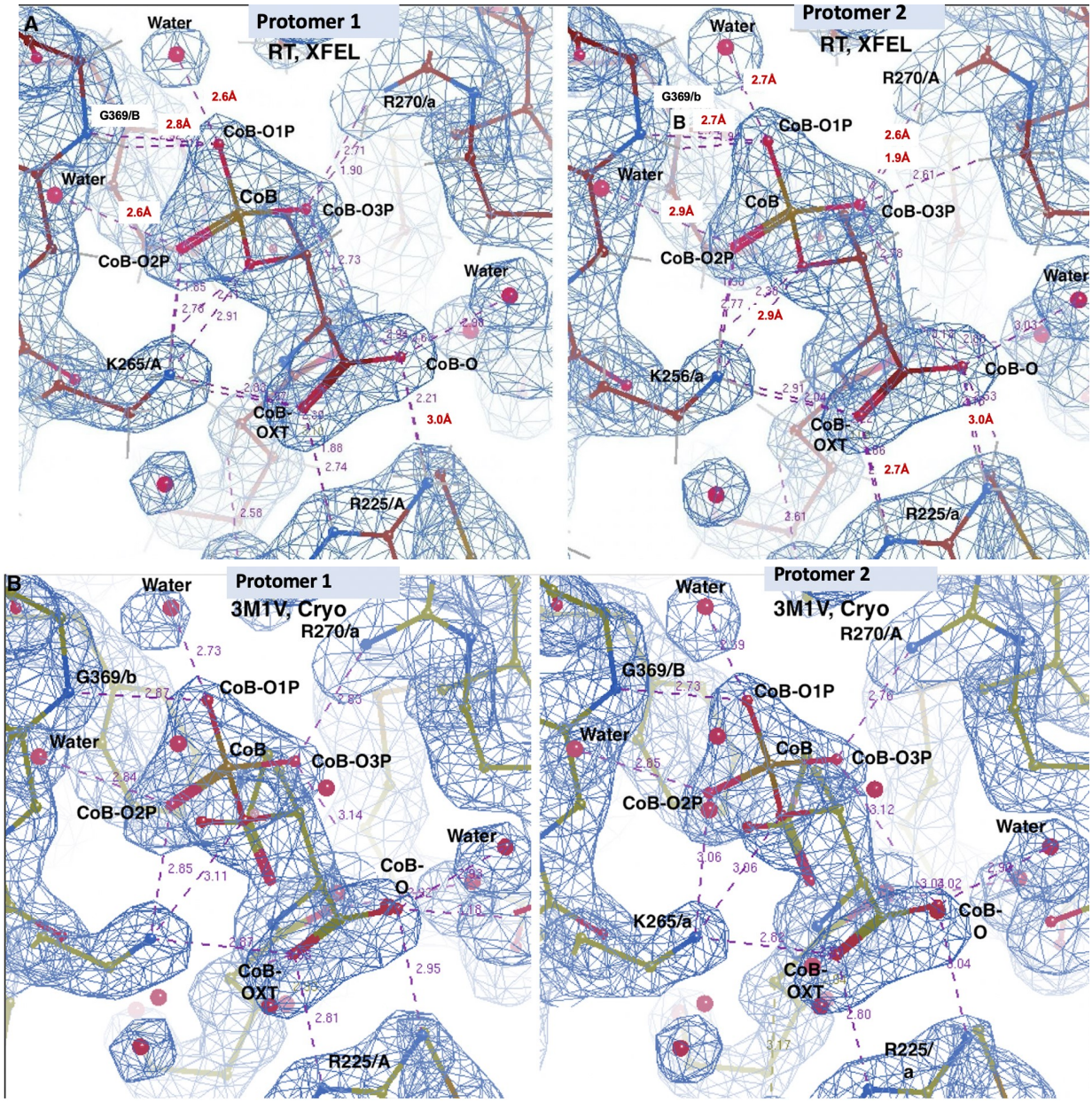

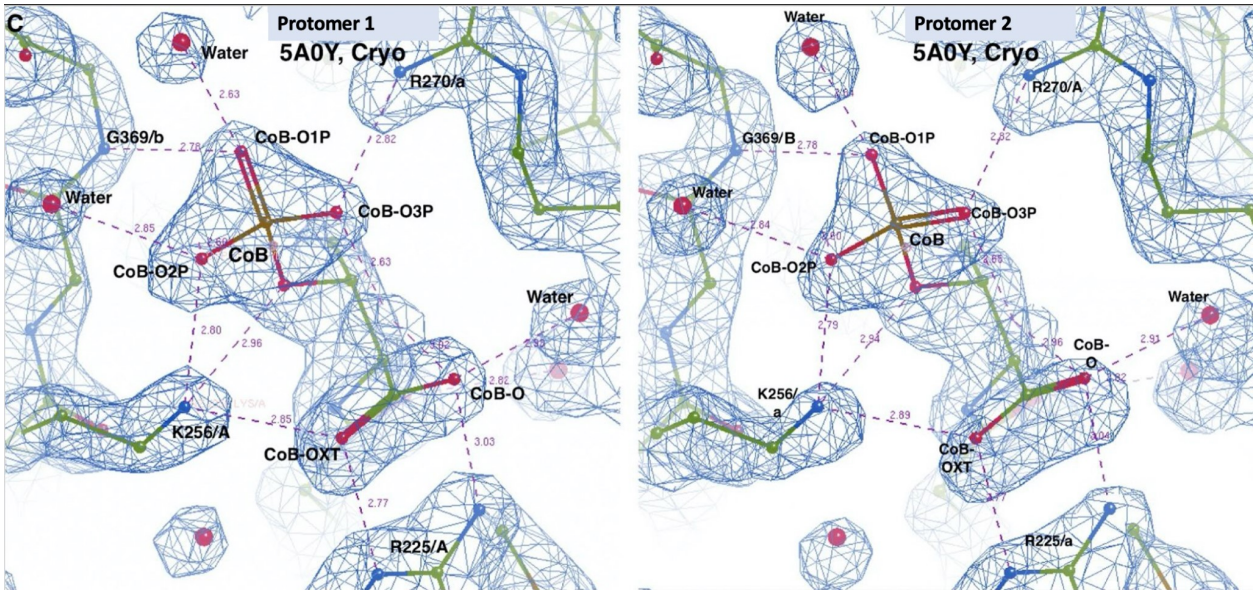

Figure B6 Coordination environment of the CoB substrate seems intact in the (A) RT as well as cryogenic (B, 3M1V and C, 5A0Y) MCRred1-silent models, further indicating the "locked" nature of the MCRred1-silent active site, following NiI to NiII oxidation. 2F0-Fc map is contoured at 1.5 sigma.

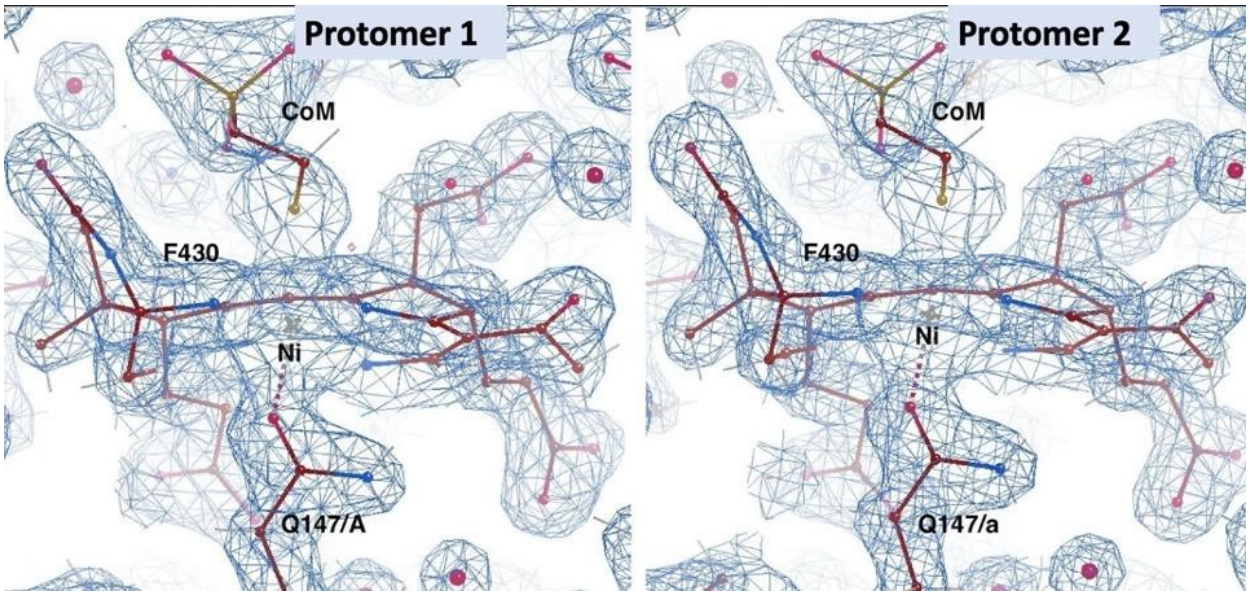

Figure B7 Coordination environment of the CoM substrate analog, along with the Ni-F430 cofactor and its coordinating partner, Gln147, shown in our MCRred1-silent models. 2Fo-Fc map is contoured at 1.5 sigma. Figure made in COOT.

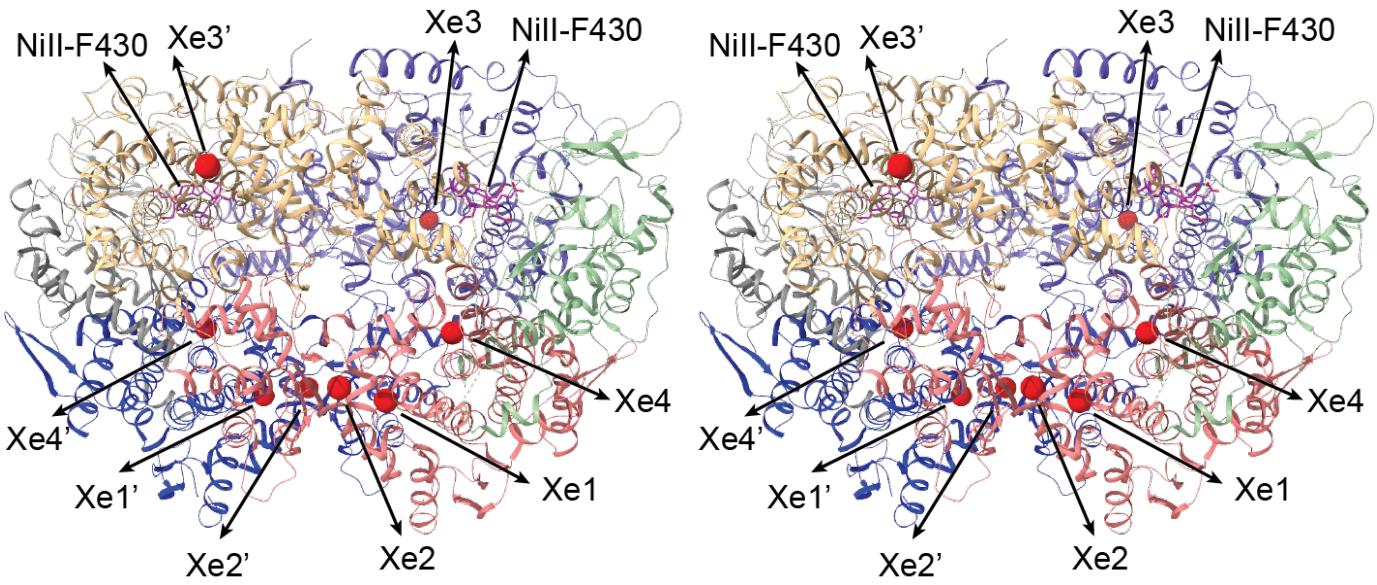

Figure B8 Structure of MCRred1-silent Xe pressurized structure shows the location of 4 xenons per trimer. Xe numbering 1,2,3,4 for Protomer 1 and 1`,2`,3` and 4` for Protomer 2. Chain coloring is the same as in Fig 2A. Figure was made with Chimera.

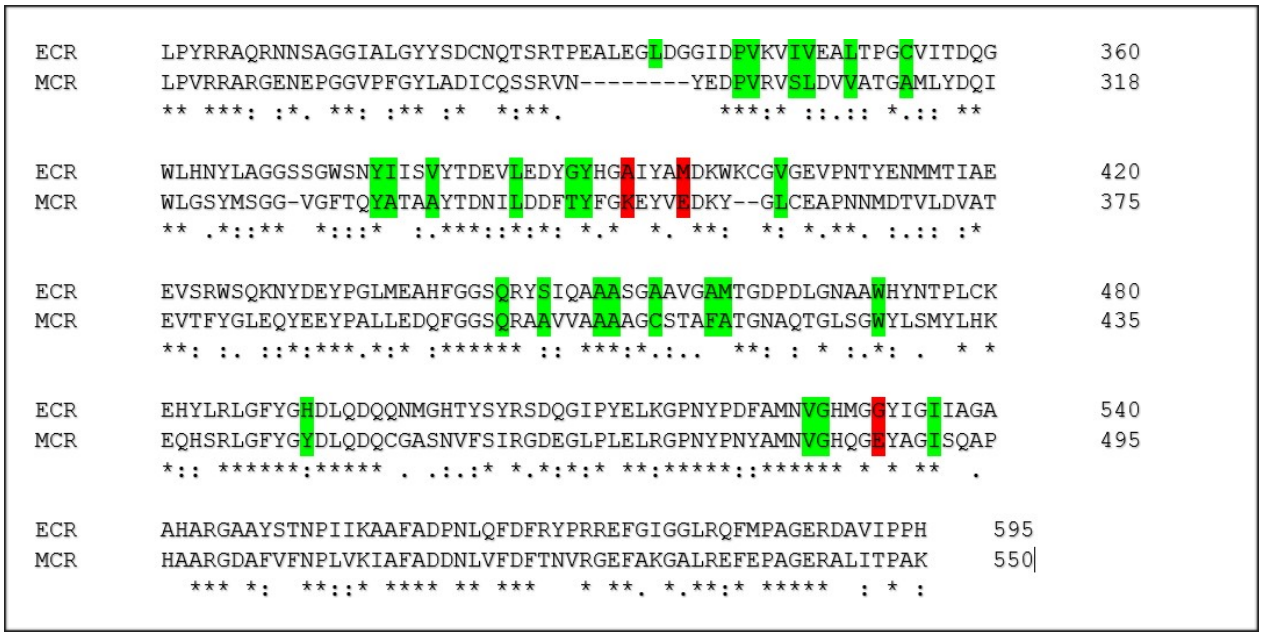

Figure B9 Pairwise sequence alignment of Ethyl Coenzyme M Reductase (ECR) (PDB: 7B1S, cryogenic) with our room temperature MCR structure to highlight the differences and similarities between key residues that form a gas tunnel in ECR. Alignments were made with the Clustal-Omega tool from EMBL. Residues in red denote changes between hydrophobic and hydrophilic of aligned structure, while green denotes residues associated with the ECR gas tunnel in Hahn *et.*

Diffraction Parameters	**data collection**	
	date collection temp	300K
	Serial	yes
	diffraction radiation	
	protocol	single wavelength
	diffraction source	
	source type	FEL
	Source details	LCLS MFX
	wavelength	1.300734
	diffraction detector	
	detector	RAYONIX MX340-HS
	detector type	CCD
Serial Measurement	sampling frequency [Hz]	30
	pulse duration [fs]	30
	photon energy [keV]	9.5
	focal spot size [um2]	16
	pulse rep rate [Hz]	30
	pulse energy [uJ]	2200
	collimation	compound refractive lenses
	collection time [h]	0.58
Data Reduction	run numbers	44-53
	total images	73742
	crystal hits	24589
	lattices indexed	22706

Collection Statistics	collection time (mins)	41
	unique reflections	189345
	completeness	99.91
	data redundancy	41.43
	res high	1.9
	CC1/2	0.979
	Rsplit	0.515
	I/s(I)	3.356
Resolution Shells	hig	1.9
	low	1.93
	unique refl	9505
	completeness	99.82%
	redundancy	9.89
	CChalf	0.379
	Rsplit	0.831
	Av I/s(I)	0.696
Softwares used and Refinement stats	data reduction	cctbx.xfel
	data scaling	cctbx.xfel.merge
	phasing	Phenix
	refinement	Phenix
	Rwork	15%
	Rfree	18%
	Ramachandran outliers	4 (0.16%)

Table B1 XFEL X-ray Diffraction Data collection at MFX, LCLS (SLAC) and Refinement statistics

	Xe-derivatived MCR-Ni(II)
Beamline	ALS 8.2.2
Space group	$P2_1$
Cell dimensions (Å)	a=82.0, b=115.7, c=123.4, β=92.5
Wavelength (Å)	1.5498
Resolution (Å)	69.6-2.50 (2.59-2.50)
# unique reflections	151627
Completeness (%)	97.1 (95.4)
Redundancy	3.0 (2.9)
<I/σI>	9.8 (2.3)
R_{sym}	0.086 (0.493)
$CC_{1/2}$	(0.731)
Resolution (Å)	69.6-2.50
# unique reflections	151575
R_{work} (%) / R_{free} (%)	17.8/21.8
RMS bond lengths (Å)	0.002
RMS bond angles (°)	0.531
Average B-factor (Å^2)	39.8
Ramachandran plot	
Favored (%)	97.14
Allowed (%)	2.86
Outliers (%)	0.00
Rotamer outliers (%)	0.30

Table B2: Xe X-ray diffraction data collection statistics and Xe refinement statistics.

aSm = sulfur (S1) atom of the CoM moiety of methyl-SCoM bSc = sulfur (S7) atom of the HSCoB moiety	**XFEL RT (Å)**	**Cryo(3M1V) (Å)**	**Cryo (5A0Y) (Å)**
Ni–OE1(Gln147/A)	2.27, 2.28	2.34, 2.31	2.31, 2.30
Ni–aSm	2.40, 2.46	2.44, 2.44	2.44, 2.44

Ni–bSc	8.76, 8.77	8.76, 8.57	8.68, 8.66
02S(CoM)-NH1(Arg120/C)	2.89, 2.83	2.92, 2.88	2.93*, 2.89
OH(Tyr367/B)-aSm	3.03, 3.04	3.11, 3.13	3.1, 3.12
O(CoB)-NE(Arg225/A)	3.79, 3.87	3.91, 3.92	3.87, 3.86
OH(Tyr333/A)-aSm	3.0, 3.14	3.08, 3.08	3.07, 3.09
O(Arg270/A)-NE2(MHS257/a)	7.34,7.16	7.26, 7.21	7.06, 6.97
aSm-bSc	6.4, 6.33	6.16, 6.34	6.26, 6.28
Water -aSm	3.05 , 3.4	3.53, 3.49	3.32, 3.28
Water -bSc	3.29, 2.99	2.64, 2.69,	2.96, 2.93

Table B3: Comparing active site distances in the RT XFEL MCRred1-silent with previously collected cryo structures (Reported here only for both protomers, separated by commas).

* Distance averaged over both conformations (A and B) of R120(C) in PDB 5A0Y.

Appendix C: Supplemental Materials for Chapter 4

State	MCRred1-Unit Cell 1	MCRred1- Unit Cell 2	MCRred1-silent
Resolution range refined (Å)	22.93 - 1.85	23.02 - 1.75	25.68 - 2.17
Resolution range upper bin (Å)	(1.916 - 1.85)	(1.813 - 1.75)	(2.248 - 2.17)
Wavelength (Å)	1.258625	1.258633	1.261531
Space group	P 1 21 1	P 1 21 1	P 1 21 1
Unit cell parameters (Å)	83.1447 117.841 124.858 90 92.5867 90	82.9573 119.798 123.044 90 91.6139 90	83.1195 119.42 123.426 90 91.8841 90
Lattices merged	16524	20050	7035
Unique reflections	204280	240895	127026
(upper bin)	(20242)	(23744)	(12644)
Completeness	99.55	99.76	99.74
(upper bin)	(96.72)	(98.69)	(99.31)
$CC_{1/2}$	97.6	97.8	89.8
(upper bin)	(33.2)	(44.7)	(27.1)
$I/\sigma_{Ha14}(I)^{\dagger}$	2.967	3.137	2.701
(upper bin)	(0.491)	(0.678)	(1.363)
Wilson B-factor	29.37	23.45	28.71
R-factor	0.1620 (0.3237)	0.1412 (0.2905)	0.1660 (0.2598)
R-free	0.2128 (0.3512)	0.1731 (0.3040)	0.2408 (0.3556)
Number non-hydrogen atoms	21359	20762	20303
Ligands	345	346	336
Waters	1064	994	591
Protein residues	2472	2472	2472
RMS (bonds)	0.012	0.010	0.012
RMS (angles)	1.24	1.09	1.14
Ramachandran favored	96.33	97.28	96.13
Ramachandran outliers	0.25	0.08	0.16
Clashscore	6.98	2.76	4.26
Average B-factor	47.28	34.96	35.03

Table C1 XFEL X-ray Diffraction Data collection at MFX, LCLS (SLAC) and Refinement statistics for Unit Cell 1, Unit Cell 2, and MCRred1-silent.

Bibliography

1. Shindell, D. T., Fuglestvedt, J. S. & Collins, W. J. The social cost of methane: theory and applications. *Faraday Discuss.* **200**, 429–451 (2017).
2. Chapter 3: Oceans and Coastal Ecosystems and their Services. https://www.ipcc.ch/report/ar6/wg2/chapter/chapter-3/.
3. Chapter 9: Africa. https://www.ipcc.ch/report/ar6/wg2/chapter/chapter-9/.
4. Chapter 7: Health, Wellbeing and the Changing Structure of Communities. https://www.ipcc.ch/report/ar6/wg2/chapter/chapter-7/.
5. Global Methane Assessment: Benefits and Costs of Mitigating Methane Emissions. *UNEP - UN Environment Programme* http://www.unep.org/resources/report/global-methane-assessment-benefits-and-costs-mitigating-methane-emissions (2021).
6. Chapter 15: Small Islands. https://www.ipcc.ch/report/ar6/wg2/chapter/chapter-15/.
7. Mills, G. *et al.* Closing the global ozone yield gap: Quantification and cobenefits for multistress tolerance. *Global Change Biology* **24**, 4869–4893 (2018).
8. Avnery, S., Mauzerall, D. L. & Fiore, A. M. Increasing global agricultural production by reducing ozone damages via methane emission controls and ozone-resistant cultivar selection. *Global Change Biology* **19**, 1285–1299 (2013).
9. Shindell, D. T. Crop yield changes induced by emissions of individual climate-altering pollutants. *Earth's Future* **4**, 373–380 (2016).

10. Höglund-Isaksson, L., Gómez-Sanabria, A., Klimont, Z., Rafaj, P. & Schöpp, W. Technical potentials and costs for reducing global anthropogenic methane emissions in the 2050 timeframe –results from the GAINS model. *Environ. Res. Commun.* **2**, 025004 (2020).
11. Kirschke, S. *et al.* Three decades of global methane sources and sinks. *Nature Geosci* **6**, 813–823 (2013).
12. Thauer, R. K., Kaster, A.-K., Seedorf, H., Buckel, W. & Hedderich, R. Methanogenic archaea: ecologically relevant differences in energy conservation. *Nat Rev Microbiol* **6**, 579–591 (2008).
13. Natural Gas Annual 2021 (NGA) - Energy Information Administration - With Data for 2021. https://www.eia.gov/naturalgas/annual/.
14. Mango, F. D. Methane concentrations in natural gas: the genetic implications. *Organic Geochemistry* **32**, 1283–1287 (2001).
15. Caballero, A. & Pérez, P. J. Methane as raw material in synthetic chemistry: the final frontier. *Chem. Soc. Rev.* **42**, 8809–8820 (2013).
16. Qyyum, M. A., Chaniago, Y. D., Ali, W., Qadeer, K. & Lee, M. Coal to clean energy: Energy-efficient single-loop mixed-refrigerant-based schemes for the liquefaction of synthetic natural gas. *Journal of Cleaner Production* **211**, 574–589 (2019).
17. Kurr, M. *et al.* Methanopyrus kandleri, gen. and sp. nov. represents a novel group of hyperthermophilic methanogens, growing at 110°C. *Arch. Microbiol.* **156**, 239–247 (1991).
18. Balch, W. E., Fox, G. E., Magrum, L. J., Woese, C. R. & Wolfe, R. S. Methanogens: reevaluation of a unique biological group. *Microbiol Rev* **43**, 260–296 (1979).
19. Stadtman, T. C. & Barker, H. A. Studies on the methane fermentation. X. A new formate-decomposing bacterium, Methanococcus vannielii. *J Bacteriol* **62**, 269–280 (1951).

20. O'Connor, F. M. *et al.* Possible role of wetlands, permafrost, and methane hydrates in the methane cycle under future climate change: A review. *Reviews of Geophysics* **48**, (2010).
21. Tassi, F., Fiebig, J., Vaselli, O. & Nocentini, M. Origins of methane discharging from volcanic-hydrothermal, geothermal and cold emissions in Italy. *Chemical Geology* **310–311**, 36–48 (2012).
22. Großkopf, R., Janssen, P. H. & Liesack, W. Diversity and Structure of the Methanogenic Community in Anoxic Rice Paddy Soil Microcosms as Examined by Cultivation and Direct 16S rRNA Gene Sequence Retrieval. *Applied and Environmental Microbiology* **64**, 960–969 (1998).
23. Mathrani, I. M., Boone, D. R., Mah, R. A., Fox, G. E. & Lau, P. P. Methanohalophilus zhilinae sp. nov., an alkaliphilic, halophilic, methylotrophic methanogen. *Int J Syst Bacteriol* **38**, 139–142 (1988).
24. Zhang, G., Jiang, N., Liu, X. & Dong, X. Methanogenesis from Methanol at Low Temperatures by a Novel Psychrophilic Methanogen, "Methanolobus psychrophilus" sp. nov., Prevalent in Zoige Wetland of the Tibetan Plateau. *Applied and Environmental Microbiology* **74**, 6114–6120 (2008).
25. Prem, E. M., Stres, B., Illmer, P. & Wagner, A. O. Microbial community dynamics in mesophilic and thermophilic batch reactors under methanogenic, phenyl acid-forming conditions. *Biotechnology for Biofuels* **13**, 81 (2020).
26. Enzmann, F., Mayer, F., Rother, M. & Holtmann, D. Methanogens: biochemical background and biotechnological applications. *AMB Express* **8**, 1 (2018).
27. Rother, M., Boccazzi, P., Bose, A., Pritchett, M. A. & Metcalf, W. W. Methanol-Dependent Gene Expression Demonstrates that Methyl-Coenzyme M Reductase Is Essential in

Methanosarcina acetivorans C2A and Allows Isolation of Mutants with Defects in Regulation of the Methanol Utilization Pathway. *J Bacteriol* **187**, 5552–5559 (2005).

28. Murakami, E. & Ragsdale, S. W. Evidence for Intersubunit Communication during Acetyl-CoA Cleavage by the Multienzyme CO Dehydrogenase/Acetyl-CoA Synthase Complex from Methanosarcina thermophila: EVIDENCE THAT THE β SUBUNIT CATALYZES C–C AND C–S BOND CLEAVAGE*. *Journal of Biological Chemistry* **275**, 4699–4707 (2000).
29. Prakash, D. *et al.* Structure and function of an unusual flavodoxin from the domain Archaea. *Proceedings of the National Academy of Sciences* **116**, 25917–25922 (2019).
30. Reeburgh, W. S. Oceanic Methane Biogeochemistry. *Chem. Rev.* **107**, 486–513 (2007).
31. Timmers, P. H. A. *et al.* Reverse Methanogenesis and Respiration in Methanotrophic Archaea. *Archaea* **2017**, e1654237 (2017).
32. McGlynn, S. E. Energy Metabolism during Anaerobic Methane Oxidation in ANME Archaea. *Microbes Environ* **32**, 5–13 (2017).
33. Yu, L. *et al.* Electricity from anaerobic methane oxidation by a single methanogenic archaeon Methanosarcina barkeri. *Chemical Engineering Journal* **405**, 126691 (2021).
34. Scheller, S., Goenrich, M., Boecher, R., Thauer, R. K. & Jaun, B. The key nickel enzyme of methanogenesis catalyses the anaerobic oxidation of methane. *Nature* **465**, 606–608 (2010).
35. Hinrichs, K.-U. & Boetius, A. The Anaerobic Oxidation of Methane: New Insights in Microbial Ecology and Biogeochemistry. in *Ocean Margin Systems* (eds. Wefer, G. et al.) 457–477 (Springer, 2003). doi:10.1007/978-3-662-05127-6_28.
36. Wang, Y., Wegener, G., Ruff, S. E. & Wang, F. Methyl/alkyl-coenzyme M reductase-based anaerobic alkane oxidation in archaea. *Environmental Microbiology* **23**, 530–541 (2021).

37. Laso-Pérez, R. *et al.* Thermophilic archaea activate butane via alkyl-coenzyme M formation. *Nature* **539**, 396–401 (2016).

38. Zehnle, H. *et al.* Candidatus Alkanophaga archaea from Guaymas Basin hydrothermal vent sediment oxidize petroleum alkanes. *Nat Microbiol* 1–14 (2023) doi:10.1038/s41564-023-01400-3.

39. Zhou, Z. *et al.* Non-syntrophic methanogenic hydrocarbon degradation by an archaeal species. *Nature* **601**, 257–262 (2022).

40. Vanwonterghem, I. *et al.* Methylotrophic methanogenesis discovered in the archaeal phylum Verstraetearchaeota. *Nat Microbiol* **1**, 1–9 (2016).

41. Wang, C. *et al.* Tolerance of Aceticlastic Methanogenesis Enhanced by Magnetite under the Condition of Ammonia Stress. *ACS Sustainable Chem. Eng.* **8**, 1417–1426 (2020).

42. Wolfe, R. S. Microbial Formation of Methane. in *Advances in Microbial Physiology* (eds. Rose, A. H. & Wilkinson, J. F.) vol. 6 107–146 (Academic Press, 1971).

43. Gunsalus, R. P. & Wolfe, R. S. Chromophoric factors F342 and F430 of Methanobacterium thermoautotrophicum. *FEMS Microbiology Letters* **3**, 191–193 (1978).

44. Whitman, W. B. & Wolfe, R. S. Presence of nickel in Factor F430 from Methanobacteriumbryantii. *Biochemical and Biophysical Research Communications* **92**, 1196–1201 (1980).

45. Duin, E. C. *et al.* Spectroscopic investigation of the nickel-containing porphinoid cofactor F430. Comparison of the free cofactor in the +1, +2 and +3 oxidation states with the cofactor bound to methyl-coenzyme M reductase in the silent, red and ox forms. *J Biol Inorg Chem* **9**, 563–576 (2004).

46. Holliger, C., Pierik, A. J., Reijerse, E. J. & Hagen, W. R. A spectroelectrochemical study of factor F430 nickel(II/I) from methanogenic bacteria in aqueous solution. *ACS Publications* https://pubs.acs.org/doi/pdf/10.1021/ja00066a034 (2002) doi:10.1021/ja00066a034.

47. Prakash, D., Wu, Y., Suh, S.-J. & Duin, E. C. Elucidating the Process of Activation of Methyl-Coenzyme M Reductase. *Journal of Bacteriology* **196**, 2491–2498 (2014).

48. Zheng, K., Ngo, P. D., Owens, V. L., Yang, X.-P. & Mansoorabadi, S. O. The biosynthetic pathway of coenzyme F430 in methanogenic and methanotrophic archaea. *Science* **354**, 339–342 (2016).

49. Chadwick, G. L., Joiner, A. M. N., Ramesh, S., Mitchell, D. A. & Nayak, D. D. McrD binds asymmetrically to methyl-coenzyme M reductase improving active-site accessibility during assembly. *Proc Natl Acad Sci U S A* **120**, e2302815120 (2023).

50. Rospert, S., Linder, D., Ellermann, J. & Thauer, R. K. Two genetically distinct methyl-coenzyme M reductases in Methanobacterium thermoautotrophicum strain Marburg and delta H. *Eur J Biochem* **194**, 871–877 (1990).

51. Wagner, T., Wegner, C.-E., Kahnt, J., Ermler, U. & Shima, S. Phylogenetic and Structural Comparisons of the Three Types of Methyl Coenzyme M Reductase from Methanococcales and Methanobacteriales. *Journal of Bacteriology* **199**, 10.1128/jb.00197-17 (2017).

52. Gendron, A. & Allen, K. D. Overview of Diverse Methyl/Alkyl-Coenzyme M Reductases and Considerations for Their Potential Heterologous Expression. *Frontiers in Microbiology* **13**, (2022).

53. Metcalf, W. W., Zhang, J. K., Apolinario, E., Sowers, K. R. & Wolfe, R. S. A genetic system for Archaea of the genus Methanosarcina: liposome-mediated transformation and construction of shuttle vectors. *Proc Natl Acad Sci U S A* **94**, 2626–2631 (1997).

54. Buan, N., Kulkarni, G. & Metcalf, W. Genetic methods for methanosarcina species. *Methods Enzymol* **494**, 23–42 (2011).

55. Nayak, D. D. & Metcalf, W. W. Cas9-mediated genome editing in the methanogenic archaeon Methanosarcina acetivorans. *Proceedings of the National Academy of Sciences* **114**, 2976–2981 (2017).

56. Ermler, U., Grabarse, W., Shima, S., Goubeaud, M. & Thauer, R. K. Crystal structure of methyl-coenzyme M reductase: the key enzyme of biological methane formation. *Science* **278**, 1457–1462 (1997).

57. Wagner, T., Kahnt, J., Ermler, U. & Shima, S. Didehydroaspartate Modification in Methyl-Coenzyme M Reductase Catalyzing Methane Formation. *Angew Chem Int Ed Engl* **55**, 10630–10633 (2016).

58. Selmer, T. *et al.* The biosynthesis of methylated amino acids in the active site region of methyl-coenzyme M reductase. *J Biol Chem* **275**, 3755–3760 (2000).

59. Lyu, Z. *et al.* Assembly of Methyl Coenzyme M Reductase in the Methanogenic Archaeon Methanococcus maripaludis. *J Bacteriol* **200**, e00746-17 (2018).

60. Radle, M. I., Miller, D. V., Laremore, T. N. & Booker, S. J. Methanogenesis marker protein 10 (Mmp10) from Methanosarcina acetivorans is a radical S-adenosylmethionine methylase that unexpectedly requires cobalamin. *J Biol Chem* **294**, 11712–11725 (2019).

61. Deobald, D., Adrian, L., Schöne, C., Rother, M. & Layer, G. Identification of a unique Radical SAM methyltransferase required for the sp3-C-methylation of an arginine residue of methyl-coenzyme M reductase. *Sci Rep* **8**, 7404 (2018).

62. Nayak, D. D., Mahanta, N., Mitchell, D. A. & Metcalf, W. W. Post-translational thioamidation of methyl-coenzyme M reductase, a key enzyme in methanogenic and methanotrophic Archaea. *eLife* **6**, e29218 (2017).

63. Nayak, D. D. *et al.* Functional interactions between posttranslationally modified amino acids of methyl-coenzyme M reductase in Methanosarcina acetivorans. *PLOS Biology* **18**, e3000507 (2020).

64. Shima, S. *et al.* Structure of a methyl-coenzyme M reductase from Black Sea mats that oxidize methane anaerobically. *Nature* **481**, 98–101 (2012).

65. Wongnate, T. & Ragsdale, S. W. The Reaction Mechanism of Methyl-Coenzyme M Reductase: HOW AN ENZYME ENFORCES STRICT BINDING ORDER *. *Journal of Biological Chemistry* **290**, 9322–9334 (2015).

66. Sarangi, R., Dey, M. & Ragsdale, S. W. Geometric and Electronic Structures of the NiI and Methyl−NiIII Intermediates of Methyl-Coenzyme M Reductase. *Biochemistry* **48**, 3146–3156 (2009).

67. Thauer, R. K. Methyl (Alkyl)-Coenzyme M Reductases: Nickel F-430-Containing Enzymes Involved in Anaerobic Methane Formation and in Anaerobic Oxidation of Methane or of Short Chain Alkanes. *Biochemistry* **58**, 5198–5220 (2019).

68. Hahn, C. J. *et al.* "Candidatus Ethanoperedens," a Thermophilic Genus of Archaea Mediating the Anaerobic Oxidation of Ethane. *mBio* **11**, 10.1128/mbio.00600-20 (2020).

69. Hahn, C. J. *et al.* Crystal structure of a key enzyme for anaerobic ethane activation. *Science* **373**, 118–121 (2021).

70. Cedervall, P. E., Dey, M., Pearson, A. R., Ragsdale, S. W. & Wilmot, C. M. Structural insight into methyl-coenzyme M reductase chemistry using coenzyme B analogues. *Biochemistry* **49**, 7683–7693 (2010).

71. Diekert, G., Weber, B. & Thauer, R. K. Nickel dependence of factor F430 content in Methanobacterium thermoautotrophicum. *Arch. Microbiol.* **127**, 273–277 (1980).

72. Jaun, B. & Pfaltz, A. Coenzyme F430 from methanogenic bacteria: reversible one-electron reduction of F430 pentamethyl ester to the nickel(I) form. *J. Chem. Soc., Chem. Commun.* 1327–1329 (1986) doi:10.1039/C39860001327.

73. Zhou, Y., Dorchak, A. E. & Ragsdale, S. W. In vivo activation of methyl-coenzyme M reductase by carbon monoxide. *Front Microbiol* **4**, 69 (2013).

74. Rospert, S., Böcher, R., Albracht, S. p. j. & Thauer, R. k. Methyl-coenzyme M reductase preparations with high specific activity from H2-preincubated cells of Methanobacterium thermoautotrophicum. *FEBS Letters* **291**, 371–375 (1991).

75. Goubeaud, M., Schreiner, G. & Thauer, R. K. Purified methyl-coenzyme-M reductase is activated when the enzyme-bound coenzyme F430 is reduced to the nickel(I) oxidation state by titanium(III) citrate. *Eur J Biochem* **243**, 110–114 (1997).

76. Telser, J., Davydov, R., Horng, Y.-C., Ragsdale, S. W. & Hoffman, B. M. Cryoreduction of Methyl-Coenzyme M Reductase: EPR Characterization of Forms, MCRox1 and MCRred1. *J. Am. Chem. Soc.* **123**, 5853–5860 (2001).

77. Telser, J., Horng, Y.-C., Becker, D. F., Hoffman, B. M. & Ragsdale, S. W. On the Assignment of Nickel Oxidation States of the Ox1, Ox2 Forms of Methyl−Coenzyme M Reductase. *J. Am. Chem. Soc.* **122**, 182–183 (2000).

78. Mahlert, F., Grabarse, W., Kahnt, J., Thauer, R. K. & Duin, E. C. The nickel enzyme methyl-coenzyme M reductase from methanogenic archaea: in vitro interconversions among the EPR detectable MCR-red1 and MCR-red2 states. *J Biol Inorg Chem* **7**, 101–112 (2002).
79. Craft, J. L., Horng, Y.-C., Ragsdale, S. W. & Brunold, T. C. Nickel Oxidation States of F430 Cofactor in Methyl-Coenzyme M Reductase. *J. Am. Chem. Soc.* **126**, 4068–4069 (2004).
80. Jaun, B. Coenzyme F430 from Methanogenic Bacteria: Oxidation of F430 Pentamethyl Ester to the Ni(III) Form. *Helvetica Chimica Acta* **73**, 2209–2217 (1990).
81. Patwardhan, A., Sarangi, R., Ginovska, B., Raugei, S. & Ragsdale, S. W. Nickel-Sulfonate Mode of Substrate Binding for Forward and Reverse Reactions of Methyl-SCoM Reductase Suggest a Radical Mechanism Involving Long-Range Electron Transfer. *J Am Chem Soc* **143**, 5481–5496 (2021).
82. Finazzo, C. *et al.* Characterization of the MCRred2 form of methyl-coenzyme M reductase: a pulse EPR and ENDOR study. *J Biol Inorg Chem* **8**, 586–593 (2003).
83. Becker, D. F. & Ragsdale, S. W. Activation of Methyl-SCoM Reductase to High Specific Activity after Treatment of Whole Cells with Sodium Sulfide. *Biochemistry* **37**, 2639–2647 (1998).
84. Pearson, R. G. Basicity and Nucleophilicity of Transition Metal Complexes. in *Nucleophilicity* vol. 215 233–244 (American Chemical Society, 1987).
85. Ahn, Y., Krzycki, J. A. & Floss, H. G. Steric course of the reduction of ethyl coenzyme M to ethane catalyzed by methyl coenzyme M reductase from Methanosarcina barkeri. *ACS Publications* https://pubs.acs.org/doi/pdf/10.1021/ja00012a059 (2002) doi:10.1021/ja00012a059.

86. Kunz, R. C., Dey, M. & Ragsdale, S. W. Characterization of the Thioether Product Formed from the Thiolytic Cleavage of the Alkyl−Nickel Bond in Methyl-Coenzyme M Reductase. *Biochemistry* **47**, 2661–2667 (2008).

87. Pelmenschikov, V. & Siegbahn, P. E. M. Catalysis by methyl-coenzyme M reductase: a theoretical study for heterodisulfide product formation. *J Biol Inorg Chem* **8**, 653–662 (2003).

88. Chen, S.-L., Blomberg, M. R. A. & Siegbahn, P. E. M. How Is Methane Formed and Oxidized Reversibly When Catalyzed by Ni-Containing Methyl-Coenzyme M Reductase? *Chemistry – A European Journal* **18**, 6309–6315 (2012).

89. Wongnate, T. *et al.* The radical mechanism of biological methane synthesis by methyl-coenzyme M reductase. *Science* **352**, 953–958 (2016).

90. Bonacker, L. G., Baudner, S., Mörschel, E., Böcher, R. & Thauer, R. K. Properties of the two isoenzymes of methyl-coenzyme M reductase in Methanobacterium thermoautotrophicum. *Eur J Biochem* **217**, 587–595 (1993).

91. Scheller, S., Goenrich, M., Thauer, R. K. & Jaun, B. Methyl-Coenzyme M Reductase from Methanogenic Archaea: Isotope Effects on Label Exchange and Ethane Formation with the Homologous Substrate Ethyl-Coenzyme M. *J. Am. Chem. Soc.* **135**, 14985–14995 (2013).

92. Zhu, Q., Costentin, C., Stubbe, J. & Nocera, D. G. Disulfide radical anion as a super-reductant in biology and photoredox chemistry. *Chem. Sci.* **14**, 6876–6881 (2023).

93. Doerr, A. Diffraction before destruction. *Nat Methods* **8**, 283–283 (2011).

94. Liu, K. E., Johnson, C. C., Newcomb, M. & Lippard, S. J. Radical clock substrate probes and kinetic isotope effect studies of the hydroxylation of hydrocarbons by methane monooxygenase. *J. Am. Chem. Soc.* **115**, 939–947 (1993).

95. Yvon-Durocher, G. *et al.* Methane fluxes show consistent temperature dependence across microbial to ecosystem scales. *Nature* **507**, 488–491 (2014).

96. Thauer, R. K. Biochemistry of methanogenesis: a tribute to Marjory Stephenson. 1998 Marjory Stephenson Prize Lecture. *Microbiology (Reading)* **144 (Pt 9)**, 2377–2406 (1998).

97. Badr, O., Probert, S. D. & O'Callaghan, P. W. Sinks for atmospheric methane. *Applied Energy* **41**, 137–147 (1992).

98. Kirschke, S. *et al.* Three decades of global methane sources and sinks. *Nature Geosci* **6**, 813–823 (2013).

99. Lashof, D. A. & Ahuja, D. R. Relative contributions of greenhouse gas emissions to global warming. *Nature* **344**, 529–531 (1990).

100. Singh, C. K., Kumar, A. & Roy, S. S. Quantitative analysis of the methane gas emissions from municipal solid waste in India. *Sci Rep* **8**, 2913 (2018).

101. Tollefson, J. IPCC climate report: Earth is warmer than it's been in 125,000 years. *Nature* **596**, 171–172 (2021).

102. Ankel-Fuchs, D. & Thauer, R. K. Methane formation from methyl-coenzyme M in a system containing methyl-coenzyme M reductase, component B and reduced cobalamin. *Eur J Biochem* **156**, 171–177 (1986).

103. Shima, S. *et al.* Structure of a methyl-coenzyme M reductase from Black Sea mats that oxidize methane anaerobically. *Nature* **481**, 98–101 (2012).

104. Heller, C., Hoppert, M. & Reitner, J. Immunological Localization of Coenzyme M Reductase in Anaerobic Methane-Oxidizing Archaea of ANME 1 and ANME 2 Type. *Geomicrobiology Journal* **25**, 149–156 (2008).

105. Wongnate, T. & Ragsdale, S. W. The Reaction Mechanism of Methyl-Coenzyme M Reductase. *J Biol Chem* **290**, 9322–9334 (2015).

106. Chen, S., Pelmenschikov, V., Blomberg, M. R. A. & Siegbahn, P. E. M. Is There a Ni-Methyl Intermediate in the Mechanism of Methyl-Coenzyme M Reductase? *J. Am. Chem. Soc.* **131**, 9912–9913 (2009).

107. Wongnate, T. *et al.* The radical mechanism of biological methane synthesis by methyl-coenzyme M reductase. *Science* **352**, 953–958 (2016).

108. Ermler, U., Grabarse, W., Shima, S., Goubeaud, M. & Thauer, R. K. Crystal Structure of Methyl-Coenzyme M Reductase: The Key Enzyme of Biological Methane Formation. *Science* **278**, 1457–1462 (1997).

109. Wagner, T., Kahnt, J., Ermler, U. & Shima, S. Didehydroaspartate Modification in Methyl-Coenzyme M Reductase Catalyzing Methane Formation. *Angewandte Chemie International Edition* **55**, 10630–10633 (2016).

110. Grabarse, W. *et al.* On the mechanism of biological methane formation: structural evidence for conformational changes in methyl-coenzyme M reductase upon substrate binding. *J Mol Biol* **309**, 315–330 (2001).

111. Cedervall, P. E., Dey, M., Pearson, A. R., Ragsdale, S. W. & Wilmot, C. M. Structural Insight into Methyl-Coenzyme M Reductase Chemistry using Coenzyme B Analogues,. *Biochemistry* **49**, 7683–7693 (2010).

112. Cedervall, P. E. *et al.* Structural analysis of a Ni-methyl species in methyl-coenzyme M reductase from Methanothermobacter marburgensis. *J Am Chem Soc* **133**, 5626–5628 (2011).

113. Weinert, T. *et al.* Serial millisecond crystallography for routine room-temperature structure determination at synchrotrons. *Nat Commun* **8**, 542 (2017).

114. Nango, E. *et al.* A three-dimensional movie of structural changes in bacteriorhodopsin. *Science* **354**, 1552–1557 (2016).

115. Kunz, R. C., Horng, Y.-C. & Ragsdale, S. W. Spectroscopic and Kinetic Studies of the Reaction of Bromopropanesulfonate with Methyl-coenzyme M Reductase*. *Journal of Biological Chemistry* **281**, 34663–34676 (2006).

116. Sierra, R. G. *et al.* The Macromolecular Femtosecond Crystallography Instrument at the Linac Coherent Light Source. *J Synchrotron Rad* **26**, 346–357 (2019).

117. Fuller, F. D. *et al.* Drop-on-demand sample delivery for studying biocatalysts in action at X-ray free-electron lasers. *Nat Methods* **14**, 443–449 (2017).

118. Alonso-Mori, R. *et al.* A multi-crystal wavelength dispersive x-ray spectrometer. *Review of Scientific Instruments* **83**, 073114 (2012).

119. Winter, G. *et al.* DIALS: implementation and evaluation of a new integration package. *Acta Cryst D* **74**, 85–97 (2018).

120. Brewster, A. S. *et al.* Improving signal strength in serial crystallography with DIALS geometry refinement. *Acta Cryst D* **74**, 877–894 (2018).

121. Hattne, J. *et al.* Accurate macromolecular structures using minimal measurements from X-ray free-electron lasers. *Nat Methods* **11**, 545–548 (2014).

122. Evans, P. R. An introduction to data reduction: space-group determination, scaling and intensity statistics. *Acta Crystallogr D Biol Crystallogr* **67**, 282–292 (2011).

123. Liebschner, D. *et al.* Macromolecular structure determination using X-rays, neutrons and electrons: recent developments in Phenix. *Acta Crystallogr D Struct Biol* **75**, 861–877 (2019).

124. McCoy, A. J. *et al.* Phaser crystallographic software. *J Appl Cryst* **40**, 658–674 (2007).

125. Emsley, P., Lohkamp, B., Scott, W. G. & Cowtan, K. Features and development of Coot. *Acta Cryst D* **66**, 486–501 (2010).

126. Adams, P. D. *et al.* PHENIX: a comprehensive Python-based system for macromolecular structure solution. *Acta Crystallogr D Biol Crystallogr* **66**, 213–221 (2010).

127. Afonine, P. V. *et al.* Towards automated crystallographic structure refinement with phenix.refine. *Acta Cryst D* **68**, 352–367 (2012).

128. *Emsley P, Cowtan K (2004). Coot: model-building tools for molecular graphics. Acta Crystallogr. D60, 2126-2132.*

129. Pettersen, E. F. *et al.* UCSF Chimera--a visualization system for exploratory research and analysis. *J Comput Chem* **25**, 1605–1612 (2004).

130. Pettersen, E. F. *et al.* UCSF ChimeraX: Structure visualization for researchers, educators, and developers. *Protein Sci* **30**, 70–82 (2021).

131. Otwinowski, Z. & Minor, W. [20] Processing of X-ray diffraction data collected in oscillation mode. *Methods Enzymol* **276**, 307–326 (1997).

132. Morin, A. *et al.* Collaboration gets the most out of software. *eLife* **2**, e01456 (2013).

133. *Jurcik, A., Bednar, D., Byska, J., Marques, S. M., Furmanova, K., Daniel, L., Kokkonen, P., Brezovsky, J., Strnad, O., Stourac, J., Pavelka, A., Manak, M., Damborsky, J., Kozlikova, B. : CAVER Analyst 2.0: Analysis and Visualization of Channels and Tunnels in Protein Structures and Molecular Dynamics Trajectories., Bioinformatics, bty386, 2018.*

134. Madeira, F. *et al.* The EMBL-EBI search and sequence analysis tools APIs in 2019. *Nucleic Acids Res* **47**, W636–W641 (2019).

135. Thauer, R. K. Methyl (Alkyl)-Coenzyme M Reductases: Nickel F-430-Containing Enzymes Involved in Anaerobic Methane Formation and in Anaerobic Oxidation of Methane or of Short Chain Alkanes. *Biochemistry* **58**, 5198–5220 (2019).

136. Nayak, D. D., Mahanta, N., Mitchell, D. A. & Metcalf, W. W. Post-translational thioamidation of methyl-coenzyme M reductase, a key enzyme in methanogenic and methanotrophic Archaea. *eLife* **6**, e29218 (2017).

137. *Protein structural ensembles are revealed by redefining x-ray eletron density noise. Lang PT, Holton JM, Fraser JS, Alber T. PNAS USA. 111 237-247*.

138. Hahn, C. J. *et al.* Crystal structure of a key enzyme for anaerobic ethane activation. *Science* **373**, 118–121 (2021).

139. Fransson, T. *et al.* X-ray Emission Spectroscopy as an in Situ Diagnostic Tool for X-ray Crystallography of Metalloproteins Using an X-ray Free-Electron Laser. *Biochemistry* **57**, 4629–4637 (2018).

140. Rabe, P. *et al.* X-ray free-electron laser studies reveal correlated motion during isopenicillin N synthase catalysis. *Sci Adv* **7**, eabh0250 (2021).

141. Albracht, S. P. J. *et al.* Five new EPR signals assigned to nickel in methyl-coenzyme M reductase from Methanobacterium thermoautotrophicum, strain Marburg. *Biochimica et Biophysica Acta (BBA) - Protein Structure and Molecular Enzymology* **955**, 86–102 (1988).

142. Butryn, A. *et al.* An on-demand, drop-on-drop method for studying enzyme catalysis by serial crystallography. *Nat Commun* **12**, 4461 (2021).

143. Johnson, T. W., Gallego, R. A., Brooun, A., Gehlhaar, D. & McTigue, M. Reviving B-Factors: Retrospective Normalized B-Factor Analysis of c-ros Oncogene 1 Receptor Tyrosine Kinase and Anaplastic Lymphoma Kinase L1196M with Crizotinib and Lorlatinib. *ACS Med Chem Lett* **9**, 878–883 (2018).

144. Tandrup, T. *et al.* Changes in active-site geometry on X-ray photoreduction of a lytic polysaccharide monooxygenase active-site copper and saccharide binding. *IUCrJ* **9**, 666–681 (2022).

145. Pfanzagl, V. *et al.* X-ray–induced photoreduction of heme metal centers rapidly induces active-site perturbations in a protein-independent manner. *Journal of Biological Chemistry* **295**, 13488–13501 (2020).

146. Sigfridsson, K. G. V. *et al.* Rapid X-ray photoreduction of dimetal-oxygen cofactors in ribonucleotide reductase. *J Biol Chem* **288**, 9648–9661 (2013).

147. Shtarkman, I. N., Gudkov, S. V., Chernikov, A. V. & Bruskov, V. I. Effect of amino acids on X-ray-induced hydrogen peroxide and hydroxyl radical formation in water and 8-oxoguanine in DNA. *Biochemistry Moscow* **73**, 470–478 (2008).

148. Ohmer, C. J. *et al.* XFEL serial crystallography reveals the room temperature structure of methyl-coenzyme M reductase. *J Inorg Biochem* **230**, 111768 (2022).

149. Schröder, G. C. & Meilleur, F. Metalloprotein catalysis: structural and mechanistic insights into oxidoreductases from neutron protein crystallography. *Acta Cryst D* **77**, 1251–1269 (2021).

150. Blakeley, M. P., Hasnain, S. S. & Antonyuk, S. V. Sub-atomic resolution X-ray crystallography and neutron crystallography: promise, challenges and potential. *IUCrJ* **2**, 464–474 (2015).

151. Michaelis, L. & Hill, E. S. THE VIOLOGEN INDICATORS. *J Gen Physiol* **16**, 859–873 (1933).

152. Jones, G. A. & Pickard, M. D. Effect of titanium (III) citrate as reducing agent on growth of rumen bacteria. *Appl Environ Microbiol* **39**, 1144–1147 (1980).

153. Otálora, F., Gavira, J. A., Ng, J. D. & García-Ruiz, J. M. Counterdiffusion methods applied to protein crystallization. *Progress in Biophysics and Molecular Biology* **101**, 26–37 (2009).

154. Arndtsen, B. A., Peterson, T. H. & Mobley, T. A. Selective intermolecular carbon - hydrogen bond activation by synthetic metal complexes in homogeneous solution. *Accounts of Chemical Research* **28**, (1995).

155. Liu, Y., Kim, J., Seo, H., Park, S. & Chae, J. Copper(II)-Catalyzed Single-Step Synthesis of Aryl Thiols from Aryl Halides and 1,2-Ethanedithiol. *Advanced Synthesis & Catalysis* **357**, 2205–2212 (2015).

156. Cumnock, K. *et al.* Trisulfide Modification Impacts the Reduction Step in Antibody–Drug Conjugation Process. *Bioconjugate Chem.* **24**, 1154–1160 (2013).